

Interrogating Liquid Surfaces via Reactive Atom Scattering

Maria Tesa Serrate

Submitted for the degree of Doctor of Philosophy

Heriot-Watt University

School of Engineering and Physical Sciences

March 2016

The copyright in this thesis is owned by the author. Any quotation from the thesis or use of any of the information contained in it must acknowledge this thesis as the source of the quotation or information.

Abstract

An investigation of the structure of various liquid surfaces has been conducted using Reactive Atom Scattering coupled to laser-induced fluorescence spectroscopy (RAS-LIF). In this technique, reactive collisions of gas-phase $O(^3P)$ atoms with hydrocarbon-based liquid surfaces produce OH radicals which are probed by laser-induced fluorescence in the gas phase. The relative fraction of the surface occupied by groups containing abstractable hydrogen atoms is quantified by the yield of OH. Therefore, RAS-LIF can be used to study the surface composition of liquids and mixtures containing alkyl groups. In addition, the technique yields information on the fundamental dynamics of gas-liquid interactions.

The dynamics of the interfacial H-abstraction reaction between $O(^3P)$ and the partially unsaturated hydrocarbon squalene ($C_{30}H_{50}$) has been studied for the first time. The yield and internal-state distribution of OH produced by this reaction have been characterised by RAS-LIF. In comparison with the fully saturated analogue, squalane ($C_{30}H_{62}$), the results show that the $O(^3P)$ atoms are extremely sensitive to the type of C–H bond where reaction takes place, and the products partially accommodate their energy at the liquid surface. There is an additional channel for $O(^3P)$ loss on squalene, inferred to be addition to exposed unsaturated sites at the liquid surface.

RAS-LIF has been employed to characterise the surfaces of ionic liquids containing alkyl chains. The $O(^3P)$ atoms react selectively with CH_2 groups, acting as a quantitative surface-specific probe of the alkyl chains at the surface. The results show that the interfacial composition is different from that of the bulk, with alkyl chains being preferentially exposed at the surface. A series of ionic liquids and mixtures containing 1-alkyl-3-methylimidazolium and 1-alkyl-1-methylpyrrolidinium cations has been investigated. It has been found that alkyl surface coverage depends strongly on the length of the alkyl chain and the chemical identity of the anion, but not on the cation headgroup (imidazolium or pyrrolidinium). Measurements on ionic liquid mixtures show that their surfaces are enriched in cations and anions that are relatively nonpolar, and depleted in polar ions.

“Utopia lies at the horizon.

When I draw nearer by two steps, it retreats two steps.

If I proceed ten steps forward, it swiftly slips ten steps ahead.

No matter how far I go, I can never reach it.

What, then, is the purpose of utopia?

It is to cause us to advance.”

— Eduardo Galeano

(The Book of Embraces)

Acknowledgements

This thesis would not have been possible without the help of many people. First, I would like to thank my primary supervisor, Prof. Ken McKendrick, whose guidance and support have been invaluable to me. I am very grateful that he always had time to listen to me despite his (very) busy schedule. My secondary supervisor, Dr Matt Costen, deserves to be equally acknowledged. His vast knowledge of laser spectroscopy and his willingness to share it have been of great help in the lab.

During these years I have worked alongside a number of students and postdocs, all of whom had some input into this thesis. More important, their presence made the lab work enjoyable (even the unsuccessful experiments!). Thanks to Grant Paterson, Kerry Relf, Apostolos Tatas, Simon Purcell, Yelena Timoshenko, Robert Bianchini, Nicolle Giuliani, Matt Bain and Elena Watts.

Much of the work presented in this thesis was carried out as part of a broader collaborative project. The other members were Lucía D'Andrea, Duncan Bruce, John Slattery (University of York); George Schatz (Northwestern University); Brooks Marshall, Eric Smoll, and Tim Minton (Montana State University). All of them have contributed greatly to this work by providing materials, complementary experiments and insightful discussion.

Thanks to other members of the Heriot-Watt Physical Chemistry section (too many to name on one page!) for their help and for providing a great working environment. Our social events and evenings out have helped me stay sane through difficult times, and I really appreciate that.

Finally, I would like to thank my friends and family in Spain, especially my grandmother, for their patience and encouragement. Thank you for always respecting my decisions.

Table of contents

| | |
|---|-----------|
| Chapter 1: Introduction | 1 |
| 1.1. Motivation and scope | 1 |
| 1.2. Previous work on gas-liquid dynamics..... | 6 |
| 1.2.1. Inelastic gas-liquid collision dynamics..... | 7 |
| 1.2.2. Reactive gas-liquid collision dynamics | 16 |
| 1.2.3. Gas-liquid collisions as an analytical probe of surfaces..... | 22 |
| 1.3. Reactive O(³ P) scattering as a probe of surface structure | 24 |
| | |
| Chapter 2: Experimental | 28 |
| 2.1. The liquid surface | 28 |
| 2.1.1. Surface generation method and general handling of liquids | 28 |
| 2.1.2. Liquid purity considerations | 30 |
| 2.2. Reaction chambers | 31 |
| 2.2.1. Single-wheel setup..... | 32 |
| 2.2.2. Multiple-wheel setup | 34 |
| 2.3. Generation of gas-phase radicals..... | 36 |
| 2.3.1. Photolysis laser | 37 |
| 2.3.2. O(³ P) generation | 37 |
| 2.3.3. HONO generation..... | 39 |
| 2.4. Detection method..... | 40 |
| 2.4.1. Fundamentals of Laser-Induced Fluorescence | 40 |
| 2.4.2. The spectroscopy of the OH radical | 41 |
| 2.4.3. Probe laser | 46 |
| 2.4.4. Detection system..... | 46 |
| 2.5. Instrument control and data acquisition | 47 |
| 2.6. Experimental outputs..... | 48 |
| 2.6.1. Appearance profiles | 48 |
| 2.6.2. Excitation spectra..... | 55 |

| | |
|---|-----------|
| Chapter 3: Interfacial reaction of O(³P) with an unsaturated hydrocarbon..... | 58 |
| 3.1. Introduction | 58 |
| 3.2. Experimental..... | 62 |
| 3.3. Results | 63 |
| 3.3.1. Appearance profiles | 63 |
| 3.3.2. Excitation spectra | 73 |
| 3.4. Discussion..... | 84 |
| 3.4.1. Relative OH yields..... | 84 |
| 3.4.2. Energy partition | 88 |
| 3.4.3. Effect of the liquid surface on the dynamics | 92 |
| 3.5. Summary points..... | 95 |
| | |
| Chapter 4: Reactive O(³P) scattering from pure imidazolium-based ionic liquids. | 96 |
| 4.1. Introduction | 96 |
| 4.1.1. Previous studies of imidazolium-based ionic liquid surfaces..... | 96 |
| 4.1.2. Reactive Atom Scattering from ionic liquids | 106 |
| 4.2. Experimental..... | 107 |
| 4.3. Results | 111 |
| 4.4. Discussion..... | 122 |
| 4.4.1. Variation of alkyl chain length | 123 |
| 4.4.2. Variation of anion | 133 |
| 4.5. Summary points..... | 141 |

| | |
|--|------------|
| Chapter 5: Reactive O(³P) scattering from pure pyrrolidinium-based ionic liquids | 142 |
| | |
| 5.1. Introduction | 142 |
| 5.2. Experimental..... | 144 |
| 5.2.1. Liquids studied and experimental conditions | 144 |
| 5.2.2. Setting up and calibration of the 4-wheel apparatus..... | 148 |
| 5.3. Results | 156 |
| 5.3.1. Effect of surface temperature on OH yields | 156 |
| 5.3.2. Excitation spectra..... | 157 |
| 5.3.3. Appearance profiles | 159 |
| 5.4. Discussion..... | 162 |
| 5.5. Summary points..... | 167 |
| | |
| Chapter 6: Reactive O(³P) scattering from ionic liquid mixtures. | 168 |
| 6.1. Introduction | 168 |
| 6.2. Experimental..... | 171 |
| 6.3. Results | 171 |
| 6.3.1. Binary mixtures with a common anion, [C ₂ mim] _(1-x) [C ₁₂ mim] _x [Tf ₂ N] | 171 |
| 6.3.2. Binary mixtures with a common cation, [C ₆ mim][BF ₄] _(1-x) [Tf ₂ N] _x | 177 |
| 6.4. Discussion..... | 180 |
| 6.4.1. Surface structure of [C ₂ mim] _(1-x) [C ₁₂ mim] _x [Tf ₂ N] | 180 |
| 6.4.2. Surface structure of [C ₆ mim][BF ₄] _(1-x) [Tf ₂ N] _x | 191 |
| 6.5. Summary points..... | 194 |
| | |
| Chapter 7: Conclusions and future work | 195 |
| | |
| References | 199 |
| | |
| Appendix: Publications | 217 |

Chapter 1.

Introduction

1.1. Motivation and scope

The structures of liquid surfaces and their interaction with gas-phase chemical species play a crucial role in many natural phenomena and industrial applications. Processes such as respiration, multiphase catalysis or heterogeneous atmospheric reactions all have one thing in common: a chemical reaction at the gas-liquid interface, or the transport of a gas-phase species through the interface, is a key step in their mechanism. An understanding of the microscopic structure of liquid surfaces and the fundamental dynamics of their interfacial reactions would be highly beneficial to a wide variety of fields. However, gas-liquid interfaces have until recently remained relatively uninvestigated compared to their gas-solid counterparts. The reason for this is that liquid surfaces are far more complex: they are disordered, less defined and highly dynamic so they are challenging to characterise. One approach for probing gas-liquid interfaces is to use controlled collisions with gas-phase projectiles, detecting the species that scatter from the surface back into the gas phase [1]. The chemical identity of the product, its internal and translational energy and scattering angle provide information on the liquid surface structure and the mechanism of the interaction, in a similar way to more traditional gas-phase studies of reaction dynamics [2].

The aim of this thesis is to study the surfaces of hydrocarbon and ionic liquids using their reaction with gas-phase atomic oxygen in its ground state, $O(^3P)$. Besides being interesting from a fundamental point of view, the dynamics of the interfacial reaction provides valuable information on the composition of the surface. This work builds on previous studies on $O(^3P)$ + liquid surface reactions [3-12], making use of their findings to interpret the new results. Here the technique is labelled as Reactive Atom Scattering (RAS). The same experimental approach has been applied to two different areas of study: the dynamics of H abstraction from an unsaturated liquid hydrocarbon (Chapter 3), and probing the surface composition of ionic liquids (Chapters 4 to 6). Below is a brief outline of the motivation for each type of experiment.

Chapter 3 is concerned with the dynamics of H abstraction by $O(^3P)$ from the surface of liquid squalene (trans-2,6,10,15,19,23-hexamethyltetracosane-2,6,10,14,18,22-hexaene), a partially unsaturated hydrocarbon. Although this research is mainly fundamental, it is of tangential interest in some applications. For example, hydrocarbon liquids are widely used as proxies for atmospheric aerosols in laboratory studies [13-15]. Aerosols are particles present in the troposphere (< 11 km altitude) and stratosphere (11 – 50 km) which significantly affect the Earth's climate as they can cause local cooling and act as cloud condensation nuclei. They can be either formed in the atmosphere or directly emitted by biogenic or anthropogenic sources, and in many cases contain organic matter such as aromatic, saturated or partially unsaturated hydrocarbons [16]. The chemical composition of an aerosol, in particular the functional groups exposed at its surface, greatly influences its chemistry and properties. Some aerosols are composed of an inorganic core with an organic coating on their outer surface [14]. This outer hydrophobic layer, which plays an important part in cloud condensation activity as it controls the size of the droplets, can be transformed into a hydrophilic layer after oxidation initiated by gas-phase radicals (mainly OH, O_3 and NO_3). This has been the main motivation behind studies of the interfacial oxidation of functionalised hydrocarbon liquids and self-assembled monolayers (SAMs) [13-15, 17]. Of particular interest to this work, the reactions of OH radicals with liquid hydrocarbons have been previously investigated by scattering OH from saturated and partially unsaturated liquid hydrocarbons [18-20]. The analogous reaction with $O(^3P)$ studied in this thesis provides complementary information on the structure and reactivity of unsaturated hydrocarbon surfaces.

Atomic oxygen does not play a significant role in aerosol chemistry because it is not present in the lower atmosphere. It is, however, a major component of the low Earth orbit (LEO), the region between 160 and 2000 km altitude where most artificial satellites orbit. $O(^3P)$ in the LEO causes substantial damage to spacecraft as it causes degradation of polymeric materials [21-23]. H abstraction is one of the possible mechanisms; in consequence, a fundamental understanding of the reaction of $O(^3P)$ with hydrocarbons may help develop erosion-resistant spacecraft materials.

The high reactivity of $O(^3P)$ atoms can also be used to advantage. Oxygen plasmas, which contain $O(^3P)$ amongst other species, are routinely used in the semiconductor industry to remove polymer coatings. In addition, polymers for biomedical applications may be treated with plasmas in order to sterilise and modify

their surfaces, improving biocompatibility [24, 25]. Recently, oxygen atoms have found unexpected applications in the restoration of damaged artwork [26]. A good knowledge of the chemical behaviour of $O(^3P)$ is necessary for developing these applications further, as well as finding new ones.

In Chapters 4, 5 and 6, RAS of $O(^3P)$ on the surface of ionic liquids has been employed to investigate their structures and to determine the fraction of hydrocarbon chains that occupy the surface. Ionic liquids (ILs) are molten salts at low temperature. They are generally composed of large organic cations and inorganic anions; these large ions result in lower melting points than those of traditional inorganic salts. The upper limit of melting temperature for a salt to be considered an IL has been arbitrarily defined as 100 °C [27]. Figure 1.1 presents the chemical structures and abbreviated names of some of the most common ions that can be found in ILs. There are many other examples of ions: it has been estimated that millions of ILs are possible [28]. The vast number of accessible ion pairs enables “fine-tuning” the physicochemical properties of the liquid by varying the composition of the cation or the anion. This tunability makes ILs suitable for a wide range of applications, some of which are discussed below.

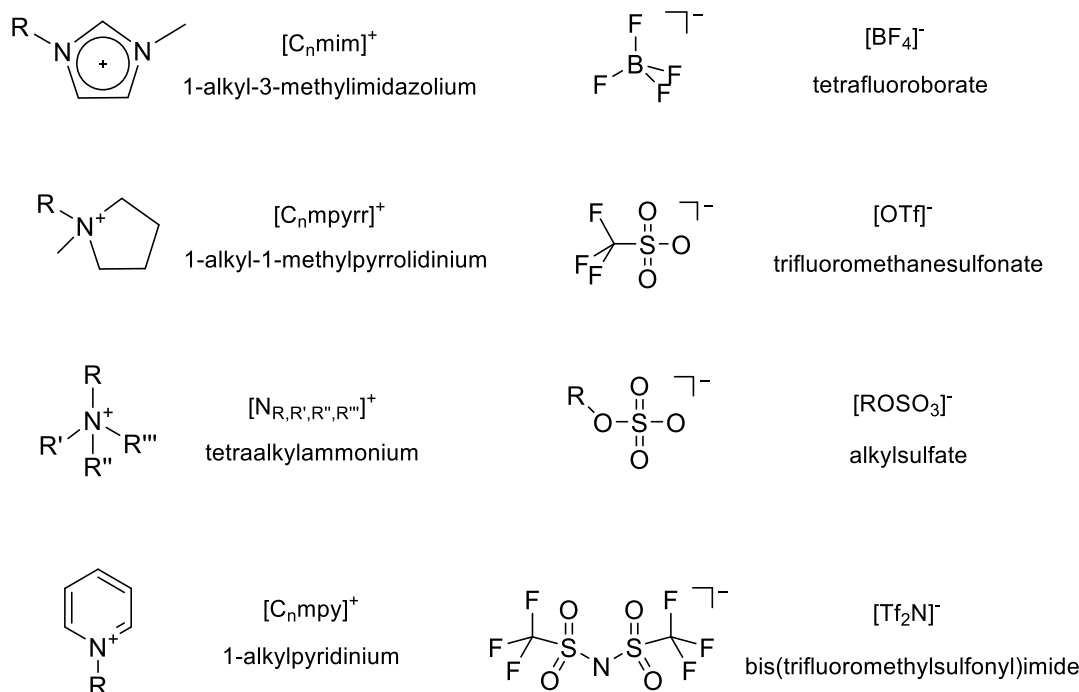


Figure 1.1. Chemical structures, names and abbreviations of cations and anions commonly used in ionic liquids.

Although low-temperature molten salts had long been known, they gained popularity in the 1990s after being proposed as “green solvents” for chemical synthesis thanks to their low vapour pressures and chemical stability [29, 30]. This prompted an exponential increase in IL research over the last two decades, which has led to many industrial applications being found for ILs [31]. The IL surface plays a crucial role in some of these applications. For example, ILs are used as solvents for extraction in analytical chemistry, stationary phases in gas chromatography and electrode modifiers in sensors [32]. Gas separation and storage is another promising application thanks to the high solubility of some gases in ILs [33]. In particular, a great deal of theoretical and experimental work has been directed towards the use of ILs for CO₂ capture [34-36]. This could be implemented with the IL immobilised inside a porous matrix through which the gas mixture to be processed circulates, increasing the surface area per unit volume with respect to traditional biphasic systems. This is known as a supported ionic liquid membrane, or SILM [37, 38]. A similar approach is followed in SILP, or supported ionic liquid phase catalysis. In this case a catalyst is dissolved in the ionic liquid for reactions such as hydrogenation and hydroformylation [39, 40].

The processes mentioned above involve the adsorption of gases or their absorption through the gas-liquid interface; in consequence, the liquid surface is expected to affect them. Despite this, the interfacial characteristics of ionic liquids have not been studied as widely as their bulk properties. Typically there are polar and non-polar regions in the ions that constitute the ionic liquids, resulting in a complex interplay of electrostatic forces that makes it difficult to predict the structure of the surface. The composition of the surface may be different from that of the bulk, and layering may occur at the interface (Figure 1.2). In order to characterise these effects, there have been many recent experimental surface analysis studies of ionic liquids, leading to some design rules being established [41]. Essentially, nonpolar (or *ionophobic*) regions of the molecule tend to be located close to the outer surface, while regions with a high charge density (or *ionophilic*) are preferentially closer to the bulk. Predicting the detailed structure of the surface, such as the relative location of cations and anions and their orientation, is still a challenge. This is partly due to the lack of accurate, surface-sensitive experimental techniques that can provide reliable information on the IL surface against which to test the predictions.

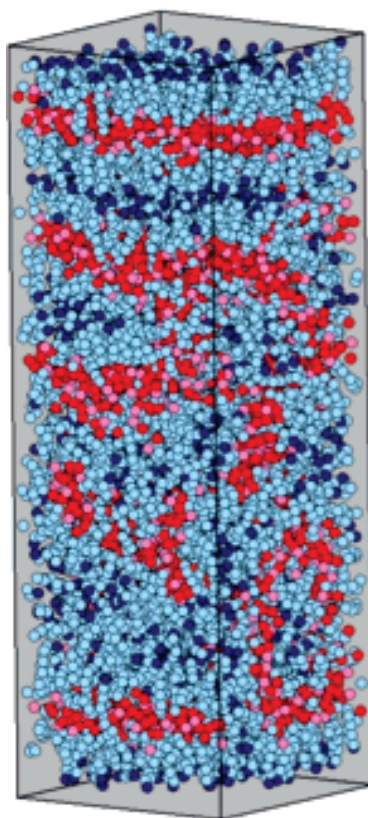


Figure 1.2. Simulation of $[\text{C}_{12}\text{mim}][\text{NO}_3]$ (1-dodecyl-3-methylimidazolium nitrate), showing layering of the ions at the surface (top and bottom faces). Imidazolium rings (red), nitrate anions (pink), CH_2 groups (light blue) and terminal CH_3 group in dodecyl (dark blue) are shown. Reprinted from Jiang *et al.* [42].

As will be discussed later below, RAS can accurately characterise differences in alkyl coverage between IL surfaces, and thus help to unravel their surface-bulk composition relationships. Alkyl chains are the nonpolar moieties in the most common types of ionic liquids. They are expected to preferentially occupy the surface, which can affect the polarity of the interface and potentially change its affinity towards gas-phase species. A detailed understanding of the hydrocarbon coverage of IL surfaces can potentially help the design of ILs for particular applications in which the interaction with a gas is important.

1.2. Previous work on gas-liquid dynamics

The dynamical features of gas-liquid interactions had not been extensively studied until recently. The past two decades have seen a rise in this area of research, starting with molecular beam experiments in the 1990s [1]. Building on this work, an increasing number of studies have contributed to the development of the field. The exact experimental techniques employed vary but they all share the same basic approach. Essentially, gas-phase projectiles are directed towards a liquid surface using a molecular beam or laser photolysis of a precursor molecule. The projectiles can be atoms, molecules, or radicals generated by electric discharge or photolysis. When they reach the surface they interact with it either through an inelastic collision, involving an energy exchange, or through a chemical reaction. The products of the reaction or the inelastic encounter then escape into the gas phase, where they are detected by a spectroscopic technique or by mass spectrometry. The distribution of scattering angles, translational and internal energies of the products contain information about the nature of the gas-liquid interaction.

In order to obtain dynamical information on the gas-liquid collision, the scattered product must be detected *before* it encounters another species in the gas phase. This means that the experiments must be conducted under vacuum so that the products have a reasonably long mean free path. One challenge that all of the experiments face is the evaporation of the liquid under vacuum, which produces secondary collisions in the gas phase. Studying liquids of high vapour pressure such as water requires the use of sophisticated techniques facing significant technical challenges. Despite some promising recent work using liquid microjets [43, 44], the study of high-vapour pressure liquids *in vacuo* is not yet fully developed. For this reason, the majority of the studies to date have focused on liquids with low vapour pressure such as long-chain hydrocarbons [45], polymers [46], liquid crystals [47], ionic liquids [48] or concentrated solutions [49]; as well as related surfaces such as SAMs [50]. Both reactive and inelastic processes have been studied using different methods of detection. In addition, a considerable amount of effort has been directed towards theoretical studies of gas-liquid collision dynamics. What follows is an overview of previous experimental and theoretical work on gas-liquid scattering, divided into inelastic and reactive scattering studies. The discussion is focused on liquid surfaces and scattering of atoms, molecules and radicals, since these are the most relevant to this thesis. Scattering from SAMs [51]

or of high-energy ions [52] is not covered generally in this introduction, except for studies that are of specific interest to this work.

1.2.1. Inelastic gas-liquid collision dynamics

Experimental studies

The fundamental dynamical features of gas-liquid collisions are perhaps best distinguished in nonreactive collisions with projectiles such as rare gas atoms. This was the approach of the first studies performed by Nathanson and co-workers, which are some of the earliest examples of gas-liquid scattering experiments [45, 53-55]. A beam of inert gas atoms was created by supersonic expansion and scattered from a liquid surface and the products were detected by mass spectrometry (MS). The surface was generated using a rotating wheel which was partially immersed in a bath containing the liquid of interest. This approach, first adopted by Lednovich and Fenn in 1977 [56], has become the most popular method to generate a continually refreshed liquid surface under vacuum. As the wheel rotates, a thin layer of liquid is formed on its surface, and this layer is regenerated on each new rotation avoiding a build-up of adsorbed species.

The use of molecular beams allows the incident angle and speed of the projectiles to be controlled. This, in combination with MS detection, provides detailed information on the scattering angles and speeds of the products. As previously observed in gas-solid collisions [57], the product distributions in the Nathanson experiments were found to be well described empirically as the sum of two components [45], which are labelled here as *impulsive scattering* (IS) and *thermal desorption* (TD). This bimodal behaviour is a general feature of gas-liquid collisions, as will be discussed later. IS products scatter at an almost-specular angle with superthermal energies that depend on the incident energy. They are thought to arise from direct, gas-phase-like encounters with the liquid surface so that a localised interaction with a few functional groups at the surface determines the outcome of the collision. The IS scattering angles are narrowly distributed around a final angle θ_f defined with respect to the surface normal. In contrast, TD products are scattered around the surface normal in a $\cos(\theta_f)$ distribution, which is much broader than for IS. They possess low translational energies, following a Maxwell-Boltzmann distribution at the temperature of the liquid surface. The simplest interpretation is that they are the result of longer, multiple-collision interactions with the surface so that the projectile exchanges energy with the surface and becomes thermalized. Figure 1.3 shows a schematic representation of typical IS and TD distributions. In the figure, θ_i is

the angle of incidence of the projectile with respect to the surface normal. Although the IS and TD distributions are a useful tool to characterise the reaction dynamics, it should not be assumed that the scattering mechanism follows this simple binary separation. The reality is more complex, as will be discussed later.

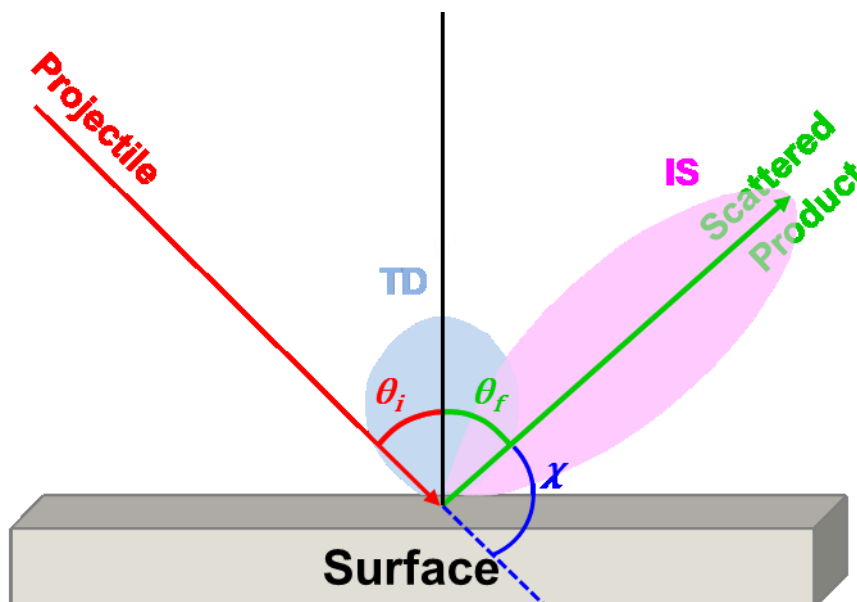


Figure 1.3. Schematic representation of a scattering trajectory showing the incident (θ_i), final (θ_f), and deflection angle (χ). Typical IS and TD angular distributions are shown in magenta and blue, respectively.

Nathanson [45, 53-55, 58] studied the inelastic scattering of inert gases from the liquid hydrocarbon squalane (2,6,10,15,19,23-hexamethyltetracosane) and the perfluorinated polymer PFPE (perfluoropolyether). Squalane is a saturated hydrocarbon composed of CH_3 , CH_2 and CH functional groups, while the chemical structure of PFPE contains ether, CF_3 , CF_2 and CF groups. Time-of-flight (TOF) mass spectra were obtained by using a chopper wheel to select fractions of the scattered products with different kinetic energy. The TOF spectra showed clear IS and TD components. It was found that squalane produced a much larger fraction of TD, and this fraction decreased with increasing collision energy for both liquids. The authors explained this difference between liquids in terms of kinematics: in a hard-sphere collision in classical mechanics, a more massive collision partner results in less efficient energy transfer. PFPE is composed of CF_x groups, while squalane exposes CH_x groups on its surface. The heavier, denser structure of PFPE produces more direct encounters while the lighter and loosely packed squalane absorbs more energy and induces thermalisation. A

similar effect was observed by Cohen in an earlier study of rare gases scattering from self-assembled monolayers [50]: the nonthermal fraction of the distribution had higher translational energy and was more significant for He scattered from a perfluorinated monolayer (hereafter abbreviated as F-SAM) than from an aliphatic monolayer (H-SAM). Comparing Ar to He, the former transferred more energy to the surface due to its larger mass. It was suggested that the aliphatic chains form a *soft* surface, that is, one that allows a large transfer of momentum [59]. The timescale of the collision with a soft surface is long and thermalisation may take place by energy transfer to internal modes of the surface. The F-SAM gives a *hard* surface, i.e. there is little transfer of momentum to the surface. In this case the interaction is shorter and the energy of the recoiling atom is correlated to its incoming translational energy, instead of being related to the surface temperature.

The trends in energy transfer with projectile mass and incidence angle are similar for all gas-liquid inelastic scattering experiments: lower (i.e. more normal) θ_i and θ_f , higher collision energy, larger projectiles and softer surfaces all lead to more energy being transferred to the liquid surface. By analogy with gas-phase dynamics, a simple model assuming a hard-sphere collision between the projectile and the surface has been proposed to describe the energy transfer [1]. This model treats the projectile and surface as two spheres of defined masses, so that the energy transferred to the surface ($\Delta E = E_i - E_f$, where E_i and E_f are the incident and final energy of the projectile, respectively) is the product of a kinematic term and a potential energy term:

$$\begin{aligned} \frac{\Delta E}{E_i} &= \frac{4\mu}{(1+\mu)^2} \cos^2 \theta_i \cdot \left[1 + \frac{V - 2RT_{liq}}{E_i} \right] \\ &= \frac{2\mu}{(1+\mu)^2} \left[1 - \cos \chi (1 - \mu^2 \sin^2 \chi)^{\frac{1}{2}} + \mu \sin^2 \chi \right] \cdot \left[1 + \frac{V - 2RT_{liq}}{E_i} \right] \end{aligned} \quad (1.1)$$

The kinematic term (first term in Equation 1.1) can be expressed in terms of the incidence angle θ_i , or the deflection angle $\chi = 180 - \theta_i - \theta_f$. It also depends on the mass ratio between the projectile and the surface, $\mu = m_{gas}/m_{surf}$. Thus, the liquid surface is characterised by an effective surface mass m_{surf} such that a small m_{surf} (large μ) induces a large ΔE . The effective surface mass decreases with E_i because the energy is dissipated less efficiently [1]. It can also be inferred from the equation that a larger angle of deflection χ (i.e. “head-on” collisions with backscattered products) increases the energy transfer, whilst a smaller χ (i.e. “glancing” collisions) leads to a smaller ΔE .

The outcome of a collision also depends on the intermolecular forces between the surface and the projectile. The second term in Equation 1.1 introduces a simple gas-surface potential V which causes acceleration of the molecule in the incident trajectory and deceleration in the exit trajectory. Thermal motions of the liquid surface produce a net acceleration of the scattered projectile, and so the liquid temperature T_{liq} has a negative effect on ΔE .

Minton and co-workers showed that the hard-sphere model breaks down for collisions of hyperthermal oxygen and argon atoms with squalane, PFPE and SAMs [60, 61]. In these cases, the effective surface mass m_s is greater for hydrocarbon surfaces, despite the fact that they lead to higher ΔE . It is therefore necessary to account for the internal excitation of the surface and scattered species to successfully describe the energy transfer. The hard sphere model was transformed into a soft sphere model with two adjustable parameters: the deflection angle χ and the internal excitation of the collision partners E_{int} . For an atomic projectile, E_{int} describes all other motions of the surface atoms other than the direct recoil of the single mass predicted by momentum conservation. The kinematic expression for a soft sphere collision is described by the following equation:

$$\frac{\Delta E}{E_i} = \frac{2\mu}{(1+\mu)^2} \left[1 - \cos\chi \left(1 - \mu^2 \sin^2\chi - \frac{E_{int}}{E_i} (\mu + 1) \right)^{\frac{1}{2}} + \mu \sin^2\chi + \frac{E_{int}}{E_i} \left(\frac{\mu+1}{2\mu} \right) \right] \quad (1.2)$$

Equation 1.2 provided a good description of the O and Ar scattering experiments [61], and showed that E_{int} was higher for hydrocarbon liquids and H-SAMs as opposed to fluorinated surfaces. Hydrocarbon chains are more labile and move cooperatively upon a projectile impact, whereas the interaction is more local in the case of the more rigid fluorinated chains. Squalane has a greater surface mass than PFPE because more CH_x groups take part in the interaction. At high incidence energies, the effect of E_{int} is reduced and the collision approaches the hard sphere limit, especially for PFPE. A similar effect was observed in separate SAMs simulations [51]: the surface internal modes were more easily excited for H-SAMs as opposed to fluorinated F-SAMs. These results reveal that the gas-surface interactions are not localised in one functional group, but rather many atoms on the surface, and hence differ from a gas-phase collision. For example, the effective surface mass for squalane on collisions with $\text{O}(^3\text{P})$ atoms was found to be ~ 76 amu for $E_i = 47 \text{ kJ mol}^{-1}$ [60], much higher than that of a single CH_3 group.

There are further fundamental differences with gas-phase collisions, such as the effect of the microscopic structure of the surface on the results. A *rough* liquid surface induces multiple encounters with surface atoms, and therefore a greater fraction of TD trajectories. In contrast, a *smooth*, less structured surface promotes single-impact collisions and IS-like trajectories. The temperature of the surface affects its roughness: thermal motion of the molecules produces a rougher, less densely-packed surface and this increases the chance of multiple collisions. Scattering experiments at different temperatures confirmed this effect for PFPE [62, 63] and squalane [6]. The surface corrugation was modelled with a sinusoidal function by Tully and co-workers, who developed the washboard with moment of inertia (WBMI) model of gas-surface scattering [64].

It is necessary to characterise the internal energy of molecular products in order to obtain a full picture of the scattering dynamics. This cannot be achieved with mass spectrometry, so it is necessary to use a spectroscopic method of detection instead. Early experiments on scattering of NO from self-assembled monolayers employed resonance-enhanced multiphoton ionization (REMPI) spectroscopy to probe the internal energy levels of the scattered NO radicals [59, 65]. A jet-cooled beam of NO was used; therefore the NO radicals impinging on the surface were rotationally cold and had a narrow distribution of translational energies. This provided well-resolved information on the translational and rotational energy transferred to the projectile. The authors found a positive correlation between translational and rotational energy: NO radicals belonging to the IS fraction of products were more rotationally excited than those in the TD channel. In addition, F-SAMs gave hotter NO rotational and translational distributions than H-SAMs. Similar results were obtained in later studies using liquid surfaces, the first of which concerned the inelastic scattering of I₂ from PFPE, squalane and PDMS (perfluorodimethylsiloxane) [46, 66, 67]. The incident I₂ was seeded in a molecular beam so it was internally cold. Using laser-induced fluorescence (LIF), the authors identified a rotational warming of the TD fraction of products for all of the liquids.

More recently, infrared absorption spectroscopy was used by Nesbitt and co-workers to probe CO₂ scattering from liquid surfaces [68-75]. Jet cooling of the incident CO₂ provided a low rotational temperature, with only a few states being populated. This allowed well-resolved information on the dynamics of rotational energy transfer to be obtained. Different liquids, collision energies [69], angles of incidence [70] and liquid

temperatures [73] were investigated. The rotational distributions of the scattered CO₂ were in all cases hotter than the incident molecular beam, indicating translation-to-rotation energy transfer at the surface. The extent of rotational excitation increased with incident energy. Vibrational excitation of CO₂ at the surface was, however, much less efficient, which the authors attributed to the timescale of the gas-surface interaction: vibrational accommodation at the surface requires more time than rotational energy transfer. The mechanism of rotational excitation at the surface was further investigated by polarization-modulated IR spectroscopy, which allowed orientation and alignment effects to be studied [72, 75]. It was found that the highly corrugated surface of PFPE induces impulsive torques on the scattered CO₂ molecules, promoting forward end-over-end tumbling.

The CO₂ rotational distributions, together with product translational energies from Dopplerimetry measurements, indicated that thermalized products accommodate both their translational and rotational energy at the surface. The Doppler-resolved absorption profiles in the direction perpendicular to the surface normal for each rotational state were fitted to a sum of IS and TD contributions. The rotational distributions were best described by the 2-temperature Boltzmann model in Equation 1.3. This model assumes that the rotational distribution extends sufficiently for the partition function to be simply proportional to the temperature.

$$\frac{P(N)}{2J+1} = C \left[\left(\frac{\alpha}{T_1} \right) e^{\frac{-E_{rot}(N)}{kT_1}} + \left(\frac{1-\alpha}{T_2} \right) e^{\frac{-E_{rot}(N)}{kT_2}} \right] \quad (1.3)$$

The cold temperature T_1 was assigned to the TD component and constrained to 300 K, while the hot temperature T_2 was assigned to the IS products. Nesbitt interpreted α as a TD fraction, that is, the fraction of incident CO₂ molecules that rotationally thermalised with the surface [68]. The values of the translational and rotational temperatures for the IS channel were similar, supporting the IS/TD model. However, it should be noted that the α parameter did not match the TD fraction inferred from the Doppler profiles, which suggests that a simple binary model is not sufficient to describe the scattering dynamics fully. Nevertheless, the results showed a clear correlation between the component of translational energy parallel to the surface and the rotational energy in the scattered CO₂.

Recent experiments in the McKendrick group interrogated the collisions of OH radicals with hydrocarbon and perfluorinated surfaces [18-20]. OH radicals were generated

from laser photolysis of a low pressure of a precursor along an axis close to the liquid surface. This approach lacks the initial velocity resolution that a molecular beam would provide but, on the other hand, it gives access to a wider range of initial rotational states. Two different OH precursors, nitrous acid (HONO) [18, 19] and allyl alcohol [20], were used. The photolysis of HONO with 355 nm light produces OH radicals with near-thermal rotational energy [76], whilst 193 nm photolysis of allyl alcohol produces OH which is both translationally and rotationally hot [77]. In the HONO experiments [18, 19], the scattered OH was well described with a single rotational temperature that was higher than the incident value, indicating the presence of an IS channel with significant translational-to-rotational energy transfer in the collision. The products were hotter for PFPE, reflecting the trends in surface stiffness introduced above. In the allyl alcohol experiments [20], OH scattered from the surface with a bimodal distribution of rotational temperatures, one corresponding to room temperature and the other being superthermal. However, the TD fraction α from the bimodal rotational fits was again in substantial disagreement with the thermal fractions inferred from translational distributions. These results cast doubt on the interpretation of the empirical parameter α as a simple and direct measure of the TD fraction.

Theoretical studies

The inelastic scattering experiments discussed so far provided an insight into gas-liquid scattering dynamics, and found some common features that are independent of the system studied. However, they left some unanswered questions, especially regarding the validity of the “IS vs TD” binary model. Theoretical studies help unravel the mechanism of the interfacial interaction, since they allow the individual trajectories of the projectiles as they scatter from the surface to be studied. It is also possible to observe the behaviour of the surface as it dissipates the collision energy, which is not accessible to current experimental methods.

In order to simulate a gas-liquid collision, the first thing needed is a realistic model of the liquid surface. This can be computationally demanding, which is why many of the early theoretical studies employed simulated SAMs instead of liquid surfaces [78-81]. SAMs possess the flexible chains and intermolecular interactions of liquid surfaces but they are less challenging to model. Scattering of gases on SAMs, as well as liquid surfaces, can be simulated by classical molecular dynamics (MD) simulations. The MD

calculations involve solving the classical equations of motion for the atoms using a suitable interatomic potential or force field.

Hase and co-workers employed a united-atom (UA) model to simulate H-SAM surfaces for Ne atom scattering, treating each CH_x unit as a single atom [78, 82, 83]. Explicit atom (EA) models have been found to provide better agreement with experiments in some cases, as they describe better the stiffness of the surface [74]. The gas-surface potential was derived from *ab initio* calculations on the gas-phase $\text{Ne} + \text{CH}_4$ system [78]. The simulations roughly agreed with the IS/TD model, but showed some effects that were not accounted for by it: although the scattered products followed a bimodal distribution, the colder fraction was not well fitted by the surface temperature [82]. It was proposed that coupling to the chain internal modes during the timescale of the collision resulted in thermalized products. In addition, it was found that single-collision products, which are expected to follow an IS distribution, were best described by a sum of two Maxwell-Boltzmann distributions, showing that thermalisation does not necessarily imply trapping at the surface [83].

The simulations were later extended to $\text{Ar} + \text{H-SAM}$ systems [84-86], and were found to agree with complementary experiments. Just like in the scattering experiments on liquid surfaces, the energy transfer dynamics was influenced by temperature and incident angle [84] as well as by the chain packing density [85]. In a later study, a nonreactive potential was used to simulate the inelastic scattering of $\text{O}(^3\text{P})$ from an H-SAM [87], and the dynamics were very similar to those for inert gas + H-SAMs. Morris studied different projectiles scattering from CF_3 -, CH_3 - and OH -terminated H-SAMs, and F-SAMs, again finding good agreement between theory and experiment [88-90]. Finally, simulated F-SAMs have been used as proxies for liquid surfaces in collisions with CO_2 [74, 91-93], OH [94], NO [95] and O_3 [96].

The $\text{CO}_2 + \text{F-SAMs}$ simulations by Hase [74, 91-93] help to interpret the results of the $\text{CO}_2 + \text{PFPE}$ scattering experiments by Nesbitt discussed above. It was found that vibrational accommodation at the surface had a timescale of ~ 50 ps, which is much longer than a direct interaction (typically < 10 ps) [93]. This result explains the low efficiency of vibrational energy transfer observed by Nesbitt [68]. The simulations were in good agreement with experiment, demonstrating that F-SAMs are good proxies for PFPE, but there were some deviations from the IS/TD binary model that are worth noting. Three different trajectory types were identified: direct scattering, penetration into the SAM, and physisorption. At high incident energies, the physisorption

trajectories (which could naively be expected to correspond to TD) were superthermal [91]. Moreover, the TD fraction α from bimodal temperature fits was not equivalent to the fraction of physisorption and/or penetration events [74]. These results indicate that the dynamics are more complex than the binary mechanism initially proposed. IS and TD are two limiting cases which help to characterise the scattering dynamics, but there is a wide range of intermediate events that cannot be unambiguously assigned to either the IS or TD fraction.

Simulations involving liquid surfaces instead of SAMs are more directly comparable to the experiments on liquids. Most of the theoretical studies to date have made use of MD-simulated squalane surfaces. Siepmann [97] developed a UA force field to describe squalane. The simulation box was periodic in the x and y directions and elongated in the z direction, forming a slab of 96 squalane molecules with two gas-liquid interfaces. A similar approach was later adopted by McKendrick [98], who used the Siepmann force field to study the structure of the squalane surface (Figure 1.4). A probe sphere was directed at the surface to identify which CH_x groups are exposed to the incoming $\text{O}(^3\text{P})$ atoms, but no simulations of the scattering event were performed. The first simulation of a gas scattering from a squalane surface was performed by Hase [99] with Ne atoms. In contrast with an early study [58] which approximated squalane molecules as spheres, Hase employed an MD-simulated squalane surface which did successfully reproduce the trends in energy transfer observed experimentally [53]. It was found that squalane is less efficient than a H-SAM on accommodating the collision energy, due to its more disordered structure which makes intermolecular energy transfer more difficult [99]. At the same time, Kim and Schatz improved the squalane model and used it for reactive scattering systems, which will be discussed later [100]. Instead of the TraPPE (Transferable Potentials for Phase Equilibria) UA force field employed by Hase and McKendrick, the simulation of the squalane surface made use of an OPLS-AA (Optimized Potential for Liquid Surfaces - All Atom) force field.

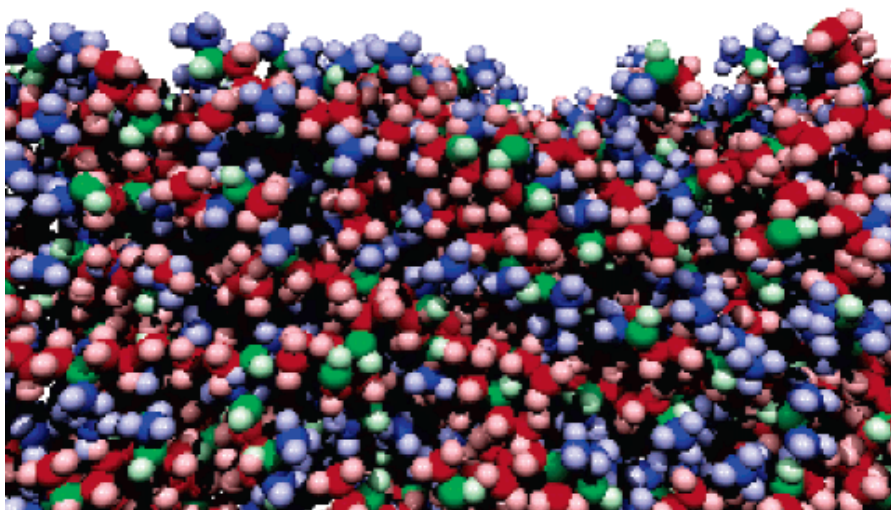
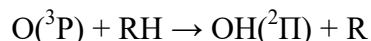


Figure 1.4. Side view of an MD simulated squalane surface. Primary, secondary and tertiary C atoms are represented in blue, red and green; respectively. H atoms are lighter in colour. Reproduced from Reference [98].

1.2.2. Reactive gas-liquid collision dynamics

Experimental studies

In reactive scattering, the basic features of gas-liquid interactions are still present, but in addition the intrinsic dynamics of the reaction affects the energy of the products. The majority of the work to date has been concerned with reactions of $O(^3P)$ atoms on liquid hydrocarbon and related surfaces, which have been studied in parallel by the Minton [48, 60, 101-103] and McKendrick [3-12, 98, 104] research groups. The main product of the reaction of $O(^3P) + \text{squalane}$ is OH from the abstraction of a hydrogen atom, similar to the reactions of $O(^3P)$ with gas-phase hydrocarbons [105]:



In addition, an OH radical can induce a second H abstraction and generate H_2O . Minton employed a molecular beam of $O(^3P)$ combined with MS detection and found two distinct velocity distributions for the scattered OH radicals, implying a binary IS/TD behaviour [101]. The H_2O products exhibited the same sort of bimodal behaviour, but they had a greater fraction of thermalized products, which is consistent with the fact that they result from at least two collisions with surface groups. The scattering dynamics of the reactive products were well described by the soft-sphere kinematic model [60]. The

dynamics of H abstraction by Cl atoms were found to be very similar [102]: both the OH and HCl reaction products showed a preference for backwards and sideways scattering in the centre-of-mass frame. This result is easily explained by the geometrical constraint imposed by the liquid surface. Besides H abstraction, additional reaction channels are available for the O(³P) reaction at hyperthermal collision energies, the most important one being C-C bond breakage [103].

The dynamics of the O(³P) + squalane reaction were further investigated by McKendrick using LIF to detect OH [3-7]. O(³P) atoms with a broad range of translational energies were generated by photolysis of bulk NO₂ gas above a squalane-coated wheel. A schematic representation of this experimental arrangement is shown in Figure 1.5. The time-of-flight translational resolution of the LIF detection method was limited, but it showed a significant fraction of direct reaction events, demonstrated by fitting the data to Monte Carlo simulated IS and TD translational product fractions [4]. More definitive evidence for IS and TD partitioning was provided by the rotational distributions of the OH radicals. In this case the IS and TD product temperatures were too similar to yield a clear 2-temperature Boltzmann fit. However, it was evident that a fraction of products had accommodated at the surface because the single rotational temperatures obtained for OH were superthermal, but lower than those from equivalent gas-phase reactions [106]. In addition, products with high translational energy were rotationally hotter than the slower products [5]. This positive correlation between rotational and translational energy is in agreement with the inelastic scattering experiments discussed above [68], and indicates that TD-like trajectories involve both rotational and translational accommodation at the surface.

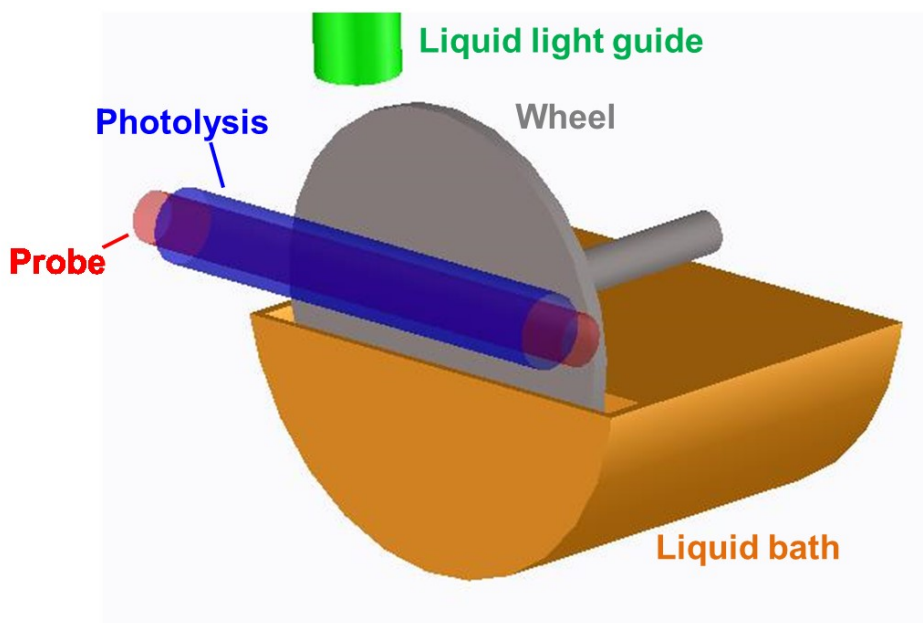


Figure 1.5. Schematic representation of the wheel, liquid bath and laser beams used in the McKendrick experiments. The wheel is 50 mm in diameter and the photolysis and probe beams propagate 6 mm above its surface. A liquid light guide is placed 20 mm above the laser axis in order to collect the OH LIF signal.

LIF measurements of vibrationally excited OH completed the understanding of the interfacial H-abstraction dynamics [4-6]. H abstraction produces a small fraction of OH ($v' = 1$), in a branching ratio $\frac{(v' = 1)}{(v' = 0)} = 0.07 \pm 0.02$ for squalane [4]. Due to the reaction energetics (see Section 1.3), this must come from reaction with secondary or tertiary C–H sites at the surface. The vibrational branching ratio was slightly lower than expected from gas-phase reactions [105]. This could be either a dynamical effect such as vibrational relaxation at the surface, or the result of a preference for the primary CH₃ units to protrude from the surface, as has been shown in theoretical studies [98-100]. The latter explanation is more plausible, given that the timescales for vibrational energy transfer are expected to be long compared to the interfacial interaction. Nevertheless, the branching ratios should not be interpreted literally, as they are difficult to measure accurately [105]. Multiple liquid-temperature measurements of the OH ($v' = 1$) kinetic energy and yield provided more interesting information [6]. OH ($v' = 1$) radicals were slower than OH ($v' = 0$), and their translational energy increased with the temperature of the liquid surface which implies that they are produced by a TD mechanism. Due to overall energy conservation in the reaction, OH ($v' = 1$) is produced with low translational energy and is therefore quite susceptible to thermalisation. In addition, the

yield of OH ($v' = 1$) increased with temperature, whilst the yield of OH ($v' = 0$) was essentially temperature-independent. It was proposed that this was a consequence of a different survival probability for vibrationally excited OH [6]. Higher temperatures induce a more open surface structure in squalane, which could potentially decrease the probability of collisional relaxation of OH ($v' = 1$).

In the O(3P) + squalane reaction there is not much energy released into translation of the products, and the collision energy dominates the scattering dynamics. In consequence, the trends in energy transfer are not very different from the inelastic scattering experiments in Section 1.2.1. In order to observe the effect of reaction energetics more clearly, reactions which are highly exoergic can be investigated using low collision energies. The reactions of squalane with F [107, 108] and O(1D) atoms [109] meet this requirement. Both the F + hydrocarbon and O(1D) + hydrocarbon reactions yield highly energetic products (HF and OH, respectively) [108, 110]. The F + squalane reaction, investigated by Nesbitt using IR absorption spectroscopy [107, 108], afforded a hot fraction of products consistent with the analogous gas-phase reaction, but there was also a cold component inferred to arise from rotational and translational thermalisation at the surface. The O(1D) + squalane reaction was studied by the McKendrick group, detecting OH by LIF with a similar setup to that described above [109]. In the corresponding gas-phase reaction, OH production can proceed through different possible mechanisms which may yield high-energy products [111]. A fraction of rotationally and translationally cold OH was observed in the O(1D) + squalane experiments, which indicated the existence of secondary encounters at the surface [109]. These results, together with the inelastic scattering experiments, support the idea that energy accommodation by secondary encounters at the surface is a universal feature of gas-liquid dynamics.

In some cases the gas-liquid reaction is more complex and can proceed through many pathways, for example, in the reactions of protic acids (HCl, HBr, HCOOH) with glycerol or water. These reactions have been investigated by Nathanson and co-workers in an extensive series of experiments which employed deuterium labelling to distinguish proton exchange events [112-121]. In this case there were strong chemical interactions between the projectile and the surface, so the projectile could react through proton exchange, become solvated into the bulk, or become temporarily trapped without leading to reaction. The interactions between HX (X = Br, Cl) and glycerol caused most of the molecules to thermalise at the surface, so that a substantial amount of TD

products were observed [114-116]. Fast proton exchange between the liquid and projectile also occurred at the surface, and the extent of this reaction depended on the nature of the liquid. In salty glycerol, interfacial ions affect proton exchange and thermalisation by disrupting the H-bond network between OH groups. Smaller ions with higher charge density bind OH more strongly and reduce trapping, while enhancing rapid interfacial exchange [117-119, 122, 123]. Using salty water instead of glycerol as the surface increased the probability of solvation and effectively eliminated the rapid interfacial H exchange channel [120]. This implies that water is more efficient than glycerol in solvating interfacial ions.

Recently, the ionization of Na atoms on a glycerol surface was studied by a combination of atomic beam scattering and MS detection, again using selective deuteration of glycerol [124, 125]. The primary encounter produced Na^+ ions and solvated electrons, which triggered a series of reactions that led to a range of scattered products, identified by MS [124]. The distribution of scattered Na atoms matched an IS distribution, indicating that thermalized products at the surface undergo ionization and solvation and therefore do not scatter back into the gas phase [125].

Theoretical studies

Simulations of bond formation and breaking in a surface cannot be undertaken with the same methodologies as the inelastic scattering systems described previously. Reactive events require a detailed quantum mechanical treatment of the system; however, a full quantum description of the liquid or SAM surface has a prohibitive computational cost. The solution is to reduce the size of the liquid surface, approximating the liquid to a cluster [125], or to employ quantum mechanics/molecular mechanics (QM/MM) hybrid methods. In QM/MM, only part of the system is treated quantum mechanically, and the rest is treated classically. When applied to gas-surface reaction scattering, the QM boundary involves a few atoms in the collision region to ensure that the reaction is modelled accurately [51]. It still involves too many atoms for a full *ab initio* description, so typically semi-empirical Hamiltonians are used in order to simplify the calculation. Hase and co-workers simulated the reaction of $\text{O}(^3\text{P})$ with H-SAMs using an EA potential for their MM model [79]. The QM part of the potential comprised the $\text{O}(^3\text{P})$ atom and the top CH_3CH_2 groups of the SAM chains. The authors used an electronic structure method reparametrized with specific reaction parameters for the reaction of $\text{O}(^3\text{P})$ with ethane. Later, Troya and Schatz improved the QM/MM model to

study the reaction of hyperthermal $O(^3P)$ atoms with H-SAMs [126]. They employed a semiempirical Hamiltonian that was shown to model the $O(^3P) + \text{hydrocarbon}$ reactions more effectively, and in addition the QM part of the model included full hydrocarbon chains instead of the top two C atoms. OH formation and C–C breakage channels were found, in agreement with the $O(^3P) + \text{squalane}$ molecular beam experiments by Minton [103]. A similar approach was followed in simulations of F + H-SAM reactions [127], which provided qualitatively similar results to the F + squalane experiments by Nesbitt [108].

Schatz performed QM/MM simulations of reactive scattering events on a squalane surface [100, 128]. The QM atoms in the squalane surface were defined “on the fly” based on their proximity to open-shell atoms. This allowed modelling less localised projectile-surface interactions, as well as the secondary reactions taking place after a reactive encounter. The reaction between hyperthermal $O(^3P)$ and squalane had similar features to the previously studied $O(^3P) + \text{H-SAM}$ analogue, but energy transfer was less efficient on squalane [100]. The simulations predicted the reaction channels observed by Minton [103], but the internal energy of the OH products was overestimated compared to the results of McKendrick and co-workers [4]. Schatz also conducted reactive scattering simulations of F + squalane [128], which are more directly comparable to Nesbitt’s results [108], and found very little thermalisation, which the authors attributed to the higher collision energy of their simulations.

A similar approach was employed to model the reaction of hyperthermal $O(^3P)$ with a more complicated surface, the ionic liquid $[\text{C}_2\text{mim}][\text{NO}_3]$ [129]. In this case five ion pairs made up the QM region. The authors identified up to 10 different types of reaction including elimination of NO_3 , O addition to the ring and H abstraction from the ethyl chain or the ring. In a related study, the inelastic scattering of CO_2 from $[\text{C}_4\text{mim}][\text{BF}_4]$ and $[\text{C}_4\text{mim}][\text{Tf}_2\text{N}]$ was simulated by QM/MM [130]. Although the simulations did not involve a chemical reaction, QM/MM was chosen because it models polarization effects which account for the dipole-dipole interaction between CO_2 and the IL surface. The results were in good agreement with related experiments that will be discussed later [36], showing that anion identity rather than surface roughness affected the energy transfer.

1.2.3. Gas-liquid collisions as an analytical probe of surfaces

The experimental and theoretical work discussed in the previous sections has provided a great deal of information on the fundamental mechanisms of gas-liquid interfacial processes. It is possible to exploit this knowledge of the collision dynamics to interrogate the structure and composition of the liquid surface. This section covers experimental work that has focused on surface structural effects, as opposed to the mainly dynamical studies reviewed so far.

In 1999, Donaldson carried out one of the first structural studies of gas-liquid collisions, involving the inelastic scattering of I₂ molecules from the surface of 5CB (4-cyano-4'-pentylbiphenyl) [131]. 5CB is a thermotropic liquid crystal with a nematic phase at room temperature and an isotropic phase above 35 °C. In the nematic phase, the molecules are preferentially oriented along a unit vector known as the director. Donaldson conducted experiments on both the nematic and isotropic phases. LIF detection of the scattered I₂ showed that the translationally thermal products were rotationally warm in comparison with the incident I₂, as a result of multiple impacts with the surface. There were some interesting dynamical differences between the nematic and isotropic surfaces. Namely, isotropic 5CB led to I₂ internal energies that were very similar to those obtained from organic liquids [46, 66, 67], while nematic 5CB produced higher fractions of thermalized products. Interestingly, the degree of thermalisation depended on the direction of incidence with respect to the director: I₂ molecules colliding perpendicular to the director encountered a rougher surface and this induced rotational excitation.

Inelastic scattering of OH from squalane and squalene, discussed in Section 1.2.1, provided some information about the surface structure of these hydrocarbons. The survival probability of OH in squalane was higher than in squalene, at two different collision energies [19, 20]. Squalene has the same basic chemical structure as squalane but is partially unsaturated; therefore, the difference in reactivity must be caused by reaction of the OH radicals in the unsaturated sites. It follows from this that squalene exposes unsaturated sites at its surface, as was confirmed by MD simulations [20].

Similar types of experiments have been employed to interrogate the surface structure of more complex samples such as ionic liquids. As discussed in Section 1.1, the main goal of ionic-liquid surface science is to quantify the exposure of the different ions at the surface in order to find bulk-surface composition relationships. Nesbitt and co-workers

have shown that the energy transfer in inelastic scattering is sensitive to the IL surface composition [36, 130, 132-134]. The authors scattered NO [133, 134] and CO₂ [36, 75] from ILs containing the [C₄mim]⁺ cation with different anions ([Tf₂N]⁻, [BF₄]⁻, or [Cl]⁻). The TD fraction and the internal energies of the scattered products were affected by the chemical identity of the anion. This result suggests, although somewhat indirectly, the presence of anions at the surface. It can be reasonably expected that alkyl moieties provide similar scattering dynamics to previously studied hydrocarbons such as squalane [69], whereas the ionic groups (i.e. anions and imidazolium rings) induce different dynamics. Studying cations with different alkyl chain lengths, Nesbitt found that a greater fraction of ionic moieties in the IL composition led to a stiffer surface [36]. The fraction of thermalisation was therefore indirectly related to the coverage of the surface by alkyl chains. However, the extent of alkyl coverage may be better characterised with a chemical reaction, as will be discussed in the next section.

Collisions with gases can also identify which components are exposed at the gas-liquid interface of liquid mixtures and solutions. For example, when an inorganic salt is dissolved in glycerol, it changes its characteristics so that hyperthermal Ar scatters with higher translational energy from it [117, 118, 122]. Ions are present at the interface of glycerol, binding to its OH groups and disrupting its hydrogen bond network. As a result, salty glycerol presents a smoother and stiffer surface compared to pure glycerol. The interfacial ions increase the effective surface mass leading to a higher kinetic energy in the IS channel. The surface of salty glycerol was also interrogated by inelastic scattering of CO₂ combined with spectroscopic detection [135]. The IS rotational distribution was hotter for salty glycerol compared to the pure liquid. In addition, the degree of rotational excitation was sensitive to the identity of the anion (Cl⁻ vs I⁻), but not the cation (K⁺ vs Na⁺). Assuming that the rotational distributions are equally sensitive to cation and anion identity, this result suggests that the anions are more surface-active than the cations.

Nathanson demonstrated that the concentration of 1-butanol on the surface of H₂SO₄ could be characterised with a combination of Ar scattering and surface tension measurements [136]. As the concentration of butanol increased, the Ar IS channel became slower and less significant, indicating a reduction in effective surface mass and an increase in surface roughness. The change in IS/TD ratio with surfactant concentration followed a similar trend to the surface tension, which was related to the concentration of butyl chains on the surface. Besides inelastic scattering, the structure

of the surfactant layer was probed indirectly by interfacial H/D exchange and H₂O/D₂O evaporation. It was found that the presence of butanol in H₂SO₄ enhances the uptake of HCl and thus leads to a higher probability of H exchange [137]. For hexanol on H₂SO₄, H exchange increases with hexyl surface coverage but falls back to the pure H₂SO₄ value when the layer becomes more compact [138]. A mixture of pentanoic acid and hexanol behaved like hexanol for most concentrations, showing that hexanol has greater surface activity on H₂SO₄ [139]. The packing density of the surfactant layer was also probed by D₂O evaporation: for butanol films, the rate of D₂O evaporation was independent of concentration, indicating that the monolayer was porous rather than tightly packed [136]. For hexanol films, D₂O evaporation starts to be hindered on less concentrated H₂SO₄ solutions, showing that these films are less porous [138]. More recently, the effect of branched chains in the surface monolayer has been studied using the HCl proton exchange reaction [140]. A surfactant with branched chains (in this case 2-ethylbutanol) covers the surface area more effectively than a linear one, and hinders the interfacial reaction more effectively.

1.3. Reactive O(³P) scattering as a probe of surface structure

As discussed above, the dynamics of unreactive gas-liquid collisions provide some indirect information on the composition of the interface. A more direct, unambiguous approach to probing liquid surfaces is to use projectiles that react selectively with certain types of atoms at the surface. This is the fundamental idea behind this thesis. The H-abstraction reaction by O(³P) from hydrocarbons can be used to quantify the fraction of hydrocarbon groups on liquid surfaces. Moreover, in a pure hydrocarbon surface, different types of C–H bonds present different intrinsic reactivities, as discussed below.

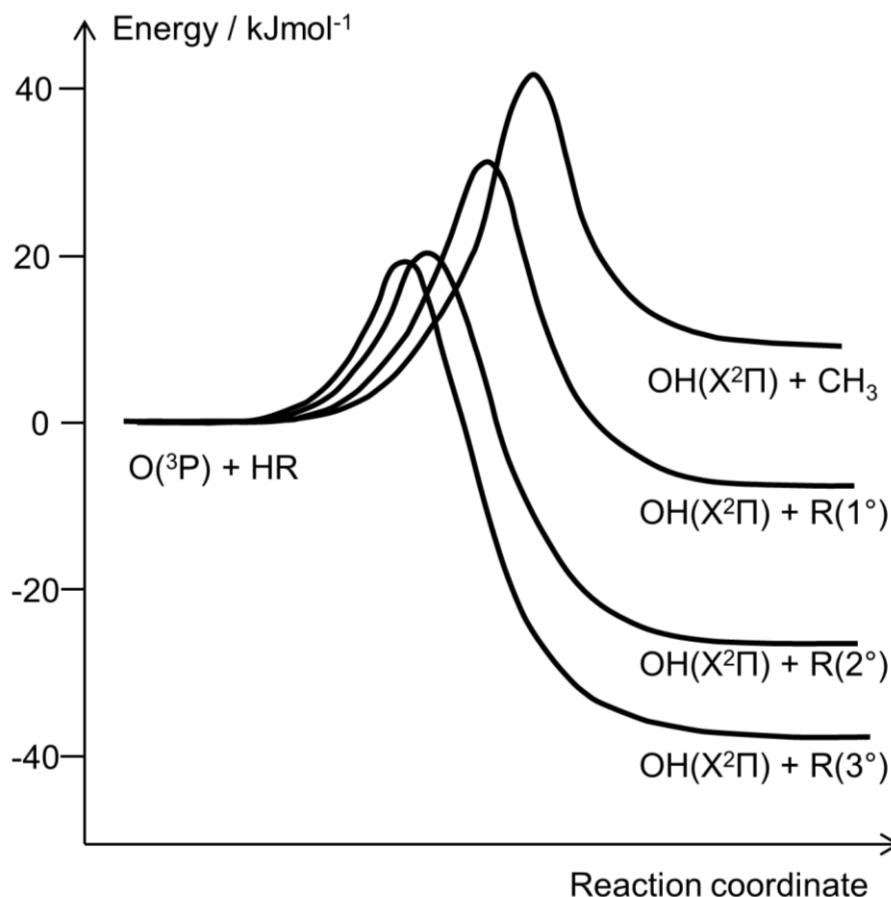


Figure 1.6. Approximate profiles of the $O(^3P)$ + hydrocarbon reactions. Adapted from Reference [105].

The reactions of $O(^3P)$ with gas-phase hydrocarbons have been characterised extensively since 1980, when Andresen and Luntz performed the first crossed molecular beam experiments using neopentane, cyclohexane and isobutane [106, 141]. A great deal of theoretical and experimental work has been conducted since then in order to understand the fundamental dynamics [105], but the details of the mechanism are not directly relevant to this introduction. The central result is that the reaction energetics depends on the type of C–H bond taking part in it. As the degree of substitution increases, the H abstraction reactions become more exothermic and have lower activation energies. Andresen and Luntz observed increasing vibrational excitation in the sequence primary < secondary < tertiary C–H, which suggests that the transition state becomes closer to the entrance channel of the reaction (that is, the barrier becomes earlier) [106]. The barriers of reaction are 29 kJ mol^{-1} for primary, 19 kJ mol^{-1} for

secondary and 14 kJ mol^{-1} for tertiary C–H bonds. The exoergicity of the reaction follows a similar trend, being approximately -10 kJ mol^{-1} for primary, -31 kJ mol^{-1} for secondary and -39 kJ mol^{-1} for tertiary C–H [105, 142]. These trends are illustrated in Figure 1.6, together with the energetics for $\text{O}(^3\text{P}) + \text{CH}_4$.

Photodissociation of NO_2 with 355 nm light, which is the source of $\text{O}(^3\text{P})$ in the experiments by McKendrick [3], produces atoms with a broad range of energies. Their translational energy distribution has an average value of 15.8 kJ mol^{-1} and a spread of 26 kJ mol^{-1} (FWHM) [143]. This means that a large fraction of $\text{O}(^3\text{P})$ projectiles have sufficient energy to react with secondary and tertiary C–H groups, but only those in the highest-energy tail of the distribution can overcome the barrier for reaction with primary CH_3 units. This difference in reactivity enables the functional groups which are exposed at the surface of pure hydrocarbon liquids to be distinguished, as was demonstrated for long-chain alkanes [8]. In their study, McKendrick and co-workers employed NO_2 photolysis combined with LIF detection of OH to compare the reactivity of branched (pristane and squalane) and linear (*n*-docosane, *n*-tetracosane and *n*-octacosane). Branched hydrocarbons were more reactive than linear ones, and longer linear molecules were more reactive than shorter ones. The higher reactivity of the branched molecules can be explained from the fact that they contain tertiary C–H bonds in their structure which are accessible to the incoming atoms. The difference in reactivity for the linear hydrocarbons was attributed to different degrees of supramolecular ordering at their surfaces. Hydrocarbon molecules display ordering perpendicular to the surface just above their melting points, so that they preferentially expose CH_3 groups at the surface, producing a lower yield of OH. This phenomenon, known as surface freezing, had been previously observed in independent studies [144]. The experiments by McKendrick demonstrated that $\text{O}(^3\text{P})$ atoms generated by photolysis are highly sensitive to this effect [8].

This structural effect on reactivity was further explored in the interfacial reaction of $\text{O}(^3\text{P})$ with SAMs [9, 12]. The high reactivity of H-SAMs with $\text{O}(^3\text{P})$ indicated that the projectiles can access CH_2 groups, instead of just colliding with terminal CH_3 groups. Selective deuteration revealed that chain end segments containing many C atoms (between 3 and 6) were accessible to the O atoms.

Recently, reactive scattering of $\text{O}(^3\text{P})$ atoms was employed as an analytical probe of the surface composition of ionic liquids [10, 11, 104]. The experiments exploited the chemical selectivity of the H-abstraction reaction to characterise the occupation of the

surface by alkyl chains: provided that there are no other reactive H atoms in the IL composition, the OH yield after dosing the surface with O(³P) atoms is an indicator of the fraction of alkyl CH₂ groups at the surface. A family of [C_{*n*}mim][Tf₂N] ILs with *n* = 2 – 12 were studied. The large differences in surface reactivity indicated that longer alkyl chains have a higher propensity to occupy the interface [11]. In addition, it was shown that the surface of long-chain ILs is not fully saturated in alkyl groups [48].

These preliminary studies served as a proof of concept for the RAS experiments on ILs in Chapters 4, 5 and 6 of this thesis. Compared to the inelastic scattering experiments in Section 1.2.3, RAS provides more direct, unambiguous information and allows the quantitative characterisation of differences in alkyl surface coverage. Complementary experiments at higher collision energy and simulations of the IL surfaces will also be reported in this thesis, in order to gain a better understanding of the reaction mechanism in RAS.

Chapter 2.

Experimental

This chapter introduces the general experimental approach. Although the experiments were performed in two different reaction chambers, they shared the same laser systems, detection scheme and general method of producing liquid surfaces. Surfaces were generated with a rotating wheel coated in the liquid of interest. Gas-phase $O(^3P)$ atoms were produced by laser photolysis of NO_2 and OH radicals were detected by laser-induced fluorescence (LIF). The following sections provide details on liquids employed, vacuum systems, photolysis and detection methods and the general types of experimental outputs. The specific details of each study will be provided in each chapter and any deviations from the general method will be highlighted appropriately.

2.1. The liquid surface

2.1.1. Surface generation method and general handling of liquids

The vacuum-liquid interface is undoubtedly crucial to the study of reaction dynamics at the liquid surface; however, generating a liquid surface under vacuum is not an easy problem. The main challenges are to prevent evaporation into the gas phase and the adsorption of contaminants and reaction products on the surface, which can potentially affect the measurements. The work presented here uses a rotating wheel, which is by far the most commonly adopted method for obtaining a “clean” surface *in vacuo* [1]. This technique involves a rotating disk which is partially immersed in a reservoir filled with liquid. On each rotation, the wheel becomes coated with fresh a layer of liquid, therefore avoiding the build-up of contaminants that might take place on a static surface. All experiments reported here employed stainless steel wheels with a diameter of 50 mm. In some cases, a stainless steel blade was mounted on the bath to act as a scraper with the purpose of obtaining a smooth liquid layer of known thickness. This could

potentially influence the results of the experiments, as variations in the layer thickness would change the distance travelled by the incoming $O(^3P)$ atoms to the surface and by the reaction products from the surface to the detection system. However, this distance was always at least 4 mm whereas the layer thickness was of the order of hundreds of micrometres. Experiments performed with and without a scraper yielded practically equivalent results, proving that this did not significantly affect the measurements.

The rotating wheel approach ensures that the surface is refreshed, but it does not solve the problem of liquid evaporation under vacuum. As discussed in Chapter 1, most of the experimental work to date has used the rotating wheel technique to study liquids of low vapour pressure that can be placed inside a vacuum chamber without significant evaporation into the gas phase. This is the approach followed in this thesis, which builds up on previous work by McKendrick and co-workers on ionic liquids [10, 11, 104] and long chain hydrocarbons such as squalane (2,6,10,15,19,23-hexamethyltetracosane; $C_{30}H_{62}$) [3-8]. Squalane is the saturated analogue of squalene (2,6,10,15,19,23-hexamethyl-2,6,10,14,18,22-tetracosahexaene; $C_{30}H_{50}$), a natural product present in most animals and plants. A study of the reactions of squalane and squalene with $O(^3P)$ is presented in Chapter 3. Both liquids have sufficiently low vapour pressures to be held under high vacuum without significant evaporation (squalane has a vapour pressure of approximately 2×10^{-8} Torr [145]). Ionic liquids, studied in Chapters 4 and 5, have in general even lower vapour pressures, often decomposing at high temperatures before evaporation takes place [28, 146-148]. However, this is not true for all existing ionic liquids: it has been reported that some very common ionic liquids can be distilled at relatively low temperatures of 200 – 300 °C and pressures of a few mbar [149, 150].

While it is important to consider the volatility and thermal stability of the liquids, in practice they were not an issue for most of the liquids studied. Liquid samples were kept in the reservoir under high vacuum for several days and heated to ≤ 100 °C without any noticeable evaporation or decomposition taking place. The samples were introduced in the vacuum chamber at atmospheric pressure through a quick-access door and loaded into the reservoir using a syringe. When studying ionic liquids which were solid at room temperature, the reservoir was heated to a temperature above the melting point and the sample was transferred into it as a solid that rapidly melted inside the bath. Whenever dealing with potentially air- and moisture-sensitive samples, a gentle flow of

dry N₂ was passed through the vacuum chamber during sample transfer to minimise contact with air and water.

Before each measurement, liquids were typically kept under high vacuum for several hours while rotating the wheel to remove water and volatile impurities. For the liquids studied in Chapter 3, this degassing time was usually much shorter (≤ 30 minutes) since the experiments required fast changing of liquids, typically several times a day. This shorter degassing time was acceptable because the liquids studied were not significantly hygroscopic or sensitive. On changing liquids, the baths were thoroughly cleaned with methanol in an ultrasound bath to prevent cross-contamination between samples.

2.1.2. Liquid purity considerations

As with most surface-science experiments, the presence of contaminants on the surface can potentially affect the results. In liquids, very small concentrations of surface-active impurities in the bulk can substantially alter the surface composition. High-purity liquids were used whenever possible in order to avoid this problem. The purity of each commercial sample is stated in its corresponding chapter. In addition to the handling precautions described in the previous section, the purity of the samples after experiments was verified by NMR spectroscopy (¹H-NMR and ¹⁹F-NMR) and attenuated total reflectance infrared spectroscopy (ATR-FTIR). NMR spectra were recorded in a 300 MHz instrument (Bruker Avance-III) using CDCl₃ or DMSO-d₆ as the solvent. Infrared spectra were acquired in the range of 400 to 4000 cm⁻¹ with a Perkin Elmer Spectrum 100 FTIR spectrometer. The composition of all samples remained unchanged after measurements, although this does not guarantee the absence of impurities that cannot be detected by these methods, either due to their chemical composition or their low concentration.

In the case of ionic liquids, the presence of water could potentially affect the structure of the surface [151-153]. In order to avoid this effect, high-purity ionic liquids were used. Some of the ILs were custom-synthesized by collaborators using glovebox techniques and contained less than 50 ppm water [48]. Commercial ionic liquids had water contents typically between 200 and 1000 ppm. The degassing time before measurements was ≥ 4 hours in order to remove as much water from the samples as possible. If possible, the water content of the samples was determined by Karl-Fischer (KF) titration before and after degassing in order to verify the removal of water. The measurements were performed in a Karl-Fischer coulometer (Metrohm 831 KF

coulometer). Table 2.1 presents KF results for a commercial ionic liquid with a high concentration of water, before and after degassing at high vacuum for different periods of time. The initial water content of the samples was ~ 1600 ppm, and the final content was always ~ 200 ppm regardless of degassing time. This result confirms that degassing under high vacuum removed most of the water present in the ionic liquids, and that just 1 hour under high vacuum was sufficient to purify the sample to an acceptable degree.

| Degassing time | Initial H ₂ O content / ppm | Final H ₂ O content / ppm | H ₂ O loss / ppm |
|----------------|--|--------------------------------------|-----------------------------|
| 1 hour | 1575 | 233 | 1342 |
| 2 hours | 1696 | 245 | 1451 |
| 4 hours | 1753 | 177 | 1576 |
| 17 hours | 1621 | 261 | 1361 |

Table 2.1. Initial and final water contents of a commercial sample of 1-butyl-3-methylimidazolium tetrafluoroborate (Sigma-Aldrich, $\geq 97\%$) for different degassing times (average of two measurements). KF titrations were carried out for each sample immediately before and after degassing.

2.2. Reaction chambers

The experiments were performed in two different reaction chambers. The main difference between these two setups was in their liquid baths and wheels: the second-generation apparatus incorporated an assembly of multiple wheels designed for studying several liquids in quick succession, whereas the previous design contained one single wheel. Details on vacuum systems and wheel assemblies for each of the chambers are provided below.

2.2.1. Single-wheel setup

In this setup, depicted in Figure 2.1, a single liquid bath was placed inside a stainless steel vacuum chamber (approximately 12 L in volume). The chamber was evacuated to a pressure of 10^{-5} mbar with a turbomolecular pump (Edwards EXT70/63DF; 65 L/s) attached to a 90° elbow at the bottom and backed by a rotary vane pump (Edwards). A gate valve was positioned between the chamber and the turbomolecular pump, so that the experiment could be vented without stopping the pump. This greatly reduced the time required to change the liquid in the bath. When bringing the chamber under vacuum from atmospheric pressure, it was first evacuated to a pressure of $\sim 10^{-2}$ mbar by another rotary pump connected directly to the chamber before opening the gate valve. Foreline traps with activated alumina and copper wool were placed upstream of the rotary pumps to prevent contamination of the reaction chamber with pump oil. On the front there was a quick-access door sealed with an O-ring. A viewport on the door enabled the wheel assembly to be monitored when the system was under vacuum. The fluorescence collection optics (Section 2.4.4) were mounted on the top flange. On the sides there were 25-cm long arms with fused silica windows ($\lambda/4$ flatness, 5 mm thick) through which the laser beams entered the chamber. The beams counterpropagated along the same axis at a carefully controlled distance from the wheel. In order to minimise scattered laser light, the windows were set at Brewster's angle and baffles were placed inside the arms. The pressure in the chamber was measured with active wide-range gauges (Edwards) for values close to atmospheric and in the high vacuum range. During experiments, the wide-range gauges were isolated from the chamber and a capacitance manometer (Edwards Barocel 0-1 Torr, ± 0.1 Torr precision) was used to monitor the pressure instead.

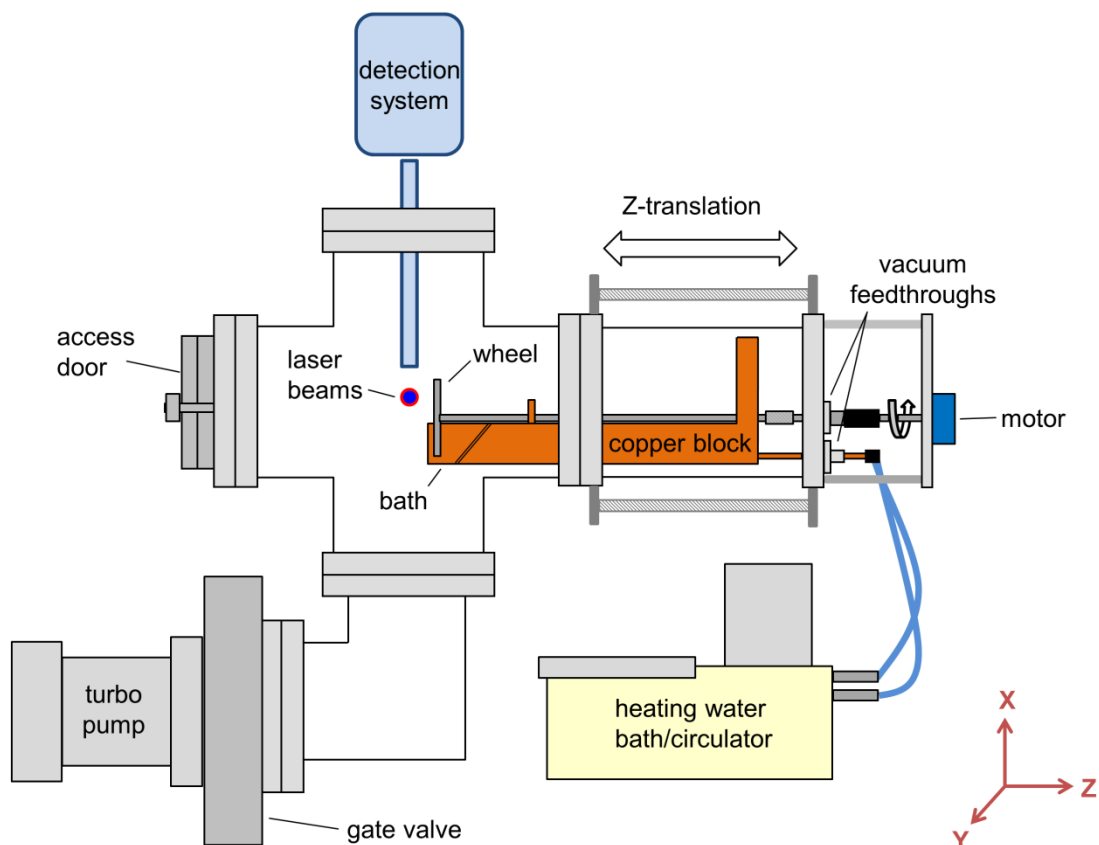


Figure 2.1. Side-view schematic diagram of the single-wheel apparatus.

The liquid bath (Figure 2.2) was mounted on a block of copper inside a flexible nipple attached to the back flange of the chamber. The assembly could be translated by a few mm in the Z (towards or away from the centre of the chamber) and X (upwards or downwards) directions. The stainless steel wheel was attached to a rotating axle that was driven by a motor (Crouzet 0.5 Nm, 3 W, 30 rpm) placed outside the chamber.

The liquid bath was made of copper and could contain up to 5 mL of liquid. Water was circulated through the main copper block to vary the temperature of the bath, which was attached to the block and therefore in thermal contact with it. The liquid bath temperature was monitored with a thermocouple. A thermostatic bath (Lauda A100) was used to circulate and heat the water up to temperatures between 20 °C and 100 °C. Both the wheel and the liquid bath could be detached from the assembly easily by loosening the screws that fixed them to the block and axle. Rapid change of liquids was achieved by having several sets of baths and wheels available, although it still involved opening the chamber to the atmosphere.

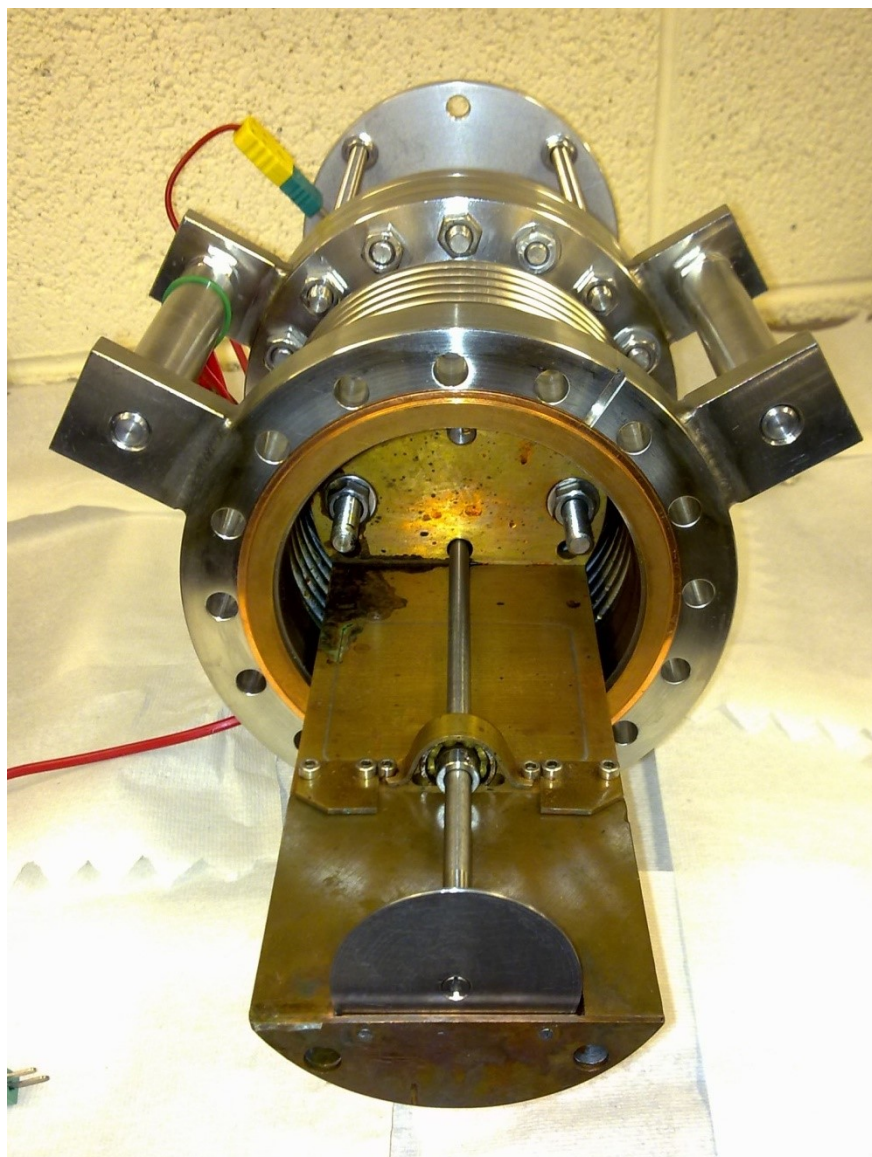


Figure 2.2. Photograph of the single-wheel assembly. The detachable copper bath and the stainless steel wheel can be seen in the front.

2.2.2. Multiple-wheel setup

A new apparatus was built in order to study several liquids without breaking the vacuum or stopping the experiments. This was achieved by having four separate stainless steel baths with their respective wheels at right angles to each other. The wheel assembly was attached to a rotatable flange so that any particular wheel could be presented in front of the laser beams to study it in isolation from the others. Rotating the flange did not take a significant amount of time (typically 1 minute), so the different liquids could be studied sequentially under nearly identical conditions making the

results directly comparable. The assembly was housed inside a cylindrical vacuum chamber (200 mm diameter), represented in Figure 2.3. The chamber was evacuated to a pressure of 10^{-7} mbar by a turbomolecular pump (Edwards nEXT 300, 300 L/s), backed by a chemically resistant dry scroll pump (Edwards nXDS 10iC). A gate valve was used to isolate the turbomolecular pump from the system, and a second dry scroll pump (Edwards nXDS 10i) was employed to pump down the chamber from atmospheric pressure to low vacuum. The pressure was monitored with wide-range gauges (Edwards) and a capacitance manometer (Inficon CDG025D).

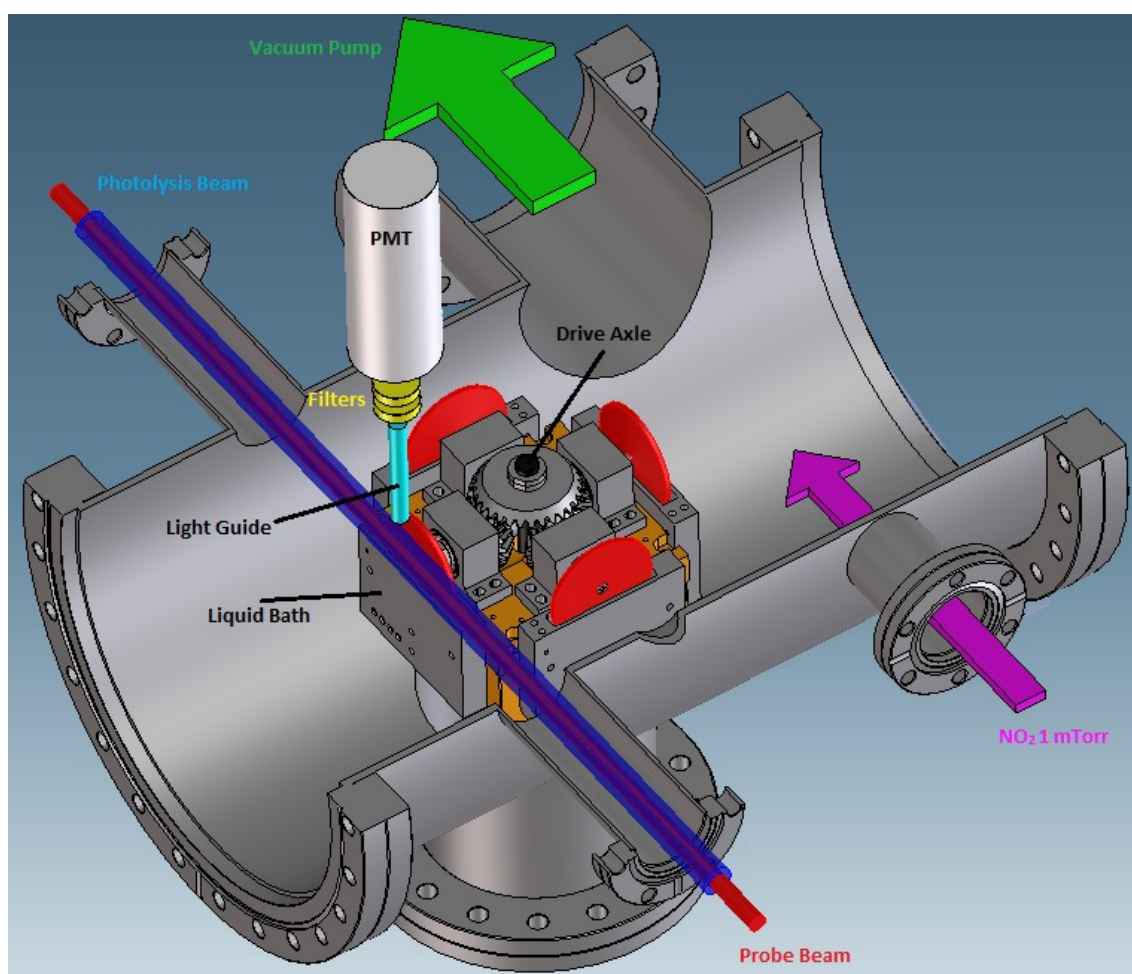


Figure 2.3. Schematic representation of the multiple-wheel reaction chamber. The wheels are highlighted in red.

The main difference from the previous experiment was in the four-wheel assembly, shown in detail in Figure 2.4. Simultaneous rotation of the four wheels was achieved via four bevel gears, at right angles to each other, which intersected a larger bevel gear attached to a central axle. This axle was turned by a motor (Parvalux MSD8) mounted

outside the vacuum chamber and operating at 30 rpm. The assembly consisted of a central block made out of copper, with four copper heaters on its sides and a top piece onto which the wheels and baths were attached. Heating fluid (SIL180) was circulated through the heaters for high-temperature measurements. An external circulator (Cole-Parmer Polystat) was used to control the temperature of the fluid. Thermocouple probes were attached to each heater to monitor the temperature. Details on temperature control and other calibration measurements for the multi-wheel apparatus are provided in Chapter 5.

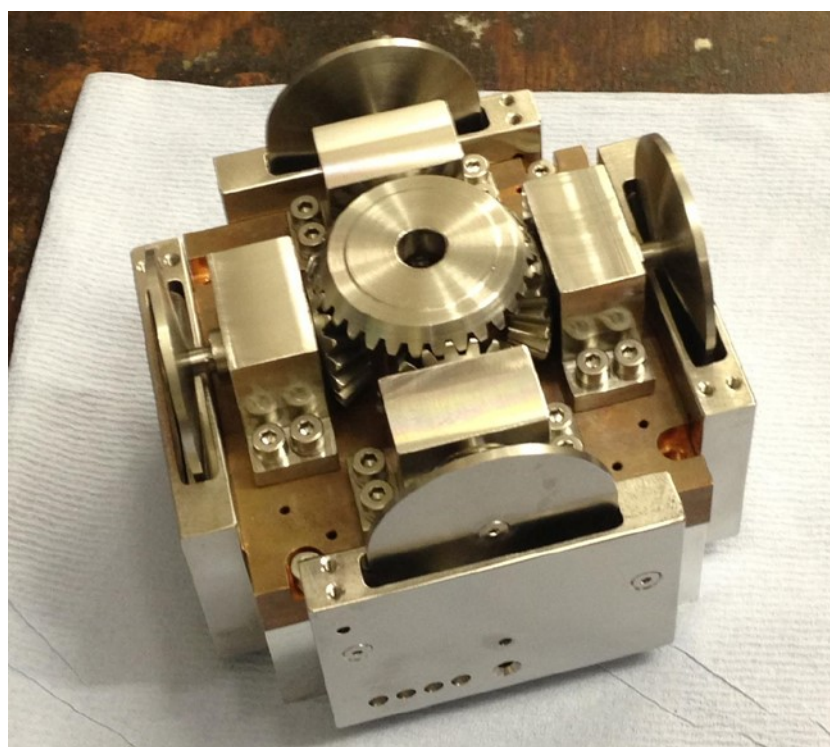


Figure 2.4. Photograph of the multiple-wheel assembly showing the top piece, gears, wheels and baths.

2.3. Generation of gas-phase radicals

Gas-phase colliders (either $O(^3P)$ atoms or OH radicals for background correction measurements) were generated by pulsed photolysis of a precursor gas with 355 nm laser light. The following sections provide details on the photolysis laser and precursors employed.

2.3.1. Photolysis laser

A pulsed Nd:YAG laser (Continuum Surelite II-10) was employed to photodissociate the precursors. The Nd:YAG rod inside the laser cavity was pumped with a xenon flashlamp emitting light over a broad range of wavelengths in 200 ns-long pulses. Short, high-power laser pulses were achieved by means of a Q-switch in the cavity. The flashlamp and Q-switch were externally triggered at a repetition rate of 10 Hz. This produced pulses of $\lambda = 1064$ nm which had a Gaussian spatial profile and a pulse length of 5-7 ns. Two sets of temperature-controlled harmonic generators (a frequency doubler and a sum frequency mixer) tripled the frequency of the input beam, yielding 355 nm light. The residual 1064 and 532-nm outputs were separated with dichroic mirrors before directing the beam into the reaction chamber. The resulting frequency-tripled pulses were horizontally polarised, 4-6 ns long and had a beam diameter of approximately 5 mm. The output energy was adjusted by varying the delay between the flashlamp and Q-switch trigger pulses. Pulse energies of ~ 80 mJ were typically employed. This value was lower than the maximum attainable output in order to prolong the life of the laser entrance windows in the chamber, while still producing $O(^3P)$ atoms at a high yield.

2.3.2. $O(^3P)$ generation

The precursor for $O(^3P)$ atoms was nitrogen dioxide (NO_2). NO_2 dissociates to $NO(^2\Pi)$ and $O(^3P)$ upon excitation of its $^2B_2 - ^2A_1$ transition with 355 nm light [154, 155]. The main reason behind this choice of O atom precursor is the high efficiency of the photodissociation: for a 355 nm photon, the absorption cross section of NO_2 is 1.05×10^{-20} cm² and its photolysis quantum yield is effectively 1 [156]. The $O(^3P)$ atoms are produced with a broad distribution of translational energies resulting from the corresponding broad range of internal states that are populated in the NO co-fragment. The average energy of the $O(^3P)$ atoms is 15.8 kJmol⁻¹ with a spread of 26 kJmol⁻¹ (FWHM) [143].

The photodissociated fragments recoil with an anisotropic angular distribution that can be characterised with an anisotropy parameter β . The angular distribution of the photofragments is given by Equation 2.1 [2]:

$$I(\theta) = \frac{1 + \beta P_2(\cos\theta)}{4\pi} \quad (2.1)$$

In this equation, β is the anisotropy parameter and θ is the angle between the electric field vector of the light, ε , and the recoil direction of the fragments. $P_2(\cos\theta)$ is the second order Legendre polynomial, $P_2(\cos\theta) = \frac{3\cos^2\theta - 1}{2}$. β can take values between -1 (perpendicular transition) and +2 (parallel transition). In a parallel transition, the photodissociated fragments recoil in a $\cos^2\theta$ distribution. In a perpendicular transition, the resulting distribution has a $\sin^2\theta$ dependence. The photodissociation of thermal (300 K) NO_2 has an anisotropy parameter $\beta = +0.7$ [143]. The resulting distribution $I(\theta)$ is more parallel ($\cos^2\theta$) than perpendicular ($\sin^2\theta$) in character, meaning that the products recoil preferentially along the direction of ε . The photolysis laser light used in the experiments was horizontally polarised in the lab frame in order to maximise the fraction of $\text{O}(^3\text{P})$ atoms that were ejected towards the surface.

During experiments, NO_2 was introduced in the reaction chamber via a needle valve. Both the needle valve and the regulator on the NO_2 cylinder were carefully adjusted to achieve constant pressure in the reaction chamber. The nominal pressure during experiments, measured with a capacitance manometer, was typically 1.0 mTorr. This value was found to be a safe compromise between maximising the production of $\text{O}(^3\text{P})$ atoms whilst ensuring the detection of OH under nascent conditions, meaning that the products did not undergo any collisions in the gas phase before reaching the probe beam. This can be simply verified by calculating the average number of collisions for a typical OH trajectory at a pressure of 1 mTorr. Assuming a typical thermal gas-kinetic collision rate constant of 10^7 collisions Torr⁻¹ s⁻¹, this means that OH radicals detected 10 μs after being produced have suffered on average 0.1 collisions. This number is sufficiently low to be confident that secondary collisions have a small effect in the experimental results, at least at short delays.

Another, more rigorous way to estimate the extent of gas-phase collisions is to calculate the mean free path of the OH radicals as they travel through 1 mTorr of NO_2 . The mean free path λ is defined as:

$$\lambda = \frac{1}{\sigma n_{\text{NO}_2}} \quad (2.2)$$

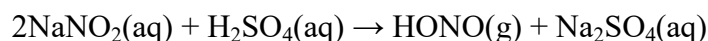
where n_{NO_2} is the number density of NO_2 in the reaction chamber and σ is the collision cross section for the OH + NO_2 system. This calculation is complicated by the fact that σ is dependent on collision energy, and the OH radicals scatter from the surface with a wide range of translational energies. In addition, experimental values of σ for OH with

NO₂ could not be found in the literature, so some approximations need to be made in order to obtain an estimate of λ . The long-range attractive potential between OH and NO₂ will result in a value of σ that decreases with collision energy. Theoretical cross sections for the formation of the OH - NO₂ hydrogen-bound complex (both unreactive and leading to reaction) have been calculated by Chen *et al.* [157]. The σ for forming the non-reactive complex will be used in this calculation as a reasonable estimate of the experimental collision cross section. In the worst-case scenario of a fully thermalised translational energy distribution of OH, the average collision energy would be 3.4 kJ mol⁻¹, which corresponds to $\sigma \sim 60 \text{ \AA}^2$ (given the translational energies in the experiment, this value is likely to be 2 or 3 times smaller in reality). Substituting this into Equation 2.2 yields $\lambda = 3.6 \text{ cm}$, which is considerably larger than the distance travelled by an OH radical from the wheel to the probe beam (the wheel-to-beam distance was in all cases $\leq 10 \text{ mm}$).

The above calculations provide a valuable estimate of the effect of secondary collisions, but they involve many approximations. For this reason, the effect of pressure on the results has been characterised experimentally. Previous work has shown that, for NO₂ pressures between 0 and 1.5 mTorr and OH flight times below 30 μs , the results are essentially independent of pressure [11]. This confirms that a pressure of 1 mTorr is in the single-collision regime, but only for detection times that are within 30 μs after the O(³P) atoms are produced.

2.3.3. HONO generation

On producing O(³P) by NO₂ photolysis, a small amount of prompt OH was found to be generated by the 355 nm laser pulse. The main source of this undesirable “photolytic” OH was nitrous acid (HONO), which is produced in the reaction of NO₂ with water [158]. In order to subtract its contribution from the data, experiments were performed using HONO as a precursor instead of NO₂ while keeping other experimental parameters (such as total pressure, laser energy and polarisation) equal. The experiments required a constant concentration of HONO in the reaction chamber, which is not easy to achieve since HONO is not a chemically stable species. A continuous-flow reaction apparatus was set up for this purpose. In this apparatus, HONO was produced in the following reaction:



The reaction conditions had been optimised in previous studies by the McKendrick group [18, 19]. A 2M aqueous solution of NaNO₂ (99%, Sigma-Aldrich) was placed in an addition funnel attached to a flask containing H₂SO₄ 2M in water. The NaNO₂ was added to the H₂SO₄ solution at room temperature with constant stirring. The addition was carried out as slowly as possible (only a few drops per minute) to avoid producing NO₂, which has been previously reported to be generated at high drop rates [159].

The HONO produced in the reaction was carried away with a constant flow of N₂, set to 70 sccm with a mass flow controller. A small fraction of this gas flow was directed into the reaction chamber and the rest of it flowed out to an exhaust. The flow of gas into the chamber was regulated with a needle valve to achieve a pressure of 1 mTorr. The pressure was similar to that of the NO₂ experiments (Section 2.3.1) so that the extent of secondary collisions was essentially the same. The cross section for rotational energy transfer between OH and N₂ is of the order of 60 Å² [160], leading to a similar value for the OH mean free path.

2.4. Detection method

OH radicals that scattered from the surface were detected by laser-induced fluorescence (LIF) on the (1,0) and (1,1) bands of the A ²Σ⁺ - X ²Π electronic transition. The following sections contain an introduction to LIF spectroscopy and provide details on the experimental detection system.

2.4.1. Fundamentals of Laser-Induced Fluorescence

Laser-induced fluorescence (LIF) is a widely used spectroscopic technique first developed by Zare and co-workers [161]. The basis of the LIF technique is to electronically excite a chemical species, normally by means of a short laser pulse, from a specific rotational-vibrational level in its ground state to a rotational-vibrational level in the excited electronic state. The excited species then falls to various levels in the ground state, emitting photons which are subsequently detected. The emission is usually detected with a photomultiplier tube (PMT) positioned at a right angle to the excitation laser axis. The wavelength of the excitation light can be varied if a tuneable laser is used. As the excitation wavelength λ changes, the molecules are excited to fluorescence when λ is resonant with a particular rovibronic transition, resulting in an

excitation spectrum. For each transition, the intensity of the fluorescence is proportional to the number density of absorbers in the lower level. Provided that the intensity factors (Franck-Condon factors and rotational line strengths) are known, the so-called excitation spectrum gives information on the internal state distribution of the absorber [162].

In order to be successfully studied by LIF, a species must have a known spectrum, a sufficiently strong electronic absorption band within the probe wavelength range, and ideally good fluorescence quantum yields with no predissociation in the excited state. A wide range of molecules, atoms and radicals satisfy these conditions, making LIF suitable for many applications. One of the major advantages of LIF over absorption spectroscopy is its sensitivity: it is, at least in principle, a zero-background technique with excellent signal-to-noise ratios. For example, it can be used to detect low concentrations of radical intermediates in flames and plasmas [163]. LIF is also a particularly useful tool for the study of gas-phase collision dynamics, as it provides the internal energy distribution of the products. In addition, polarised laser-induced fluorescence can be used to obtain detailed information about the stereodynamics of the reaction [164].

2.4.2. The spectroscopy of the OH radical

The OH radical is a good candidate to be studied by LIF as it has a convenient fluorescence lifetime (~ 700 ns) and does not dissociate upon transitions to low vibrational levels. In this thesis, OH in its ground vibrational state was probed by excitation in the (1,0) band and detection of photons emitted in the (1,1) band. Excitation and detection on different bands prevents the interference of scattered probe light in the LIF signal. The diagonal (1,1) band has the strongest Franck-Condon overlap and therefore the strongest emission. OH in $v = 1$, studied in Chapter 3, was excited in the (1,1) band while detecting the emission in the (1,0) band. Both schemes are represented in Figure 2.5.

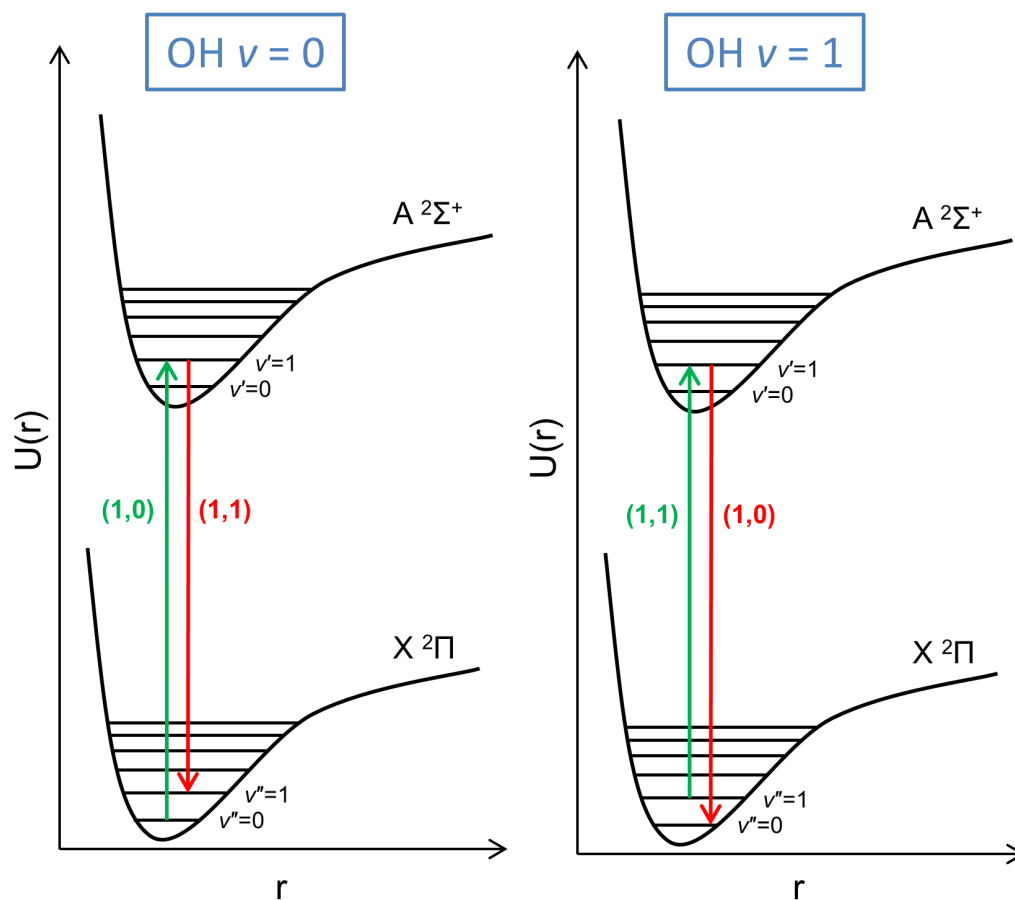


Figure 2.5. LIF excitation and detection schemes for detecting OH $v = 0$ (left) and $v = 1$ (right).

Due to its open-shell electronic structure, OH has nonzero electronic (spin and, for some states, orbital) angular momentum. The electronic spin angular momentum couples in a state-dependent way to the rotation of the molecule and, if present, to its orbital angular momentum; resulting in fine splitting of its rotational levels. The rotational fine structure of OH in the A and X states and the selection rules for its LIF transitions are discussed below. The quantum numbers that need to be considered for this discussion are listed in Table 2.2.

| Angular momentum | Symbol | Projection on molecular axis |
|---|-------------------|------------------------------|
| Electronic orbital angular momentum | L | $\Lambda\hbar$ |
| Electronic spin angular momentum | S | $\Sigma\hbar$ |
| Total angular momentum | $J (= L + S + R)$ | $\Omega\hbar$ |
| Total angular momentum excluding spin | $N (= J - S)$ | $\Lambda\hbar$ |
| Rotational angular momentum of the nuclei | $R (= N - L)$ | - |

Table 2.2. Angular momentum vectors used to characterise OH in its ground and first electronically excited states.

In its electronic ground state (X), OH has an electronic configuration $(1\sigma)^2(2\sigma)^2(3\sigma)^2(1\pi)^3$ giving rise to a molecular term symbol of $^2\Pi_i$. In this state it is best described as an intermediate between Hund's cases (a) and (b). Hund's cases are ideal models of the different possible schemes of coupling of angular momenta [165, 166]. Case (a) is valid for diatomic molecules in the absence of highly charged nuclei and low J . Coupling between L and S is weak and they couple instead to the field produced by the nuclei. L precesses around the internuclear axis with such a high frequency that its magnitude is not defined. Its projection along the axis, $\Lambda\hbar$, is defined and quantised taking values of $\Lambda \geq 0$. S in turn couples to the magnetic field along the internuclear axis caused by the orbital motion of the electrons. S is defined and its axial component Σ combines with Λ to give the total angular momentum along the internuclear axis $\Omega\hbar$, so that $\Omega = |\Lambda + \Sigma|$. Λ -doubling and spin-orbit coupling lift the degeneracy of the rotational levels so that each J value of the OH X state is split into four fine structure levels.

Spin-orbit coupling splits the different Ω components of each state into two fine-structure states ($^2\Pi_{3/2}$ and $^2\Pi_{1/2}$) separated by 126 cm^{-1} . The resulting two rotational manifolds are labelled F_1 ($^2\Pi_{3/2}$) and F_2 ($^2\Pi_{1/2}$). The component with the lower Ω ($^2\Pi_{1/2}$) is higher in energy; that is, OH X is an inverted multiplet.

The nonzero value of A implies that there are two possible senses of rotation of the electrons around the molecular axis, and therefore the states are doubly degenerate. Rotation of the molecule removes this degeneracy so that each J level splits into two Λ -doublet components. The components have opposite (+ or -) parity and are labelled e ($(-1)^{J-1/2}$ parity) or f ($(-1)^{J-1/2}$ parity). As J increases, the splitting in energy between Λ doublets increases and between Ω components decreases, and Hund's case (b) becomes a better descriptor for OH X.

The OH A state has an electronic configuration $(1\sigma)^2(2\sigma)^2(3\sigma)^1(1\pi)^4$ with a corresponding term symbol $^2\Sigma^+$. Since $A = 0$ and $S \neq 0$, Hund's coupling case (b) is appropriate to describe this state. S couples to the nuclear rotation R resulting in spin-rotation doublets with components F_1 ($J = N + 1/2$) and F_2 ($J = N - 1/2$). The e/f parity alternates with J as in the ground state.

The relevant selection rules that apply to OH A – X transitions are:

- (1) $\Delta J = 0, \pm 1$
- (2) $+ \leftrightarrow -$ but $+ \leftrightarrow +$ and $- \leftrightarrow -$
- (3) $\Delta A = 0, \pm 1$
- (4) $\Delta S = 0$

Rules (3) and (4) are specific to Hund's cases (a) and (b) and are satisfied by the A – X transition. Rules (1) and (2) give rise to six main spectroscopic branches:

| | | | |
|-----------------|----------------|---------------|-----------------------|
| $\Delta J = -1$ | $\Omega = 3/2$ | \rightarrow | P ₁ branch |
| $\Delta J = -1$ | $\Omega = 1/2$ | \rightarrow | P ₂ branch |
| $\Delta J = 0$ | $\Omega = 3/2$ | \rightarrow | Q ₁ branch |
| $\Delta J = 0$ | $\Omega = 1/2$ | \rightarrow | Q ₂ branch |
| $\Delta J = +1$ | $\Omega = 3/2$ | \rightarrow | R ₁ branch |
| $\Delta J = +1$ | $\Omega = 1/2$ | \rightarrow | R ₂ branch |

Throughout this thesis, main-branch spectroscopic transitions are labelled as $X_F(N)$; where X is P, Q or R depending on the branch, N is the value of the corresponding quantum number N in the ground state, and F is 1 or 2 depending on the ground-state spin-orbit manifold (F_1 or F_2 , respectively). Figure 2.6 illustrates all possible main-branch transitions arising from the same N in the ground state.

In addition, there are six satellite branches due to transitions for which $\Delta J \neq \Delta N$. The selection rule $\Delta J = 0, \pm 1$ is still obeyed but values of ΔN other than 0 or ± 1 are allowed. These branches are labelled O_{12}, P_{12}, Q_{12} if arising from the F_2 manifold; and Q_{21}, R_{21}, S_{21} if arising from the F_1 manifold.

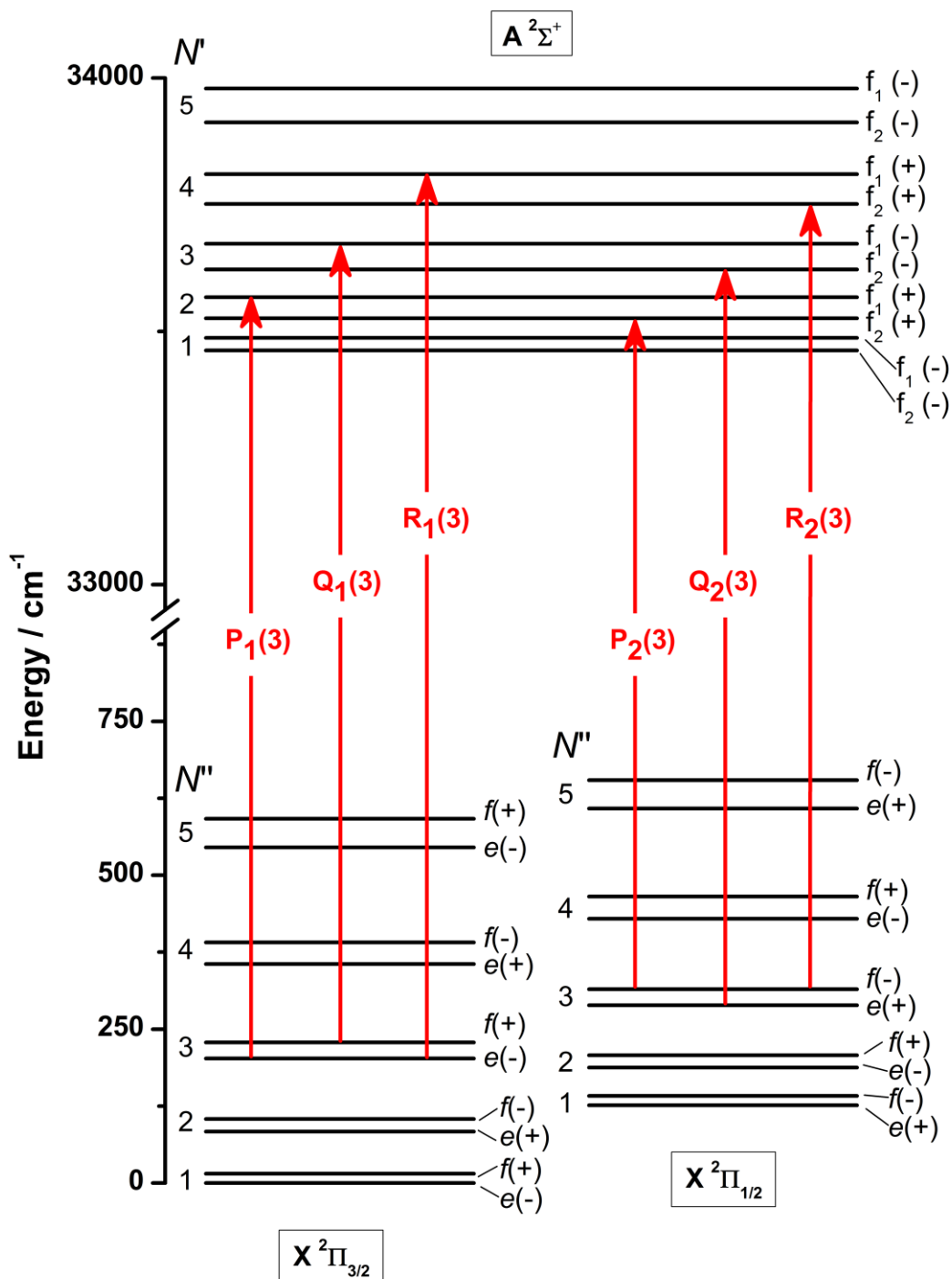


Figure 2.6. Main-branch A – X transitions for OH arising from the same N level in the ground state ($N = 3$). Λ -doubling and spin-rotation splitting are exaggerated for clarity.

2.4.3. Probe laser

The LIF excitation pulses were produced by a pulsed dye laser (Sirah Cobra-Stretch, CSTR-LG-24) pumped with 532 nm light from a frequency-doubled pulsed Nd:YAG laser (Continuum Surelite II-10). The lasing medium was a solution of an organic dye circulating through two quartz cuvettes. The vertically-polarised 532 nm beam was split into three components that pumped three different stages: resonator, preamplifier and amplifier. In the resonator, the emission wavelength was selected by means of a diffraction grating. The grating had a groove density of 2400 lines/mm, resulting in an approximate linewidth of 0.0012 nm. The light transmitted through the output coupler was then rotated by 180° with two prisms and passed again through the resonator cell at a different height (preamplifier). In the final stage or amplifier, the light was further amplified by passing through a second cuvette. It then entered the frequency conversion unit (FCU), where a KDP second-harmonic crystal produced laser light in the UV region. The frequency-doubled output was separated from the fundamental wavelength by means of Pellin-Broca prisms.

The fluorescent dyes used were rhodamine 6G for the (1,0) band (laser light in the 280-285 nm range after frequency doubling) and a combination of DCM in the resonator and rhodamine 101 in the amplifier for the (1,1) band (312-316 nm), all dissolved in methanol. The output beam was horizontally polarised and approximately 5-6 mm in diameter. The output energy was adjusted by varying Q-switch delay of the pump laser. A combination of a polariser and a $\lambda/2$ waveplate was used to attenuate the UV output, allowing further fine-tuning of the energy. The energy was kept constant over the range of wavelengths used by recording an FCU calibration curve for each laser dye. This calibration involved varying the angle of the FCU crystal to change its conversion efficiency to the desired output energy.

2.4.4. Detection system

LIF photons were collected with a liquid light guide (Ultrafine 300) placed in front of the wheel and perpendicular to the laser axis. The liquid light guide sat inside a stainless steel tube with an o-ring sealed window on its end, 20 mm above the laser axis. The collection angle of the light guide was $2\alpha = 72^\circ$, so it was only possible to detect photons along a 29-mm long segment of the laser axis. The emission was collected in a different band from the excitation transition (Figure 2.5) in order to reduce the amount of scattered probe light reaching the detector. This was achieved with optical filters

placed between the liquid light guide and the PMT. The filters selectively transmitted photons corresponding to one particular emission band, while filtering out most of the scattered light from the probe pulse. For (1,1) emission, two dichroic filters centred at $\lambda = 317$ nm with FWHM = 8 nm (Laser Components) were used in tandem to increase the discrimination. Emission in the (1,0) band was isolated with one narrow bandpass filter (Melles Griot, 281 nm, 16 nm FWHM) and one broadband filter (Corion Solar Blind SB-300-F). The PMT (Thorn EMI 9813QB) operated at gain voltages between 1.3 kV and 1.8 kV (typically 1.5 kV). The signal from the PMT was transmitted to a digital oscilloscope.

2.5. Instrument control and data acquisition

LabVIEW software [167] was used to control the timing of the experiment and acquire the data. The specific instruments used were sometimes different for the one-wheel and the multiple-wheel chambers. If that was the case, the model used in the 1-wheel apparatus is mentioned first in brackets.

The digital oscilloscope and lasers were triggered by an 8-channel delay generator (BNC 565 or Quantum Composers 9520) controlled from LabVIEW. This generated a primary trigger (T_0) at 10 Hz. Each channel produced TTL pulses that triggered the flashlamp and Q-switch delay for both Nd:YAG lasers (photolysis laser and dye pump laser), as well as the digital oscilloscope. The delay of each channel with respect to T_0 was varied from the software. The oscilloscope (LeCroy Wavesurfer 434 or Wavesurfer 3024) operated at a sample rate of 2 GS/s and was triggered synchronously with the probe so that the laser pulse was always at the same point on the acquired waveform. The timebase on the oscilloscope was 5 - 10 μ s. The LIF signal was collected by the software in a 2 μ s-long gate after the probe pulse. In addition, the electronic baseline was recorded with a shorter gate (typically 0.5 μ s) before the probe. Figure 2.7 shows a typical waveform as displayed in the data acquisition program. The data in the signal and baseline gates were averaged by the program. Multiple laser shots were averaged in the oscilloscope before transfer to LabVIEW (1-wheel setup); or, in the multiple-wheel setup, single waveforms were transferred to the data acquisition program, which subsequently averaged them. The software also provided control of the probe laser wavelength, allowing the user to record excitation spectra or to find the peak of a LIF transition prior to acquisition of appearance profiles (Section 2.6).

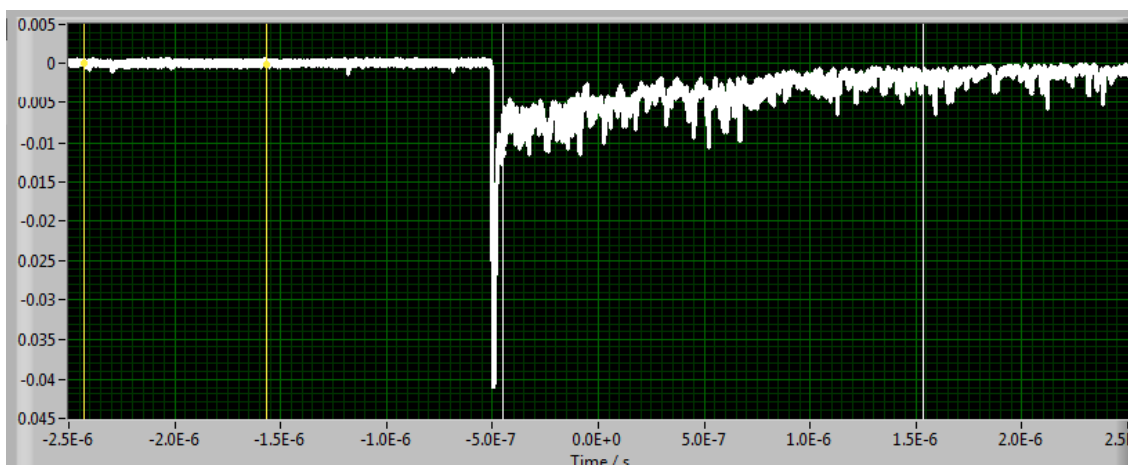


Figure 2.7. A screenshot of the LabVIEW data acquisition program displaying an acquired waveform (the vertical axis represents voltage in V). The waveform is an average of 5 laser shots. The voltage spike at time = $-0.5 \mu\text{s}$ is caused by scattered light from the probe laser, and the subsequent decay corresponds to OH fluorescence. The signal (white) and baseline (yellow) gates are delimited by vertical lines.

2.6. Experimental outputs

Two different data acquisition programs were used to obtain two types of experimental outputs: appearance profiles and excitation spectra. Varying the delay between photolysis and probe pulses with constant excitation wavelength resulted in OH appearance profiles. In contrast, excitation spectra were recorded by scanning the excitation wavelength at a fixed delay between photolysis and probe. The general features of each type of output are discussed below.

2.6.1. Appearance profiles

Experimental appearance profiles

Appearance profiles were recorded on particular LIF transitions to obtain information about the yield and translational energy of OH in the corresponding rotational levels. The OH yield is given by the relative signal intensity, whilst the average translational energy is related to the shape of the profile: slower OH radicals arrive in the probe volume at later delays, assuming a similar angular distribution for all products.

Prior to data acquisition, the probe laser wavelength was varied to find the peak of the transition, i.e. the value of λ providing maximum LIF signal. This “tune-up” procedure

was carried out before each set of appearance profiles (approximately every 30 minutes) to correct any potential wavelength drift of the probe laser. Once the probe wavelength was set, appearance profiles were recorded by scanning the delay of the probe pulse with respect to the photolysis pulse in steps of 1 μs . For each delay, the LIF signals from several laser shots (typically 20 – 30) were acquired and averaged before moving on to the next delay. Usually, several profiles were recorded consecutively to ensure reproducibility.

Figure 2.8 shows representative raw OH appearance profiles resulting from the reaction of $\text{O}(^3\text{P})$ with squalane. There are three different sources of background in the data, over and above the desired LIF signal from OH molecules formed in the reaction of $\text{O}(^3\text{P})$ at the squalane surface. The first one is scattered light from the probe laser pulse that occasionally appeared in the signal gate. This can be corrected by recording some data points at negative photolysis-probe delays (-10 μs to 0 μs) and subtracting the average from each point in the profile. There is also a contribution of scattered light from the photolysis pulse as it goes through the signal and electronic background gates. This photolysis background was recorded by acquiring profiles with the probe laser off (shown in blue in Figure 2.8) which were then subtracted from the raw data. Lastly, there was often a detectable fraction of OH produced by the photolysis pulse as it photodissociated small amounts of HONO present in the reaction chamber. This can be seen in Figure 2.8 as a spike which peaks at 0 μs and then decays away in the following 3 μs as the OH radicals leave the probe volume. Despite its rapid decay, it is possible that a significant amount of OH scatters inelastically from the surface and returns to the probe laser volume at later delays, therefore adding to the reactive OH appearance profile. To account for this contribution, profiles of inelastically-scattered OH were recorded employing HONO as a precursor (Section 2.3.2) and subtracted, with the appropriate normalisation, from the reactive profiles. Details on this background subtraction are provided in the relevant chapters.

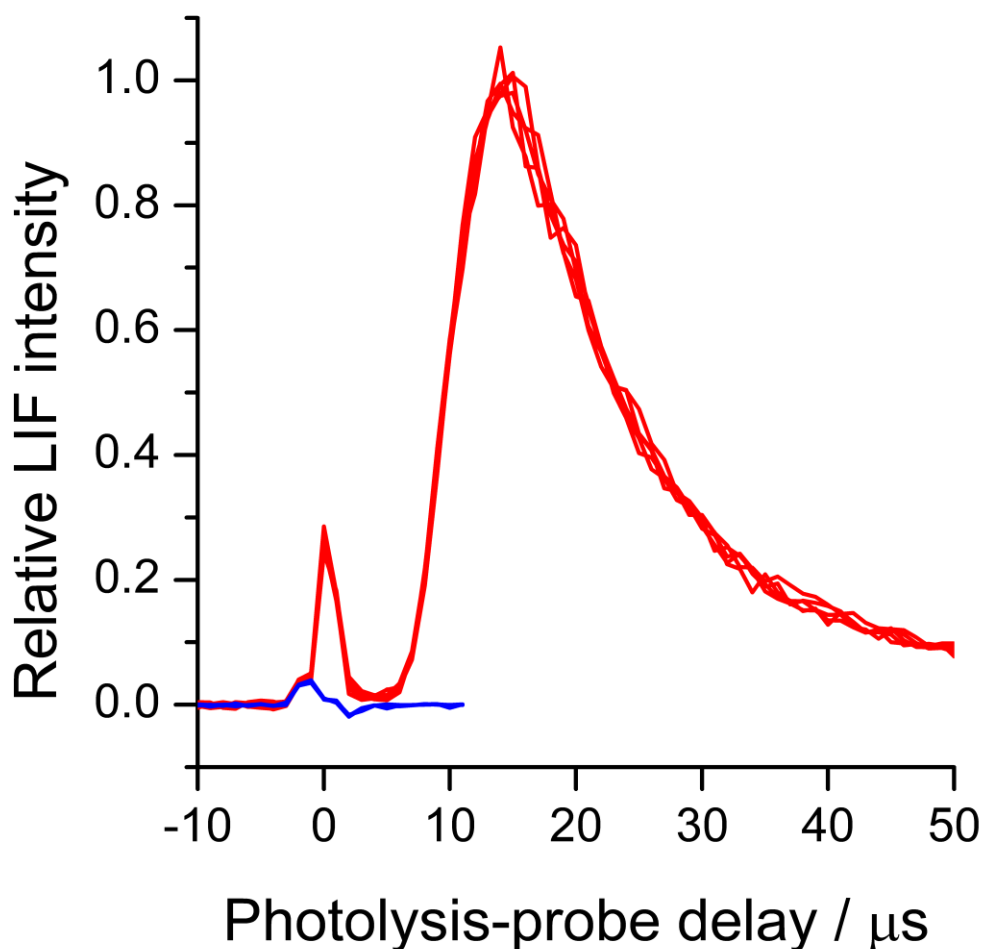


Figure 2.8. Representative OH appearance profiles (red lines) acquired consecutively in the reaction of $O(^3P)$ with squalane, with a distance of 6.5 mm between the wheel and the laser axis. The probe laser background has been subtracted from the profiles. The blue lines represent the contribution of the photolysis laser to the profiles.

Monte Carlo simulations of appearance profiles

OH appearance profiles were simulated with a LabVIEW Monte Carlo simulation previously developed in the McKendrick group [4]. The main purpose of the simulations was to aid the interpretation of the experimental profiles, de-convoluting the translational information blurred by the spread in speeds and angles in the experiment. In addition, the Monte Carlo simulations were employed to carry out a density-to-flux transformation to obtain reliable relative values of OH flux from different liquid surfaces (see Chapter 4 for details).

The simulation accounted for the velocity distribution resulting from 355-nm NO₂ photolysis and the geometry of the detection system. Parameters such as beam size and shape (round beam or rectangular sheet), beam-to-surface distance and the dimensions of the liquid surface were set to match the experiments. Appearance profiles were simulated by calculation of a large number of individual OH trajectories with correctly weighted Monte Carlo sampling over the experimental parameters. First, the initial position of the NO₂ molecule in the photolysis beam was selected from a uniform distribution. The velocity of the resulting O(³P) atom was sampled from the known distribution from 355 nm photolysis of NO₂ [143]. If the resulting trajectory intersected the liquid surface, the impact point and flight time to the surface were used as the starting point for an OH recoil trajectory. The IS or TD character (see Chapter 1) of the returning trajectory was assigned by sampling from a binary distribution given by a user-set IS/TD ratio. IS and TD trajectories were sampled from different distributions. Impulsively scattered OH was assumed to follow a $\cos^4\theta$ distribution tilted away from the surface normal with a speed given by the hard-sphere model of energy transfer [1]. The final-to-incidence angle ratio and effective surface mass for squalane were obtained from previous molecular beam experiments by Minton and co-workers [60, 101, 102]. For TD trajectories, a user-defined surface temperature T characterised a Maxwell-Boltzmann distribution from which the speed of the recoiling OH was selected. The recoil direction was sampled from a cosine-weighted distribution about the surface normal. If the returning OH trajectory intersected the detection volume (i.e. the fraction of the probe beam viewed by the liquid light guide), the range of delays at which the OH was within the volume was calculated, and the intensity of the simulated appearance profile was incremented by 1 at the relevant delays. An appearance profile simulated with typical experimental parameters and a 1:1 IS/TD ratio is presented in Figure 2.9.

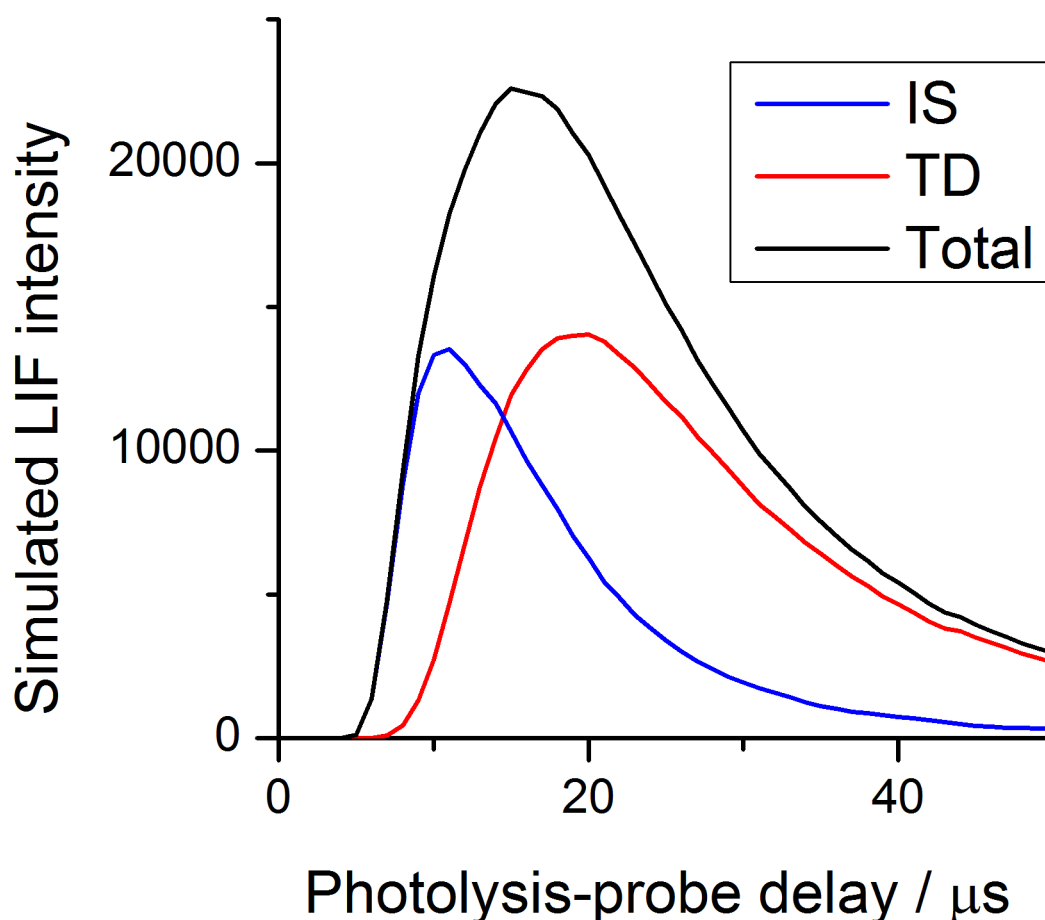


Figure 2.9. Monte Carlo simulated appearance profile (black line) for a beam-to-surface distance of 6 mm. 20×10^6 trajectories were simulated with an IS/TD ratio of 0.5, a TD temperature $T = 300$ K and a detection time step of $1 \mu\text{s}$. The Y axis represents the number of successful trajectories intersecting the probe volume at the corresponding delay. The IS and TD contributions are represented by blue and red lines, respectively.

The Monte Carlo simulations of the scattering experiments also provide a way to visualise information about the experiment such as the distribution of scattering angles or the fraction of trajectories that can be detected. Due to the geometrical constraints of the detection system and the photolytic method of producing $\text{O}(^3\text{P})$, only a fraction of the scattered products return to the probe volume at a point where they can be successfully detected. This is illustrated in Figure 2.10, which shows the simulated distribution of $\text{O}(^3\text{P})$ atoms impinging on the surface of the wheel plotted as a heat map. The broad angular distribution in NO_2 photolysis results in a broad distribution of

incidence points on the surface of the wheel, represented in Figure 2.10 (a). Instead of travelling in a horizontal line and colliding perpendicularly to the surface, the $O(^3P)$ atoms can hit the surface at a considerably different height from that of the laser axis. However, only a small fraction of these incidence points will give rise to a returning trajectory that intersects the probe volume. Figure 2.10 (b) corresponds to the same simulation as 2.10 (a), but only the successfully detected trajectories are plotted. This shows that the OH detected in the experiment originates from incident $O(^3P)$ atoms hitting the area of the wheel close to the laser axis and viewed by the liquid light guide. It is useful to be aware of this, since it implies that poor coverage in the centre of the wheel (a problem frequently encountered in the experiments) does not significantly affect the results.

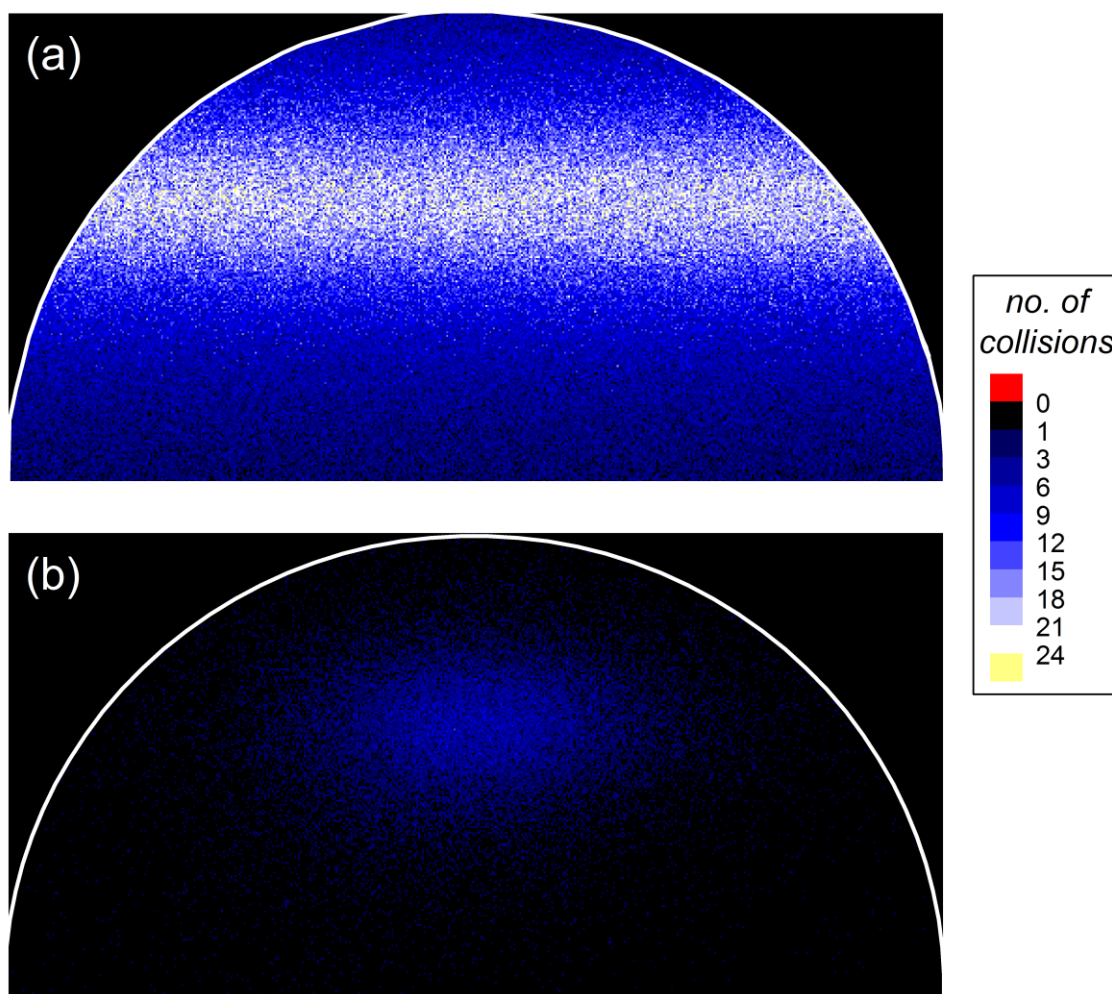


Figure 2.10. Monte Carlo simulated spatial distributions of O(³P) scattering on the surface of the wheel. The data are displayed in a 500×250 2D matrix so that each pixel corresponds to a 0.1×0.1 mm area on the wheel surface. The number of collisions per pixel is represented by its colour as indicated in the legend. The upper half of the wheel is encircled in white. Panel (a) shows all of the O(³P) impacts on the surface, and panel (b) shows the impacts that led to detected products. A total of 6×10^6 trajectories were simulated with a 1:1 IS /TD ratio and a 50- μ s upper limit for the detection time. The laser axis was 6 mm away from the surface in the Z direction and 15 mm above the centre of the wheel in the X direction. The laser beam diameters were 5 mm (photolysis) and 3 mm (probe).

2.6.2. Excitation spectra

Experimental excitation spectra

OH excitation spectra were recorded by scanning the wavelength of the probe laser over the relevant vibronic band for a constant photolysis-probe delay, averaging several laser shots for each wavelength. The probe wavelength was typically varied in steps of 0.0025 nm, omitting regions that did not contain any transitions of interest. This approach considerably reduced the data acquisition time and ensured more constant conditions over the course of a spectrum. This is particularly important because drifts in chamber pressure and probe laser energy could potentially affect the relative intensities of the different spectral lines. For this reason, their values were carefully monitored during acquisition of excitation spectra. The data acquisition software also allowed near-simultaneous acquisition of interleaved data at several photolysis-probe delays. This was achieved by sequentially varying between delays at each wavelength before changing to the next one. A representative example of an OH excitation spectrum, acquired in the reaction of $O(^3P)$ with squalane, is shown in Figure 2.11.

Fitting of rotational distributions

Rotational state distributions of OH were obtained by fitting the experimental spectra to simulations in LIFBASE [168]. This software simulates LIF excitation spectra using previously known spectroscopic constants for OH and taking into account experimental factors such as line broadening, resolution of the probe laser and shifts in wavelength and baseline. The population of the individual N levels for each spin-orbit and Λ -doublet manifold was manipulated in the simulation to match the experimental spectrum. An experimental spectrum and its corresponding simulation are presented together in Figure 2.11.

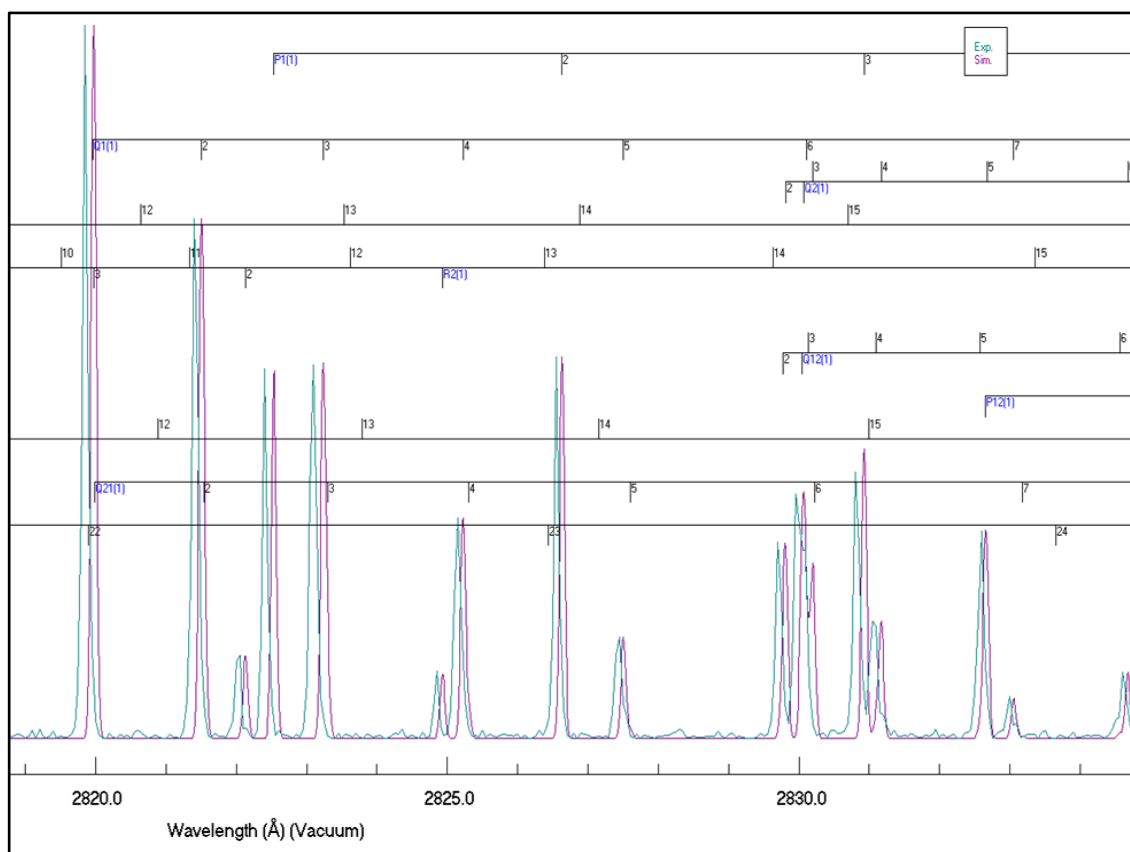


Figure 2.11. LIFBASE screenshot showing an experimental OH excitation spectrum (green) and its matched simulation (purple) with labelled transitions (the spectra are offset for clarity). The experimental spectrum was recorded in the reaction of $O(^3P) +$ squalane at a photolysis-probe delay corresponding to the peak of the appearance profile.

Despite the fact that OH was not produced under equilibrium conditions, in some cases the rotational populations of the OH products could be well characterised by a Boltzmann distribution. Such a distribution is described by the following equation:

$$P(N_i) = \frac{g_i}{Z} e^{-\frac{E_i}{kT}} \quad (2.3)$$

Here $P(N_i)$ is the relative population in the rotational level N_i , E_i is the energy of said level, g_i is its degeneracy, k is Boltzmann's constant and T is the temperature of the distribution. Z is the partition function, defined as $Z = \sum_i g_i e^{-\frac{E_i}{kT}}$.

The experimental rotational populations were employed to construct Boltzmann plots. The populations of the levels were divided by their degeneracy, the natural logarithm was taken and plotted against their energy, and the resulting points were least-squares

fitted to a line of slope $-\frac{1}{kT}$. The rotational temperature T indicated the degree of rotational excitation of the OH radicals. Product distributions with higher average rotational energy yielded higher values of T ; however, this does not imply that they were truly thermal distributions at temperature T .

The populations obtained in the LIFBASE analysis can potentially differ from the actual distribution due to variations in detection sensitivity with wavelength (mostly given by the absorption curve of the bandpass filters) and the effect of saturation. The simulations assume the ideal case in which there is no saturation and the population of the excited state is linearly proportional to the laser intensity, but this is only true for low intensities. The experimental probe energies were expected to cause partial saturation of the LIF transitions, which could potentially affect the obtained relative populations [169].

In order to assess the effect of the saturation, thermal OH spectra were acquired and analysed. The spectra were recorded in the O(³P) + squalane reaction by admitting 0.25 Torr N₂ to the chamber and detecting OH at a photolysis-probe delay of 30 μs. This ensured that the products were detected after a large number of gas-phase collisions so that their rotational distributions were fully thermalised. The expected OH rotational temperature should in consequence be close to room temperature. Reassuringly, the population distribution of thermal OH yielded a value of $T = 303 \pm 6$ K, indicating that these effects do not substantially alter the result of the population analysis.

Chapter 3.

Interfacial reaction of O(³P) with an unsaturated hydrocarbon

3.1. Introduction

As discussed in the general introduction (Chapter 1), the reaction between gas-phase O(³P) atoms and the liquid hydrocarbon squalane has been well characterised in previous work [3-7, 60, 101, 102, 170]. This knowledge can be applied to the study of other hydrocarbon-containing liquids, using squalane as a benchmark. In this chapter, the interfacial reaction of O(³P) with squalene (trans-2,6,10,15,19,23-hexamethyltetracos-2,6,10,14,18,22-hexaene) is investigated and compared against the O(³P) + squalane reaction. Squalene is a partially unsaturated liquid hydrocarbon which is analogous to squalane but contains six double bonds along its backbone. The chemical structures of both molecules are shown in Figure 3.1.

The purpose of this study is to investigate how the presence of unsaturated sites affects the interfacial reaction dynamics of hydrocarbons, and what role the liquid surface plays in the reaction mechanism. It is known from gas-phase experiments that the H-abstraction reaction from unsaturated hydrocarbons is more exothermic and has a lower activation energy. This is due to the presence of allylic C(sp³)-H bonds, which are lower in energy and lead to more energetically stable products. In squalene, all of the C(sp³)-H bonds are allylic, with 24 primary bonds (corresponding to a terminal methyl group) and 20 secondary bonds. Squalane, in contrast, has a mixture of primary, secondary and tertiary C(sp³)-H bonds (24, 32 and 6 H atoms, respectively), none of which have allylic character. The enthalpies of H abstraction from these sites, listed in Table 3.1, have been estimated from bond dissociation energies¹ extracted from thermodynamic data [142]. The barriers of reaction for the different alkyl [106, 171]

¹ The exact values of C-H bond energy vary significantly depending on the alkane studied and the literature source used. Similarly, kinetically determined reaction barriers differ from dynamic thresholds, although the latter are in better agreement with the calculated barriers in [171]. See [105] for alternative values.

and allyl [172] C(sp³)–H sites, determined from gas-phase hydrocarbons by Luntz and co-workers, are also presented in the table. The six C(sp²)–H vinyl bonds in squalene are not considered due to the high barriers of H abstraction from unsaturated sites: the reaction has a positive enthalpy of approximately 25 kJ mol⁻¹, and a threshold of ~ 50 kJ mol⁻¹ [173]. Considering the average collision energy in the present experiments, it can be safely assumed that H abstraction from the vinyl bonds in squalene does not contribute significantly to the reaction.

| C–H bond type | No. of sites in squalane | No. of sites in squalene | E ₀ / kJ mol ⁻¹ | Δ _r H / kJ mol ⁻¹ |
|---------------------------|--------------------------|--------------------------|---------------------------------------|---|
| 1 ^{ry} alkyl C–H | 24 | - | 29 | -7 |
| 2 ^{ry} alkyl C–H | 32 | - | 19 | -19 |
| 3 ^{ry} alkyl C–H | 6 | - | 14 | -26 |
| 1 ^{ry} allyl C–H | - | 24 | 7 | -72 |
| 2 ^{ry} allyl C–H | - | 20 | 8 | -85 |
| Vinyl C–H | - | 6 | - | - |

Table 3.1. Different types of C–H bonds in squalane and squalene. Dynamic thresholds of reaction (E₀) were obtained from small gas-phase hydrocarbons [106, 172]. Δ_rH is the standard enthalpy of reaction for similar small hydrocarbons. The vinyl C–H sites in squalene are not considered due to their low expected reactivity.

The large difference in reaction barriers, in combination with the relatively low kinetic energy of the O(³P) atoms, induces very different intrinsic reactivities depending on the type of C–H site. Figure 3.1 presents the energy distribution of the O(³P) atoms produced by 355 nm NO₂ photolysis [143], compared against the relative energies of the products and transition states from Table 3.1. It can be appreciated that H abstraction from a primary C(sp³)–H bond in squalane is considerably disfavoured with respect to the other sites, as only the high-energy tail of the O(³P) distribution can lead to reaction. Focusing on the reaction energetics alone, squalene (on the left side of Figure 3.1) is expected to be more reactive towards H abstraction than squalane (on the right of the figure). Despite this, the presence of double bonds might have a negative effect in the yield of H abstraction from squalene. The reaction of O(³P) with alkenes at low collision energies proceeds *via* addition to the double bond, which does not lead to

OH products [174]. The effect of this additional reaction channel in squalene is investigated in this chapter. Previous studies of OH inelastic scattering on squalene showed that unsaturated sites reduce the survival probability of the radical products at the interface [19, 20]. This effect might be expected to be larger for the reaction with $O(^3P)$, but it could be compensated by the favoured H-abstraction energetics. It is an interesting unanswered question what relative yields of OH should be expected, and what effect the liquid surface would have on these yields.

Although the gas-phase H-abstraction dynamics of $O(^3P)$ with some small unsaturated hydrocarbons have been previously characterised [172, 175-177], this is the first study of these types of reactions at the interface. The closest relevant examples focused exclusively on the $O(^3P)$ addition reaction (which is the dominant reaction path at low temperatures) with condensed films of alkenes [178], or with alkenes adsorbed on metal and ice surfaces [179]. Preliminary results for $O(^3P)$ + squalene were reported in a previous PhD thesis from the McKendrick group [180]. The present work expands on this preliminary study, including the detection of vibrationally excited OH radicals to provide a full picture of the scattering dynamics.

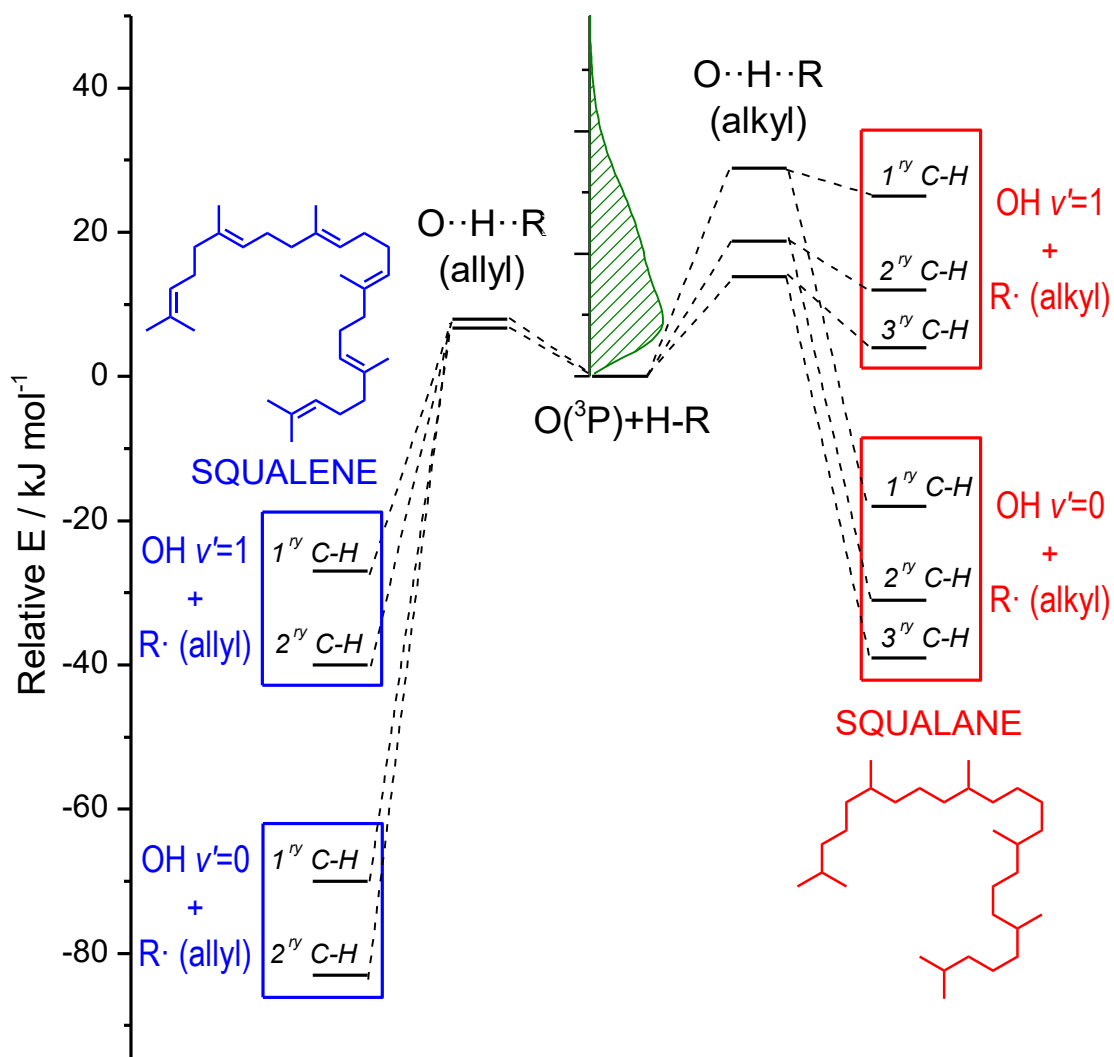


Figure 3.1. Energetics of H abstraction for different C–H sites. The kinetic energy distribution of $O(^3P)$ produced by NO_2 photolysis is presented in the inset graph (green line). The chemical structures of squalane (red) and squalene (blue) are also shown.

3.2. Experimental

The experiments were performed in the 1-wheel reaction chamber described in Section 2.2.1. Changing the liquid sample required approximately 1 hour and involved venting the experiment to the atmosphere, which could potentially affect the experimental conditions (particularly the beam-to-wheel distance, the concentration of water in the chamber and the zero point of the pressure gauge). For this reason, the laser energy and alignment were monitored before each experiment, and care was exercised to maintain the same precursor pressure for all of the measurements in order to make the results comparable between liquids. Typically, 3 or 4 datasets were acquired each day, alternating between squalane and squalene. Each dataset involved acquiring 5 – 10 appearance profiles with their corresponding background measurements, or 1 excitation spectrum. Each liquid was always studied in the same bath with the same wheel in order to avoid cross-contamination between samples. In addition to squalane and squalene, perfluoropolyether (PFPE) was used as a blank for background correction purposes. The chemical structure, commercial supplier and purity of each liquid are presented in Table 3.2.

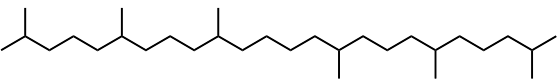
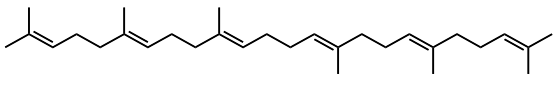
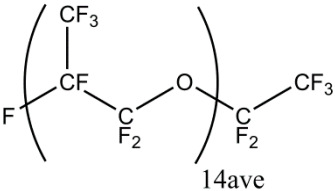
| Name | Chemical Structure | Supplier | Purity |
|---|--|---------------|--------|
| Squalane (2,6,10,15,19,23-hexamethyltetracosane) |  | Sigma-Aldrich | 99% |
| Squalene (trans-2,6,10,15,19,23-hexamethyltetracosane-2,6,10,14,18,22-hexaene) |  | Sigma-Aldrich | ≥98% |
| PFPE (perfluoropolyether Krytox 1506) |  | DuPont | 100% |

Table 3.2. Liquids studied, chemical structures and percentage purity as stated by the commercial supplier.

The photolysis and probe laser beams counterpropagated along an axis 6 mm above the liquid surface. The photolysis energy was approximately 90 mJ pulse^{-1} and the beam was 6 mm in diameter. The probe laser fluence was kept relatively low to minimise the saturation of the transitions. Both OH radicals in their ground ($v' = 0$) and first vibrationally excited ($v' = 1$) states were detected, using the probe schemes introduced in Section 2.4.2. When detecting OH ($v' = 0$), the probe energy was $125 \text{ } \mu\text{J pulse}^{-1}$ and the beam diameter was 3 mm. For OH ($v' = 1$), excitation took place in the diagonal (1,1) band so lower probe energies were employed ($20 \text{ } \mu\text{J pulse}^{-1}$ for a 4-mm beam).

3.3. Results

3.3.1. Appearance profiles

Appearance profiles provide two types of information. First, the intensity of the profiles is proportional to the yield of OH in the selected rovibrational level. The LIF signal intensity does not give the absolute yield, so the appearance profiles must be recorded under the same experimental conditions in order to be comparable. Secondly, the profiles provide a measure of the translational energy of the OH radicals in the corresponding level. The rising edge of the profile corresponds to OH products that have a short flight time from the surface to the probe laser, and therefore are translationally hot. Slower TD products are detected at later photolysis-probe delays and contribute to the tail of the profile. To some extent, the shape of the appearance profile is related to the IS/TD branching of the products, although this information is convoluted by the spread in angles and collision energies.

Appearance profiles of OH produced by squalane (hereafter OH_{ane}) and by squalene (OH_{enc}) were recorded for different lines in the Q_1 branch. This spectral branch was chosen for its higher intensity and better signal-to-noise ratio than the others. As discussed later (Section 3.3.2), the rotational distributions were found to be very similar independently of Λ -doublet or spin-orbit manifold, so the choice of branch should not affect the comparison between N' levels. Each profile presented here is an average of 22 measurements taken over 3 different days to ensure reproducibility. Photolysis and probe background were subtracted following the method described in Section 2.6.1.

When detecting OH in the (1,0) band, there was an OH LIF signal present at early photolysis-probe delays, appearing at 0 μs and decaying away in the following 4 μs . This signal, whose intensity varied between datasets, was only observed when NO_2 was present in the reaction chamber and both lasers were on, with the probe wavelength on an OH LIF transition. The signal intensity appeared to be dependent on the amount of water contaminating the chamber: it decreased with time if the sample was kept under vacuum, but returned to a high level after opening the chamber to air. The most likely source of this background signal is nitrous acid (HONO), produced in the heterogeneous reaction between NO_2 and H_2O [158]. Large concentrations of water adsorbed on the chamber walls can lead to high gas-phase concentrations of HONO, which is photolysed by 355 nm light to yield OH and NO [156]. HONO has been previously reported to be a contaminant in experiments using 355 nm photolysis of NO_2 [181], and its complete removal from the NO_2 precursor is difficult to achieve. This “photolytic” OH background was kept as low as possible by minimising the exposure of the reaction chamber to the atmosphere; however, there was always a noticeable amount.

The photolytic OH signal decayed to essentially zero before the main “reactive” OH profile appeared. Despite this, it is possible that some of the photolytic OH radicals scattered from the liquid surface and were detected in their return trajectory at delays between 5 and 50 μs , therefore interfering with the reactive appearance profile. In order to investigate this, appearance profiles were recorded with the unreactive liquid perfluoropolyether (PFPE). It has been previously shown that both squalane and squalene react with OH radicals and provide a lower survival probability of OH than PFPE in inelastic scattering experiments [19]. The experiments with PFPE therefore establish an upper limit for the contribution of photolytic OH to the appearance profiles. Typical profiles from PFPE are presented in Figure 3.2 together with squalane and squalene. The profiles are scaled to their LIF signal at early times (1 μs), which is expected to be caused exclusively by HONO photolysis. The returning photolytic OH signal was substantially smaller than the early-times signal, which in turn was smaller than the reactive OH signal. Although it was still detectable, the returning OH contribution was in all cases not significant considering the experimental error. It can therefore be assumed that the OH radicals detected at photolysis-probe delays of 5 – 50 μs arise overwhelmingly from reaction of $O(^3P)$ atoms at the surface, and the intensities of the appearance profiles are a reliable measure of the surface reactivity.

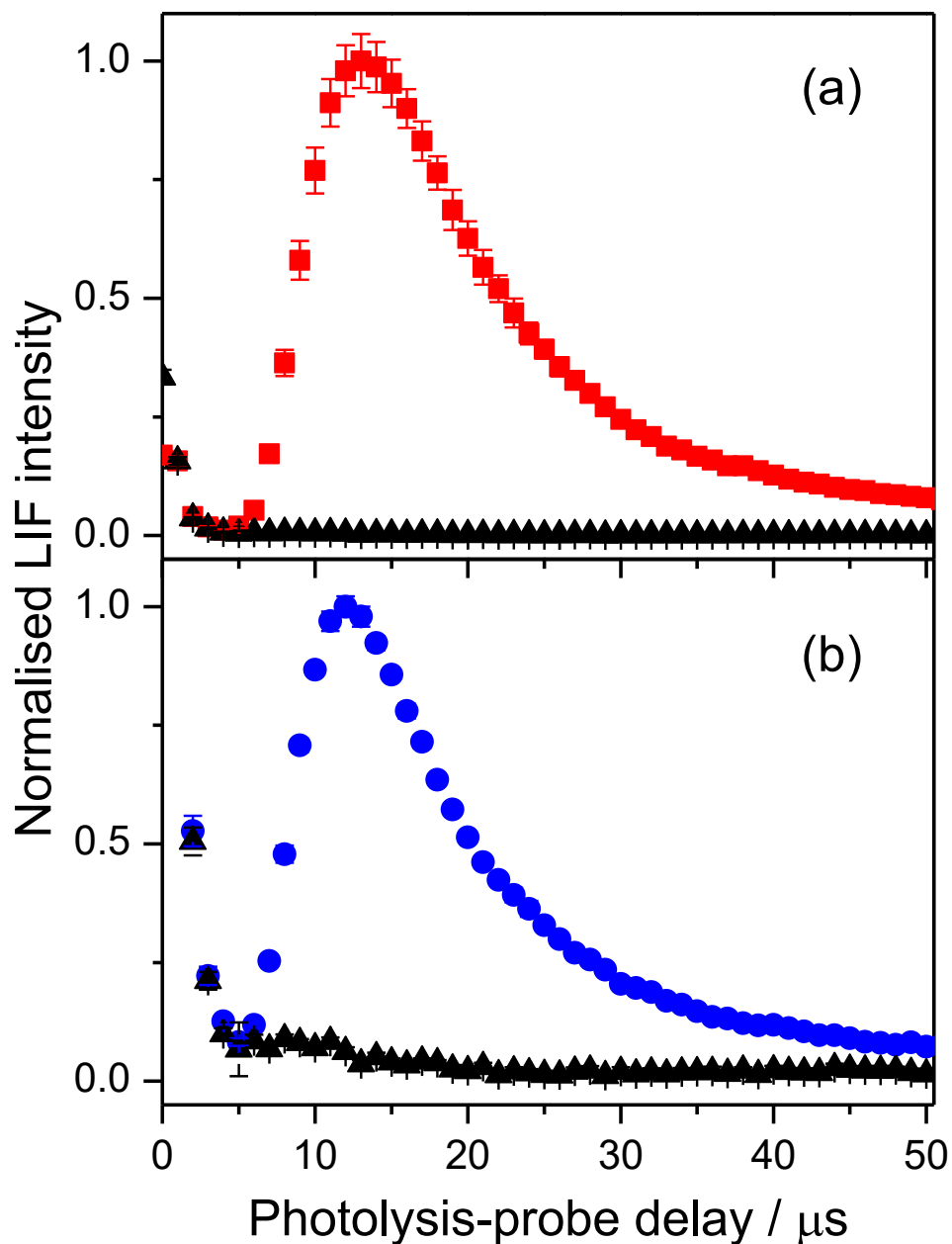


Figure 3.2. Average OH ($v' = 0$) appearance profiles recorded on the $Q_1(1)$ transition from (a) squalane (red squares) and (b) squalene (blue circles); together with profiles recorded under the same conditions from the inert blank PFPE (black triangles, scaled to the 1- μ s signal of the profiles). The peak signal of the main appearance profiles is normalised to 1. Error bars correspond to $\pm 1\sigma$ standard error of the mean (SEM).

Figure 3.3 shows the average background-subtracted appearance profiles of OH_{ane} and OH_{ene} recorded on the $Q_1(1)$, $Q_1(5)$ and $Q_1(7)$ lines of the (1,0) band. It should be noted that there is a small contribution from the (much less intense) $R_2(3)$ line to the $Q_1(1)$ signal, since these two lines are partially overlapped in the spectrum. The profiles are normalised to the most intense signal for each N' to help comparison between liquids. Therefore the relative intensities between different N' levels cannot be appreciated in the figure; instead, that information is contained in the excitation spectra and population plots in Section 3.3.2. The most striking difference between the OH_{ane} and OH_{ene} profiles is their intensity: squalane produces almost five times as many OH radicals in $N' = 1$. The difference becomes smaller as N' increases, so that both liquids produce a very similar yield of OH in $N' = 7$. This indicates that squalene produces OH with substantially higher average rotational energy. Additionally, more subtle differences can be found in the shape of the profiles: those from squalene peak at slightly earlier delays, indicating higher translational energy. It can also be appreciated that appearance profiles for higher N' are earlier than low- N' profiles, indicating a positive correlation between translational and rotational energy of the products.

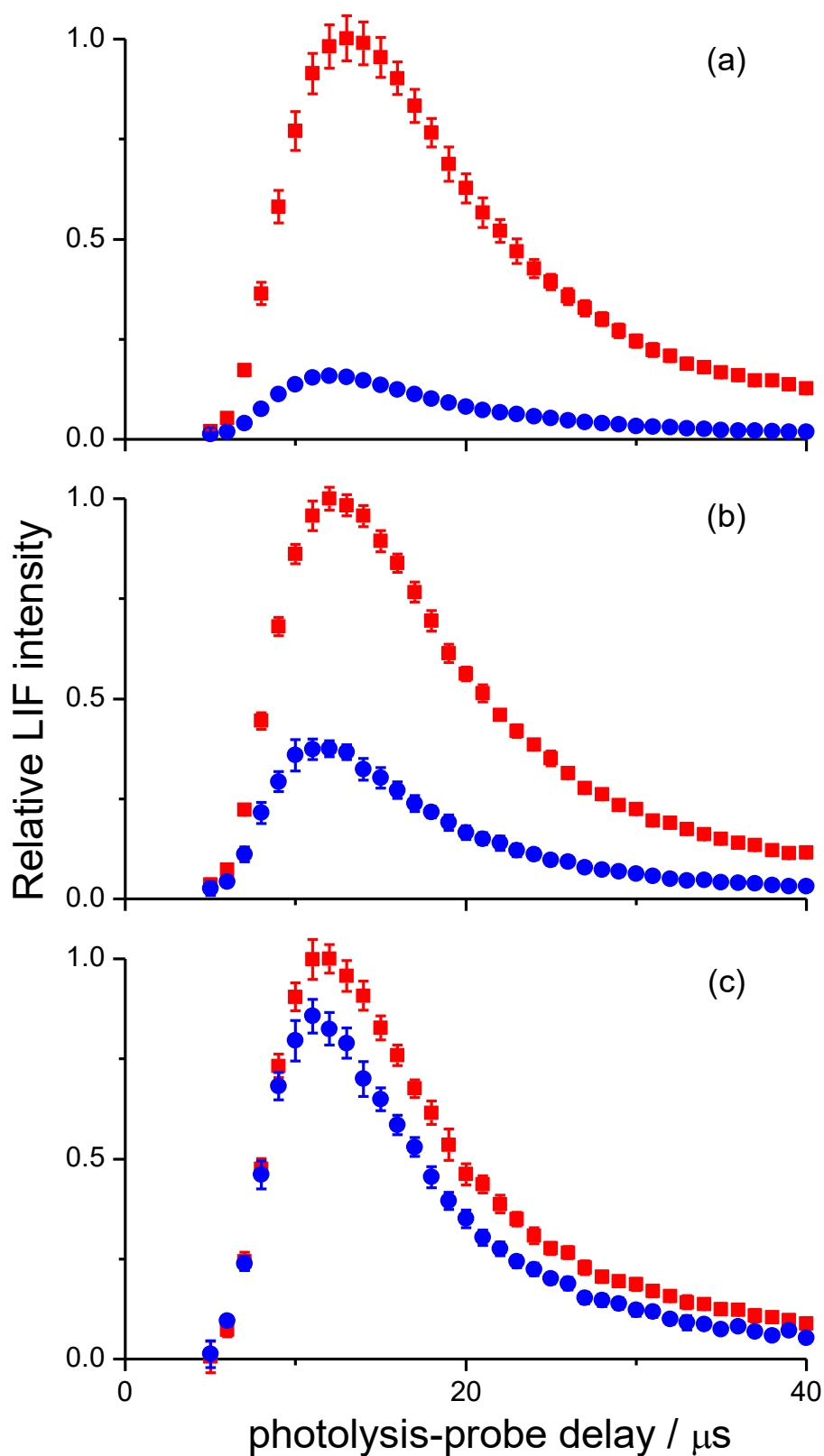


Figure 3.3. OH ($v' = 0$) appearance profiles recorded for (a) $N' = 1$, (b) $N' = 5$ and (c) $N' = 7$, from squalane (red squares) and squalene (blue circles). Profiles are normalised to the most intense signal in each panel. Error bars represent $\pm 1\sigma$ SEM.

Appearance profiles in the (1,1) vibronic band were recorded for the $Q_1(1)$, $Q_1(3)$ and $Q_1(5)$ transitions, and are presented in Figure 3.4. The maximum recorded value of N' was lower for OH ($v' = 1$) because the rotational distribution was significantly colder than that of OH ($v' = 0$). Again, OH_{ene} was substantially more rotationally excited than OH_{ane} , resulting in a higher yield of $N' = 5$ for squalene. In contrast with $v' = 0$, the total OH ($v' = 1$) yield is similar for both liquids. This indicates that OH produced on a squalene surface is more vibrationally excited. The difference in translational energy is more marked in the OH ($v' = 1$) profiles: it can be easily appreciated that the OH_{ene} appearance profiles peak about 2 μs earlier than the corresponding OH_{ane} profiles. There is not a clear translational-rotational correlation in this case.

In order to better appreciate the differences in translational energy with N' , peak-normalised appearance profiles are presented in Figure 3.5. The profiles are displayed in different plots depending on the liquid and vibrational level. Additionally, each graph shows the corresponding $N' = 1$ profile from the other liquid (blue dotted lines) to facilitate comparison between squalane and squalene, as well as a simulated TD profile (black lines, details on the simulations are provided in Section 2.6.1). For OH_{ane} ($v' = 0$) ((a)(i)), both the rising edges and the tails of the profiles shift to earlier delays as N' increases. The OH_{ene} ($v' = 0$) profile for $N' = 1$ is substantially earlier than OH_{ane} ($v' = 0$) in $N' = 1$, indicating that OH_{ene} ($v' = 0$) is on average faster. Reciprocally, this is also seen by comparing OH_{ane} ($v' = 0, N' = 1$) with OH_{ene} in graph (b)(i).

Inspection of the OH_{ane} profiles in (a)(i) and (a)(ii) reveals that OH ($v' = 1$) is slower than OH ($v' = 0$), and there are no marked differences between internal energy levels of OH_{ane} ($v' = 1$). Both OH_{ane} ($v' = 0$) and OH_{ane} ($v' = 1$) are significantly IS in character, as shown by comparison to a fully thermal profile (black lines in Figure 3.5). In the case of squalene, the differences between appearance profiles are more subtle. OH_{ene} ($v' = 1$) is slower than OH_{ene} ($v' = 0$), but they both are considerably superthermal and have very similar shapes. There is, however, a very noticeable contrast between OH_{ene} ($v' = 1$) and OH_{ane} ($v' = 1$). The trends in translational energy for OH_{ene} are analogous to OH_{ane} : higher rotational levels in ($v' = 0$) scatter with more translational energy (although the differences are smaller), but the progression is not so clear for OH_{ene} ($v' = 1$). Vibrationally excited OH appears to leave squalene with higher translational energy, and the degree of translational thermalisation is less sensitive to product quantum state.

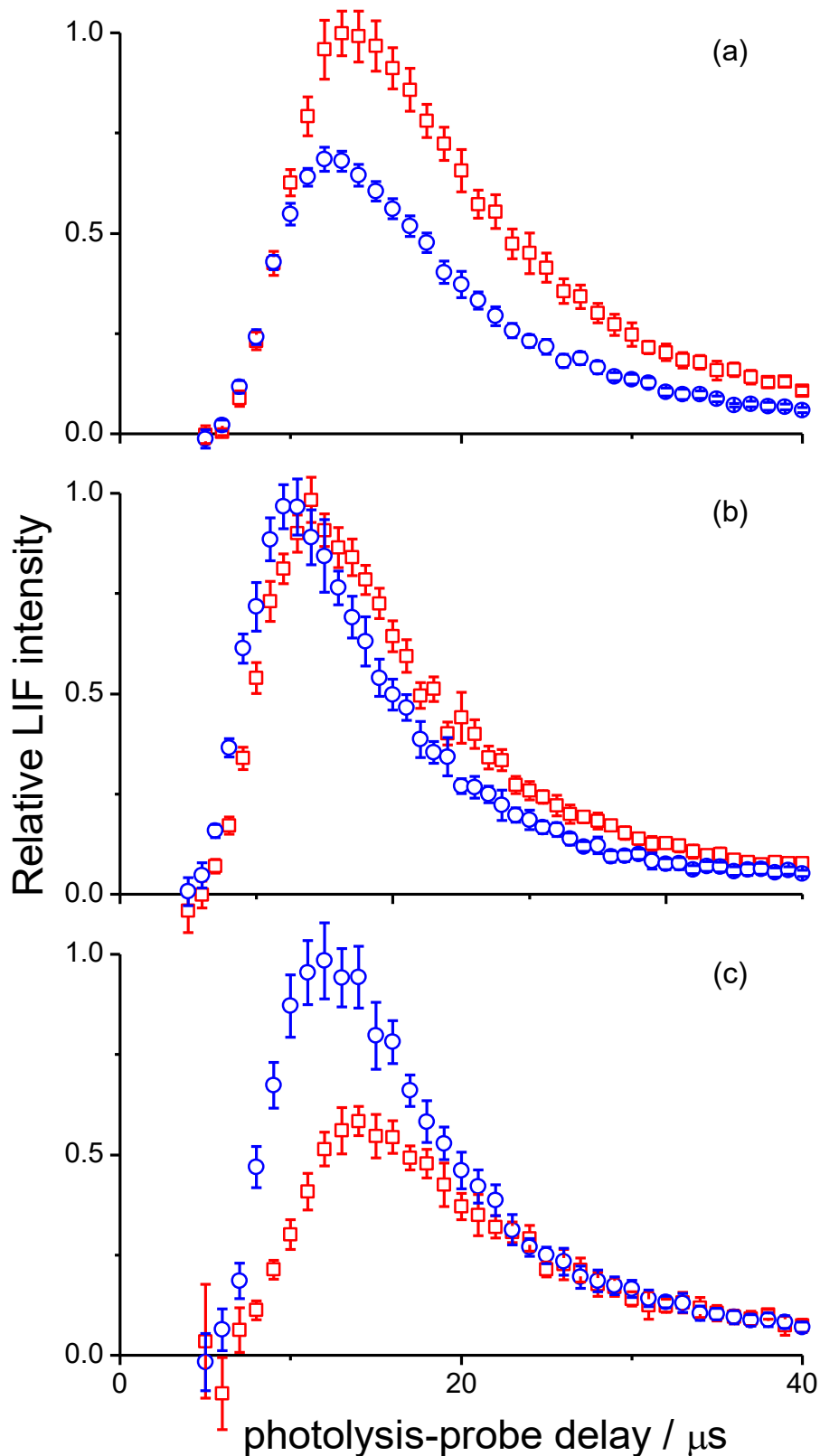


Figure 3.4. OH ($v' = 1$) appearance profiles recorded with squalane (red open squares) and squalene (blue open circles) for (a) $N' = 1$, (b) $N' = 3$ and (c) $N' = 5$. Profiles are normalised to the most intense signal in each panel. The apparent negative intensities for $N' = 5$ are an artefact due to imperfect background subtraction.

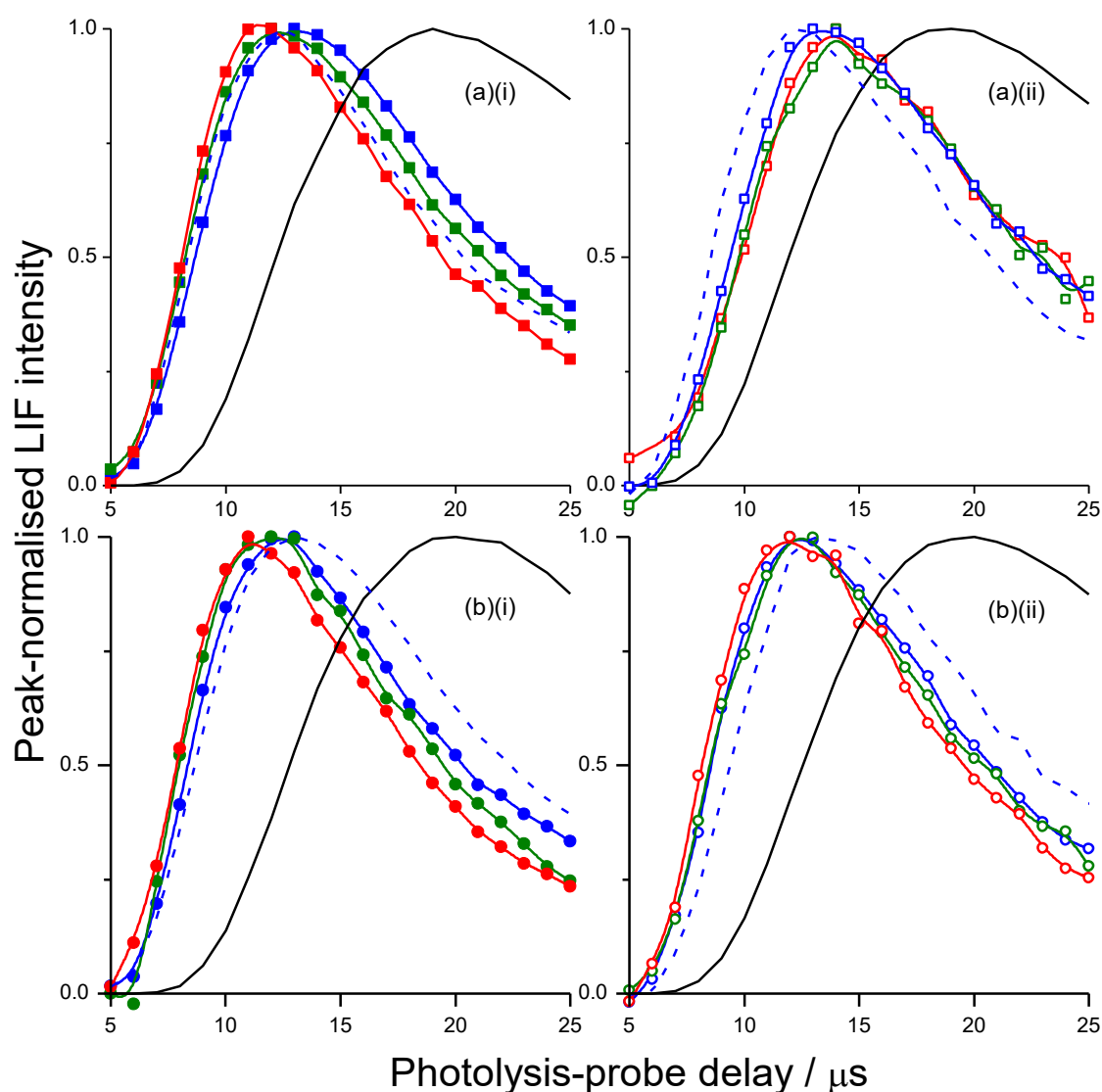


Figure 3.5. Peak-normalised (i) OH ($v' = 0$) and (ii) OH ($v' = 1$) appearance profiles for (a) squalane and (b) squalene. Filled symbols are $v' = 0$ ($N' = 1$ (blue), $N' = 5$ (green) and $N' = 7$ (red)) and the lines are a spline fit to the data. Open symbols represent $v' = 1$ ($N' = 1$ (blue), $N' = 3$ (green) and $N' = 5$ (red)). The dashed blue lines correspond to the peak-normalised $N' = 1$ profiles in the same vibrational level from the opposite liquid, i.e. $\text{OH}_{\text{enc}} (v' = 0)$ in (a)(i), $\text{OH}_{\text{enc}} (v' = 1)$ in (a)(ii), $\text{OH}_{\text{anc}} (v' = 0)$ in (b)(i), and $\text{OH}_{\text{anc}} (v' = 1)$ in (b)(ii). The black lines are a Monte Carlo-simulated room-temperature thermal desorption component.

The appearance profiles give the qualitative trends in translational energy release; however, it is not easy to quantify the product translational energy. The incoming $O(^3P)$ atoms strike the surface at different times with a broad range of incident velocities, which complicates the analysis since the collision energy and the starting time of the returning trajectory are not well defined. The results are further convoluted by the lack of angular resolution of the detection system. Furthermore, an additional complication arises from the barriers of reaction: a greater fraction of slow oxygen atoms can lead to H abstraction from the squalene surface. As a result, OH_{ene} produced with the same translational energy as OH_{ane} has a later average detection time. In theory, this last problem could be corrected for using the excitation functions previously measured for gas-phase hydrocarbons [106, 172], but these are relative and cannot be applied without knowing the scaling factor. Despite all these complications, it is possible to quantify the differences in translational energy to some extent. The procedure is described in detail below.

The OH appearance profiles were fitted to simulated profiles with a known distribution of translational energies. Monte Carlo simulations (Section 2.6.1) were performed for different average OH translational energies, and the results were then compared with the experimental profiles. Experimental appearance profiles for the $Q_1(1)$ transition were taken as representative of all of the scattered OH. This assumption is not unreasonable considering that $N' = 1$ was the most populated energy level in all cases. In the simulated profiles, the product speeds followed a Maxwell-Boltzmann distribution defined by a temperature T , and the scattering angles were distributed around the surface normal with a $\cos\theta$ weighting. Typically 2.5×10^6 trajectories were sampled for each simulated profile, of which approximately 2×10^5 were successful. Temperatures T were adjusted to give the best match of the simulated profiles to the experimental ones. Despite the fact that there is no *a priori* reason for the scattered OH to follow a single-temperature translational distribution, good agreement was found for all experimental profiles and their simulations. Figure 3.6 shows the experimental $Q_1(1)$ appearance profiles and their matched simulations. The temperature of each simulation is indicated in the figure, as well as the average speeds of the products at particular photolysis-probe delays corresponding to the rising edge, peak and tail of the profiles. The same delays were studied in the excitation spectra discussed in Section 3.3.2. It should be emphasized that the products are unlikely to follow a perfect Boltzmann distribution, since the interfacial reaction is not an equilibrium process. Strictly speaking, the simulated profiles correspond to TD distributions emerging from a surface with

temperature T , but this is not the intended physical interpretation: the product-state-specific translational energy distributions are the result of the combination of the initial translational energy of those $O(^3P)$ atoms which react to form them and the dynamical release of exothermicity in the reaction. The approximation is nevertheless sufficient to characterise the trends in translational energy with delay, vibrational level and liquid. As logically required, the average speed increases in all cases for earlier delays. The trends in translational energy already observed in Figure 3.5 become evident in the values of translational temperature. The average translational energy follows the order $OH_{ane}(v' = 1) < OH_{ane}(v' = 0) < OH_{ene}(v' = 1) < OH_{ene}(v' = 0)$.

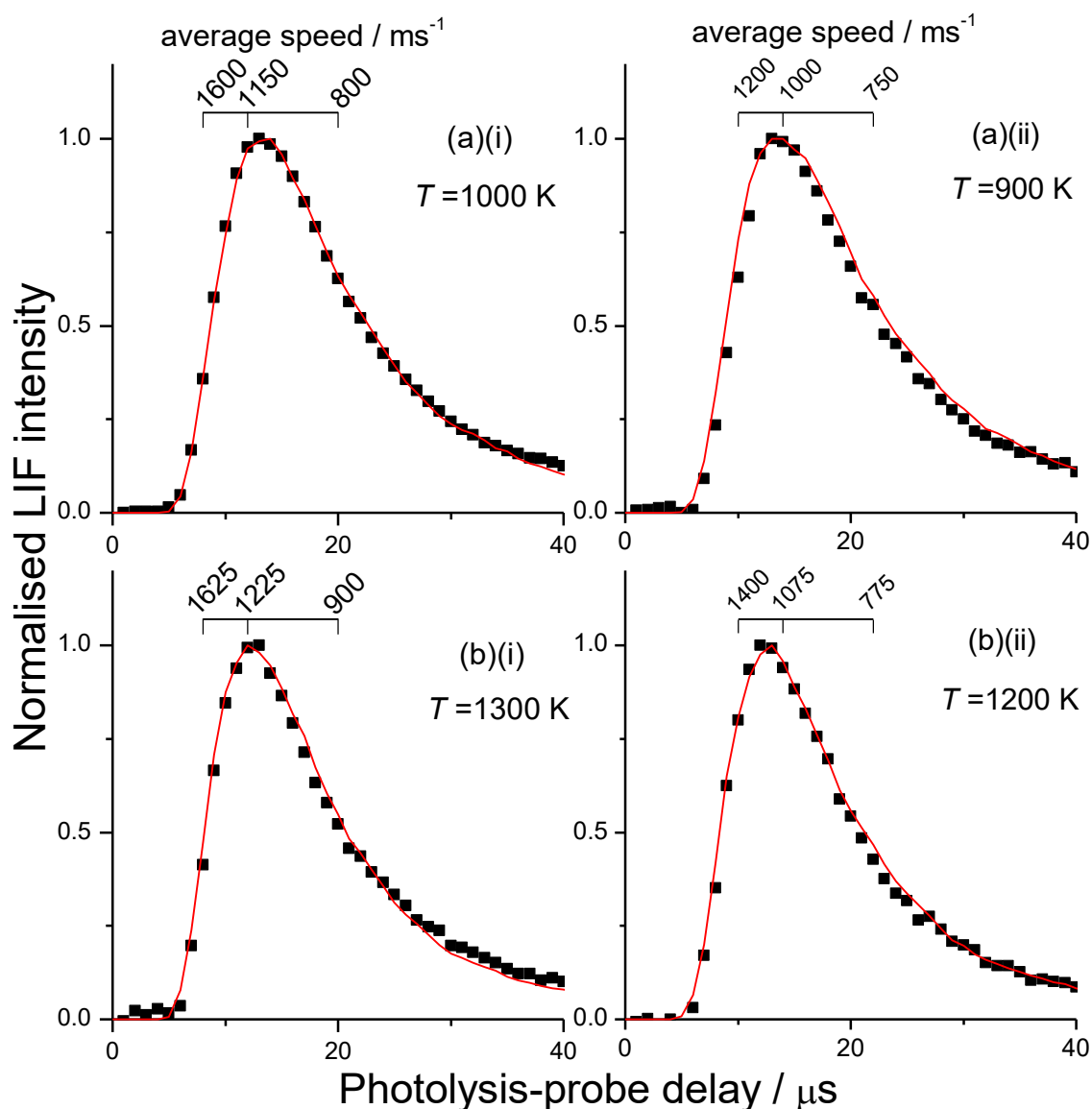


Figure 3.6. Experimental (black squares) and simulated (red lines) OH appearance profiles for the $Q_1(1)$ transition: (a)(i) OH_{ane} ($v' = 0$), (a)(ii) OH_{ane} ($v' = 1$), (b)(i) OH_{ene} ($v' = 0$), (b)(ii) OH_{ene} ($v' = 1$). The values of T for the simulated profiles are indicated in each of the panels. Average OH speeds as a function of delay derived from the Monte-Carlo simulation are also shown.

3.3.2. Excitation spectra

LIF excitation spectra were recorded to obtain the population distribution across the rotational N' levels, allowing more detailed comparison between liquids. In order to characterise the relationship between product translational and internal energy, spectra were recorded at different photolysis-probe delays corresponding to the rising edge, peak and tail of the appearance profiles. The values chosen were 8, 12 and 20 μ s for

OH ($v' = 0$); and 10, 14 and 22 μs for ($v' = 1$) as vibrationally excited OH produced slower profiles, as demonstrated above. The delays were varied sequentially for each wavelength and some regions of the spectrum were omitted, as described in Section 2.6.2.

Similar to the appearance profiles, the spectra from OH ($v' = 0$) possessed a small background contribution from photolysis of HONO. The concentration of photolytic OH in each experiment was monitored by simultaneously recording a spectrum at an early delay (3 μs). This early-delay spectrum was found to match that of OH produced by 355-nm photolysis of HONO [76], confirming this as the source of the background. Fitting the 3- μs spectra to a Boltzmann distribution provided a rotational temperature $T = 333 \pm 26$ K, in reasonable agreement with the previously reported value, $T = 364 \pm 20$ K [76]. In order to obtain an upper limit for the contribution of the HONO background, spectra were recorded with PFPE at photolysis-probe delays of 3, 8, 12 and 20 μs . The OH LIF signal at later delays was always smaller than the 3- μs signal, as expected from the previously recorded appearance profiles (Figure 3.2). The intensity of each line in the PFPE spectrum was then used to obtain an upper contribution to the squalane and squalene spectra, by scaling it to the corresponding 3- μs signal. This contribution was in all cases less than 5% of the total intensity for squalane. In squalene, the lower OH yield meant that the relative photolytic contribution to the signal was slightly higher. The upper contribution was estimated to be < 10 % at 12 μs , and could reach up to 20 % of the signals at 8 and 20 μs . However, it should be considered that a squalene surface can potentially react with OH, resulting in a lower yield of inelastically scattered OH compared to PFPE. The survival probability for OH in squalene, measured under similar conditions to the present experiments, has been determined to be 0.61 with respect to PFPE [19]. In consequence, it is not unrealistic to assume a HONO background contribution of $\sim 10\%$ for squalene. This contribution could in principle be removed by subtracting the previously measured distribution of OH that scatters inelastically from squalene, using the pre-collision spectra as a scaling factor. However, this approach would neglect the fact that the concentration of HONO varied over the course of an experiment, and the experiments were not performed under exactly the same conditions. Any correction to account for the photolytic background would introduce a large amount of uncertainty in the results without making a substantial change in them. For this reason, the HONO background has not been subtracted from the spectra. Typical spectra of the Q_1 branch are shown in Figure 3.7

for different delays. The small relative signal intensities at $3 \mu\text{s}$ indicate that the HONO background contribution is expected to be small.

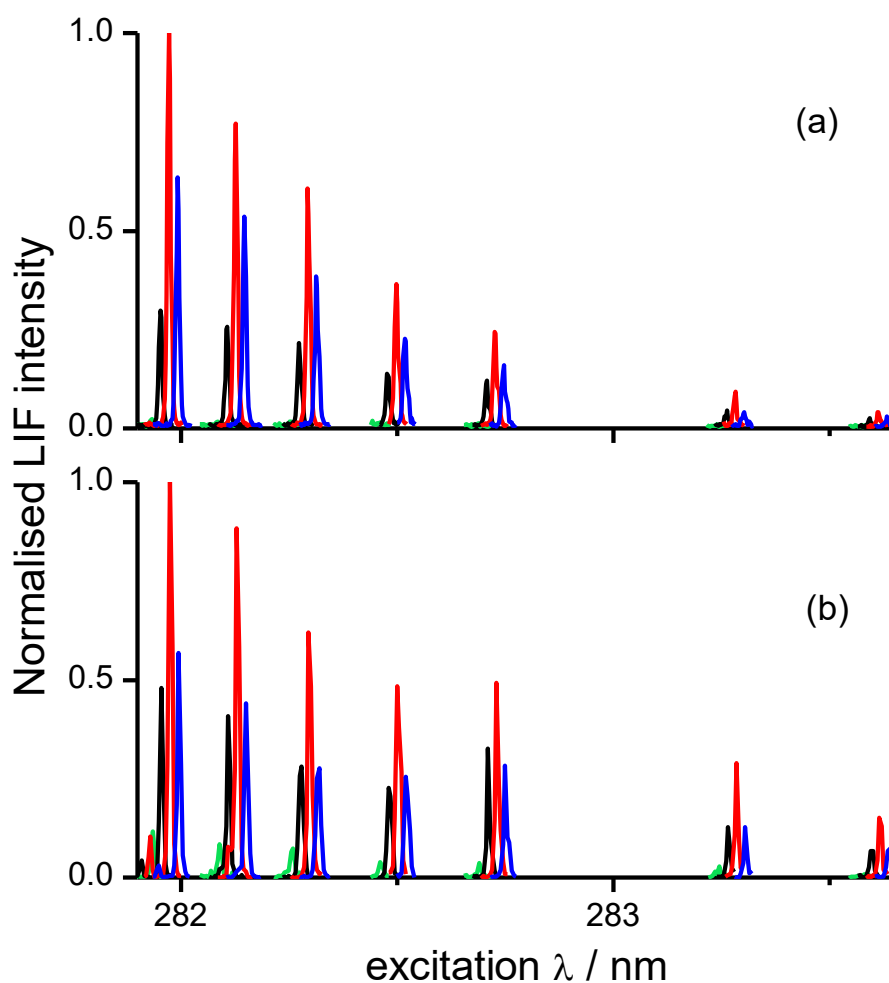


Figure 3.7. OH ($v' = 0$) LIF excitation spectra from (a) squalane and (b) squalene, recorded at photolysis-probe delays of $3 \mu\text{s}$ (green), $8 \mu\text{s}$ (black), $12 \mu\text{s}$ (red) and $20 \mu\text{s}$ (blue). The lines shown, from shorter to longer λ , are $Q_1(1)$ to $Q_1(8)$ with the omission of $Q_1(6)$. The spectra are offset for clarity.

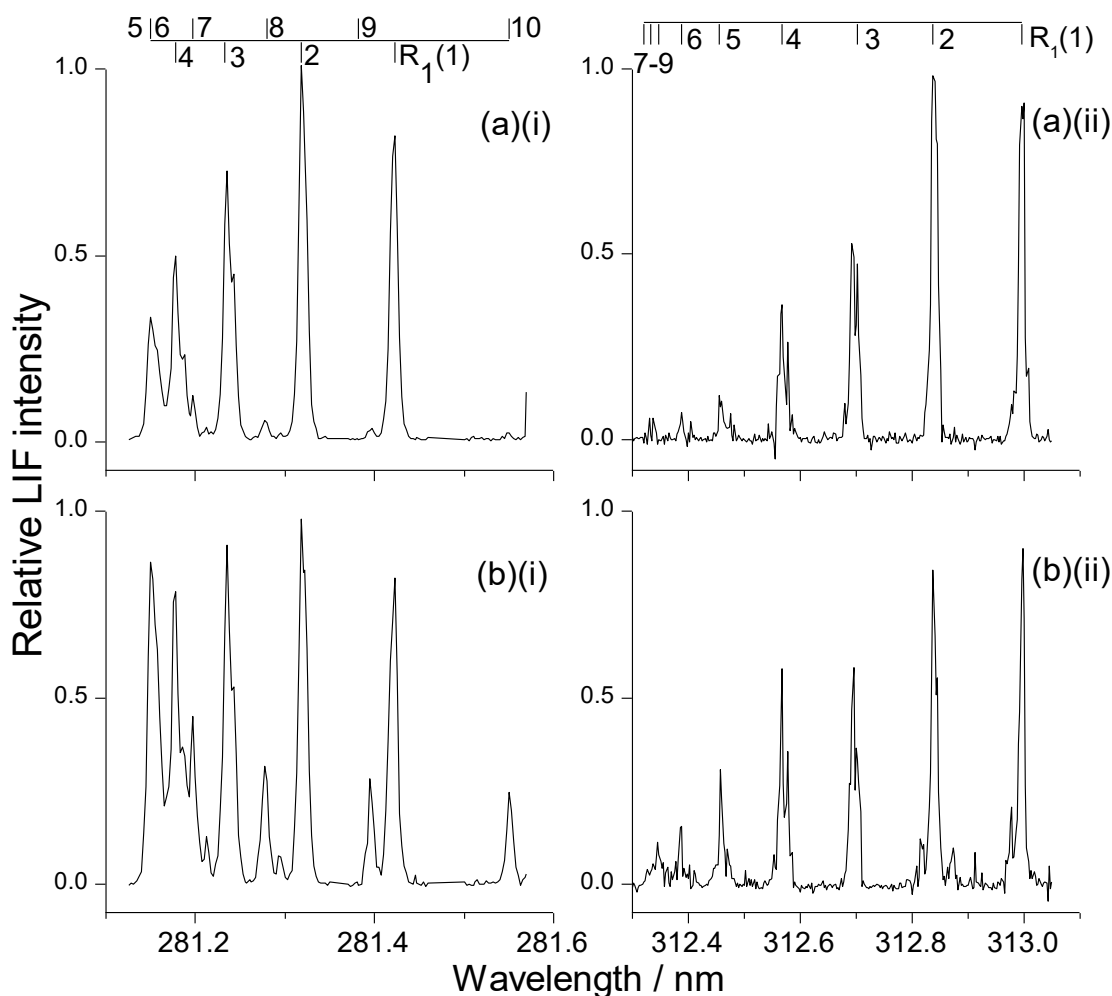


Figure 3.8. Representative OH LIF excitation spectra for the peak of the appearance profiles: (a)(i) $\text{OH}_{\text{ane}} (v' = 0)$, (a)(ii) $\text{OH}_{\text{ane}} (v' = 1)$, (b)(i) $\text{OH}_{\text{ene}} (v' = 0)$, (b)(ii) $\text{OH}_{\text{ene}} (v' = 1)$. Only the R_1 branch is shown.

Figure 3.8 presents the R branch regions of typical OH ($v' = 0$) and ($v' = 1$) spectra from squalene and squalane, recorded at the peak of the appearance profiles. Comparing OH ($v' = 0$) with ($v' = 1$) it can be seen that vibrationally excited OH is rotationally colder. OH_{ene} is higher in average rotational energy than OH_{ane} , and the difference is greater for $v' = 0$. In order to quantify these differences, the population of each N' level was obtained by fitting the experimental spectrum to a LIFBASE simulation. All rotational branches were recorded, but only the Q_1 and R_1 branches were used for the final analysis as they had fewer mixed lines. If the LIF signals were intense enough, the rotational distributions in other branches were analysed to ensure consistency with the R_1 and Q_1 distributions. It was found that, for both squalane and squalene, the product internal state distributions were similar to those from gas-phase $O(^3P) + \text{hydrocarbon}$

reactions: there was no preference for a particular Λ -doublet, and the F_1 spin-orbit manifold was favoured over F_2 [105, 182, 183]. The R_1 branch was stronger than expected, but this is thought to be a consequence of the partial-saturation conditions of the experiment or the λ dependence of the detection sensitivity instead of a real effect. The relative populations of the different N' levels were obtained independently for the R_1 and Q_1 branches. If a spectral line was caused by multiple blended transitions, the corresponding N' levels were omitted from the simulation. This was not carried out for the $Q_1(1)$ transition in OH ($v' = 0$), which is mixed with $R_2(3)$, because omitting $N' = 1$ from the simulation would substantially distort the distribution. Instead, the contribution from $R_2(3)$ was estimated and subtracted individually from each spectrum. This was done by first fitting the R_1 distribution to a temperature T , and then using T as an input in the LIFBASE simulation. The LIFBASE thermal spectrum provided a theoretical $R_2(3):Q_1(1)$ ratio that is expected to be similar to the experimental one, provided that the rotational distribution is independent of the spin-orbit or Λ -doublet probed. The $R_2(3)$ contribution, which was typically between 15% and 20% of the $Q_1(1)$ population, was subtracted from each spectrum. The resulting R_1 and Q_1 distributions were found to be very similar in all cases; consequently, both branches were averaged together to construct population plots.

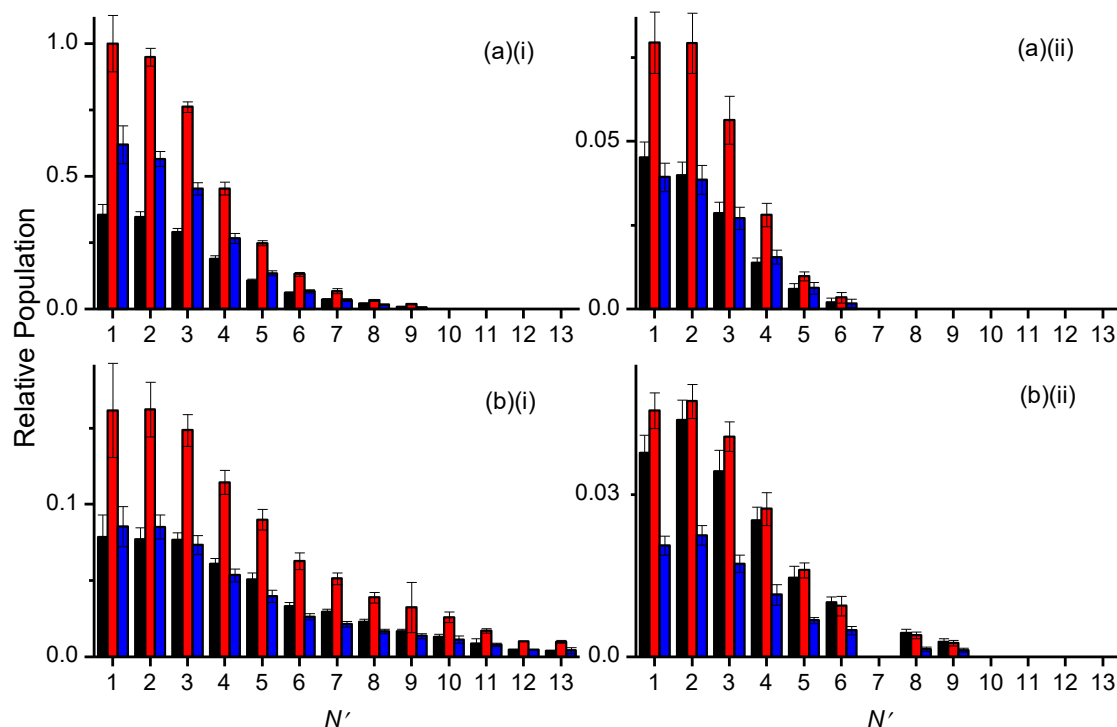


Figure 3.9. OH rotational distributions at the rising edge (black bars), peak (red bars) and tail (blue bars) of the appearance profiles, scaled according to their relative signal intensities. The results are normalised to the largest population ($N' = 1$ for the peak in (a)(i)): (a)(i) $\text{OH}_{\text{ane}} (v' = 0)$, (a)(ii) $\text{OH}_{\text{ane}} (v' = 1)$, (b)(i) $\text{OH}_{\text{ene}} (v' = 0)$, (b)(ii) $\text{OH}_{\text{ene}} (v' = 1)$. N' levels with no significant population (less than 1% of the total) are omitted.

The population distributions were scaled to the LIF intensity of the corresponding appearance profiles so that the relative OH yields could be directly compared. For each delay, the average populations were normalised so that they all sum to unity, and then multiplied by the $Q_1(N)$ LIF signal at the corresponding photolysis-probe delay of the appearance profiles. This was carried out independently for all 3 N' values measured in the profiles. The resulting distributions were virtually the same regardless of the N' level that they were scaled to, verifying that the relative intensities of the appearance profiles are a reliable indicator of the distribution across rotational levels. The distributions scaled to different N' levels were averaged together to obtain population plots. The OH_{ane} and OH_{ene} populations scaled in this fashion can be directly compared for the same vibrational level, but comparison of the LIF intensities between vibrational levels is not meaningful since the detection sensitivities were different for the (1,0) and (1,1) bands. For this reason, the OH_{ane} vibrational branching ratio $(v' = 1)/(v' = 0)$,

previously reported to be 0.07 ± 0.02 at the peak of the appearance profiles [4], was applied as a further scaling factor to the populations. This yielded the population plots shown in Figure 3.9.

Comparing squalane against squalene in Figure 3.9, the differences seen in the experimental excitation spectra become more evident in the population distributions. Higher N' levels are relatively more populated for squalene in both vibrational levels. In addition, rotational distributions appear to be hotter at earlier delays, in agreement with the translational-rotational correlation observed in the appearance profiles (this is perhaps more obvious in the OH_{ene} distributions). Since the y-axis scales in Figure 3.9 are very different, it may be useful to plot the OH_{ane} and OH_{ene} distributions together to help visualising their relative reactivity. This is presented in Figure 3.10, which shows the OH rotational distributions at the peak of the appearance profiles.

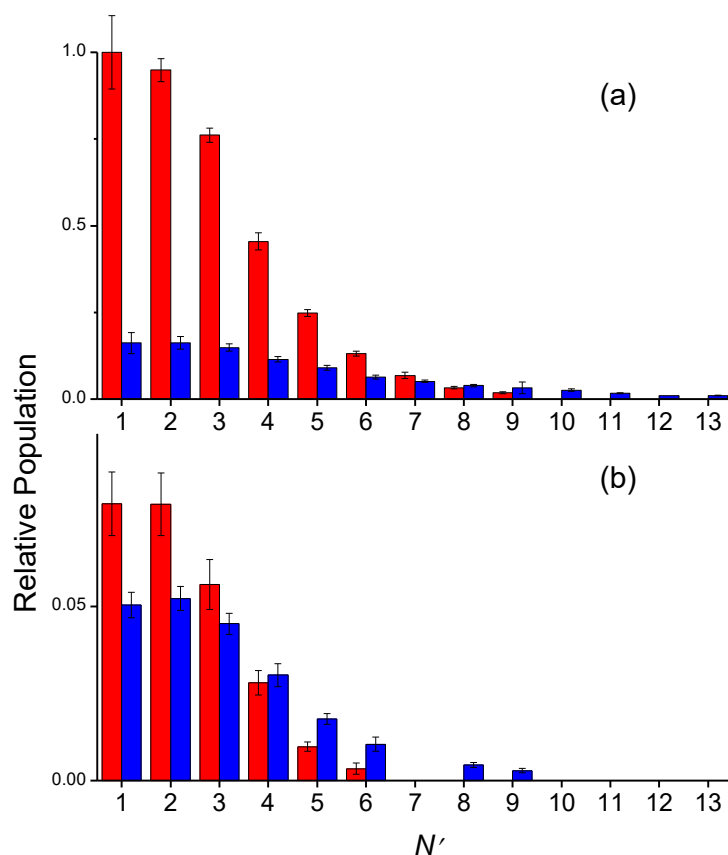


Figure 3.10. Relative OH rotational distributions at the peak of the appearance profiles, for OH_{ane} (red) and OH_{ene} (blue): (a) $\text{OH} (v' = 0)$, (b) $\text{OH} (v' = 1)$.

The total relative OH yield is obtained by summing over all N' levels, interpolating the population of any missing levels. All the distributions were extrapolated up to $N' = 13$. Although the extrapolation to high levels introduced a large relative error in such levels, their contribution to the total population was in all cases $< 1\%$ and therefore this did not have a large effect in the final result. At the peak of the appearance profiles, the relative squalene:squalane OH yield is 0.25 ± 0.01 for OH ($v' = 0$) and 0.87 ± 0.13 for OH ($v' = 1$) (uncertainties are $\pm 1\sigma$ standard error of the mean). Using the OH_{ane} vibrational branching ratio [4] and the relative OH_{ane}:OH_{ene} yields, a ($v' = 1$)/($v' = 0$) ratio of 0.24 ± 0.08 is obtained for squalene. This calculation has been also carried out for the early and late photolysis-probe delays, and the results are presented in Table 3.3. It should however be noted that the same OH_{ane} vibrational branching ratio, corresponding to the peak, was assumed for all delays. In practice this does not make a large difference in the results, as shown by the very similar branching ratios obtained for squalene.

| OH appearance time | $\frac{OH_{ene}(v' = 0)}{OH_{ane}}$ | $\frac{OH_{ene}(v' = 1)}{OH_{ane}}$ | $\frac{OH_{ene}(v' = 1)}{OH_{ene}(v' = 0)}$ |
|--------------------|-------------------------------------|-------------------------------------|---|
| Rising edge | 0.35 ± 0.02 | 1.41 ± 0.23 | 0.28 ± 0.10 |
| Peak | 0.25 ± 0.01 | 0.87 ± 0.13 | 0.24 ± 0.08 |
| Tail | 0.22 ± 0.02 | 0.71 ± 0.13 | 0.23 ± 0.08 |

Table 3.3. OH_{ene}/OH_{ane} relative yields and OH_{ene} vibrational branching ratios at the rising edge, peak and tail of the appearance profiles.

The rotational distributions of the scattered products can often be characterised by a temperature (see Section 2.6.2). However, many of the distributions shown in Figure 3.7 are not well described by a single rotational temperature. Instead, they have been fitted to a 2-temperature model first employed by Nesbitt and co-workers and subsequently applied in other gas-liquid scattering experiments [20, 69, 109]. The model, introduced in Chapter 1, assumes contributions from high- and low-temperature components to the population, $P(N)$:

$$\frac{P(N)}{2J + 1} = C \left[\left(\frac{\alpha}{T_1} \right) e^{\frac{-E_{rot}(N)}{k_B T_1}} + \left(\frac{1 - \alpha}{T_2} \right) e^{\frac{-E_{rot}(N)}{k_B T_2}} \right] \quad (3.1)$$

In Equation 3.1, T_1 is the lower rotational temperature, T_2 is the higher rotational temperature, α is the fraction of the population with the lower temperature T_1 , and C is an arbitrary scaling factor. The average population distributions in Q_1 and R_1 were plotted together (each branch normalised to a summed population of 1) and least-squares fitted to Equation 3.1 to obtain the values of C , T_1 , T_2 and α . None of the parameters was constrained in the fitting. As an example, Boltzmann plots for the peak of the appearance profiles are presented in Figure 3.11.

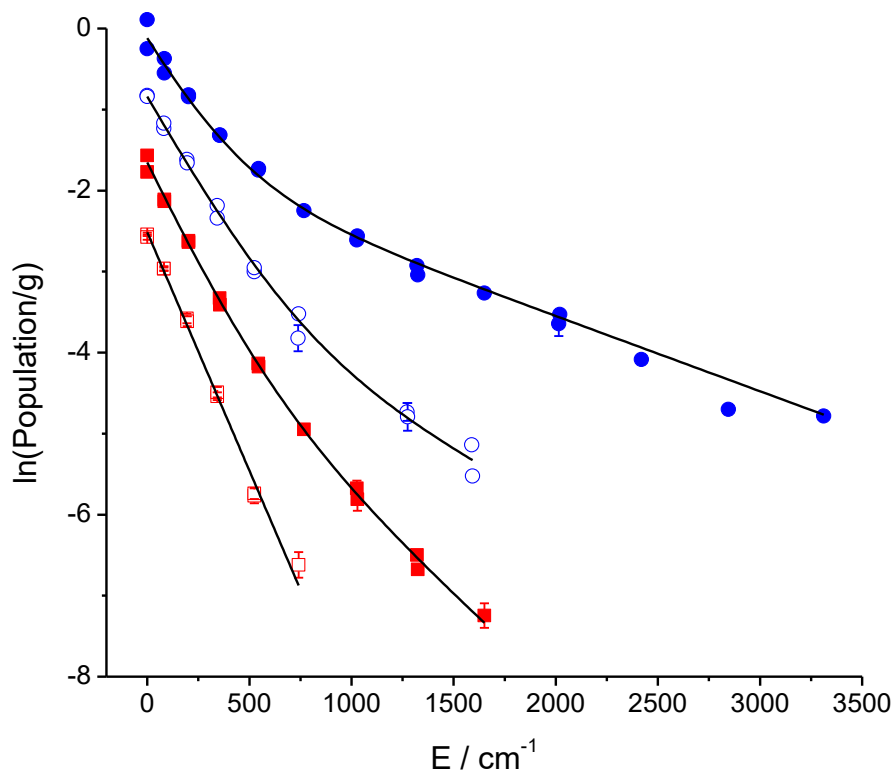


Figure 3.11. Boltzmann plots of the rotational distributions at the peak of the appearance profile (12 μ s and 14 μ s for squalane and squalene, respectively). From top to bottom: $\text{OH}_{\text{ene}} (v' = 0)$ (blue filled circles), $\text{OH}_{\text{ene}} (v' = 1)$ (blue open circles), $\text{OH}_{\text{ane}} (v' = 0)$ (red filled squares) and $\text{OH}_{\text{ane}} (v' = 1)$ (red open squares). Points from the Q_1 and R_1 branches have been included in each plot. Black lines represent the fits to a 2-temperature model as described in the text. All plots except for $\text{OH}_{\text{ane}} (v' = 1)$ are offset for clarity, and error bars smaller than the symbol have been omitted.

The 2-temperature model provided good fits to the distributions of OH_{ene} in both vibrational levels and OH_{ane} in ($v' = 0$). $\text{OH}_{\text{ane}} (v' = 1)$, in contrast, was better described by a single temperature (fixing $\alpha = 1$), as can be appreciated in Figure 3.11. The OH_{ene} distributions have a larger fraction of rotationally excited component compared to

OH_{ane} . For a given liquid, vibrationally excited OH is rotationally colder. The values of α , T_1 and T_2 for different delays, liquids and vibrational levels are presented in Table 3.4. Whilst the values of T_2 vary considerably between the distributions, T_1 is in all cases close to room temperature, and slightly subthermal for OH_{ane} ($\nu' = 0$). Due to correlations between parameters, the variation in all three parameters should be considered when comparing the results. For example, in OH_{ene} the value of α decreases for longer photolysis-probe delays, consistent with an increase in the fraction of thermalized products. This also happens in OH_{ane} ($\nu' = 0$), but it is not reflected in the value of α , showing a decrease in T_2 instead.

| $\text{OH}_{\text{ane}} (\nu' = 0)$ | | | | $\text{OH}_{\text{ane}} (\nu' = 1)$ | | | |
|---|-----------|-----------|-----------|---|-----------|-----------|-----------|
| <i>Delay</i> <i>/ μs</i> | α | T_1 / K | T_2 / K | <i>Delay</i> <i>/ μs</i> | α | T_1 / K | T_2 / K |
| 8 | 0.73±0.12 | 290±28 | 818±239 | 10 | 1.00 | 243±6 | - |
| 12 | 0.70±0.13 | 256±26 | 625±124 | 14 | 1.00 | 245±5 | - |
| 20 | 0.70±0.20 | 249±34 | 559±143 | 22 | 1.00 | 267±5 | - |
| $\text{OH}_{\text{ene}} (\nu' = 0)$ | | | | $\text{OH}_{\text{ene}} (\nu' = 1)$ | | | |
| <i>Delay</i> <i>/ μs</i> | α | T_1 / K | T_2 / K | <i>Delay</i> <i>/ μs</i> | α | T_1 / K | T_2 / K |
| 8 | 0.35±0.06 | 268±38 | 1106±275 | 10 | 0.63±0.10 | 296±28 | 1003±251 |
| 12 | 0.43±0.05 | 301±34 | 1588±128 | 14 | 0.74±0.12 | 310±33 | 1058±405 |
| 20 | 0.53±0.03 | 290±19 | 1606±216 | 22 | 0.67±0.09 | 270±30 | 1135±318 |

Table 3.4. Values of T_1 , T_2 and α obtained by fitting the OH rotational distributions to a 2-temperature Boltzmann plot. Errors correspond to $\pm 1\sigma$ SEM.

The total average rotational energy can be obtained by simply averaging the energy of all rotational levels using their populations as weighting factors:

$$\langle E_{\text{rot}} \rangle = \frac{\sum_i (P(N_i) \times E(N_i))}{\sum_i P(N_i)} \quad (3.2)$$

In Equation 3.2, $P(N_i)$ is the population of a level with $N = i$ and $E(N_i)$ is its energy. Populations of levels N_i that had not been experimentally determined were estimated by interpolation of the Boltzmann fitting curve. The average rotational energy over both vibrational levels was obtained using the vibrational branching ratios in Table 3.3 as weighting factors. The branching ratios were also used to calculate the average vibrational energy, using the value of the first vibrational quantum for OH, 3570 cm^{-1} [184]. The average OH rotational and vibrational energies for all delays are presented in Table 3.5, together with the average translational energy at the corresponding delay obtained from the average speeds in Figure 3.6.

| | Rising edge | | | | | |
|-----------------|---|---|---------------------------------|---------------------------|---------------------------------------|---------------------------------------|
| | $\langle E_{rot} \rangle$ ($v' = 0$) | $\langle E_{rot} \rangle$ ($v' = 1$) | Total $\langle E_{rot} \rangle$ | $\langle E_{vib} \rangle$ | $\langle E_t \rangle$ ($v' = 0$) | $\langle E_t \rangle$ ($v' = 1$) |
| <i>Squalane</i> | 3.10 | 1.66 | 3.00 | 2.80 | 22 | 12 |
| <i>Squalene</i> | 6.63 | 3.96 | 6.05 | 9.36 | 22 | 17 |
| | Peak | | | | | |
| | $\langle E_{rot} \rangle$ ($v' = 0$) | $\langle E_{rot} \rangle$ ($v' = 1$) | Total $\langle E_{rot} \rangle$ | $\langle E_{vib} \rangle$ | $\langle E_t \rangle$ ($v' = 0$) | $\langle E_t \rangle$ ($v' = 1$) |
| <i>Squalane</i> | 2.62 | 1.67 | 2.56 | 2.80 | 11 | 9 |
| <i>Squalene</i> | 6.42 | 3.58 | 5.89 | 8.29 | 13 | 10 |
| | Tail | | | | | |
| | $\langle E_{rot} \rangle$ ($v' = 0$) | $\langle E_{rot} \rangle$ ($v' = 1$) | Total $\langle E_{rot} \rangle$ | $\langle E_{vib} \rangle$ | $\langle E_t \rangle$ ($v' = 0$) | $\langle E_t \rangle$ ($v' = 1$) |
| <i>Squalane</i> | 2.42 | 1.79 | 2.38 | 2.80 | 5 | 5 |
| <i>Squalene</i> | 6.00 | 3.75 | 5.58 | 8.01 | 7 | 5 |

Table 3.5. Average rotational energy for each vibrational level, overall average rotational energy $\langle E_{rot} \rangle$, average vibrational energy $\langle E_{vib} \rangle$ and average translational energy $\langle E_t \rangle$ at different points of the appearance profile, for squalane and squalene (errors have been omitted). All values in kJ mol^{-1} .

3.4. Discussion

The interfacial H-abstraction dynamics by $O(^3P)$ from liquid hydrocarbons change significantly with the introduction of unsaturated sites in the molecule, as evidenced by the substantial differences between OH_{ane} and OH_{ene} . Squalene produces fewer OH radicals, but they possess higher translational and internal energies. For both liquids, the appearance profiles and excitation spectra reveal a positive correlation between translational and rotational energy. The rotational distributions have a bimodal character, which is particularly clear in the case of squalene. The following sections expand on these points and provide a detailed comparison between the liquids.

3.4.1. Relative OH yields

The most striking difference between the saturated and the partially unsaturated liquid is the significantly lower OH yield from squalene. This can be partially explained by the fact that the $C(sp^2)-H$ bonds are not expected to produce OH, but this effect alone does not account for the large difference. It could be argued that there is a tendency for the double bonds in squalene to occupy the surface over the $C(sp^3)-H$ groups, but this would not be a realistic explanation considering the magnitude of the divergence: the squalene/squalane ratio of potentially reactive $C(sp^3)-H$ sites is $44:62 = 0.71:1$, whereas the ratio of OH_{ene}/OH_{ane} yields is $0.24:1$. Another potential cause is the addition of the *product* OH to the unsaturated sites, which has been previously shown to cause a noticeable difference in the OH *inelastic* scattering yields from squalane and squalene [19, 20]; however, this effect is again much smaller than the observed difference. Most importantly, a substantial fraction of the squalane surface is predicted in MD simulations to be covered in relatively unreactive methyl groups [98, 100]. Considering that the allylic $C(sp^3)-H$ bonds in squalene are expected to be more reactive, it is clear that there must be an additional reason for the lower OH_{ene} yield. The most obvious explanation is an additional reaction channel for $O(^3P)$ in the unsaturated sites leading to products other than OH.

The addition reaction of $O(^3P)$ to double bonds has long been known to occur in smaller gas-phase alkenes [174]. The mechanism of the $O(^3P) +$ ethylene reaction has been extensively studied in both experiments [173, 185-189] and theory [190]. In this reaction, $O(^3P)$ adds to the double bond to form a triplet biradical which then yields fragmentation products (mainly $H + CH_2CHO$), or undergoes intersystem crossing to a

singlet biradical giving different products (mainly $CH_3 + CHO$). Six main reaction channels have been identified [189], although the detailed product branching ratios depend on the experimental conditions. In substituted alkenes, O addition to the unsaturated sites still takes place, in many cases outweighing H abstraction from the $C(sp^3)-H$ groups. This is due to the fact that O addition is a more energetically favourable, almost barrierless, reaction and it is expected to dominate the mechanism at room temperature. Calculated barriers for O addition to propene are $\sim 2 \text{ kJ mol}^{-1}$ [191], which is substantially lower than H-abstraction barriers. Experiments on a variety of small unsaturated alkanes with low collision energies and mass spectrometric detection failed to detect OH, or they reported it as a minor product [185, 192-194]. At higher collision energies, OH can easily be detected using LIF [172, 175, 176].

The large decrease in OH_{ene} yield compared to OH_{ane} indicates that unsaturated sites are present at the surface of squalene and accessible to the incoming $O(^3P)$ atoms. This is in agreement with previous studies of inelastic OH scattering from these liquids conducted by the McKendrick group [19, 20] and others [195]. McKendrick and co-workers obtained reactive OH uptake coefficients (defined as the fraction of collisions leading to OH loss) of 0.30 for squalane and 0.39 for squalene [19]. The higher reaction probability for squalene was assumed to be caused by addition of OH to the unsaturated sites. Consistent with this interpretation, slow and rotationally cold OH radicals were preferentially lost, due to the low barrier for addition relative to H abstraction. Furthermore, molecular dynamics simulations confirmed that double bonds are exposed at the squalene surface [20]. The chemical reactivity of the squalene surface is dramatically affected by the presence of double bonds, so that it behaves differently from the fully saturated squalane surface. This result is particularly relevant to the atmospheric oxidation of organic aerosols: while the heterogeneous oxidation of saturated hydrocarbons primarily takes place via H abstraction by OH, the reactions in unsaturated hydrocarbon surfaces are initiated by OH addition to a double bond [196]. Returning to the $O(^3P)$ results, the difference in between OH_{ane} and OH_{ene} yields is much larger here because the double bonds affect both the entry and exit channels of the reaction. In addition, the difference between H-abstraction and addition barriers is larger for $O(^3P)$ atoms compared to OH radicals.

Given the large difference between the OH_{ane} and OH_{ene} yields, it would be interesting to draw a comparison with gas-phase reactions. If theoretical “gas-phase” OH_{ane} and OH_{ene} yields were obtained, it would then be possible to determine the effect of the interface on the reaction. Unfortunately, the OH yield depends strongly on the specific molecule studied and the collision conditions, and is therefore not easy to predict. As discussed above, in $O(^3P)$ + unsaturated hydrocarbon reactions there is a competition between the H-abstraction and O-addition mechanisms. Due to the lower dynamic thresholds in alkenes (Table 3.1), H abstraction is favoured in allylic sites, but at the same time there is an important loss of $O(^3P)$ in the unsaturated sites (besides the loss in intrinsic reactivity from introducing $C(sp^2)$ -H groups that do not lead to abstraction). Early kinetics studies of the reaction with 1-butene showed that the rate of H abstraction increased with temperature at the expense of O addition to the double bond. The fraction of abstraction was estimated to be 20-39% at 500 K [197]. Later, measurements on four different butene isomers were performed by Adusei *et al* [198], who estimated an H-abstraction contribution lower than 4% at 500 K but between 12% and 31% at 1100 K. Substituted double bonds gave lower rates of O-addition and favoured H-abstraction instead. In addition, the authors obtained temperature-dependent rate constants for the abstraction of different types of hydrogen atoms. Using their expressions for primary and secondary alkyl and allyl C-H bonds, and estimating the tertiary C-H rate constant from literature values [199], the theoretical H-abstraction rate constants (k_{abs}) for squalane and squalene have been obtained. The results for a temperature range of 270 – 1200 K are presented in Figure 3.12.

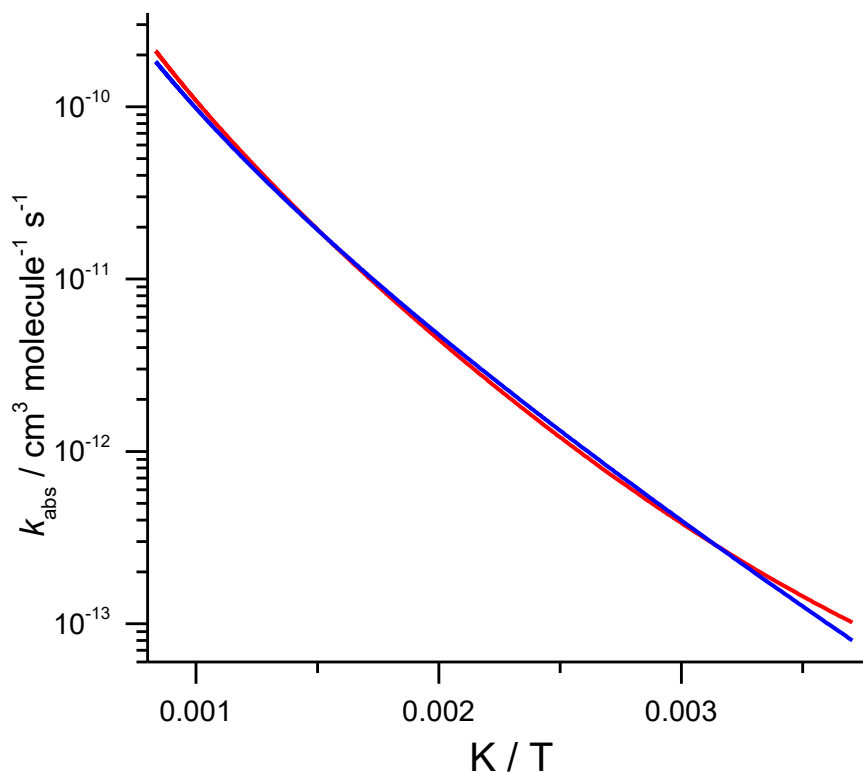


Figure 3.12. Theoretical H-abstraction rate constants for squalane (red) and squalene (blue) as a function of temperature, estimated from kinetics data in [198].

Squalane and squalene have similar theoretical H-abstraction reactivities, meaning that the enhanced reactivity of the allylic sites in squalene is compensated by the loss of reactive H atoms on introducing six double bonds. It follows that the large difference in OH yield observed in the interfacial reaction must arise from the loss of $O(^3P)$ at the unsaturated sites (which is not accounted for in the theoretical k_{abs}), or from an additional surface-induced effect.

The dependence of the OH yield on C-H bond type and collision energy was also shown by the excitation functions measured by Luntz and co-workers [106, 172]. At the collision energies studied, it was reported that “the OH reactive signals [from unsaturated hydrocarbons] were comparable in intensity (per H atom) to those obtained with saturated hydrocarbons at high E_c ” [172]. However, the authors did not offer a quantitative comparison. Perhaps the best attempt to compare the OH yield quantitatively between saturated and unsaturated compounds was carried out by Bersohn and co-workers [176, 177]. They compared OH LIF signal intensities from the reactions between $O(^3P)$ and a range of unsaturated hydrocarbons, using cyclohexane as

a reference. The $O(^3P)$ atoms were produced by 351 nm photolysis of NO_2 , giving similar collision energies to the present experiments. The relative OH yield between cyclohexene and cyclohexane was approximately 0.50, and yields for other small alkenes were in the range of 0.15 – 0.51 [176]. This is again not directly comparable to the squalene/squalane relative yield, because the proportion of bond types is not the same, and there was no correction to account for the different number of H atoms and collision cross-sections of the alkenes. It does, however, show that the OH yield in all cases decreases upon introduction of unsaturated sites; and the ratio between unsaturated and saturated compounds is similar to the squalene:squalane ratio. This could indicate that the interfacial reaction takes place *via* direct encounters that resemble single gas-phase collisions. If the incoming $O(^3P)$ atoms suffered on average many encounters at the surface before forming OH, they would be more efficiently scavenged by the unsaturated sites, leading to a much lower OH_{ene}/OH_{ane} ratio than the gas-phase equivalent. As this is not the case, it can be concluded that direct, IS-like encounters contribute significantly to the formation OH. A similar conclusion was reached in previous studies of the $O(^3P)$ + squalane reaction: the reactivity was essentially independent of the liquid temperature, indicating that $O(^3P)$ is not thermally accommodated before reacting [6]. This argument is supported by the appearance profiles in Figure 3.5, which show that a large fraction of the products scatter with high translational energies and cannot be assigned to a fully thermalised distribution. There are, however, some dynamical differences with gas-phase reactions that indicate that partial accommodation takes place at the surface. These effects will be discussed in detail in Section 3.4.3.

3.4.2. Energy partition

The fact that squalene produces OH with greater internal and translational energy is explained by its more exothermic reaction compared to squalane. In order to appreciate the differences between squalane and squalene, the energy available to the products, E_{av} , has been estimated. This is calculated as $E_{av} = E_{coll} - \Delta_r H$ (where E_{coll} is the collision energy and $\Delta_r H$ is the enthalpy of reaction) and therefore depends on the type of C–H site where abstraction takes place. The calculation is complicated by the fact that the collision energy is not well defined: the broad translational distribution of the $O(^3P)$ atoms and the different reaction thresholds and excitation functions depending on the site make it difficult to estimate E_{coll} . For this calculation, the collision energy has been assumed to be 21 kJ mol^{-1} , which is approximately equal to the activation energy for

reaction at secondary or tertiary sites in squalane [105]. This is undoubtedly a very simplified approach, but in practice the differences in E_{av} are dominated by the Δ_rH term, given by the bond energies for the different types of C–H site.

The energy partition analysis has been performed separately for OH ($v' = 0$) and ($v' = 1$), and for different C–H reactive sites. The results are presented in Table 3.6. Primary C–H sites in squalane and all of the squalane sites leading to OH ($v' = 1$) have been excluded from the calculation because they require collision energies higher than 21 kJ mol^{-1} for reaction. Although OH ($v' = 1$) is observed in the experiments, only the high-energy tail of the $O(^3P)$ distribution can produce it. The values of average rotational energy, $\langle E_{rot} \rangle$, are those calculated in Section 3.3.2 for the peak of the appearance profiles. In the absence of average values over the total product distribution, values at the peak of the profiles are employed because they correspond to the majority of the scattered OH. The average translational energies $\langle E_t \rangle$ have been obtained from the Monte Carlo simulations in Section 3.3.1, by simply applying the expression $\langle E_t \rangle = \frac{3}{2}kT$, where k is Boltzmann's constant and T is the temperature of the simulated profile.

| $\text{OH}_{\text{ane}} (\nu' = 0)$ | | | | | | | | |
|-------------------------------------|--------------|-----------------|-----------------------|----------------------------------|----------------------------------|-------|------------------|------------------|
| | $\Delta_r H$ | E_{av} | $\langle E_t \rangle$ | $\langle E_{\text{rot}} \rangle$ | $\langle E_{\text{sur}} \rangle$ | f_t | f_{rot} | f_{sur} |
| <i>2^y alkyl C-H</i> | -19 | 40 | 12 | 3 | 25 | 0.31 | 0.07 | 0.62 |
| <i>3^y alkyl C-H</i> | -26 | 47 | 12 | 3 | 32 | 0.27 | 0.06 | 0.68 |
| $\text{OH}_{\text{ene}} (\nu' = 0)$ | | | | | | | | |
| | $\Delta_r H$ | E_{av} | $\langle E_t \rangle$ | $\langle E_{\text{rot}} \rangle$ | $\langle E_{\text{sur}} \rangle$ | f_t | f_{rot} | f_{sur} |
| <i>1^y allylic C-H</i> | -72 | 93 | 16 | 6 | 70 | 0.17 | 0.07 | 0.76 |
| <i>2^y allylic C-H</i> | -85 | 106 | 16 | 6 | 83 | 0.15 | 0.06 | 0.79 |
| $\text{OH}_{\text{ene}} (\nu' = 1)$ | | | | | | | | |
| | $\Delta_r H$ | E_{av} | $\langle E_t \rangle$ | $\langle E_{\text{rot}} \rangle$ | $\langle E_{\text{sur}} \rangle$ | f_t | f_{rot} | f_{sur} |
| <i>1^y allylic C-H</i> | -72 | 50 | 15 | 4 | 32 | 0.30 | 0.07 | 0.63 |
| <i>2^y allylic C-H</i> | -85 | 63 | 15 | 4 | 45 | 0.24 | 0.06 | 0.71 |

Table 3.6. Reaction energetics (all energies in kJ mol^{-1}) for each C–H site and vibrational level: enthalpies of reaction ($\Delta_r H$), available energy for a collision energy of 21 kJ mol^{-1} (E_{av}), measured average OH energies in translation ($\langle E_t \rangle$) and rotation ($\langle E_{\text{rot}} \rangle$), and average energy deposited in the surface ($\langle E_{\text{sur}} \rangle$), inferred by difference. Corresponding fractions of available energy appearing in OH translation (f_t), rotation (f_{rot}) and the liquid surface (f_{sur}).

It is clear from the values of $\langle E_{\text{rot}} \rangle$ that OH_{ene} is more rotationally excited than OH_{ane} . This is in contradiction with previous gas-phase experiments, which reported a much smaller broadening of the rotational distributions for unsaturated hydrocarbons [105]. However, the resolution of the experimental spectra was relatively low, and it is possible that the extent of rotational excitation was underestimated. Kleinermaans and Luntz [172] reported a slight broadening for unsaturated compounds that was independent of collision energy, and concluded that $\Delta_r H$ is more efficient than E_c in promoting rotational excitation. Despite the slightly higher $\langle E_{\text{rot}} \rangle$ reported here, it is only a small fraction of E_{av} : the values of f_{rot} in Table 3.6 are 0.06 – 0.07, essentially independent of the liquid studied. The low rotational excitation of the products evidences that the reaction takes place via a collinear transition state, similar to other

H-abstraction reactions from hydrocarbons [105, 106, 141, 172]. The “heavy + light-heavy” (H + LH) mass combination of the O + HR system means that, in a bent configuration, repulsion between products in the exit channel should induce considerable torque in the OH which would result in rotational excitation [200]. The fact that this does not occur demonstrates that the reactive trajectories must take place at an O–H–R angle close to 180° . For example, the H abstraction reaction between $O(^3P)$ and HBr has similar reaction energetics to $O(^3P)$ + squalene ($\Delta_rH = -61.5 \text{ kJ mol}^{-1}$), but in this case there is not a collinear constraint. Collisions at $E_{\text{coll}} = 24.5 \text{ kJ mol}^{-1}$ produced highly excited OH with rotational energies of up to $\sim 90 \text{ kJ mol}^{-1}$ [181]. When comparing to the 6 kJ mol^{-1} obtained from squalene, it is clear that the collinear constraint applies to the squalene reaction.

The fraction of energy transformed into vibration has not been considered in the partition because, as noted above, this calculation is not meaningful for a collision energy of 21 kJ mol^{-1} . However, the $\langle E_{\text{vib}} \rangle$ values obtained from vibrational branching ratios (Table 3.5) indicate that OH from squalene is considerably more vibrationally excited. This is in agreement with Polanyi’s rules [201], which state that reactions with lower and earlier barriers are more efficient in promoting vibrational excitation in the exit channel. Due to the H + LH kinematics and collinear configuration of the reaction, repulsion in the exit channel should efficiently produce vibrational excitation. Going from primary to tertiary C–H and from alkyl to allyl sites, the potential energy surface becomes more attractive (i.e. the transition state becomes closer to the reactants in the reaction coordinate and lowers in energy), producing a greater fraction of vibrationally excited OH. The vibrational branching ratios for gas-phase hydrocarbons essentially agree with this, despite scatter in the values due to the difficulty of the measurements [105].

The average OH translational energy, $\langle E_t \rangle$, does not vary much between liquids, with squalene releasing an extra $3 - 4 \text{ kJ mol}^{-1}$ kinetic energy into the products. This small variation is surprising considering the large discrepancy in E_{av} : in terms of f_t , the contribution for squalene is almost twice the value of f_t for squalene. As a result, the energy absorbed by the surface, inferred from the remaining E_{av} not converted into rotation or translation, is substantially larger for squalene. This difference could in principle be a result of different properties of the liquids, such as surface stiffness. However, the surface stiffness is not expected to vary much between squalene and squalene: both liquids are composed of CH_x groups and should therefore absorb similar

amounts of energy in collisions with oxygen atoms. The microscopic structure of the surface could potentially be different and affect the IS/TD ratio of the products (for example surface roughness could be induced by a different arrangement of the hydrocarbon chains), but this effect is also expected to be small considering previous observations [20]. A more likely reason for this is the excitation of the hydrocarbon radical cofragment. There is previous evidence of the internal excitation of the R radical produced in H abstraction from hydrocarbons, both saturated [106, 175, 182, 202-205] and unsaturated [172, 175]. This could imply that the triatomic model, which successfully explains the qualitative trends in the energy of the OH radicals considering R as a spectator, might be insufficient to fully describe the reaction. It has been proposed that H abstraction takes place through a “vertical” mechanism [204], meaning that the hydrocarbon fragment does not change its configuration during the abstraction and produces an R radical with the geometry of the parent alkane RH. The rearrangement of R to its optimal geometry results in vibrational excitation of the radical product. Since allyl radicals distort more substantially due to their additional resonance stabilisation, they can be expected to deposit a larger fraction of E_{av} into the radical framework. As a result, OH produced from alkenes has lower vibrational energy than otherwise might be expected from the larger total available energy, as observed by Luntz [172] and Whitehead [175]. The interfacial reactions studied here appear to follow the same mechanism: the difference in $\langle E_{surf} \rangle$ between squalane and squalene is of the order of 40 kJ mol^{-1} (Table 3.6), in agreement with the values of resonance stabilisation energy for alkyl and allyl radicals (21 kJ mol^{-1} and 50 kJ mol^{-1} , respectively [142]).

3.4.3. Effect of the liquid surface on the dynamics

It has been shown in the previous sections that the reaction of $O(^3P)$ with liquid hydrocarbons is not profoundly different from related gas-phase reactions in terms of OH yield and energy transfer. This suggests that the reaction takes place by a direct IS mechanism with similar dynamics to the gas phase. In fact, the appearance profiles in Figure 3.5 and the hot rotational distributions in Figure 3.9 demonstrate that a large fraction of the products are ejected with superthermal translational and rotational energies and clearly cannot be described by a TD distribution.

Despite the dominant IS character of the reaction, there is significant evidence of partial thermalisation of the products at the surface. Firstly, there is a positive correlation

between kinetic and rotational energy of the detected OH radicals. This is shown by the fact that higher N' levels in $v' = 0$ present earlier appearance profiles (Figure 3.5). Equivalently, the rotational temperatures in Table 3.4 (or the values of $\langle E_{\text{rot}} \rangle$ in Table 3.5) decrease for longer delays. This indicates that OH radicals are initially produced with superthermal rotational and translational energies and subsequently interact with the surface, accommodating (either fully or partially) their energy. This translational-rotational correlation is a common feature of gas-liquid scattering systems, and has been previously observed in reactive $O(^3P) + \text{squalane}$ scattering [5] and inelastic scattering of OH [18-20] and CO_2 [68] from liquid surfaces, among others. The trend appears at first sight to be reversed in $\text{OH}_{\text{anc}} (v' = 1)$: $N' = 1$ has slightly earlier appearance profiles than $N' = 3$ and 5, and the rotational distributions correspond to subthermal temperatures that increase for later delays. However, this is simply a result of the reaction energetics: vibrational excitation of OH requires 43 kJ mol^{-1} so, at the collision energies employed, there is not much available energy left for excitation of the products. This leads to subthermal rotational energies, also observed in gas-phase reactions [106]. As the OH thermalizes with the surface, it gains rotational energy. Despite the higher E_{av} , this energetic constraint appears to also be affecting the results for squalene, which does not show a very clear translation-rotation correlation. Additional factors potentially affecting the $v' = 1$ product channel should also be considered. For example, the yield and kinetic energy of OH ($v' = 1$) from the $O(^3P) + \text{squalane}$ reaction has been shown to depend strongly on the temperature of the liquid, while OH ($v' = 0$) is almost insensitive to it [6]. This could indicate the presence of additional loss mechanisms for OH ($v' = 1$) at the surface, and if that were the case, they could also affect the OH ($v' = 1$) product from squalene.

The bimodal rotational distributions constitute further evidence of partial accommodation of OH at the surface. The values of T_1 in Table 3.4 are close to room temperature, even for the hotter OH_{enc} distributions with $T_2 > 1000 \text{ K}$. This suggests that a fraction of the products accommodate at the surface and scatter with thermal energy. The bimodality is clearer in OH_{enc} , whereas it is not very strong for $\text{OH}_{\text{anc}} (v' = 0)$ and is absent in the $\text{OH}_{\text{anc}} (v' = 1)$ distributions. The latter result is not unexpected considering that the nascent product distribution is close to room temperature, so the two components cannot be clearly distinguished. It could be argued that the two components result from H-abstraction at different sites in the molecule, but the differences in $\Delta_r H$ are relatively small compared to the total available energy (7 and 13 kJ mol^{-1} for squalane and squalene, respectively, out of 40 and 100 kJ mol^{-1}). In

addition, such bimodal distributions have not been identified in gas-phase reactions of $O(^3P)$ with hydrocarbons, which supports the idea that the colder component of products is the result of a surface-induced process. Furthermore, the two-temperature model can successfully describe the product distributions in the interfacial reactions of F and O (1D) with squalane [107, 109]. These reactions are highly exothermic, resembling the $O(^3P)$ + squalene reaction, and the nascent products are highly energetic so it is easy to distinguish between direct and thermalized products experimentally.

It has previously been proposed that the parameter α , which corresponds to the fraction of the distribution described by the cold temperature T_1 , quantifies the fraction of TD products scattering from the surface [69]. This interpretation is in disagreement with some of the results presented here. For example, the appearance profiles in Figure 3.5 show that the TD products should have a minor contribution to the rising edge and peak of the scattered distributions; however, this is not reflected in the values of α . In addition, T_2 depends on the photolysis-probe delay, whereas it should have the same value if it corresponds to the same IS product distribution. The same type of behaviour has been observed in the inelastic scattering of OH from liquid surfaces [20]. It should be considered that α and T_2 are correlated so they are not meaningful in isolation. It follows that, although the cold component most likely results from thermal accommodation at the surface, a binary division into IS or TD products is an oversimplification of the reaction mechanism. Molecular dynamics simulations of gas-liquid scattering trajectories fully support this interpretation, as discussed in Chapter 1. For example, simulations of Ne atoms scattering from hydrocarbon self-assembled monolayers (SAMs) [80, 82, 83] and squalane [99] found bimodal distributions of products in which the Boltzmann component did not arise from physisorption trajectories. Similarly, theoretical studies on the scattering of CO_2 from fluorinated SAMs found that single encounters could result in low-energy products, whereas multiple-collision trajectories do not necessarily result in thermalisation [74, 91]. It was found that the parameter α describing the bimodal distributions was not equivalent to the fraction of physisorption and penetration trajectories. These results suggest that, although α is useful for characterising empirically the degree of rotational accommodation at the surface, it should not be interpreted literally as an IS/TD branching ratio.

3.5. Summary points

- (1) In the H-abstraction reaction by $O(^3P)$ atoms, the unsaturated hydrocarbon squalene produces fewer OH radicals than its fully saturated counterpart, squalane, despite more favourable reaction energetics. The measured ratio, 0.29 ± 0.03 , implies that a significant fraction of $O(^3P)$ atoms react with squalene through another route, inferred to be addition to the double bonds, instead of abstracting a hydrogen atom. This demonstrates that double bonds are exposed at the squalene surface.
- (2) The interfacial reaction predominantly takes place *via* a direct, impulsive scattering mechanism on both liquid surfaces. This is shown by the superthermal translational energies derived from the OH appearance profiles, as well as the fact that the relative OH yields are similar to the equivalent gas-phase results.
- (3) Hydrogen abstraction from squalene produces OH_{ene} radicals that are, on average, translationally and internally hotter than OH_{ane} . More energy is released to OH_{ene} as a result of the weaker allylic C–H bonds in squalene.
- (4) A larger fraction of the total available energy is transferred to the surface of squalene compared to squalane. This result is consistent with the higher stabilisation energy of the allyl radicals, and is consistent with the H abstraction taking place through a sudden, nonadiabatic mechanism.
- (5) The bimodal OH rotational distributions are a clear confirmation of partial thermal accommodation of the products at the surface. These distributions are observed in both OH_{ane} and OH_{ene} , but the bimodality is much clearer for squalene thanks to the more exoergic character of the reaction.
- (6) The fractions of translationally and rotationally thermalised products are not equal. This and other features of the translational-rotational correlations indicate that the reaction does not proceed by a simple IS/TD binary mechanism, supporting the conclusions from previous gas-liquid interfacial studies.

Chapter 4.

Reactive O(³P) scattering from pure imidazolium-based ionic liquids

4.1. Introduction

In this chapter, reactive scattering of O(³P) atoms has been employed to study the surface composition of a series of ionic liquids containing the 1-alkyl-3-methylimidazolium cation ([C_nmim]⁺), with different alkyl chain lengths *n* and anions. As discussed in Chapter 1, characterising IL surfaces is relevant for the design of ILs tailored for particular applications. In the last decade, a large number of different surface analysis techniques have been applied to the study of ionic liquids; however, no one technique has been shown to be superior to all others. Issues such as chemical specificity and surface sensitivity are important, sometimes causing disagreements between techniques. To obtain a full picture of the IL surface, results from complementary experimental and theoretical studies should be compared. What follows is a brief review of the current state of the field of ionic liquid surface analysis. The purpose is to familiarise the reader with the techniques employed so far and discuss their strengths and disadvantages, without offering a thorough discussion of their results. This introduction covers exclusively experiments and simulations on imidazolium-based ILs, as these are the type of ILs studied in the present chapter. Studies on different alkyl chain lengths and anions will be reviewed. For an introduction to pyrrolidinium-based ILs and IL mixtures, see Chapters 5 and 6, respectively.

4.1.1. Previous studies of imidazolium-based ionic liquid surfaces

Optical spectroscopy

Most laser-spectroscopic methods are not surface-sensitive, so it is necessary to use second-order nonlinear spectroscopies. Sum frequency generation spectroscopy (SFG)

has been successfully applied to the study of IL-vacuum or IL-gas interfaces, mostly by Baldelli and Ouchi [151, 206-216]. In SFG, two laser beams, a resonant beam in the infrared and a second fixed-frequency beam typically in the visible region, overlap at the interface to generate a third beam with a frequency equal to the sum of the incident frequencies. This nonlinear frequency mixing process is allowed by the break in inversion symmetry at the interface. The outgoing beam propagates in a well-defined direction determined by the phase-matching condition. The vibrational modes of the chemical groups at the surface provide a resonant contribution to the outgoing laser beam, so that a spectrum can be obtained by scanning the frequency of the incoming infrared light.

Sum frequency generation only takes place at the interface, which means that there are no contributions from the bulk liquid. This surface specificity is a great advantage but, on the other hand, the technique suffers from drawbacks such as the fact that it does not produce quantitative results. In complex systems with many different functional groups like ILs, it might be interesting to characterise the relative concentrations of the functional groups exposed at the surface. Although SFG does not provide this information, it is a very powerful method to determine the preferential orientation of each ion. Using different polarisations for the incident and detected beams, the orientation of the different chemical moieties at the surface can be elucidated. For example, several SFG experiments on $[C_4mim]^+$ ILs with a variety of anions found the imidazolium ring parallel to the surface and the butyl chains extending into the vacuum phase [151, 206, 208, 209, 212, 214, 216], at an angle from the normal that was somewhat dependent on the identity of the anion. For shorter chain lengths ($n = 1 - 4$) [211], the ring was in a tilted orientation for some $n = 1$ and $n = 2$ ILs, again depending on the anion. Iimori *et al* [210] investigated $[C_nmim][BF_4]$ ILs with longer chains ($n = 4 - 11$). There were fewer gauche defects in the chains as n increased, meaning that the alkyl chains became more ordered and closely packed, and chain-chain interactions were enhanced. It was proposed that the chains form bundles that are closer to the vacuum than the polar groups (imidazolium headgroups and anions), which packed closely below the alkyl chains. When alkyl chains were present on cation and anion, such as in $[C_nmim]^+$ ILs with alkyl sulphate anions, both the cation and anion alkyl chains oriented themselves towards the gas phase [212, 215].

Electron spectroscopy

Several types of electron spectroscopy have been applied to IL-vacuum interfaces. Amongst them, X-ray photoelectron spectroscopy (XPS) is the most widely used technique. In XPS, an X-ray beam irradiates the surface and induces the emission of photoelectrons from the core energy levels of the surface atoms. An electron-energy analyser is used to measure the flux of photoelectrons emitted with different kinetic energies. The kinetic energy of a photoelectron is equal to the difference between the energy of the incident X-ray photon and the binding energy, which is the energy required to abstract the electron from its corresponding orbital. The binding energy depends on the atom probed and its chemical environment, therefore an XPS spectrum provides the chemical composition of the sample.

Although the X-rays penetrate deep into the liquid, the photoelectrons have a limited mean free path for propagation without being inelastically scattered in the bulk. Therefore, only the top surface layers contribute to the main features of the spectrum. This surface sensitivity can be further improved if a shallower detection angle is used, increasing the distance travelled through the liquid prior to escape from a given depth. This is the basis of angle-resolved XPS (ARXPS), in which the emission angle is varied in order to probe the surface at different depths. ARXPS of ionic liquids has shown that the ratio of aliphatic carbons to ring C atoms is greater for the more surface-sensitive shallow detection angles [217-223]. In agreement with the SFG results, it was found that the alkyl chains orient themselves preferentially towards the vacuum phase. This is true in general for all imidazolium-based ionic liquids, regardless of their anion or chain length, although the ARXPS studies detected quantitative differences in the degree of alkyl surface enrichment between ILs. The results of some of these experiments are further discussed in Section 4.4.

Metastable impact electron spectroscopy (MIES) is a surface analysis technique that employs metastable atoms (normally He^*) which de-excite when they encounter a surface atom. In this process, an electron from the valence orbital of the target atom is transferred to the He^* atom, which emits an electron from its 2s orbital. The kinetic energy of the electron depends on the binding energy of the target, making the technique chemically specific. The He^* atoms possess thermal kinetic energy (< 100 meV), so they only probe the outermost surface. However, it is very difficult to obtain quantitative information by MIES since the ionisation cross sections of the various molecular orbitals in the target are usually unknown. The qualitative results from MIES

of ILs agree with other techniques: all of the studies have found that the imidazolium rings orient their alkyl chains towards the vacuum [224-227].

Ultraviolet photoelectron spectroscopy (UPS) is a technique similar to XPS which uses photons in the vacuum ultraviolet (VUV) region (10 – 200 nm). It probes the valence energy levels of the surface, instead of its core levels, but it does so with higher resolution than XPS. UPS is sometimes used in combination with MIES. As MIES is more surface-sensitive, comparison between the two techniques can provide insight into the relative depths of functional groups. For example; in $[C_4mim][Tf_2N]$, the anion molecular orbitals from SO_2 are observed in UPS but not in MIES, whereas its CF_3 groups are detected in both techniques [226]. This is evidence that the $[Tf_2N]^-$ anions preferentially expose their CF_3 groups at the surface, whereas the SO_2 groups are located deeper into the bulk. High-resolution electron energy loss spectroscopy (HREELS), which involves the inelastic scattering of electrons from the surface, has also been applied to ILs in order to probe the vibrational modes of the surface and complement the UPS and MIES results [225].

Inelastic scattering of neutrons and photons

Neutron and X-ray scattering from IL surfaces probe the density of atoms or electrons as a function of surface depth in the first few molecular layers (their penetration depth is of the order of tens of Å). Both neutron [228] and X-ray reflectivity [229] of imidazolium-containing ILs revealed an increase in density at IL surfaces. It was proposed that the surfaces of ILs are arranged in ordered layers; however, the orientation of molecular components within such layers could not be elucidated. In these techniques, the interpretation of the results relies on fitting the data to models. This is often ambiguous, with several possible molecular arrangements leading to the same result. In addition, surface roughness (either intrinsic or from thermally induced capillary waves) affects the density profiles, which further complicates the interpretation of the results. X-ray reflectivity experiments on $[C_4mim][PF_6]$ and $[C_4mim][BF_4]$ found that these ILs presented a rougher surface than predicted from capillary wave theory [229]. This was later confirmed by theoretical studies, but the source of this additional roughness could not be identified [230].

Dynamic light scattering (DLS) on IL surfaces [231-233] probes the surface roughness and its time-dependent dynamics. That is, DLS probes the capillary waves, and therefore can help unravel some of the issues introduced above. X-ray photon

correlation spectroscopy (XPCS, the X-ray equivalent of DLS) [234] is a related technique that probes the surface structure on a smaller scale. Again, the interpretation of the results is based on theoretical models of the capillary waves, and this could be a source of disagreements between experiments. Capillary wave spectra from [C₄mim][PF₆] found high dipole-moment densities, suggesting significant charge ordering at the interface [231]. However, further DLS results on this liquid [232] as well as [C₄mim][Tf₂N] [235], and XPCS results on [C₄mim][BF₄] [234], were not consistent with such high dipole densities at the interface. It is clear that the structure of the IL surface cannot be elucidated by these scattering techniques alone, and they need to be paired with other techniques that are chemically specific.

Ion scattering

Surface analysis techniques that are based on the scattering of ions under high vacuum can be divided into low and high-energy ion scattering. Rutherford backscattering spectrometry (RBS), which can be classified as high-energy ion scattering, has been applied to some imidazolium-based IL surfaces [236-238]. In this technique, a highly energetic (100 keV to several MeV) beam of He⁺ is scattered from the IL surface and detected by an energy-sensitive detector at a defined scattering angle. The surface atoms are identified by their masses from the kinetic energy of the scattered helium ions, assuming hard-sphere collisions and conservation of momentum. In addition, the scattered particles lose some of their kinetic energy as they travel through the liquid. Provided that the stopping power of the liquid is known, this allows the depth profiling of the surface. RBS experiments have enough depth resolution to elucidate the relative positions of cations and anions at the IL surface: for example, in an RBS study of [C₄mim][PF₆], the [PF₆] anions were found to be located close to the imidazolium rings but slightly closer to the surface, and the butyl chains on the cation were oriented towards the vacuum phase [236]. A disadvantage of RBS is that it probes the surface to a depth of at least a few nm due to the high energies of the incident ions. Studying the outermost layer in isolation requires a different, surface-specific technique.

Low-energy ion scattering (LEIS) has the same working principle as RBS but employs He⁺ ions of lower kinetic energy (0.5 – 20 keV) that do not penetrate so deeply into the liquid [239, 240]. Moreover, He⁺ ions that penetrate into the bulk have a high probability of being neutralised to He. By detecting exclusively ions, the technique probes only the outermost surface layer. Although LEIS is surface sensitive and

chemically specific, it has some deficiencies: so far, it has failed to provide fully quantitative concentrations of each atom at the surface. The cross section and neutralisation probabilities of He^+ for the atoms in imidazolium ILs are unknown. Furthermore, because the mass of the surface atom must be larger than that of the projectile, it does not detect H atoms in the surface, which means that information such as coverage of the surface by alkyl chains is difficult to obtain. It also lacks resolution between heavier atoms which, for kinematic reasons, scatter the He^+ projectiles at an asymptotically constant energy.

Neutral impact collision ion scattering spectroscopy (NICISS) is a variation of LEIS that has been applied to imidazolium IL surfaces [153, 241-244]. In NICISS, only recoiling He projectiles (both ions and neutral atoms) that scatter at a small angle to the incident beam are detected. These backscattered projectiles can only result from head-on collisions with the outer layers of the surface. As with other ion scattering techniques, depth profiling is possible by measuring the kinetic energy loss of the scattered He projectiles. Typical experiments probe a depth of 20 nm with a resolution of 10 Å [241]. In addition, if the sample is rotated with respect to the incident beam, without changing the scattering angle, it can provide further orientational information. This is known as angle-resolved NICISS (ARNICISS). The results from different NICISS experiments do not always agree: Morgner [241] and Andersson [243] reached different conclusions about the position of the ring and orientation of the alkyl chain in imidazolium IL surfaces, although it should be noted that they studied different anions.

The first studies of the ionic liquid-vacuum interface, performed by Watson and Seddon, employed another type of ion scattering known as direct recoil spectrometry (DRS) [245-247]. In these experiments, a low-energy (2 – 3 keV) beam of inert gas ions is directed at the surface, and scattered ions and recoiled surface atoms are detected by a channel electron multiplier at a fixed angle. The kinetic energy of the recoil atom indicates its identity, and the energy of the scattered rare gas atoms also depends on the mass of the surface atoms with which they collided. Experiments on $[\text{C}_n\text{mim}][\text{PF}_6]$ and $[\text{C}_n\text{mim}][\text{BF}_4]$ with $n = 4, 8$ and 12 found both cations and anions exposed at the surface, and the cation rings oriented perpendicular to the surface, contradicting the ring orientation detected by SFG. The orientation of the cations was inferred from the element ratios at different sampling depths, by comparison with simulations of ion pairs in different orientations. It should be considered that, even at the most surface-sensitive configuration (3-4 Å), there was a significant amount of penetration into the liquid.

Recoils that originate from multiple collisions obscure the direct recoil signals and complicate the interpretation of the results, which could explain why the authors were not able to distinguish any deviations from stoichiometric composition at the surface.

Lastly, time-of-flight secondary ion mass spectrometry (ToF-SIMS) [248, 249] is a related scattering technique that uses a pulsed ion beam of 2 – 25 keV and detects all charged fragments that scatter from the surface. A time-of-flight mass analyser separates the fragments according to their mass/charge ratio, providing evidence of which functional groups are exposed at the surface. ToF-SIMS studies of imidazolium ILs found both cations and anions at the surface [248]. However, due to the relatively large depth of penetration (1 – 2 nm), information on the relative positions of the ions could not be obtained.

Inelastic scattering of molecules and radicals

Nesbitt and co-workers have scattered molecular beams of CO_2 [36, 132] and NO [134, 250] from IL surfaces, using spectroscopic methods to detect the molecules and radicals escaping from the surface. The advantage of this approach, as opposed to the inert gas scattering techniques discussed above, is that it probes the internal energy of the products and gives a full picture of the energy transfer processes at the interface. This dynamical information may be of interest in real-life applications involving the interaction of gas-phase molecules with ILs. In addition, the incident energies of the molecular beams are several orders of magnitude smaller than those in the ion scattering methods, which guarantees that only the surface is probed. Despite this, it is quite limited as a surface analysis technique, as it does not provide direct information on the composition of the surface. Some aspects can be inferred from the dynamics: alkyl chains make the surface softer and lead to translationally and rotationally colder products. Comparing different ILs, the trends in energy transfer agreed with the expected degree of alkyl coverage [36], although these trends are not by any means a direct measure of alkyl coverage.

MD simulations

Theoretical simulations of the ionic liquid surface provide very useful complementary information to experimental results. The surface structure of pure 1-alkyl-3-methylimidazolium ILs has been extensively studied theoretically using molecular dynamics (MD) simulations [42, 230, 251-267]. Typically, a slab of several hundreds

of ion pairs is simulated, using periodic boundary conditions. Different intermolecular potentials have been used, based on popular molecular mechanics force fields such as AMBER [255], OPLS [252] or CHARMM [264]. One of the most widely used force fields is the one developed by Canongia Lopes and Padua [252], a variation of OPLS-AA with added terms to better describe ionic liquids. As the name suggests, OPLS (Optimized Potentials for Liquid Simulations) is typically used to model liquids. AA stands for all-atom, meaning that the calculation includes each atom explicitly. An alternative to all-atom methods that greatly reduces the computational cost is to use coarse graining (CG), which involves grouping chemically similar atoms together. Coarse-grained simulations by Voth of imidazolium ILs [42] found that alkyl chains were oriented towards the vacuum, and the calculated surface tensions were in agreement with experiment.

Polarisation effects are expected to be important in ionic liquids. The partial charges of each ion are often artificially reduced in order to account for them [254]; however, including polarisation explicitly in the model is a more reliable (albeit computationally expensive) approach. When a polarisable and a nonpolarisable model were applied to the same IL, the former showed weaker charge oscillation and stronger segregation of cations at the surface, as well as physical properties in better agreement with experiment [256].

In general, MD simulations successfully reproduce the experimental properties of IL surfaces. There is an increase in density at the interface, in agreement with scattering experiments [230]. The simulated density profiles show oscillations of cations and anions at the interface, evidencing that the ions arrange themselves in layers [254]. However, although the simulations come to the same general conclusions as the experiments, their quality depends on the quality of the force field used, as well as on the method employed to analyse the results. In liquids, an apparently simple problem like identifying which atoms are exposed at the surface is complicated by the presence of thermally-induced surface roughness. In order to decouple the intrinsic density profiles from this structure, probe spheres can be dropped from the vacuum phase or rolled over the surface to identify the truly interfacial atoms [259, 263, 264, 268]. Additional useful tools include orientational analysis of the ions and radial distribution functions to identify which functional groups preferentially pair together. The different chemical moieties involved in ILs give rise to rather disordered surfaces, where many ion conformations are possible. For this reason, ideally MD studies should aim to

produce quantitative results and report all possible ion orientations at the surface, not just the most probable one. For example, a study by Hantal and co-workers [263] found different orientations of the $[C_4mim]^+$ cation coexisting at the surface. The rings were preferentially oriented perpendicular to the surface with their butyl chains towards the vacuum, but a significant fraction of them were parallel to the surface. This could perhaps explain why DRS experiments found cations in a perpendicular orientation, while SFG detected parallel imidazolium rings.

A further step towards characterising the IL surfaces is to simulate how these surfaces interact with gas-phase compounds. In this case, classical force fields are insufficient to model the process, particularly if a chemical reaction takes place. Instead, a hybrid quantum mechanics/molecular mechanics (QM/MM) approach has been used to model the scattering of CO_2 [130] and atomic oxygen and argon [129] from ionic liquids. The interaction region was treated quantum mechanically in order to characterise it accurately, whereas the rest of the surface was modelled by molecular mechanics to save computational cost. The simulations successfully reproduced the trends observed in the corresponding scattering experiments [48, 132].

Summary

A general picture of the imidazolium IL surface emerges from the studies discussed above, so that a set of “design rules” can be proposed [41]. The arrangement of ions at the surface is driven by a balance of electrostatic and van der Waals forces. The most general rule is that the nonpolar alkyl chains on the imidazolium cations preferentially protrude out of the surface, in order to minimise the surface energy. Below the outer alkyl layer, the imidazolium headgroups and the anions, which are more polar in character, pack together. However, in detailed comparisons of alkyl surface coverage between ILs, different techniques reach different conclusions. These disagreements most likely arise from differences in surface sensitivity, or even in the interpretation of the results (i.e. defining different depths as belonging to the surface). A summary of the strengths and weaknesses of each surface analysis technique, excluding the reactive-atom scattering method that is the subject of the current work, is presented in Table 4.1.

| Technique | Strengths | Weaknesses |
|---|---|--|
| SFG | <ul style="list-style-type: none"> • Surface-specific • Orientation information | <ul style="list-style-type: none"> • Not quantitative • Assignment of modes is not always straightforward; selective deuteration might be required |
| ARXPS | <ul style="list-style-type: none"> • Quantitative comparison between ILs • Angle resolution provides relative depths of functional groups | <ul style="list-style-type: none"> • Not very surface-sensitive: information depth is 1 – 1.5 nm in the most sensitive configuration |
| MIES | <ul style="list-style-type: none"> • Surface-specific (uses thermal He*) | <ul style="list-style-type: none"> • Not quantitative • Interpretation of results relies on DFT calculations |
| Neutron and light scattering | <ul style="list-style-type: none"> • Probe surface layering to a depth of tens of nm • DLS provides dynamical information | <ul style="list-style-type: none"> • Not chemically specific • Ambiguous interpretation of results |
| Ion scattering | <ul style="list-style-type: none"> • Chemically specific • Some methods are quantitative • Depth profiling is possible | <ul style="list-style-type: none"> • Contributions from the bulk due to the high ion energies employed (keV range) |
| Inelastic molecule and radical scattering | <ul style="list-style-type: none"> • Surface-specific • Dynamical information | <ul style="list-style-type: none"> • Not chemically specific • Not quantitative |
| MD simulations | <ul style="list-style-type: none"> • Characterise surface structure to a greater level of detail than experimental techniques | <ul style="list-style-type: none"> • The results depend on the force field used and their analysis is not straightforward • Size of the systems is restricted by computational constraints |

Table 4.1. Summary of the strengths and weaknesses of the experimental and theoretical techniques used for the analysis of ionic liquid surfaces.

4.1.2. Reactive Atom Scattering from ionic liquids

As discussed above, there are not many surface analysis methods that can quantitatively characterise the alkyl coverage of an IL surface. However, alkyl chains are the most nonpolar and surface-active moiety of imidazolium-based ionic liquids, and understanding their behaviour at the surface would be very beneficial for practical applications. Most of the quantitative results so far have been obtained by ARXPS, which found variations in alkyl coverage with chain length [219] and anion [218]. ARXPS is however not a truly surface-specific technique, so it is very possible that these results were influenced by the bulk.

The McKendrick and Minton research groups have previously used reactive scattering of $O(^3P)$ atoms to characterise the alkyl surface coverage of a family of $[C_n\text{mim}][\text{Tf}_2\text{N}]$ ionic liquids, with $n = 2 - 12$ [10, 11, 48, 104]. As seen in the previous chapter, the OH radicals resulting from the interfacial H-abstraction reaction must arise from the outermost layer, because penetration into the bulk would likely produce H_2O from a second H abstraction. More subtly, provided the OH products with IS characteristics can be distinguished, they must also have been produced in direct processes at the extreme outer layer with few, or no, secondary encounters. Thus, the technique is more surface-sensitive than ARXPS. In addition, OH radicals can only be a product of the reaction with C–H groups at the surface. This makes the method chemically specific, as opposed to the inelastic scattering of molecular beams discussed above.

This chapter expands on the previous proof-of-concept experiments on $O(^3P)$ scattering on $[C_n\text{mim}]^+$ ILs, by studying the trends in alkyl coverage for other anion families. Namely, $[C_n\text{mim}][\text{BF}_4]$ ($n = 4, 6, 8, 12$), $[C_n\text{mim}][\text{OTf}]$ ($n = 4, 6, 8$) and $[C_6\text{mim}][\text{I}]$ have been studied in addition to the $[C_n\text{mim}][\text{Tf}_2\text{N}]$ ILs investigated previously. The influence of the chain length n and anion identity will be discussed. The experimental approach is very similar to that in the previous chapter: $O(^3P)$ atoms are produced from NO_2 photolysis, and OH radicals detected by LIF spectroscopy. The low energy of the photolytic $O(^3P)$ atoms means that they react preferentially with CH_2 units in the alkyl chains. Due to their higher bond strengths, C–H bonds from terminal CH_3 groups and imidazolium rings are expected to contribute very little or nothing, respectively, to the detected OH yield. Therefore, using this approach, the flux of OH produced by an IL surface is a very good measure of its alkyl coverage. In addition, detection by LIF provides the internal-state distribution of the OH radicals produced at the surface.

Besides the LIF experiments, which are the focus of this chapter, complementary O(³P) scattering experiments have been carried out by Timothy Minton and co-workers in Montana State University, USA. Some of their results will be presented in the Discussion section, along with MD simulations of the IL surfaces performed in Montana under joint supervision with George Schatz (Northwestern University). The Montana apparatus employed a hyperthermal beam of O(³P) atoms with translational energies of 504 to 511 kJ mol⁻¹, much higher than in the LIF approach. This means that they were able to overcome the barriers for abstraction of all H atoms in the molecule, including the imidazolium ring hydrogens [48]. The scattered products were detected by mass spectrometry, enabling detection of inelastically scattered O(³P) atoms and H₂O resulting from two H abstractions, besides OH. The incidence angle of the beam and the detection angle could be varied, affording well-defined velocity distributions of the products at different incident angles. Throughout this chapter, the two complementary approaches are labelled Reactive Atom Scattering-Laser Induced Fluorescence (RAS-LIF) and Reactive Atom Scattering-Mass Spectrometry (RAS-MS). The Experimental and Results sections consider the RAS-LIF experiments exclusively. The Discussion focuses on the RAS-LIF results, but makes use of RAS-MS and MD results where relevant.

4.2. Experimental

The liquids were studied in the 1-wheel apparatus described in Section 2.2.1, following the general procedures outlined in Chapter 2. The main difference is that, instead of using a cylindrical beam, the probe laser was expanded into a sheet by means of a pair of plano-concave and plano-convex lenses in a telescope arrangement. The laser sheet was 18 mm long in the x direction (height) and 3 mm long in the z direction (width). The purpose of this configuration was to maximise the detection of the scattered products, while minimising the effect of any potential differences in angular distributions to obtain a more reliable comparison of integral OH yields between liquids. Besides, expanding the cylindrical probe beam into a larger volume decreased the laser fluence, which had the additional advantage of reducing saturation.

Table 4.2 lists all of the studied ILs and provides the abbreviations of their chemical names. Most of the liquids were purchased from commercial suppliers. Their purity, if provided by the supplier, is given in the table, as well as their water content. In

addition, a sample of $[C_4mim][Tf_2N]$ was synthesised by the group of John Slattery in the University of York. This IL was synthesised under dry conditions using standard Schlenk techniques in order to ensure that its water content was below 100 ppm. All of the liquids were degassed prior to measurements. The degassing procedure involved loading the liquid sample into the reaction chamber and leaving it under high vacuum and 60 °C for several hours (at least four hours, but typically overnight). Additionally, some of the more hygroscopic liquids were pre-degassed at low vacuum before transfer to the chamber.

The liquid hydrocarbon squalane (see Chapter 3 for its chemical structure) was used as a reference against which to compare the results for the ionic liquids. The experiments required the same measurement conditions for each ionic liquid and its squalane reference. For this reason, the squalane reference was measured immediately after each IL dataset, always on the same day. As noted in Chapter 2, this procedure involved opening the chamber to atmosphere and potentially modifying the experimental conditions. For this reason, care was exercised to minimise exposure to air and ensure constant conditions.

Most of the ILs were investigated at room temperature, as indicated in Table 4.2. The exceptions were $[C_6mim][OTf]$, which has a melting point close to room temperature (~ 25 °C) and $[C_{12}mim][BF_4]$, which is a solid at room temperature and liquid crystalline in the range of 26.4 °C to 38.5 °C [269]. The latter IL was studied at a temperature corresponding to its isotropic phase, in order to avoid any potential surface ordering effects arising from liquid crystal order. The temperature of the squalane reference measurements in all cases matched that of the corresponding IL. Water circulating through the bath assembly was used to control the temperature of the liquid, as indicated in Chapter 2. The temperature of the copper bath, quoted in Table 4.2, was monitored with a thermocouple probe. The temperature of the liquid itself was not monitored during experiments, but it was found to be close to the bath temperature (within 5 °C) in separate tests, and to be systematically correlated with it with a similar absolute precision.

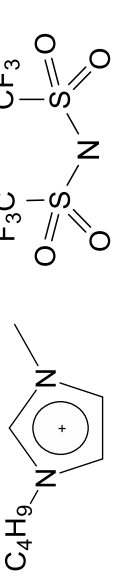
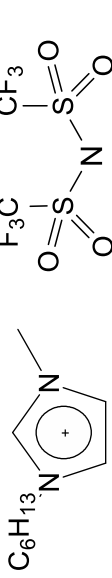
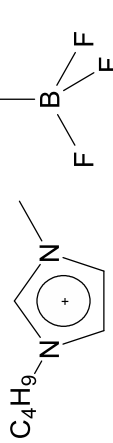
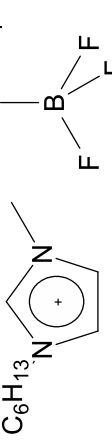
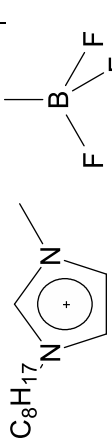

| Name and abbreviation | Structure | Supplier | Purity | [H ₂ O] | Temperature |
|---|--|-------------------|--------|--------------------|-------------|
| [C ₄ mim][Tf ₂ N] 1-butyl-3-methylimidazolium bis(trifluoromethylsulfonyl)imide |  | IoLiTec | >99% | 30 ppm | r.t. |
| [C ₆ mim][Tf ₂ N] 1-hexyl-3-methylimidazolium bis(trifluoromethylsulfonyl)imide |  | U. of York | | | r.t. |
| [C ₄ mim][BF ₄] 1-butyl-3-methylimidazolium tetrafluoroborate |  | IoLiTec | >99% | 70 ppm | r.t. |
| [C ₆ mim][BF ₄] 1-hexyl-3-methylimidazolium tetrafluoroborate |  | Sigma- Aldrich | >98% | <0.5% | r.t. |
| [C ₈ mim][BF ₄] 1-methyl-3-octylimidazolium tetrafluoroborate |  | IoLiTec | >99% | 150 ppm | r.t. |
| [C ₈ mim][BF ₄] 1-methyl-3-octylimidazolium tetrafluoroborate |  | IoLiTec | >99% | 20 ppm | r.t. |

Table 4.2. Ionic liquids studied and temperature of the measurements. Purity and water content are those stated by the supplier.

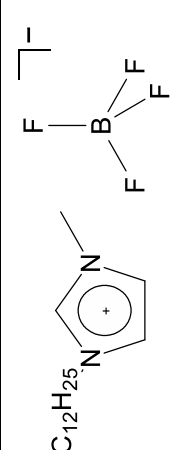
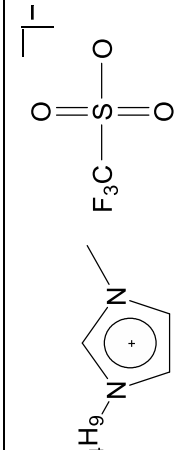
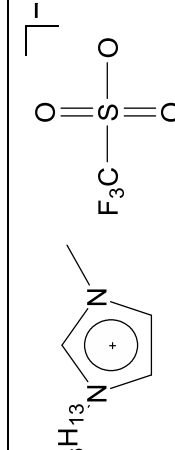
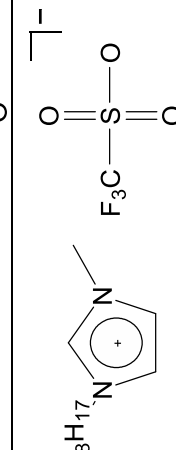
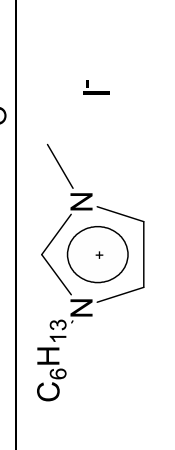
| Name and abbreviation | Structure | Supplier | Purity | [H ₂ O] | Temperature |
|---|--|----------|--------|--------------------|-------------|
| [C ₁₂ mim][BF ₄] 1-dodecyl-3-methylimidazolium tetrafluoroborate |  C ₁₂ H ₂₅ | IoLiTec | >98% | 0.055% | 60 °C |
| [C ₄ mim][OTf] 1-butyl-3-methylimidazolium trifluoromethanesulfonate |  C ₄ H ₉ | IoLiTec | >99% | 380 ppm | r.t. |
| [C ₆ mim][OTf] 1-hexyl-3-methylimidazolium trifluoromethanesulfonate |  C ₆ H ₁₃ | IoLiTec | >99% | 0.045% | 34 °C |
| [C ₈ mim][OTf] 1-methyl-3-octylimidazolium trifluoromethanesulfonate |  C ₈ H ₁₇ | IoLiTec | >99% | 0.053% | r.t. |
| [C ₆ mim][I] 1-hexyl-3-methylimidazolium iodide |  C ₆ H ₁₃ | IoLiTec | >98% | <2500 ppm | r.t. |

Table 4.2 (contd.). Ionic liquids studied and temperature of the measurements. Purity and water content are those stated by the supplier.

4.3. Results

The focus of this study was to characterise the reactivity of the surfaces rather than to study the fundamental dynamics of the reaction. In Chapter 3, the OH rovibrational distributions were carefully measured and integrated for different photolysis-probe delays to obtain relative yields from each liquid. In this chapter, in contrast, the OH yields for some of the ILs were too low to accurately obtain full rotational distributions. Instead, the relative OH yields were derived from the relative intensities of the appearance profiles. Profiles were recorded on the most intense spectroscopic transition ($Q_1(1)$ of the A-X (1,0) band, which has a small contribution from $R_2(3)$) in order to achieve the best possible signal-to-noise ratios. As discussed below, each dataset was normalised to the peak LIF signal of the appearance profiles from squalane, acquired immediately after the corresponding IL profiles, and the ratio between the OH $N' = 1$ yields from the IL and squalane was taken as a measure of reactivity. This approach assumes that all liquids produce equivalent rotational distributions, so that the relative OH $N' = 1$ yield is representative of the total relative yield. To verify this assumption, OH excitation spectra were acquired from each IL. The purpose of the spectra was not to accurately characterise the OH internal-state distribution, but to ensure that the contribution of $N' = 1$ to it was similar for all liquids.

LIF excitation spectra were recorded at a fixed delay between photolysis and probe pulses. The probe wavelength was scanned from 281 to 283.5 nm in steps of 0.0025 nm, omitting sections that did not contain any transitions of interest. The spectra were recorded simultaneously for photolysis-probe delays of 12 μs (delay at which the highest density of scattered OH was detected) and 3 μs . The 3 μs spectra were acquired to determine the relative concentration of photolytically generated OH (Section 2.6.1). Small dynamical differences were detected for different ILs (these differences will be discussed in Section 4.4), however, the distributions were sufficiently similar for the approximation to remain valid: the contribution of $N' = 1$ to the overall population was always between 27 % and 34 %, including squalane (33%). This is illustrated in Figure 4.1, which presents different LIF excitation spectra in the R_1 branch region for ILs containing the $[\text{C}_6\text{mim}]^+$ cation with different anions, as well as squalane. It can be appreciated in the figure that the distributions are not very different.

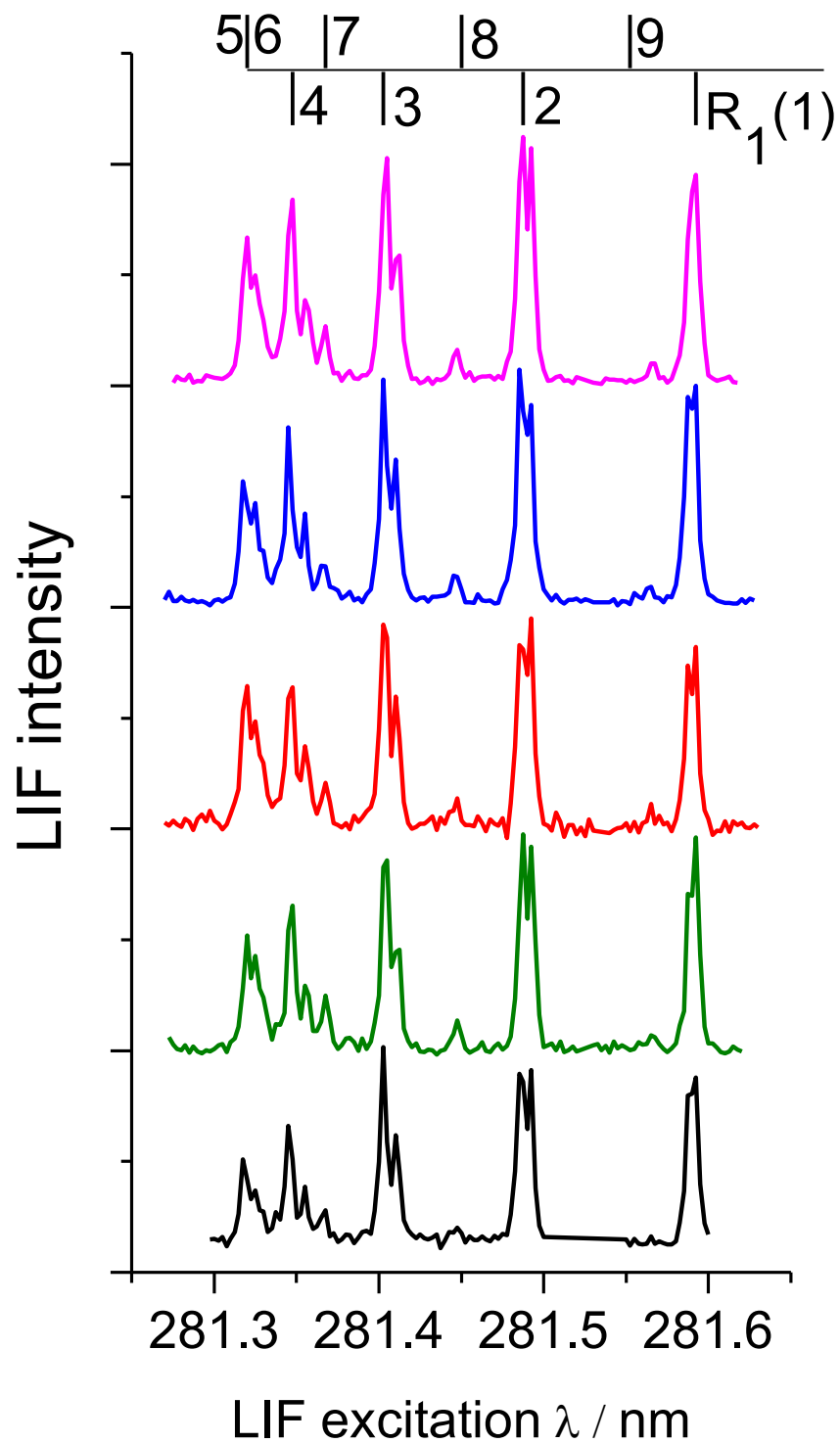


Figure 4.1. R_1 branches of the OH LIF excitation spectra recorded at a photolysis-probe delay of 12 μ s, from $[C_6mim][I]$ (magenta), $[C_6mim][BF_4]$ (blue), $[C_6mim][OTf]$ (red), $[C_6mim][Tf_2N]$ (green) and squalane (black).

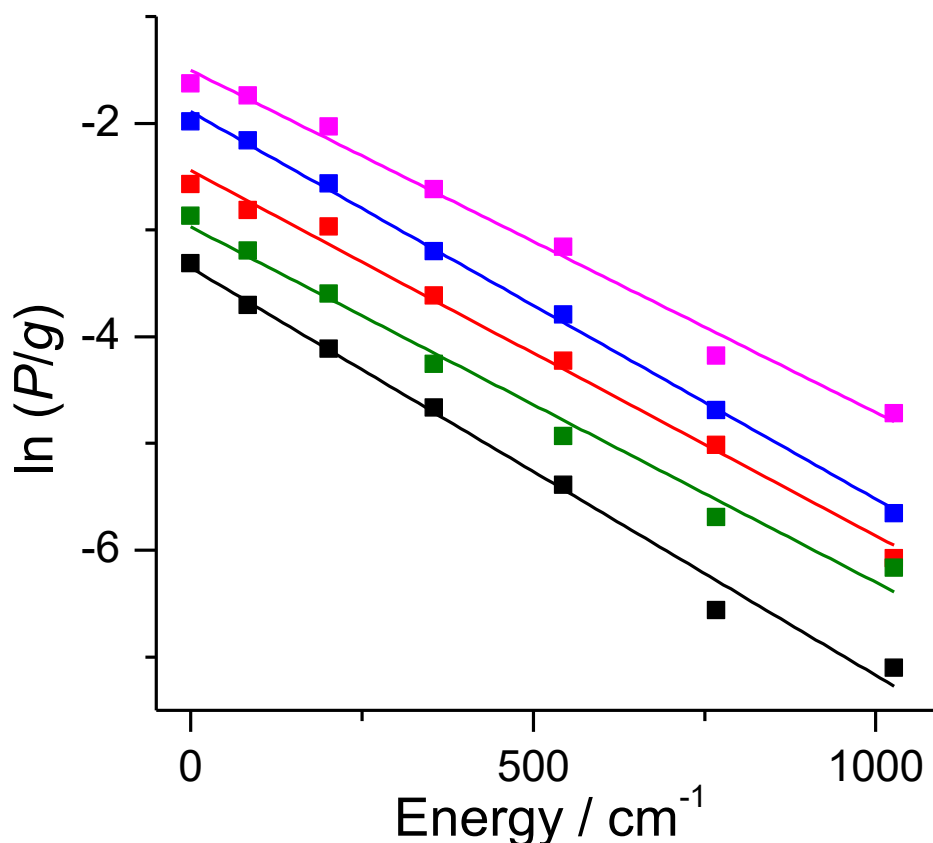


Figure 4.2. Representative Boltzmann plots for the OH R_1 branches acquired from $[C_6mim][I]$ (magenta), $[C_6mim][BF_4]$ (blue), $[C_6mim][OTf]$ (red), $[C_6mim][Tf_2N]$ (green) and squalane (black). The plots are offset for clarity.

The rotational distributions were obtained independently for the Q_1 and R_1 rotational branches of each spectrum, spanning the levels $N' = 1 - 7$ except for the blended $Q_1(6)$ transition. The population distribution of each branch was then fitted to a single-temperature Boltzmann distribution. Figure 4.2 shows example Boltzmann plots for the R_1 branches of ILs containing $[C_6mim]^+$. Although there are significant differences between individual spectra, these are due to experimental variation rather than true dynamical differences. This becomes evident when the rotational temperatures from several (at least 3) spectra are averaged together: as shown below, the resulting rotational temperatures T_{rot} are the same within error for all liquids. Only the Q_1 distributions were used to obtain the average T_{rot} values, due to the higher signal-to-noise ratio of the transitions in this branch.

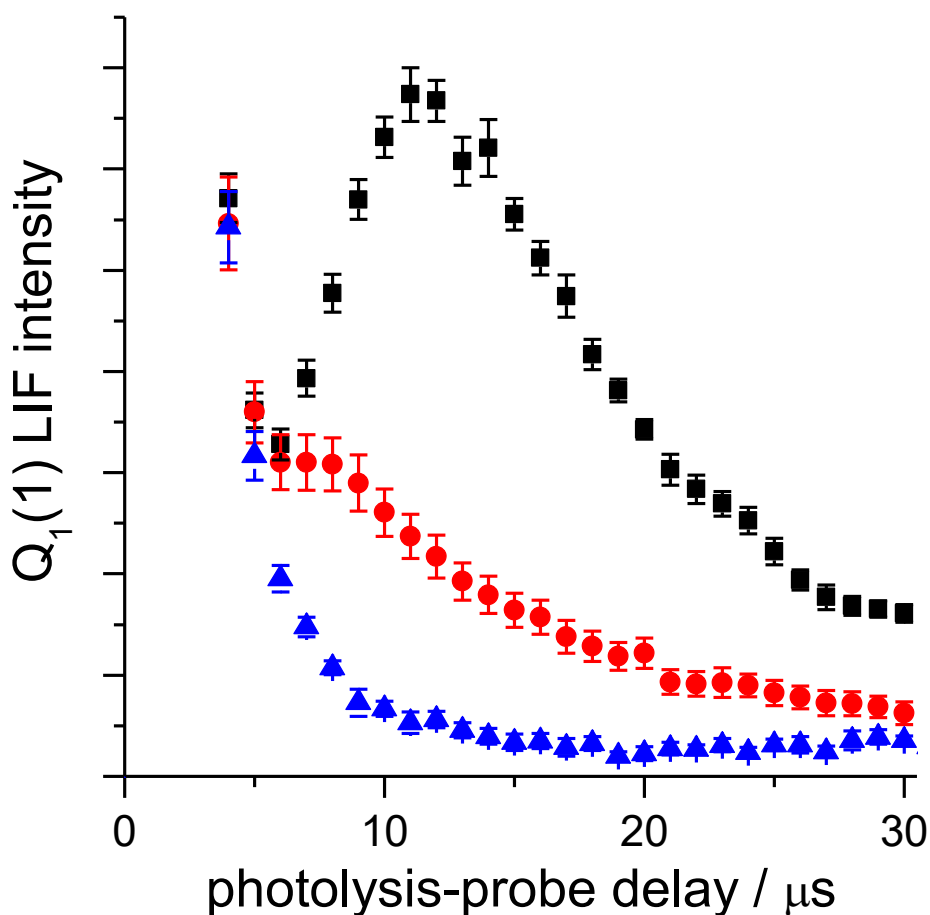


Figure 4.3. OH appearance profiles recorded from $[C_4mim][BF_4]$ with NO_2 (black squares) and HONO (red circles), and without a liquid surface with NO_2 (blue triangles). Each set is an average of 10 profiles recorded under the same conditions, and error bars represent the $\pm 1\sigma$ standard error of the mean. The HONO and no-surface profiles are scaled to the 3- μs LIF signal of the reactive profile.

Appearance profiles were recorded in sets of 5 or 10 consecutive profiles. A set of profiles from squalane was acquired as soon as possible after each IL set, by venting the chamber and changing the liquid bath. Scattered laser light was characterised and subtracted for photolysis and probe lasers as described in Section 2.6.1. As with the excitation spectra, a background of OH radicals originating from HONO photolysis appeared in the measurements. The concentration of photolytic OH was in general higher for ILs with higher water content, indicating that water plays a role in HONO formation. The HONO contamination was not noticeably reduced by degassing the IL before the measurements, but it was observed to decrease during data acquisition. Photolytic OH appearance profiles were recorded using HONO as a precursor instead of

NO_2 , as described in Section 2.3.2. Although the HONO background did not significantly affect the OH yield from squalane, its relative contribution was significant for some ILs, especially those with low alkyl coverage and high water content. To illustrate this, typical NO_2 and HONO appearance profiles recorded for $[\text{C}_4\text{mim}][\text{BF}_4]$ are shown in Figure 4.3. An appearance profile recorded under the same conditions without the liquid surface is also presented in the figure. The figure shows that there is a significant fraction of photolytic OH that scatters from the surface and is detected at late delays, evidenced by comparison of the HONO (red circles) and “no-wheel” (blue triangles) profiles. More importantly, comparison with the reactive NO_2 appearance profile shows that the contribution of inelastic scattering is not negligible, even at long photolysis-probe delays.

The HONO profiles did not differ significantly between liquids. In each dataset, the HONO profile was scaled to the early (3 μs) LIF signal in the NO_2 profile and subtracted from it. The resulting background-subtracted profiles were normalised to the peak signal of the squalane profile. In some cases the absolute intensity of the appearance profiles varied considerably between days due to fluctuations in pressure and build up of contaminants on the chamber windows. The relative intensity of the appearance profiles with respect to squalane, however, stayed constant. Different sets of profiles, acquired on different days, are presented in Figure 4.4 to illustrate the day-to-day reproducibility of the results. Appearance profiles averaged over all datasets for all of the studied ILs, as well as squalane, are presented in Figure 4.5. The qualitative trends with chain length and anion are clearly seen in the figure: the yield of OH increases with chain length and consistently follows the same trend for the different anions: $[\text{Tf}_2\text{N}]^- < [\text{OTf}]^- < [\text{BF}_4]^-$.

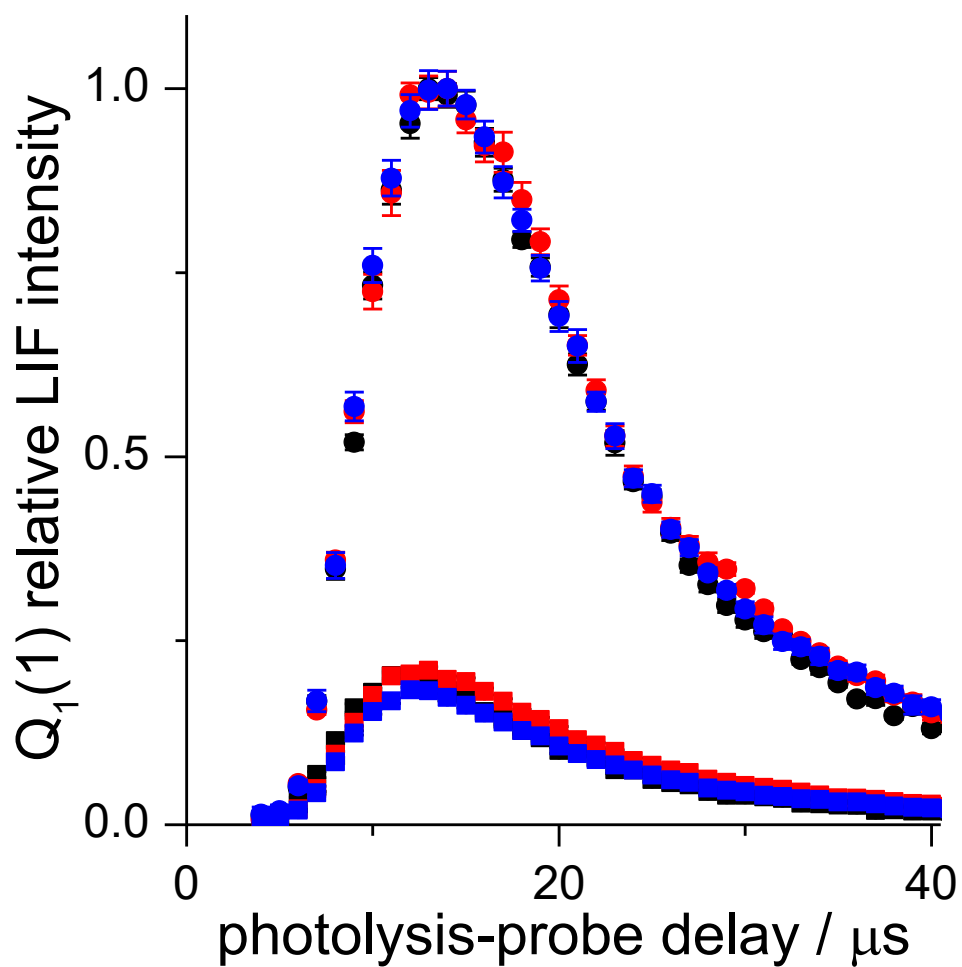


Figure 4.4. OH $Q_1(1)$ appearance profiles datasets from $[C_6mim][OTf]$ (squares) and its squalane reference measurements (circles). Each dataset, plotted in a different colour, is normalised to the squalane peak signal. The profiles are an average of 10 measurements from each liquid acquired on different days, and errors are $\pm 1\sigma$ standard error of the mean.

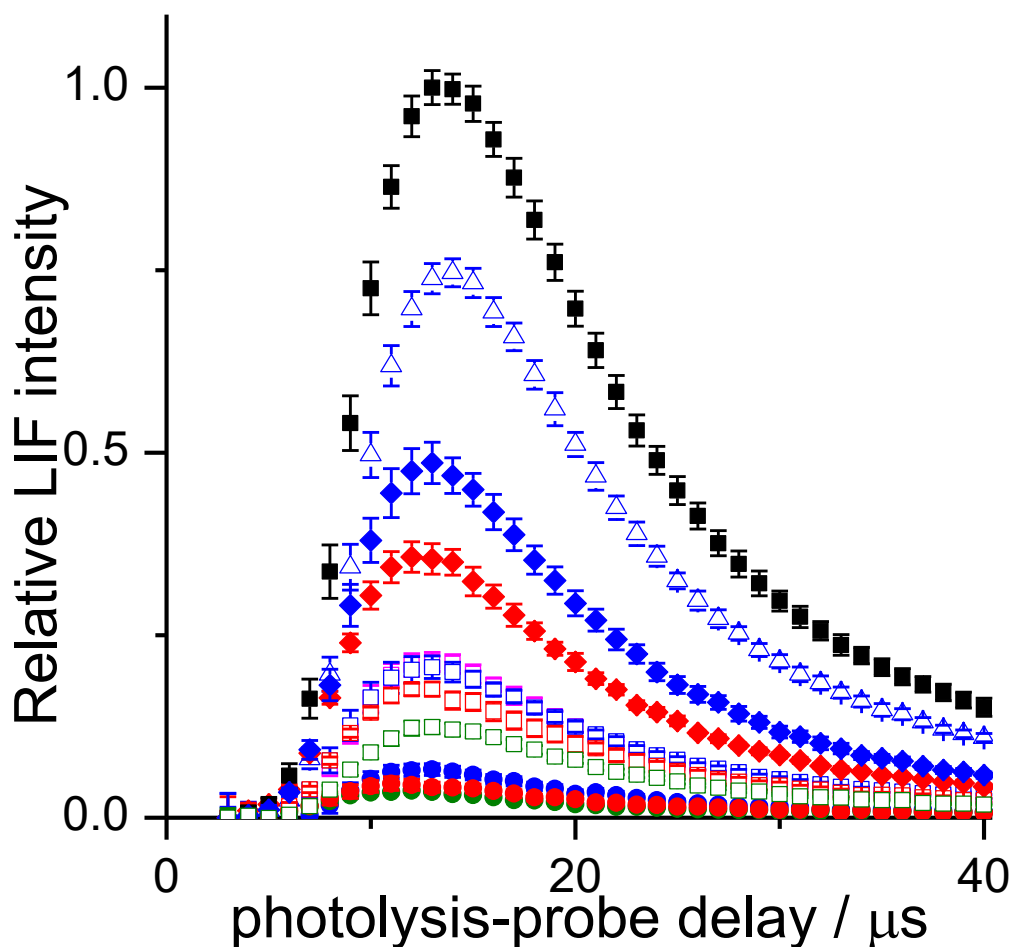


Figure 4.5. $Q_1(1)$ appearance profiles from all liquids investigated: $[C_4mim][Tf_2N]$ (green filled circles), $[C_4mim][OTf]$ (red filled circles), $[C_4mim][BF_4]$ (blue filled circles), $[C_6mim][Tf_2N]$ (green open squares), $[C_6mim][OTf]$ (red open squares), $[C_6mim][BF_4]$ (blue open squares), $[C_6mim][I]$ (magenta open squares), $[C_8mim][OTf]$ (red filled diamonds), $[C_8mim][BF_4]$ (blue filled diamonds), $[C_{12}mim][BF_4]$ (blue open triangles), squalane (black filled squares). Each profile is an average of at least 3 different sets of 10 profiles each. The peak values are normalized to that for squalane. Error bars indicate $\pm 1\sigma$ standard error of the mean values.

Besides providing the yield of OH produced at the surface, the appearance profiles contain information on the translational energy of the radicals. There are small differences in the shape of the profiles for different liquids, with earlier profiles corresponding to faster OH radicals. These differences are more evident if the profiles are peak-normalised. Figure 4.6 presents average peak-normalised appearance profiles for $[C_nmim][BF_4]$ with $n = 4 - 12$. For this IL family, the profiles are earlier for shorter

chains. A simulated profile corresponding to a room-temperature Boltzmann distribution of products (Section 2.6.1) is also shown in the figure. Comparing the experimental profiles with the thermal simulation, it is obvious that the experimental profiles follow speed distributions that are substantially faster than thermal.

The differences in translational energy can be quantified by fitting the results to Monte-Carlo simulated profiles. As in the previous chapter, the simulations assume a single-temperature Maxwell-Boltzmann speed distribution and a $\cos\theta$ angular distribution around the surface normal. The resulting effective translational temperature, T_{trans} , is simply a convenient parameter which turns out to characterise rather well the differences between the OH produced at different surfaces. It might well be expected that in reality the products arise from a range of scattering mechanisms and might be fit phenomenologically by the usual mixture of IS and TD distributions. However, this approach was not followed because the fraction of fully thermalized products is small for all liquids, as can be inferred from Figure 4.6. Each Monte Carlo profile was the result of 5×10^6 simulated trajectories, of which only a fraction were successful, i.e. they intersected the probe volume and contributed to the profile. The value of T_{trans} in the simulation was varied from 300 K to 2200 K in intervals of 100 K. Each experimental profile was then matched to the simulation that provided the best result in a correlation analysis. As an example, a Monte Carlo simulation that matched the experimental $[\text{C}_6\text{mim}][\text{BF}_4]$ profile ($T_{\text{trans}} = 1500$ K) is plotted in Figure 4.6. Effective translational temperatures were obtained for independently measured appearance profiles (at least 3) and averaged together for each liquid. The resulting T_{trans} values for all ILs and squalane are presented in Figure 4.7, together with the rotational temperatures T_{rot} from the analysis of the spectra discussed above.

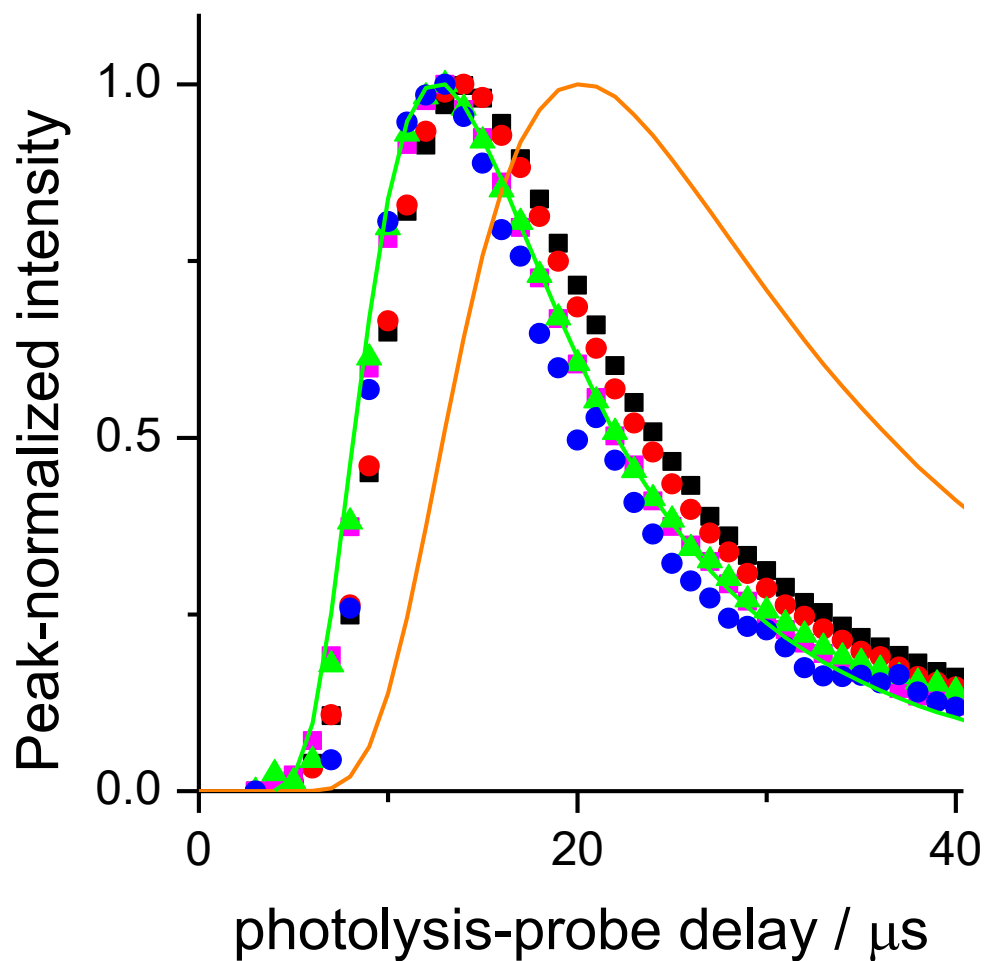


Figure 4.6. Peak-normalised average appearance profiles acquired from $[C_4mim][BF_4]$ (blue circles), $[C_6mim][BF_4]$ (green triangles), $[C_8mim][BF_4]$ (magenta squares), $[C_{12}mim][BF_4]$ (red circles) and squalane (black squares). The lines correspond to simulated 300 K (orange) and 1500 K (green) Maxwell-Boltzmann distributions.

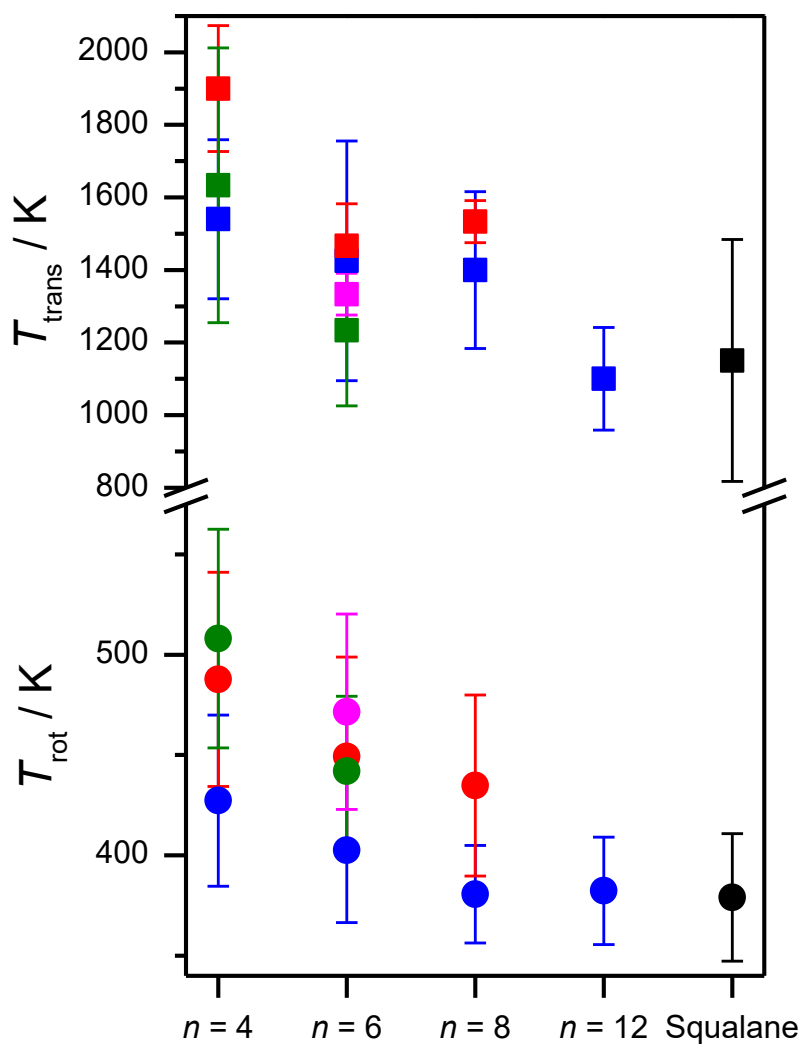


Figure 4.7. Values of OH rotational temperature T_{rot} (circles) and effective OH translational temperature T_{trans} (squares) for squalane (black symbols) and $[C_n\text{mim}]^+$ ILs with $n = 4 - 12$ and $[\text{Tf}_2\text{N}]^-$ (green symbols), $[\text{OTf}]^-$ (red symbols), $[\text{BF}_4]^-$ (blue symbols), and $[\text{I}]^-$ (magenta symbols) as the anions. Error bars indicate $\pm 1\sigma$ standard error of the mean.

Returning to the comparison of OH yields, the differences between liquids can be quantified by integrating the flux of detected OH between 0 and 30 μs . Photolysis-probe delays $> 30 \mu\text{s}$ should not be considered, since gas-phase secondary collisions can noticeably affect the OH radicals detected at such delays [11]. However, simply integrating the measured appearance profiles does not give the flux of OH, since detection by LIF measures OH number density instead of flux. OH radicals that travel slowly have a higher probability of being detected than fast OH radicals. This would

not be problematic if the product velocity distributions were the same for all liquids but, as seen above, the shapes of the appearance profiles vary modestly but systematically with the liquid studied. Consequently, a density-to-flux conversion of the experimental profiles was performed. This conversion made use of the Monte Carlo simulations discussed above. For each translational temperature, the number of successful trajectories in the simulation was divided by the integral of the simulated density profile, from 0 to 30 μs . The result was a density-to-flux correction factor for the corresponding T_{trans} . The experimental appearance profiles were integrated over the same delays and multiplied by their corresponding density-to-flux correction factors to obtain relative IL:squalane OH flux ratios. These correction factors ranged from ~ 1.05 for the slowest appearance profiles to ~ 1.20 for the earlier profiles. The resulting flux ratios are presented in Table 4.3.

| Ionic liquid | Relative OH yield |
|---|-------------------|
| [C ₄ mim][Tf ₂ N] | 0.038 \pm 0.002 |
| [C ₆ mim][Tf ₂ N] | 0.12 \pm 0.01 |
| [C ₈ mim][Tf ₂ N] ^a | 0.27 \pm 0.01 |
| [C ₁₂ mim][Tf ₂ N] ^a | 0.62 \pm 0.03 |
| [C ₄ mim][OTf] | 0.052 \pm 0.004 |
| [C ₆ mim][OTf] | 0.184 \pm 0.007 |
| [C ₈ mim][OTf] | 0.370 \pm 0.018 |
| [C ₄ mim][BF ₄] | 0.062 \pm 0.003 |
| [C ₆ mim][BF ₄] | 0.213 \pm 0.016 |
| [C ₈ mim][BF ₄] | 0.510 \pm 0.029 |
| [C ₁₂ mim][BF ₄] | 0.740 \pm 0.002 |
| [C ₆ mim][I] | 0.211 \pm 0.003 |

Table 4.3. OH yields from RAS-LIF measurements for different ionic liquids relative to squalane. The uncertainties correspond to $\pm 1\sigma$ standard error of the mean.^a Values from Reference [11].

In addition to the ILs characterised here, Table 4.3 presents the interfacial reactivities of $[C_8mim][Tf_2N]$ and $[C_{12}mim][Tf_2N]$ obtained in a previous RAS-LIF study by Waring *et al.* [11]. However, the experimental conditions in this study differed slightly: instead of a planar beam, the authors used a cylindrical beam at a distance closer to the surface (4 mm as opposed to 6 mm). Although using squalane as a reference should make the results more comparable, it is possible that the different conditions cause systematic deviations in the results. In order to test this, the ionic liquid $[C_4mim][Tf_2N]$, previously studied by Waring, was measured again by RAS-LIF with the new experimental configuration. Additionally, two different samples of $[C_4mim][Tf_2N]$ were studied: a commercial sample supplied by IoLiTec and a custom-synthesised sample by the University of York (details in Table 4.2). The purpose of this comparison was to establish whether the differences in liquid purity between the commercial and custom-synthesised samples affected the result. The results, presented in Table 4.4, show no difference between the previous measurements of the York IL and the present measurements of the commercial sample. The new results for the custom-synthesised $[C_4mim][Tf_2N]$ sample showed slightly higher reactivity (although still within the error limits), possibly due to the higher concentration of HONO in the chamber which introduced larger deviations between sets of measurements.

| Supplier | Studied in | Relative OH yield |
|--------------------|--------------------------|-------------------|
| University of York | Waring <i>et al</i> [11] | 0.038 ± 0.002 |
| University of York | This chapter | 0.043 ± 0.007 |
| IoLiTec | This chapter | 0.038 ± 0.002 |

Table 4.4. OH yields from RAS-LIF measurements for different samples of $[C_4mim][Tf_2N]$ relative to squalane. The uncertainties correspond to $\pm 1\sigma$ standard error of the mean.

4.4. Discussion

The discussion of the results focuses on two aspects: the effect of varying the alkyl chain length on 1-alkyl-3-methylimidazolium cations, and the effect of varying the

anion. In the first part (Section 4.4.1), only the results for $[C_n\text{mim}][\text{BF}_4]$ will be used for the discussion. In addition, the RAS-MS experiments and MD simulations of the same family of ILs, performed by collaborators in Montana State University, will be presented to aid the discussion. The anion effect discussed in Section 4.4.2 will also make use of some MD simulations, along with the previously obtained results for $[\text{C}_8\text{mim}][\text{Tf}_2\text{N}]$ and $[\text{C}_{12}\text{mim}][\text{Tf}_2\text{N}]$ [11].

4.4.1. Variation of alkyl chain length

Effect of chain length on alkyl surface coverage

The effect of chain length on alkyl surface coverage has been characterised for $[C_n\text{mim}][\text{BF}_4]$ ILs with $n = 4, 6, 8$ and 12 . In addition to the RAS-LIF experiments reported in the previous section, RAS-MS measurements of $n = 4, 8$ and 12 were performed by collaborators. In that work, time-of-flight (TOF) distributions of OH and H_2O were collected with $O(^3P)$ incidence angles $\theta_i = 30^\circ, 45^\circ,$ and 60° , and final angles θ_f in increments of 5° ranging from 20° to $70^\circ, 5^\circ$ to $70^\circ,$ and -10° to 70° for $\theta_i = 30^\circ, 45^\circ,$ and $60^\circ,$ respectively. As in previous work [48, 60, 103], an analysis was carried out that empirically separated the products into IS and TD distributions. The distributions were converted to flux, corrected for ionization cross-sections and integrated over the range of final angles in order to obtain the total IS and TD product yields. The IS OH and TD H_2O yields for each θ_i are compared against the RAS-LIF OH yields obtained here in Figure 4.9. The RAS-LIF results are scaled to the product flux from squalane at $\theta_i = 45^\circ$ (the reason for this choice of angle is discussed below). There is a significant increase in the yield of both products as the chain length increases, and on going from $[\text{C}_{12}\text{mim}][\text{BF}_4]$ to squalane. The general trend in the RAS-MS results follows the RAS-LIF OH yields, but there is a large discrepancy between them for the shorter chains. The potential causes of this disagreement are discussed below.

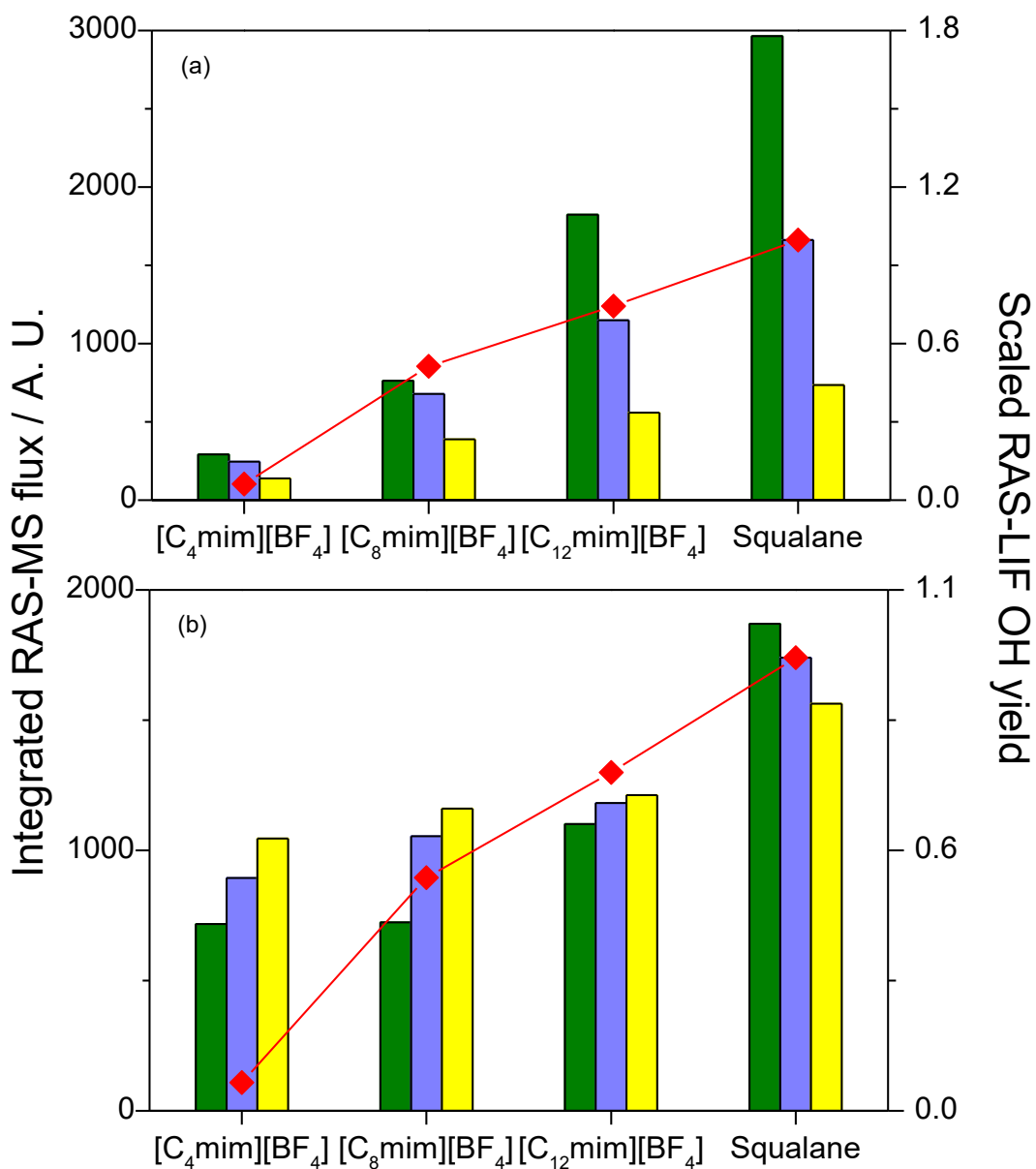


Figure 4.8. Integrated relative product fluxes from RAS-MS and RAS-LIF experiments. Bars represent the fluxes of (a) TD (thermal) H_2O and (b) IS (nonthermal) OH, with incidence angles $\theta_i = 30^\circ$ (green), $\theta_i = 45^\circ$ (blue), and $\theta_i = 60^\circ$ (yellow), from the RAS-MS experiments. Red symbols show the same RAS-LIF data for OH in panels A and B, scaled such that the maximum value of the OH flux from RAS-LIF matches the RAS-MS product flux for $\theta_i = 45^\circ$, normalized to that for squalane.

As seen in Table 4.3, the $[C_n\text{mim}][\text{BF}_4]$ family of ILs show a dramatic increase in OH yield with n , which is partly due to simple stoichiometry. There is a greater fraction of abstractable secondary H atoms in the IL composition for larger n values: from $n = 4$ to $n = 12$, there are 6, 10, 14 and 22 secondary hydrogens in the ILs studied. If the IL surface had the same composition as the bulk, or if the RAS-LIF technique did not truly probe the surface, an increase in reactivity would still be observed. This stoichiometric effect can be removed from the results if they are divided by the number of CH_2 units in the alkyl chain of the IL. The resulting n -corrected reactivities are plotted as a function of chain length in Figure 4.9. If the IL surfaces had stoichiometric composition, the values would be constant; however, the figure shows a marked increase with n , at least up to $n = 8$, demonstrating that it is not a purely stoichiometric effect: there is a stronger preference for longer chains to occupy the surface of $[C_n\text{mim}][\text{BF}_4]$ ILs.

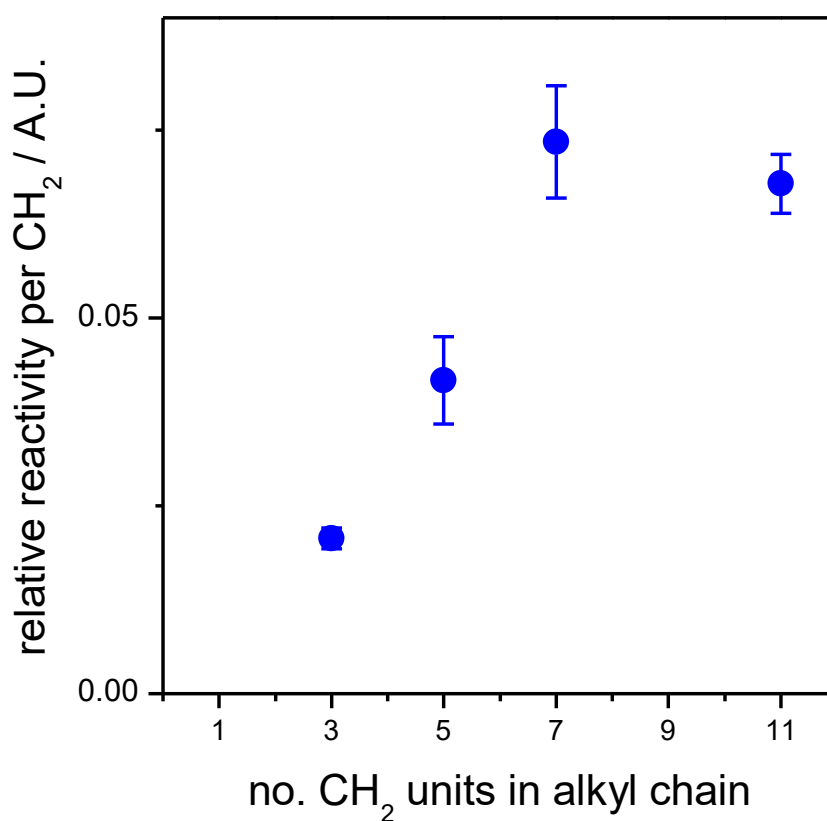


Figure 4.9. Relative RAS-LIF OH yields from $[C_n\text{mim}][\text{BF}_4]$, normalised to the number of reactive CH_2 units in their alkyl chains.

The nonstoichiometric increase in reactivity with n is evidence of an alkyl enrichment of the surface for longer chains, also seen by other experimental techniques [41], as well as RAS of $[C_n\text{mim}][\text{Tf}_2\text{N}]$ ionic liquids [11]. Longer alkyl chains are more nonpolar in character and tend to orient themselves toward the vacuum phase in order to minimise the surface energy. In Figure 4.9, this tendency is very clear for the short-chain ILs ($n = 4 - 8$), whereas there is apparently no additional enrichment going from $n = 8$ to $n = 12$, indicated by the plateau in the n -corrected reactivities. However, this does not mean that these IL surfaces are completely covered with alkyl chains: full alkyl saturation would correspond to a decline proportional to $1/n$ in Figure 4.9. This is clearly not the case: there is a significant increase in the uncorrected OH yields (Table 4.3), so $[C_8\text{mim}][\text{BF}_4]$ must have some unreactive groups exposed at the surface. This result is in contradiction with a previous MIES study by Iwahashi *et al.* [226], who did not find anions or cation rings on the surfaces of $[C_8\text{mim}][\text{BF}_4]$ and $[C_{12}\text{mim}][\text{BF}_4]$. Their claim was based on the fact that the MIES spectra for both ILs were qualitatively similar, but no quantitative results were offered. Features from the anion were still observed in the UPS spectra, which the authors attributed to the higher penetration depth of the UPS photons. The disagreement between MIES and RAS-LIF highlights the importance of surface sensitivity in the experimental measurements. Similarly, Nesbitt and co-workers [36] argued that long-chain ILs ($n = 8$ and 12) have a completely alkyl-saturated surface because they produced the same fraction of thermalized CO_2 in molecular beam scattering experiments. In this case, alkyl surface coverage was inferred from the trends in energy transfer, rather than directly measured with a chemically-specific method.

Other studies are in better agreement with the RAS-LIF results. NICISS experiments on $[C_n\text{mim}][\text{BF}_4]$ ($n = 6, 8$ and 10) provided atom depth profiles of the interfacial region to a depth of 20 \AA . It was found that the alkyl chains were preferentially at the surface for all of the ILs but, in addition, F atoms from the anions were always observed near the top layers but still below the hydrocarbon chains. The fact that the anions are located below the chains does not contradict the RAS-LIF results. It is possible that the alkyl chains are preferentially oriented towards the vacuum, but they are not packed tightly so that the polar groups situated below are still accessible to an incoming $O(^3P)$ atom. This picture of a rough, loosely-packed surface is in agreement with the MD simulations presented below, as well as other simulations of IL surfaces [258, 263]. As a consequence of this loose packing, the results change depending on the interpretation of what the “surface” is: if it is defined as a 2D plane intersected by the outermost

atoms, the alkyl enrichment effect could become blurred by the microscopic structure of the surface.

It is clear from the results above that the [C₈mim][BF₄] surface is not completely covered in hydrocarbon groups. Whether the [C₁₂mim][BF₄] surface is, in contrast, remains open to interpretation. Its reactivity is lower than that of squalane, which might indicate that it is not fully saturated, but it does not confirm it due to the different C–H bond reactivities for squalane and the ILs in RAS-LIF. However, the effect of different bond strengths is expected to be negligible in the RAS-MS experiments due to the high energy of the O(³P) atoms. Figure 4.8 shows a significant difference in reactivity between [C₁₂mim][BF₄] and squalane, which suggests that the surface is not fully alkyl in character.

MD simulations of the IL surfaces, performed by collaborators in Montana State University and Northwestern University, help to interpret the results. The details on the methodology of the simulations have been reported elsewhere [270]. The composition of the simulated ILs surfaces has been quantified by the double cubic lattice method [268], which is widely used in protein surface simulations. In this analysis, a probe particle of radius 0.15 nm was translated across the simulated IL surface. Atoms were defined to be present at the surface if they came in contact with the probe sphere, in which case they contributed to the surface density for their atom type. The results for different types of H atom (primary, secondary or cationic) are presented in Figure 4.10.

In Figure 4.10, the secondary H density increases steeply with n , while there is a slight decrease in the primary and cationic H densities. This is further evidence of the preferential surface occupation of the long alkyl chains and, in addition, it partially explains the differences between RAS-LIF and RAS-MS results. Since the RAS-MS experiments are sensitive to all types of H atoms, including those in the imidazolium ring, the change in product yield reflects the change in total hydrogen density, which is not as marked as the increase in secondary H density.

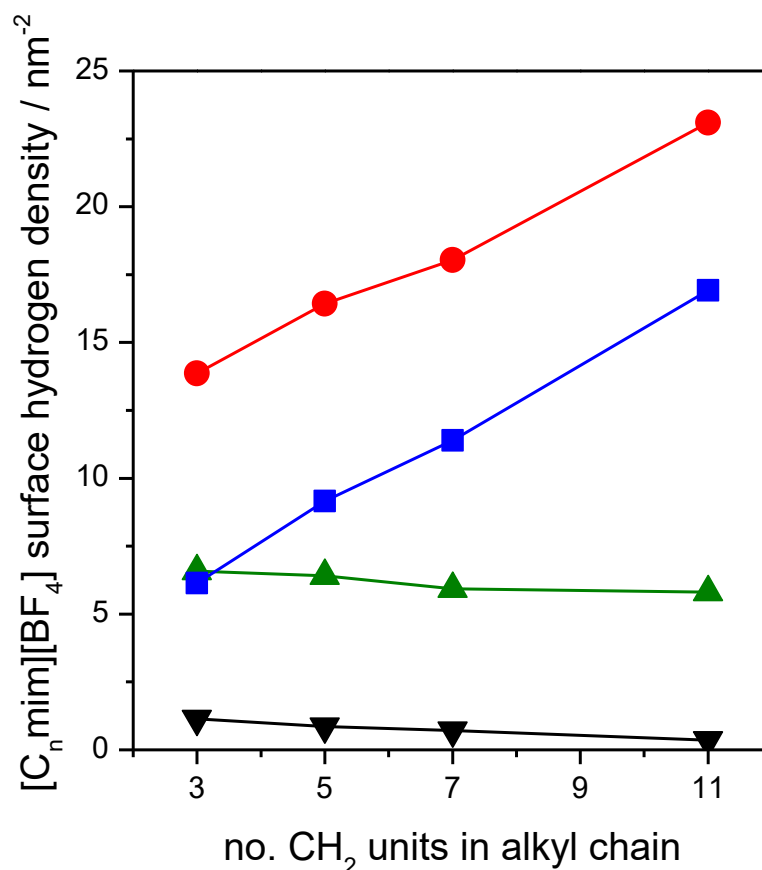


Figure 4.10. Simulated surface densities of different H atom types for $[C_n\text{mim}][\text{BF}_4]$ liquids. Aliphatic primary hydrogens are shown in green; secondary hydrogens are in blue; hydrogens attached to the imidazolium ring are in black; and the total hydrogen density is in red.

The different regioselectivities of RAS-LIF and RAS-MS explain part of the discrepancy seen in Figure 4.8; however, they do not justify the large disagreement for a chain length $n = 4$. The growth of both total H and secondary H density in the MD results agrees well with the increase in IS OH yield for RAS-MS, but not that for RAS-LIF. This could indicate a greater propensity for the short butyl chains to point towards the vacuum phase, so that methyl groups (essentially unreactive in RAS-LIF) preferentially encounter the $O(^3P)$ atoms. It has been previously proposed that short chains ($n = 4-8$) preferentially orient themselves normal to the surface plane, whereas longer chains tend to fold over exposing more of their CH_2 groups in their backbone [41, 48]. The MD simulations do not contradict this interpretation: there is a very slight decrease of primary H atoms with chain length, which could be an indication of this, but

further analysis (e.g. quantitative characterisation of chain orientations) is needed to obtain conclusive results.

It should be considered that the MD analysis method does not account for the incidence angle of the O(³P) atoms. In addition, RAS-LIF does not provide angle-dependent yields, so its results cannot be directly compared to those of RAS-MS. Using the Monte Carlo simulation of the scattering described in Section 2.6.1, the distribution of θ_i that lead to detected OH in RAS-LIF can be predicted. These angles (integrated from detection times of 0 to 30 μ s) are shown in Figure 4.11, together with the total distribution of incidence angles. The figure shows a very broad distribution peaking near 45°. Consequently, the best RAS-MS angle to compare the results to is 45°, but it should be emphasized that the scattering dynamics of RAS-LIF are very different due to the broader θ_i distribution and the lower collision energy. The differences between the two methods could also arise from penetration depth: the higher kinetic energy of the RAS-MS O(³P) atoms could induce deeper penetration into the bulk. However, it should be noted that a large fraction of the scattered products arise from direct, IS-like encounters and therefore have interacted with the outer surface layer only.

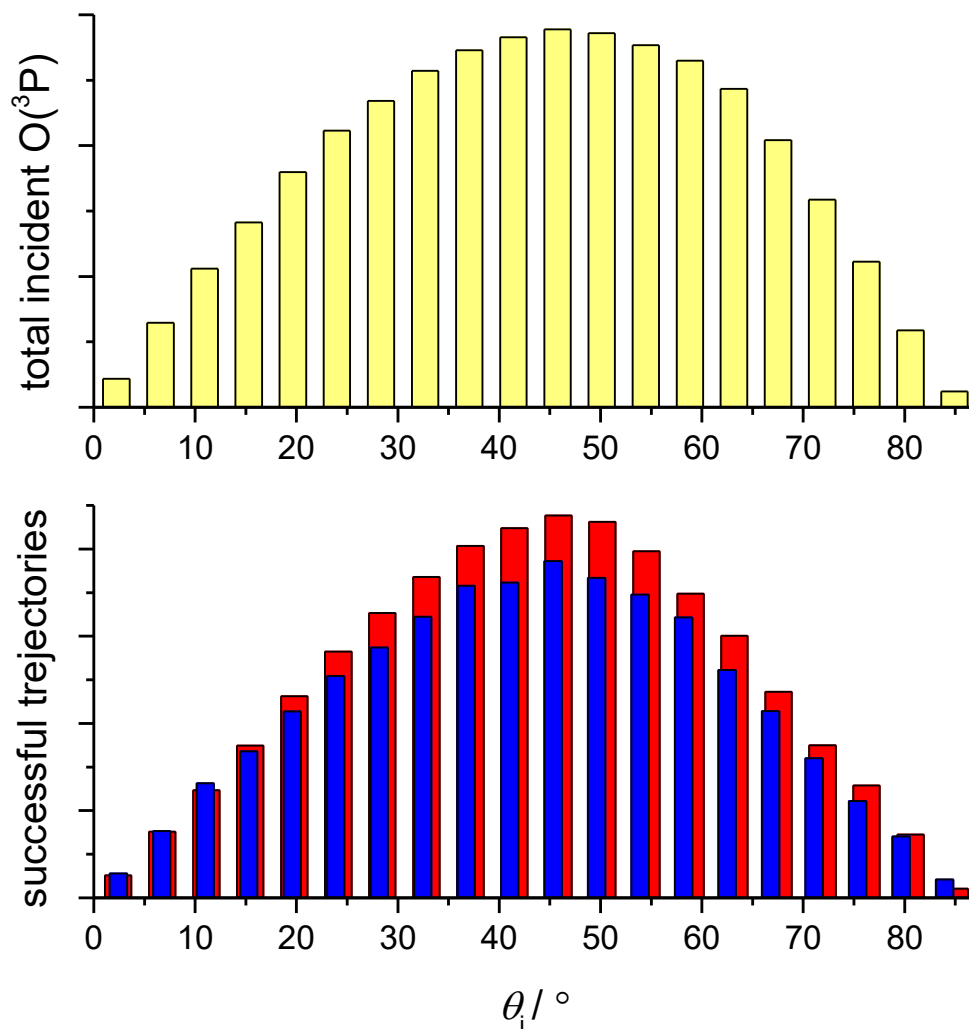


Figure 4.11. Distribution of incident angles of $O(^3P)$ in a Monte Carlo simulation of the RAS-LIF experiment. The upper histogram corresponds to all of the $O(^3P)$ atoms that impinge on the surface, in arbitrary units. The lower histogram presents the distribution of incidence angles that lead to detected products, divided into IS (blue bars) and TD (red bars) trajectories.

In RAS-MS, the angle of incidence θ_i greatly affects the yield and the fraction of thermalized products. This is best observed in the yield of TD H_2O , which increases steeply for smaller θ_i (Figure 4.8). Since H_2O formation involves two H abstractions, a large fraction of the H_2O flux is expected to be the result of thermalisation of either the primary OH or the secondary product H_2O at the surface (this is corroborated by the fact that the majority of water fits to a TD distribution). The angle dependence of the TD H_2O yield is thus consistent with the idea that collisions closer to normal incidence

result in greater energy transfer and a larger fraction of thermalized products. The IS OH yield follows the opposite trend for the ILs but, interestingly, it reverses again in squalane. This could be a consequence of different surface roughness or orientation of the chains at the liquid surfaces. Detailed simulations of the scattering, such as QM/MM calculations, are required to clarify this.

The RAS-MS yield of TD H₂O follows the trend in RAS-LIF OH yield much better than the IS OH. As noted above, H₂O production is likely to be the result from multiple collisions at the surface. A significant fraction of these products will be formed by a second H abstraction by low-energy OH radicals, resulting from thermal accommodation of OH at the surface. These thermalised OH radicals would be sensitive to the barriers for abstraction of a second H atom, which are of the order of 4-5 kJ mol⁻¹ for secondary C-H and 8-9 kJ mol⁻¹ for primary C-H bonds [271]. The difference between the barriers therefore mimics the trend in H-abstraction barriers that induces regioselectivity in RAS-LIF. This qualitative similarity of the reaction energetics, with a strong preference for abstraction of secondary hydrogens, might be the reason why there is a similar trend with chain length.

Effect of chain length on scattering dynamics

The RAS-LIF results for [C_nmim][BF₄] contain some dynamical information besides the interfacial reactivities. Firstly, the peak-normalised appearance profiles in Figure 4.6 are evidence that, in all cases, a large fraction of the OH radicals are detected at delays that are too early for TD products. The scattering dynamics must therefore be predominantly direct and IS-like. This reinforces the idea that RAS is a surface-sensitive analytical technique, since penetration of the O(³P) atoms into the bulk liquid would involve multiple collisions and produce translationally thermalized OH radicals.

The IL appearance profiles are earlier than the squalane profile, and consistently earlier for shorter chains. This can be seen in the normalised profiles in Figure 4.6, as well as the translational temperatures in Figure 4.7. Since the H-abstraction reaction is expected to have the same intrinsic dynamics independently of the liquid, this is probably the result of different surface stiffness values. Although this is the first time that such an effect has been observed in reactive scattering, similar results were found in inelastic scattering studies by Minton [48] and Nesbitt [36]. Minton and co-workers studied the scattering of hyperthermal O(³P) from [C₂mim][Tf₂N] and [C₁₂mim][Tf₂N]. For inelastically scattered O atoms, the efficiency of momentum transfer followed the

trend squalane > $[C_{12}mim][Tf_2N]$ > $[C_2mim][Tf_2N]$. ILs with shorter chains have a more dense, stiffer surface due to the presence of polar groups; whereas ILs with long and flexible alkyl chains absorb energy more efficiently and redistribute it to the bulk (in other words, they have higher effective surface masses). Interestingly, the O and OH products scattered from squalane followed the same dynamics, whereas in the ILs there was a difference between inelastic and reactive scattering dynamics, which was more marked for $[C_2mim][Tf_2N]$. This indicates that polar groups are accessible to the $O(^3P)$ atoms in the IL surfaces (more so for the shorter-chain IL) and therefore affect the inelastic scattering dynamics, while in squalane both reactive and inelastic scattering occur at hydrocarbon sites. The RAS-LIF results for $[C_nmim][BF_4]$ ILs in this chapter agree with this interpretation; however, the trends in energy transfer observed here were not so clear in the *reactive* scattering results from Minton. One possible explanation is the large difference in collision energy: in RAS-LIF, the OH products could be more susceptible to thermalisation. The effect could therefore arise from the microscopic structure of the surfaces instead of the kinematics: alkyl-rich surfaces might be rougher and therefore promote OH thermalisation. This explanation is, however, in disagreement with the chain orientation effect proposed earlier.

A similar effect was observed in the inelastic scattering of CO_2 from ILs performed by Nesbitt [36]: the fraction of thermalisation increased with chain length for both $[C_nmim][Tf_2N]$ and $[C_nmim][BF_4]$ ILs. The scattered products were both translationally and rotationally thermalised. Rotational thermalisation was evidenced by both higher values of α (the TD fraction in the bimodal Boltzmann fits, see Chapter 3) and lower values of IS rotational temperature. It was argued that the alkyl chains absorb translational energy instead of promoting translation-to-rotation transfer.

In RAS-LIF of $[C_nmim][BF_4]$, the product rotational energies also decrease with chain length, although only slightly: going from $n = 4$ to $n = 12$, T_{rot} decreases from 427 ± 43 K to 382 ± 27 K (Figure 4.7). The decrease in temperature supports the idea that the surface becomes softer as the alkyl chain length is increased. Longer chains and fewer exposed ionic groups result in reduced translational and rotational energies, in agreement with the CO_2 inelastic scattering experiments by the Nesbitt group [36].

4.4.2. Variation of anion

Effect of anion on alkyl surface coverage

The previous discussion has shown that, for $[C_n\text{mim}][\text{BF}_4]$ ILs, it is possible to “fine-tune” the alkyl coverage of the IL surface (i.e. its nonpolar character) by varying the length of the alkyl chain on the cation. A similar trend was observed in previous reactive atom scattering studies of $[C_n\text{mim}][\text{Tf}_2\text{N}]$ surfaces [10, 11, 48, 104]. This section focuses on the influence of the anion on alkyl coverage for $[C_n\text{mim}]^+$ ionic liquids, making use of the RAS-LIF results for different anions presented in Section 4.3. In particular, the following questions will be answered definitively for the first time: 1) Does the chemical identity of the anion affect the alkyl surface coverage? 2) If that is the case, how strong is the anion effect compared to the chain length effect studied in the previous section? 3) Are there any identifiable trends that can be explained by the chemical properties of the anions?

To answer these questions, the RAS-LIF results for ILs containing different anions will be compared. The anions chosen (See Table 4.2) were $[\text{BF}_4]^-$, $[\text{OTf}]^-$, $[\text{Tf}_2\text{N}]^-$ and $[\text{I}]^-$. These anions are all relatively inert and form chemically stable ILs, but have different characteristics in terms of ionic volume and polarizability. Previous results for the ionic liquids $[\text{C}_8\text{mim}][\text{Tf}_2\text{N}]$ and $[\text{C}_{12}\text{mim}][\text{Tf}_2\text{N}]$ [11] will be included in the discussion, as indicated earlier. By comparing ionic liquids that are very similar in composition (for example, same n but different anion or same anion but only a difference of 2 C atoms in the alkyl chain), the sensitivity of the RAS-LIF technique will be tested.

The answers to questions 1) and 2) are evident from the appearance profiles in Figure 4.5, or the integrated OH fluxes in Table 4.3: for any given chain length, the OH yields consistently follow the order $[\text{Tf}_2\text{N}]^- < [\text{OTf}]^- < [\text{BF}_4]^- \sim [\text{I}]^-$. Moreover, there is the strong increase already noted above in interfacial reactivity as the alkyl chain on the cation becomes longer, observed for $[\text{BF}_4]^-$, $[\text{OTf}]^-$ and $[\text{Tf}_2\text{N}]^-$ anions. The effect of the anion appears to be smaller than the chain length effect, but it is still very clearly distinguished by RAS-LIF. In addition, shorter-chain ILs appear to give slightly earlier appearance profiles, as seen above for $[C_n\text{mim}][\text{BF}_4]$ ionic liquids.

As described for the $[C_n\text{mim}][\text{BF}_4]$ results, the stoichiometric contribution to the interfacial reactivity has been removed by dividing by the number of CH_2 units in the alkyl chain. The normalised reactivities are plotted in Figure 4.12 as a function of chain

length. The almost-linear increase in reactivity for $n \leq 8$ observed before in $[C_n\text{mim}][\text{BF}_4]$ ionic liquids is also observed for the $[C_n\text{mim}][\text{Tf}_2\text{N}]$ and $[C_n\text{mim}][\text{OTf}]$ series, indicating that the preference for longer chains to occupy the surface occurs for all of the anions. The influence of the anion is also strongest for these short-to-medium chains, with $[\text{BF}_4]^-$ producing almost twice as much OH as $[\text{Tf}_2\text{N}]^-$ for chain lengths $n = 6$ and $n = 8$. The effect appears to lessen for $n = 12$: $[\text{BF}_4]^-$ shows no increase in reactivity per CH_2 going from $n = 8$ to $n = 12$, as discussed earlier, whereas there is still an increase for $[\text{Tf}_2\text{N}]^-$. The similar OH yields from $[\text{C}_{12}\text{mim}][\text{Tf}_2\text{N}]$ and $[\text{C}_{12}\text{mim}][\text{BF}_4]$ could be due to the onset of saturation for this chain length. As discussed earlier, the surfaces of $[\text{C}_{12}\text{mim}]^+$ ILs are very rich in hydrocarbon groups, although they still have some polar groups accessible to the incoming $O(^3P)$ atoms due to the disordered, loosely-packed structure of the surface.

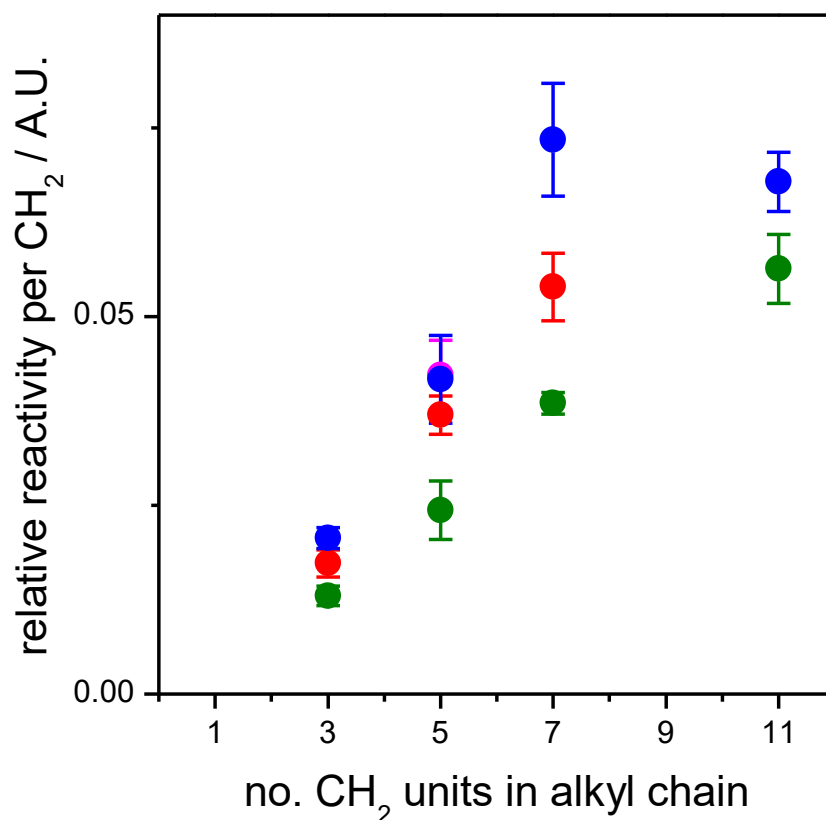


Figure 4.12. Relative RAS-LIF OH yields from $[C_n\text{mim}][\text{Tf}_2\text{N}]$ (green), $[C_n\text{mim}][\text{OTf}]$ (red), $[C_n\text{mim}][\text{BF}_4]$ (blue) and $[\text{C}_6\text{mim}][\text{I}]$ (magenta), normalised to the number of reactive CH_2 units in their alkyl chains.

The trends in alkyl coverage are further supported by the MD simulations introduced above. All nine possible $[C_n\text{mim}][X]$ ILs with $n = 4, 6, 8$ and $X = \text{BF}_4, \text{OTf}$ and Tf_2N were simulated. Snapshots of each IL surface are presented in Figure 4.13. The simulated surfaces follow the qualitative trends observed in RAS-LIF: as the chain length becomes shorter or the anion becomes larger, more polar groups (green anions or purple imidazolium rings) are exposed at the surface and, in turn, fewer alkyl chains are observed. Interestingly, the influence of the anion appears to be larger than the chain length effect: the increase in alkyl coverage is stronger across a row ($[\text{BF}_4]^-$ to $[\text{Tf}_2\text{N}]^-$) than down a column ($n = 4$ to $n = 8$). Assuming that the MD simulations predict the correct structure of the surface, there are many possible reasons for this apparent disagreement with RAS-LIF. For example, the alkyl C–H bonds may have slightly different strengths along the chain: if shorter chains are intrinsically less reactive, this difference would be observed at the low collision energies of RAS-LIF but not in RAS-MS. This effect is thought to be small, though, as will be discussed in detail in Chapter 5. Another possibility is a different orientation of the alkyl chains. It can be appreciated in the simulations that the octyl chains tend to lie more horizontally and expose CH_2 groups, while butyl chains are oriented more perpendicularly. While RAS-MS might be insensitive to the type of C–H site, RAS-LIF can distinguish between chain orientations. Regardless of this, the MD snapshots clearly show that the IL surfaces are relatively disordered and microscopically rough, with cation headgroups and anions accessible to the gas-phase atoms. A LEIS study on a wide range of ILs found anions at the surface of most liquids [240], which supports the idea that this is a general feature of IL surfaces.

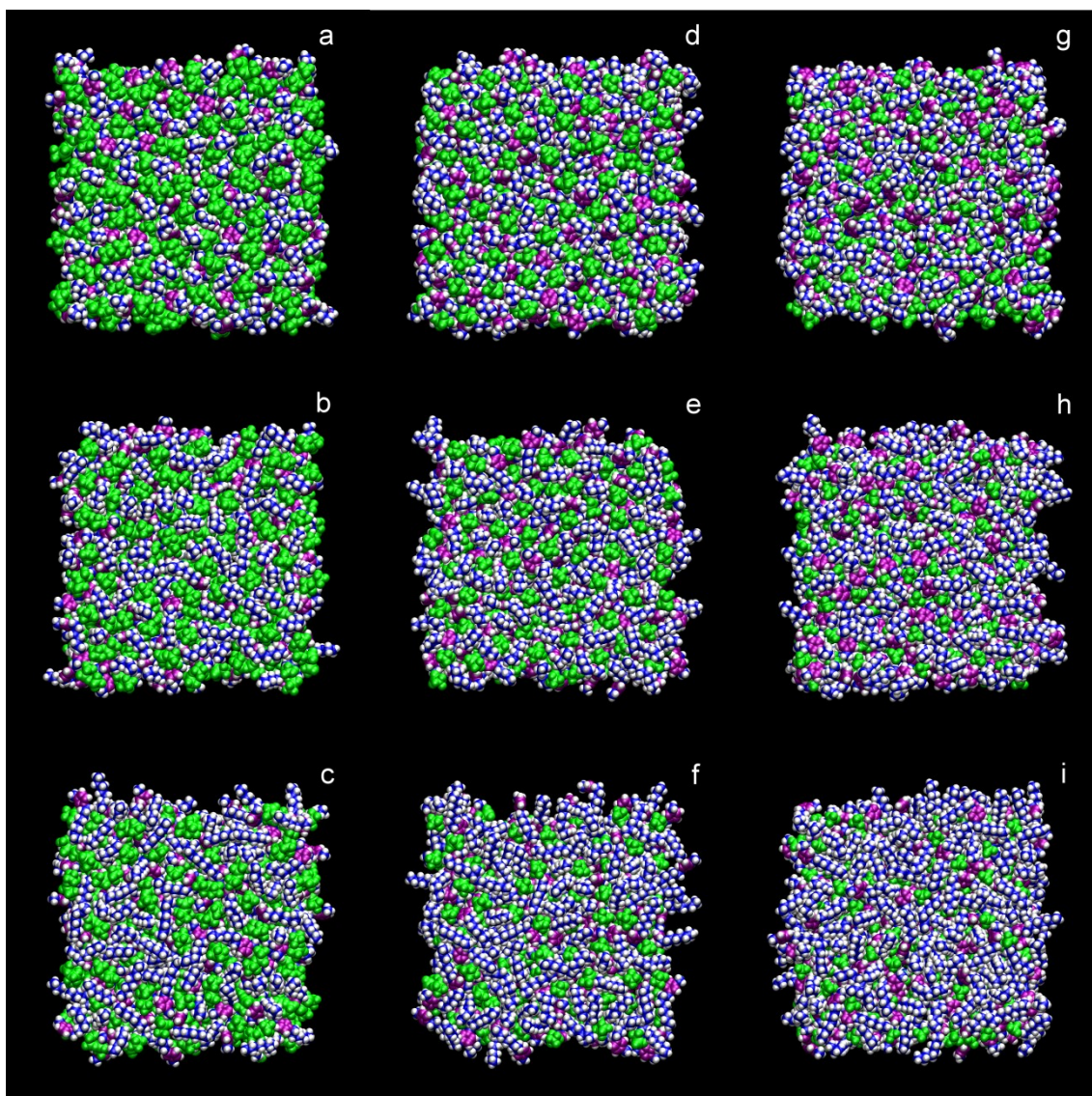


Figure 4.13. Snapshots looking down onto the liquid–vacuum interface of nine ionic liquids: (a) $[\text{C}_4\text{mim}][\text{Tf}_2\text{N}]$, (b) $[\text{C}_6\text{mim}][\text{Tf}_2\text{N}]$, (c) $[\text{C}_8\text{mim}][\text{Tf}_2\text{N}]$, (d) $[\text{C}_4\text{mim}][\text{OTf}]$, (e) $[\text{C}_6\text{mim}][\text{OTf}]$, (f) $[\text{C}_8\text{mim}][\text{OTf}]$, (g) $[\text{C}_4\text{mim}][\text{BF}_4]$, (h) $[\text{C}_6\text{mim}][\text{BF}_4]$, and (i) $[\text{C}_8\text{mim}][\text{BF}_4]$. All hydrogen atoms are shown in white. All atoms of the anion are shown in green. The carbon and nitrogen atoms of the imidazolium ring are shown in purple, while the carbon atoms of the alkyl and methyl substituents on the ring are shown in blue.

Returning to question 3), the alkyl coverage follows a clear trend with anion, being in the order $[\text{Tf}_2\text{N}]^- < [\text{OTf}]^- < [\text{BF}_4]^- \sim [\text{I}]^-$ for all chain lengths. This trend is opposite to that in anionic volumes, which follow the order $[\text{I}]^- \sim [\text{BF}_4]^- > [\text{OTf}]^- > [\text{Tf}_2\text{N}]^-$. A similar behaviour was observed by Kolbeck in an ARXPS study of $[\text{C}_8\text{mim}]^+$ ILs with different of anions [218]. The authors characterised the ratio between the signals from alkyl and ring C atoms, $C_{\text{alkyl}}/C_{\text{hetero}}$, using a detection angle of 80° (i.e. an information

depth of 1 – 1.5 nm). The alkyl fraction at the surface followed the order $[I]^- > [BF_4]^- \sim [OTf]^- > [Tf_2N]^-$, in general terms compatible with the RAS-LIF interfacial reactivities. However, $C_{\text{alkyl}}/C_{\text{hetero}}$ was almost equal for the last three ILs. In contrast, in RAS-LIF the differences are more marked, and the trend with anion is consistently the same for all chain lengths. It can be concluded that the surface-specific nature of the RAS-LIF technique enables it to determine alkyl coverage more precisely than in the ARXPS experiments.

Kolbeck proposed that the anion-dependence of the alkyl surface coverage is a consequence of the different anionic volumes. Underneath the alkyl overlayer, the polar groups (cation headgroups and anions) pack together. In order to maintain the electroneutrality of the interface, there must be as many anions as cations at the surface. Smaller anions allow the packing of more ion pairs in the polar layer and, as a consequence, there are more cationic alkyl chains in the outer layer. This simple picture agrees remarkably well with the results observed by ARXPS as well as RAS-LIF. In Figure 4.14, the effect of the anion has been isolated from the chain length effect by normalising the OH yields to $[BF_4]^-$ for each chain length. The normalised yields are plotted against the fraction of the molecular volume occupied by the anion, $V_{\text{anion}}/V_{\text{m}}$. V_{m} is the sum of the ionic volumes of cation and anion, $V_{\text{m}} = V_{\text{cation}} + V_{\text{anion}}$, where V_{cation} and V_{anion} are the van der Waals volumes of each individual ion determined from crystal structures [272]. For all chain lengths, a larger $V_{\text{anion}}/V_{\text{m}}$ value induces lower alkyl coverage. Moreover, the trend is very similar for all values of n with the exception of $n = 12$ (black symbols in Figure 4.14). The discrepancy for the longest chain could be the result of a different chain orientation or partial saturation of the surface, as discussed earlier.

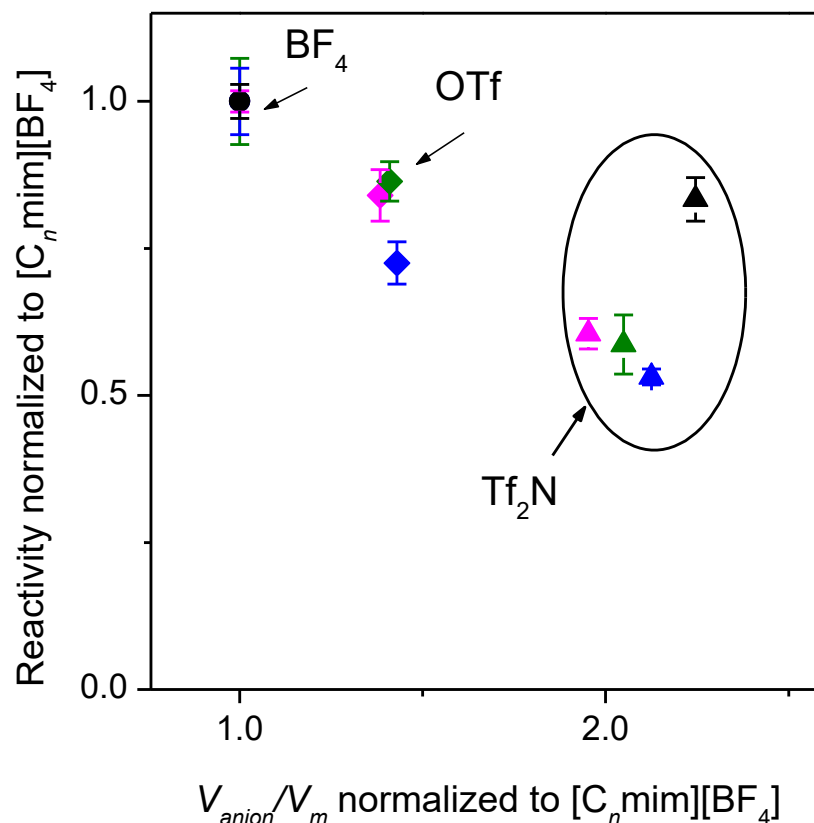


Figure 4.14. Correlation between interfacial reactivity and V_{anion}/V_m , normalised to $[C_n\text{mim}][BF_4]$. Colours indicate a common chain length: $[C_4\text{mim}]^+$ = magenta, $[C_6\text{mim}]^+$ = green, $[C_8\text{mim}]^+$ = blue, $[C_{12}\text{mim}]^+$ = black. Symbols indicate an anion type: $[Tf_2N]^-$ = triangles, $[OTf]^-$ = diamonds, $[BF_4]^-$ = circles.

Despite the correlation observed in Figure 4.14, it should not be interpreted as a consequence of the anion steric bulk exclusively. The interactions between cation and anion depend on other factors such as polarizability and H bond formation. Stronger cation-anion interactions induce closer packing at the surface, and thus greater alkyl coverage. Therefore, other anion-dependent empirical parameters could be used to rationalise the trend. It has been suggested [218] that Kamlet-Taft parameters might be better descriptors of the cation-anion interactions at the surface. These experimental parameters, employed to characterise solvent polarity, are classified into H bond acidity (α), H bond basicity (β), and polarizability effects (π^*) [273-275]. The parameter β is related to the ability of the solvent to donate electronic density in a hydrogen bond and, in ILs, it depends on the identity of the anion [276]. In a study of the IL bulk interaction, XPS binding energies and simulated charge distributions demonstrated that

charge transfer between ions was stronger for smaller anions [277]. The variation in charge transfer followed the trend in β better than the anionic volume. Despite this, the correlation with ionic volume observed here should not be disregarded. Larger anions are in general more polarisable, and smaller anions are more coordinating, hence both V_{anion} and β are good (and not independent) choices to describe the properties of the anions.

The simple scenario discussed above assumes that the cation and anion are situated at the same depth, but it is very possible that different anions are located preferentially at different surface depths. In simulations of IL cation-anion pairs, the anion identity influences its position relative to the cation [278, 279]. In solutions of ions in water, large and polarizable anions are present at the interface whereas small anions are excluded from it [280]. In molten LiCl, the Cl^- anions are closer to the interface than Li^+ [281]. It is very likely that a similar effect takes place in the imidazolium-based ILs studied here. Indeed, density profiles from the MD simulations presented here show that the F atoms in $[\text{BF}_4]^-$ are located close to the imidazolium ring, while those in $[\text{Tf}_2\text{N}]^-$ are further away from it and closer to the outer surface [270]. Other studies have found anions at different depths from the imidazolium rings [214, 236, 243], and $[\text{Tf}_2\text{N}]^-$ anions with their CF_3 groups oriented towards the surface [224, 226, 238, 239], in agreement with this result.

Effect of anion on the scattering dynamics

If the anions are exposed at the surface of the ionic liquids, they can potentially affect the dynamics of the interfacial reaction. The effect of anion identity on the energy of the scattered products can be seen in the T_{trans} and T_{rot} values in Figure 4.7. Although the uncertainty in the results is too large to confidently establish a definite trend (like in the $[\text{BF}_4]^-$ case discussed earlier, the temperatures are averages of only 3 spectra), there appears to be a weak decrease in T_{rot} with chain length independently of the anion identity. In addition, rotational temperatures are slightly lower for $[\text{BF}_4]^-$ than for other ILs. The OH translational energy appears to follow a similar trend, although in this case there is greater error in the results. The fact that the dynamics is anion-dependent further confirms that anions are present at the surface.

In the inelastic CO_2 scattering studies discussed above [36, 130], the product rotational excitation increased with anion size from $[\text{C}_n\text{mim}][\text{BF}_4]$ to $[\text{C}_n\text{mim}][\text{Tf}_2\text{N}]$. The authors explained this behaviour in terms of a greater surface mass for the larger, more exposed

$[\text{Tf}_2\text{N}]^-$ anions. As discussed earlier, the degree of thermalisation α increased with chain length. However, this effect was smaller for $[\text{C}_n\text{mim}][\text{Tf}_2\text{N}]$, suggesting that the larger $[\text{Tf}_2\text{N}]^-$ anions are located closer to the outer surface. This is consistent with the weaker increase in alkyl coverage for $[\text{Tf}_2\text{N}]^-$ seen in Figure 4.12.

Nesbitt and co-workers have also studied the inelastic scattering of NO radicals from $[\text{C}_4\text{mim}]^+$ ILs with $[\text{BF}_4]^-$, $[\text{Tf}_2\text{N}]^-$ and $[\text{Cl}]^-$ as the anions [132, 134]. In this case the rotational energy also increased with anion size, and there was evidence for thermal roughening of the $[\text{C}_4\text{mim}][\text{Tf}_2\text{N}]$ surface. Spin-orbit excitation of the NO radicals was observed, particularly at high collision energy (84 kJ mol^{-1}). The extent of electronic excitation increased with liquid temperature and depended on the anion identity, again indicating the presence of anions at the interface. In contrast, the OH spin-orbit ratios studied here did not show a clear dependence on the anion, being in all cases consistent with gas-phase reactions. It should however be noted that a careful characterisation of the spin-orbit ratios was beyond the scope of this study.

In the RAS-LIF results, the dependence of the dynamics on anion is not as clear as in the NO and CO_2 scattering experiments. However, the inelastic scattering experiments are more sensitive to the kinematics of the interfacial collision, since the molecular beams scattered from both polar and nonpolar groups, and the collision energies employed were relatively high. The RAS-LIF experiments, in contrast, might be more sensitive to effects such as surface roughness. It is possible that the lack of a clearly defined trend in T_{trans} and T_{rot} is the result of two opposite competing effects (kinematics and surface roughness) on the reactive scattering dynamics.

4.5. Summary points

- (1) RAS-LIF is a surface-sensitive and chemically specific analytical tool to characterise the alkyl surface coverage of imidazolium-based ionic liquids. It can distinguish and quantify small differences between liquids much better than other traditional techniques such as ARXPS.
- (2) RAS-LIF measurements of $[C_n\text{mim}][\text{BF}_4]$ ILs show that alkyl surface coverage increases with cation chain length in a nonstoichiometric way, and there is a preference for the nonpolar alkyl chains to occupy the surface. The results indicate that the surface is not saturated for $[C_8\text{mim}][\text{BF}_4]$ and $[C_{12}\text{mim}][\text{BF}_4]$, in contradiction to some previous measurements.
- (3) RAS-MS and MD results qualitatively agree with the RAS-LIF experiments. The quantitative differences can be explained from the differences between the techniques, such as collision energy, regioselectivity and angular resolution.
- (4) Alkyl surface enrichment depends on the identity of the anion in a way expected from its ionic volume, for $n < 12$. Alkyl surface enrichment is observed for all studied anions, not just $[\text{BF}_4]^-$. For $n = 12$, the dependence of alkyl coverage on anion identity is not so clear. This could be a result of the onset of saturation, or a different orientation of the alkyl chains at the surface.
- (5) The ability to characterise the alkyl coverage at a fine level of detail opens up the possibility of fine-tuning the nonpolar character of the surface by choosing the right pair of ions. The alkyl coverage of the studied ILs is correlated with their ionic volumes; but other possible causes, such as different orientations or surface depths of the ions, should not be disregarded.
- (6) The scattering dynamics are dominated by direct, IS-like encounters, proving that that the $O(^3P)$ atoms only probe the outer layer of the IL. The energy transfer is weakly dependent on the chain length and anion, reflecting the trends in alkyl coverage: more alkyl-covered surfaces produce more rotationally and translationally thermalized OH radicals.

Chapter 5.

Reactive O(³P) scattering from pure pyrrolidinium-based ionic liquids

5.1. Introduction

Ionic liquids based on the 1-alkyl-methylimidazolium cation, such as those studied in Chapter 4, are by far the most common type of ILs. However, the field of ionic liquid research has recently seen an increasing interest in other types of cations that provide different physicochemical properties. One such cation is 1-alkyl-1-methylpyrrolidinium ($[C_n\text{mpyrr}]^+$), which has many potential applications thanks to its wider electrochemical window and lower production costs [282]. Although pyrrolidinium-based IL surfaces have not been characterised as extensively as their imidazolium counterparts, there have been some recent reports in the literature. The surface composition of $[C_n\text{mpyrr}]^+$ ILs has been investigated by SFG [283], ARXPS [220, 221, 284], LEIS [240] and MD simulations [285]. This research showed that the alkyl groups on the cation preferentially protrude from the surface in a similar fashion to $[C_n\text{mim}]^+$ ILs. However, there have not been many direct comparisons of alkyl coverage between imidazolium and pyrrolidinium-based ionic liquids. The only example is a study by Lockett *et al.* [221], who characterised the surfaces of $[C_4\text{mpyrr}][\text{Tf}_2\text{N}]$ and $[C_4\text{mim}][\text{Tf}_2\text{N}]$ by synchrotron XPS at variable photon energies.

This chapter expands on the previous one, using RAS-LIF to characterise the surfaces of $[C_n\text{mpyrr}][\text{Tf}_2\text{N}]$ ionic liquids of chain lengths $n = 2, 4, 6, 8$ and 12 ; as well as the equivalent $[C_n\text{mim}][\text{Tf}_2\text{N}]$ surfaces. The alkyl coverage of pyrrolidinium will be compared against imidazolium ILs in order to unravel the effect of the cation headgroup on the surface structure. As in the previous chapter, squalane will be used as a reference liquid. The chemical structures of $[C_n\text{mpyrr}][\text{Tf}_2\text{N}]$ and $[C_n\text{mim}][\text{Tf}_2\text{N}]$ ILs, as well as squalane, are presented in Figure 5.1.

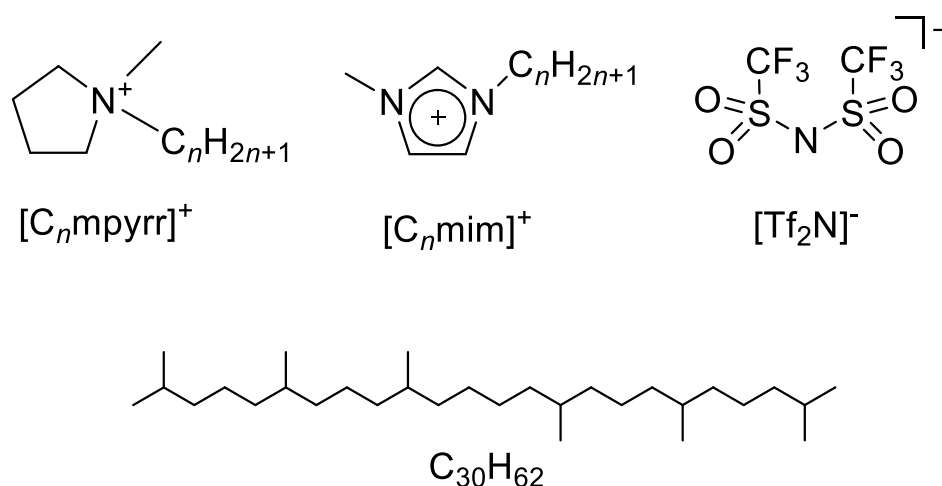


Figure 5.1. Chemical structures of the 1-alkyl-1-methylpyrrolidinium cation ($[C_nmpyrr]^+$), 1-alkyl-3-methylimidazolium cation ($[C_nmim]^+$), bis(trifluoromethylsulfonyl)imide anion ($[Tf_2N]^-$) and squalane ($C_{30}H_{62}$).

Looking at the chemical structures in Figure 5.1, it is evident that the reactivity of the two different headgroups towards H abstraction by relatively low-energy $O(^3P)$ atoms will not be the same, and this will affect the RAS-LIF results. As discussed in Chapter 4, the H atoms in the imidazolium ring are aromatic and therefore highly unlikely to be abstracted by the $O(^3P)$ atoms in RAS-LIF, which have an average kinetic energy of 16 kJ mol^{-1} . The hydrogen atoms in the pyrrolidinium headgroup are not aromatic, so they are expected to be abstractable by the oxygen atoms. In order to quantify the differences, the bond dissociation energies (BDEs) of the different C–H bonds in imidazolium and pyrrolidinium have been calculated using a composite method with a Gaussian 4 (G4) level of theory. The calculations were carried out in the University of York by John Slattery, using an alkyl chain length $n = 4$ on both the imidazolium and pyrrolidinium cations. The BDEs, listed in Table 5.1, are not a direct measure of the reactivity (the barriers for reaction should be used instead), but they provide some useful information. The most important result is that the imidazolium ring C–H bonds are much stronger than the pyrrolidinium bonds (a minimum of 515 kJ mol^{-1} in contrast to a maximum of 411 kJ mol^{-1} , respectively). The detailed differences between the two cations will be discussed in Section 5.4.

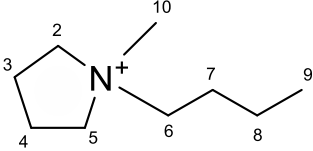
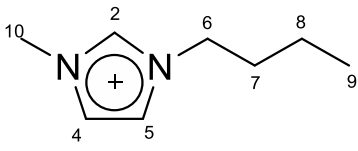
|  | |  | |
|---|----------------------------|---|----------------------------|
| C – H site | BDE / kJ mol ⁻¹ | C – H site | BDE / kJ mol ⁻¹ |
| C _(2,5) – H | 411 | C ₍₂₎ – H | 518 |
| C _(3,4) – H | 399 | C ₍₄₎ – H | 515 |
| C ₍₆₎ – H | 418 | C ₍₅₎ – H | 515 |
| C ₍₇₎ – H | 401 | C ₍₆₎ – H | 393 |
| C ₍₈₎ – H | 405 | C ₍₇₎ – H | 409 |
| C ₍₉₎ – H | 416 | C ₍₈₎ – H | 404 |
| C ₍₁₀₎ – H | 432 | C ₍₉₎ – H | 416 |
| | | C ₍₁₀₎ – H | 405 |

Table 5.1. Calculated (G4) bond dissociation energies for each of the C–H bonds in [C₄mpyrr][Tf₂N] and [C₄mim][Tf₂N], from the reaction [C₄mpyrr]⁺ → [C₄mpyrr]^{•+} + H[•] at 298 K.

5.2. Experimental

The experiments were performed in the 4-wheel apparatus described in Section 2.2.2. A series of calibration measurements were performed to ensure that all four wheels were comparable to each other and gave results compatible with the 1-wheel experiment. The following sections provide details on this calibration, as well as the ionic liquids studied in this chapter.

5.2.1. Liquids studied and experimental conditions

The ionic liquids studied, their purity and content of water are listed in Table 5.2. Some of the ILs were purchased from commercial suppliers, while others were provided by collaborators in the University of York. The identity and purity of the ILs was confirmed independently by ¹H-NMR spectroscopy. The York ILs were synthesized under dry conditions, so their water content is expected to be minimal. The handling of

ILs and the data acquisition conditions were almost identical to those in Chapter 4. When several liquids were studied together, they were loaded simultaneously into the reaction chamber under a gentle flow of dry N_2 in order to avoid contamination with water. The main difference with Chapter 4, besides the multiple-wheel assembly, was the geometry of the probe beam: instead of a rectangular sheet propagating 6 mm above the surface, a round beam at 7 mm from the surface was used. This beam had a diameter of 4 mm.

Most of the liquid surfaces in this chapter were studied at room temperature; however, ILs that are solid at room temperature were heated above their melting point for the measurements (the temperature of the external circulator is quoted in Table 5.2). The reference liquid was studied at the same temperature as the corresponding IL. The reference was squalane in most cases, except for $[C_2\text{mpyrr}][\text{Tf}_2\text{N}]$ and $[C_2\text{mim}][\text{Tf}_2\text{N}]$, which were measured against $[C_{12}\text{mim}][\text{Tf}_2\text{N}]$ because squalane evaporated significantly at the temperature used.

Pyrrolidinium and imidazolium ILs of the same chain length were studied simultaneously to make them as directly comparable as possible. Appearance profiles were acquired with $[C_n\text{mim}][\text{Tf}_2\text{N}]$ and $[C_n\text{mpyrr}][\text{Tf}_2\text{N}]$ in opposite baths, with the reference liquid bath placed at 90° to both of them. The approach was different for $n = 2$: these ILs did not produce any OH above the detection limit of RAS-LIF, but there was a small contribution from the adjacent reference wheel. In order to avoid this, the $n = 2$ ILs were studied in two separate sets with the reference wheel placed at 180° to the IL wheel.

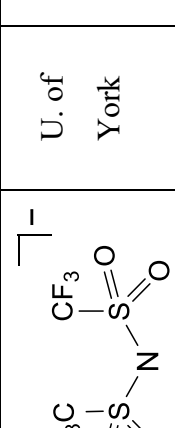
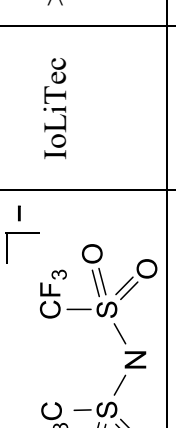
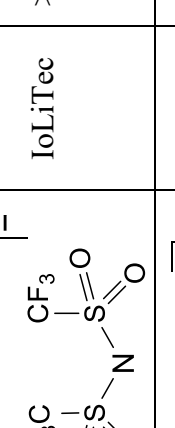
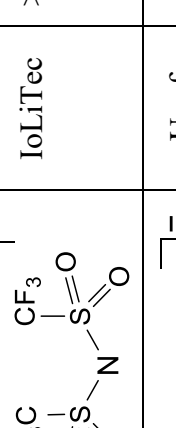
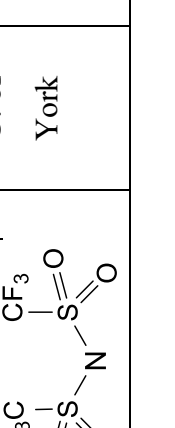
| Name and abbreviation | Structure | Supplier | Purity | [H ₂ O] | Temperature |
|--|--|---------------|--------|--------------------|-------------|
| [C ₂ mim][Tf ₂ N] 1-ethyl-3-methylimidazolium bis(trifluoromethylsulfonyl)imide |  | U. of York | | | 120 °C |
| [C ₄ mim][Tf ₂ N] 1-butyl-3-methylimidazolium bis(trifluoromethylsulfonyl)imide |  | IoLiTec | >99% | 30 ppm | r.t. |
| [C ₆ mim][Tf ₂ N] 1-hexyl-3-methylimidazolium bis(trifluoromethylsulfonyl)imide |  | IoLiTec | >99% | 70 ppm | r.t. |
| [C ₈ mim][Tf ₂ N] 1-octyl-3-methylimidazolium bis(trifluoromethylsulfonyl)imide |  | IoLiTec | >99% | 53 ppm | r.t. |
| [C ₁₂ mim][Tf ₂ N] 1-dodecyl-3-methylimidazolium bis(trifluoromethylsulfonyl)imide |  | U. of York | | | 50 °C |

Table 5.2. Ionic liquids studied and temperature of the measurements (r.t. stands for room temperature). Purity and water content are those stated by the supplier.

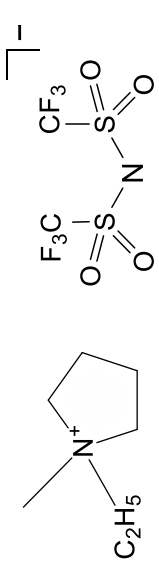
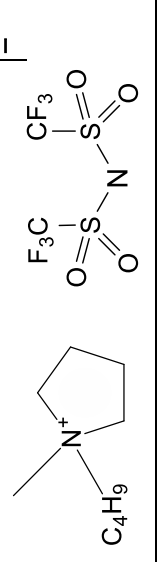
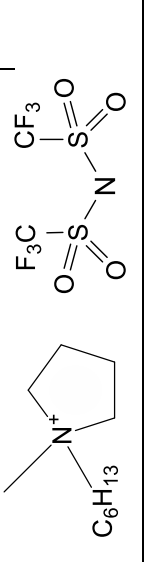
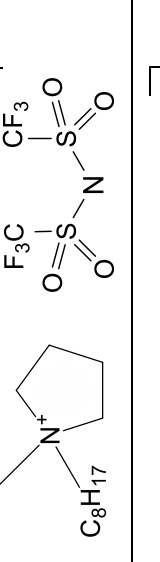
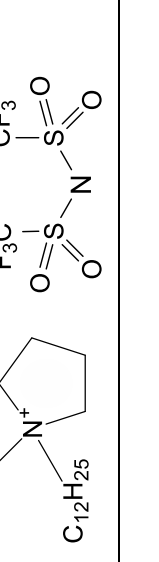
| Name and abbreviation | Structure | Supplier | Purity | [H ₂ O] | Temperature |
|--|--|---------------|--------|--------------------|-------------|
| [C ₂ mpyrr][Tf ₂ N] 1-ethyl-1-methylpyrrolidinium bis(trifluoromethylsulfonyl)imide |  | IoLiTec | >99% | 390 ppm | 120 °C |
| [C ₄ mpyrr][Tf ₂ N] 1-butyl-1-methylpyrrolidinium bis(trifluoromethylsulfonyl)imide |  | IoLiTec | >99% | 41 ppm | r.t. |
| [C ₆ mpyrr][Tf ₂ N] 1-hexyl-1-methylpyrrolidinium bis(trifluoromethylsulfonyl)imide |  | IoLiTec | >99% | 80 ppm | r.t. |
| [C ₈ mpyrr][Tf ₂ N] 1-methyl-1-octylpyrrolidinium bis(trifluoromethylsulfonyl)imide |  | U. of York | | | r.t. |
| [C ₁₂ mpyrr][Tf ₂ N] 1-dodecyl-1-methylpyrrolidinium bis(trifluoromethylsulfonyl)imide |  | U. of York | | | 50 °C |

Table 5.2 (contd.). Ionic liquids studied and temperature of the measurements (r.t. stands for room temperature). Purity and water content are those stated by the supplier.

5.2.2. Setting up and calibration of the 4-wheel apparatus

Wheel distances and angles

The bath assembly has been described in Chapter 2 (see Figure 2.4). The volume of the liquid baths was reduced to 3-5 mL with stainless steel spacers, placed under and in front of the wheel. Stainless steel blades were occasionally used as surface scrapers, especially with viscous liquid samples, to achieve similar thicknesses of the liquid films. The main source of irreproducibility between wheels was expected to be their Z distance (i.e. the distance to the laser axis) and angle. For this reason, the distances and angles were measured and set precisely before each set of experiments.

The angle of the bath assembly was optimised for each wheel so that its surface was parallel to the laser axis passing through the centre of the chamber arms. The wheel angle was established using a HeNe laser beam, aligned through baffles with 1 mm-diameter orifices placed inside the arms. The beam was translated horizontally towards the wheel whilst rotating the assembly around the vertical axis so that the wheel surface was parallel to the beam. This procedure was repeated several times for each wheel to obtain angles with a precision of 0.1° . In practice, the results of the experiments did not change significantly with variations in angle smaller than 1° . This was verified by acquiring appearance profiles at angles different from the parallel configuration (see Section 2.6.1 or the preceding two chapters for details on the acquisition of appearance profiles). The profiles, shown in Figure 5.2, do not vary significantly for a deviation of 1° . In contrast, deviations of 2° or 3° show considerable discrepancies from the parallel profiles.

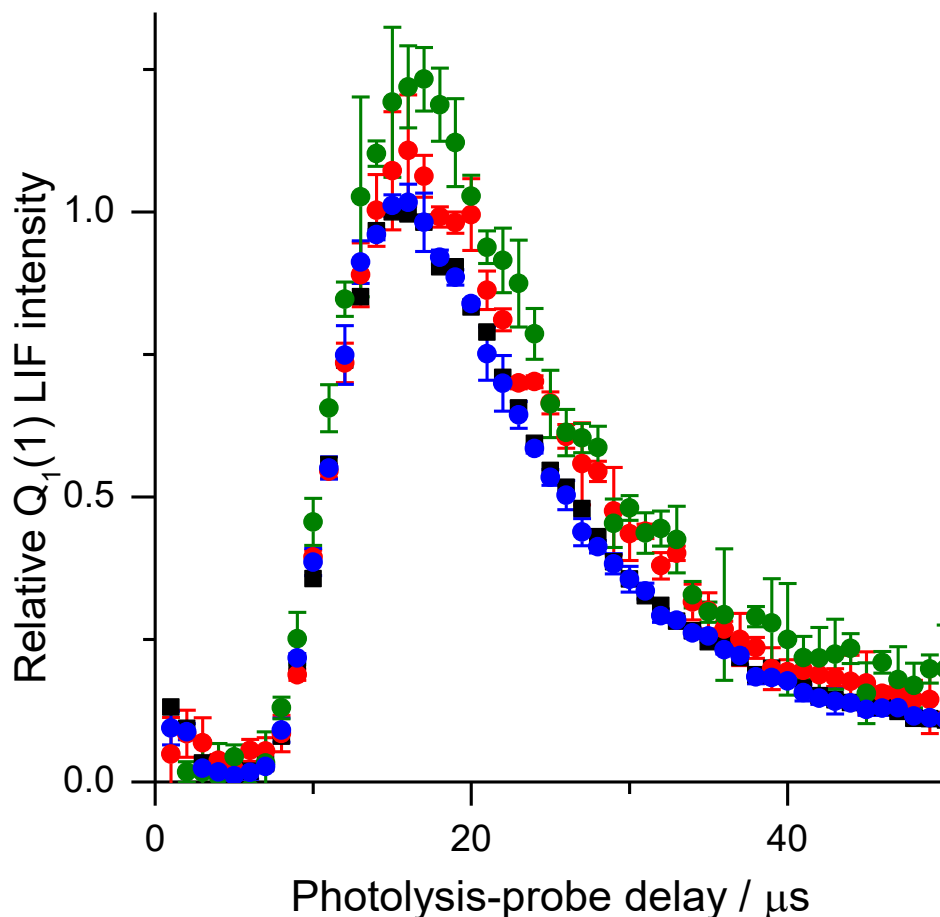


Figure 5.2. $Q_1(1)$ OH appearance profiles recorded from squalane with the probe laser (4 mm in diameter) propagating at 7 mm from the liquid surface. Profiles were recorded with the beam parallel to the surface (black squares), and at angles of 1° (blue circles), 2° (red circles) and 3° (green circles) from it. The profiles are scaled relative to the peak signal in the parallel configuration, and are an average of 4 consecutive measurements with error bars of $\pm 1\sigma$ standard error of the mean.

The wheel-to-beam distance varied slightly between wheels due to small differences in axle lengths and positions. Equivalent distances were achieved by placing stainless steel washers of different thicknesses between the wheels and their axles. The corrected distances were equal within $100\ \mu\text{m}$, and the resulting common wheel-to-beam distance was typically between 6.5 and 7 mm.

The reproducibility between wheels was tested with measurements of the same liquid sample in all baths. The calibration was performed with squalane because it produces a high yield of OH radicals, and it had previously been characterised extensively. $Q_1(1)$

appearance profiles recorded from different wheels do not show significant differences (Figure 5.3), confirming that the wheel distances and angles were sufficiently similar to each other for reliable comparative measurements to be made between non-equivalent liquids.

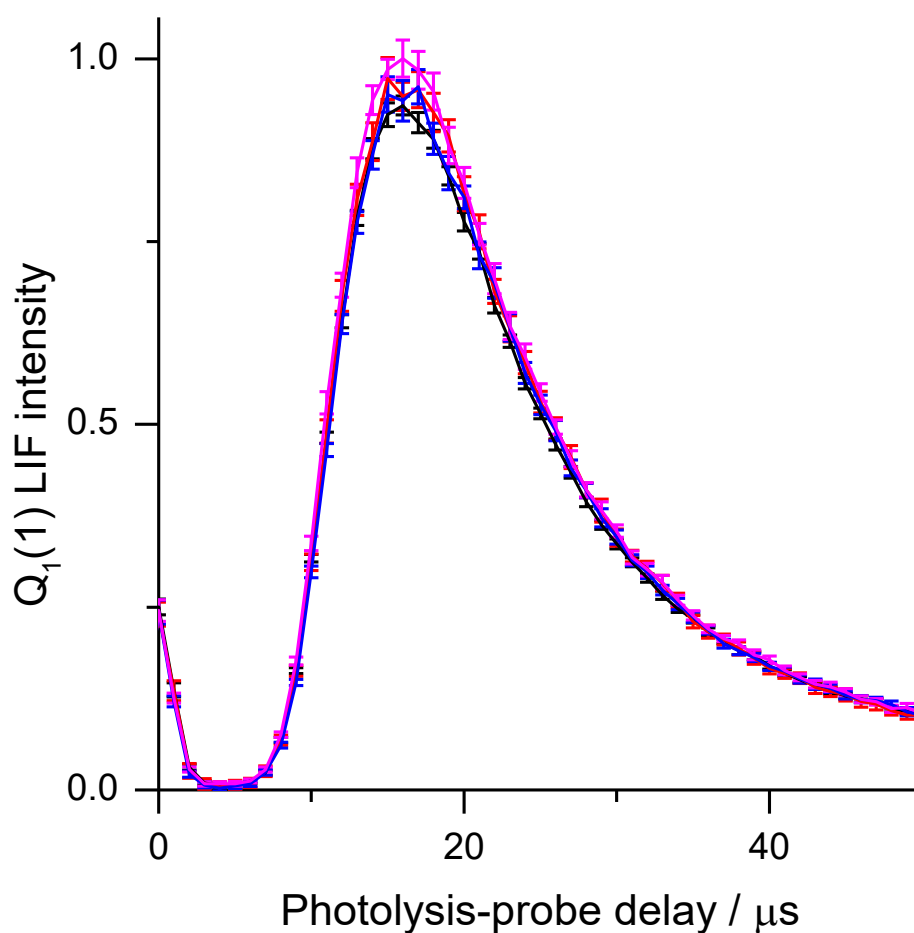


Figure 5.3. OH $Q_1(1)$ appearance profiles from squalane, acquired sequentially from each of the four wheels in the 4-wheel apparatus. Lines of different colours (black, red, blue and magenta) correspond to different wheels. Error bars represent $\pm 1\sigma$ standard error of the mean. The HONO background has not been subtracted from the profiles.

Although the ILs in this chapter were studied in a different reaction chamber, the liquid surfaces, O(³P) generation and detection systems were identical to the approach described in Chapter 4. The main difference was that in the single-wheel experiments the probe beam was expanded into a sheet, while the multi-wheel apparatus employed a round probe beam. The wheel-to-beam distance varied as well: 6 mm in the single-wheel setup and 7 mm in this chapter. However, using squalane as a reference should minimise the effect of these discrepancies so that both setups provide comparable results. This was verified by measuring the same liquid in both chambers. Q₁(1) appearance profiles were recorded for [C₄mim][BF₄], [C₈mim][BF₄] and squalane in both reaction chambers, one year apart (see Table 4.2 for chemical names and structures of these ILs). The results (Figure 5.4) show very similar signal intensities relative to squalane for the same IL, with the expected difference in arrival times caused by the slightly different wheel-laser axis distances employed. Integrating the intensity of the appearance profiles and performing a density-to-flux conversion (details in Section 5.3.3) yielded the relative OH yields listed in Table 5.3. Despite the differences in wheel distances, beam shapes and sizes, there is very reasonable agreement between the values. The results differ slightly beyond the estimated statistical error limits for [C₄mim][BF₄], possibly due to the fact that the HONO background was not subtracted from the multi-wheel result.

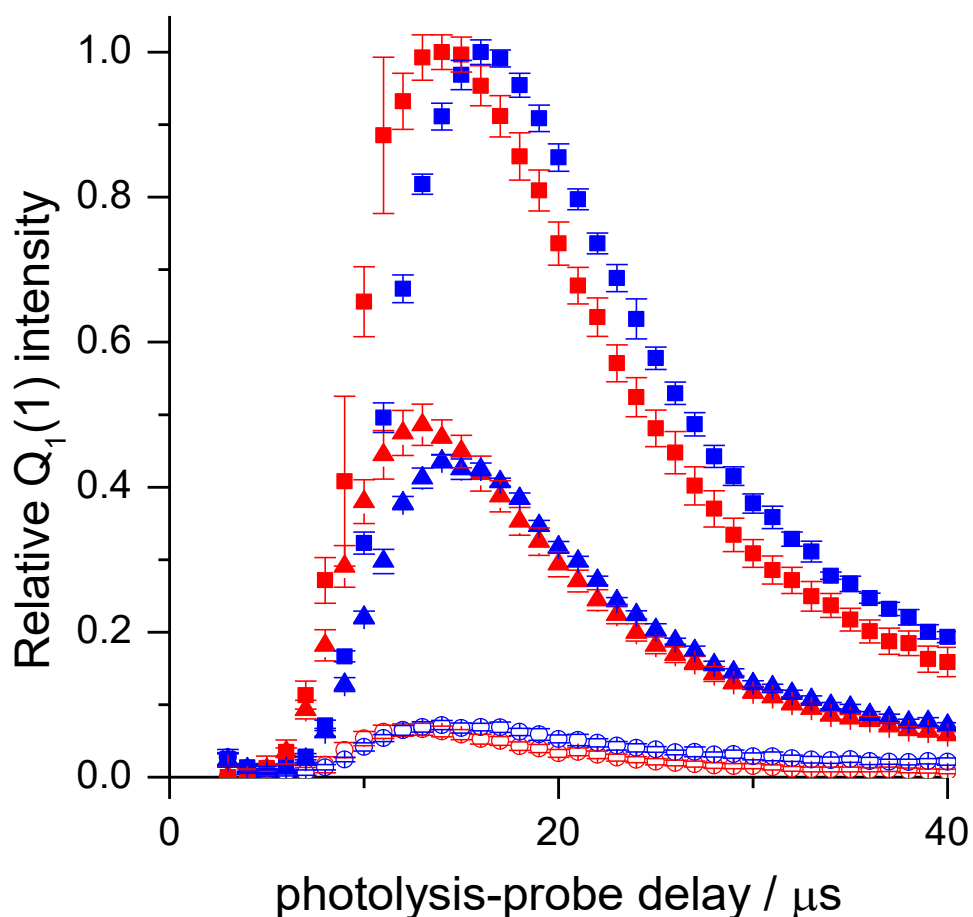


Figure 5.4. OH $Q_1(1)$ appearance profiles acquired in the 1-wheel experiment (red symbols) and the 4-wheel experiment (blue symbols), from $[C_4mim][BF_4]$ (blank squares), $[C_8mim][BF_4]$ (filled triangles) and squalane (filled squares). The results are an average of 14 profiles acquired in two sets, normalised to the peak signal from squalane. Error bars represent $\pm 1\sigma$ standard error of the mean.

| | $[C_4mim][BF_4]$ | $[C_8mim][BF_4]$ |
|--------------------|-------------------|-------------------|
| 1-wheel experiment | 0.062 ± 0.004 | 0.514 ± 0.052 |
| 4-wheel experiment | 0.085 ± 0.013 | 0.480 ± 0.042 |

Table 5.3. Integrated OH flux, relative to squalane, obtained from the appearance profiles in Figure 5.4. Errors are $\pm 1\sigma$ standard error of the mean

Effect of the reference bath on the neighbouring ionic liquid wheels

The use of squalane as a reference liquid has many advantages but also some disadvantages. Namely, bath temperatures above 80 °C resulted in significant evaporation of squalane. Even at room temperature, there was always a small concentration of squalane in the gas phase due to its nonzero (higher than the ILs') vapour pressure. This brings up the possibility of cross-contamination between samples. Squalane is not miscible with most ILs, so it is not expected to be absorbed by them. However, due its nonpolar character, it could potentially be a surface-active impurity. A test was carried out by deliberately contaminating a sample of $[C_4\text{mpyrr}][\text{Tf}_2\text{N}]$ with 1% mol squalane. $Q_1(1)$ OH appearance profiles were practically identical for the “clean” and “contaminated” IL samples, corroborating that contamination by small concentrations of hydrocarbon does not have a measurable effect on the results.

The use of squalane and other liquids with high surface concentrations of hydrocarbon did however slightly affect the measurements of the samples in the adjacent baths at 90° to it, especially when such samples had a low hydrocarbon surface coverage. In the appearance profiles, a “tail” of slow OH radicals appeared at delays $> 30 \mu\text{s}$ whenever the neighbouring bath contained squalane. In order to characterise the effect of this unwanted signal in the results, appearance profiles were acquired without a wheel in the bath exposed to the beam, keeping the squalane wheel at 90° from it. This eliminated any reactive and inelastic OH scattering on the wheel surface, leaving only the contribution from squalane. An example is shown in Figure 5.5, where the LIF signal is scaled to the peak signal of the reference squalane profile to show the relatively minor contribution of the OH tail. There is an early OH signal from HONO photolysis, most of which decays without returning to the probe beam due to the absence of the wheel, although a small fraction could be scattered from the liquid bath. The reactive OH signal from squalane starts to rise at 20 μs , and peaks at 40 μs at a value of 4% of the reference squalane profile. Due to its relatively low intensity and late appearance, it is not expected to have a significant effect for most of the ILs measured here, with the exception of the $n = 2$ ILs, as discussed in Section 5.2.1. In this particular case, the reference liquid $[C_{12}\text{mim}][\text{Tf}_2\text{N}]$ was used instead of squalane, but it also caused a noticeable “tail” in the profiles due to its high reactivity. For this reason the $[C_2\text{mim}][\text{Tf}_2\text{N}]$ and $[C_2\text{mpyrr}][\text{Tf}_2\text{N}]$ samples were studied in separate datasets, with the

reference wheel at 180° to the IL wheel. This effectively eliminated the spurious contribution at later times.

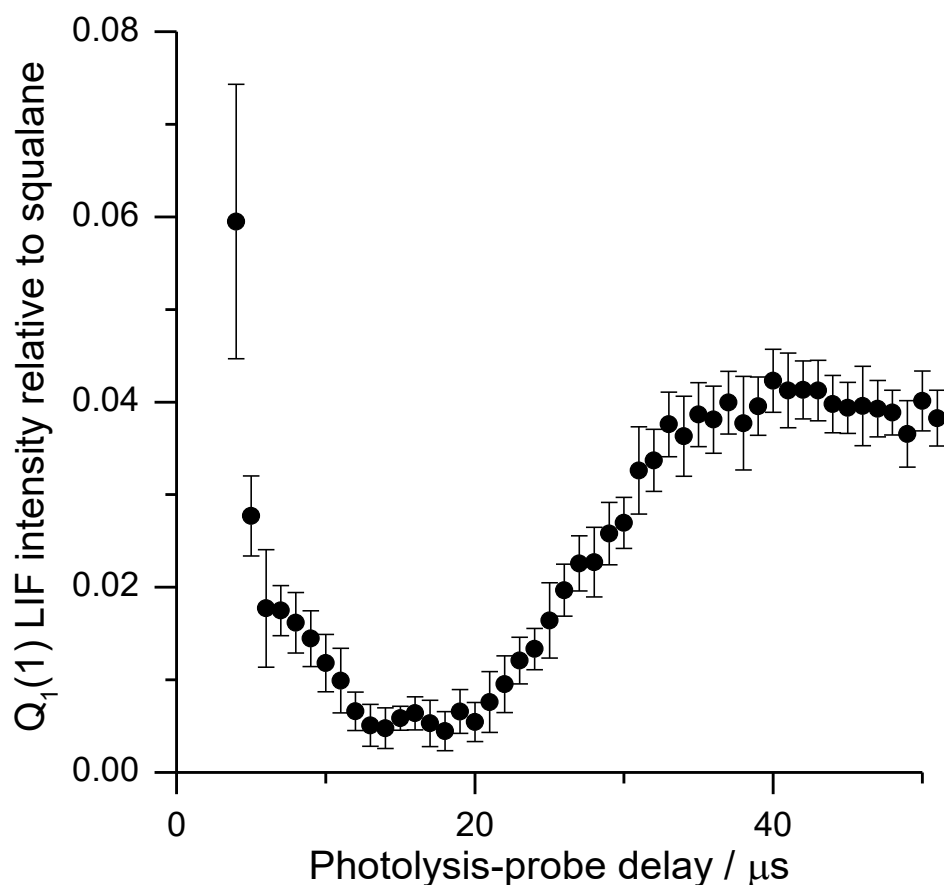


Figure 5.5. Appearance profile recorded without a liquid surface to illustrate the effect of the adjacent squalane wheel, as described in the text. The data points are an average of 10 measurements ($\pm 1\sigma$ standard error of the mean) and are scaled to the peak LIF signal in the squalane reference measurement.

Temperature control

The temperature control system in the 4-wheel assembly was tested and calibrated. Heating fluid circulated through 4 blocks of copper to which the baths were attached. After setting the temperature in the circulator, the time required to achieve a constant temperature of the liquid sample was approximately 1 hour. There was a small temperature gradient between the circulator, the stainless steel bath and the liquid. The

relationship between these temperatures was characterised by measurements under vacuum. A simultaneous comparison between baths was also carried out to confirm that the temperature was not significantly different between them. Thermocouple probes were attached to each of the copper heaters and immersed into the liquid baths. With the exception of very high temperatures (120 °C), the temperature of the heaters was always within 10 °C below the circulator temperature, and the liquid surface was ≤ 5 °C below the heater temperature. Due to the difficulty of measuring the surface temperature during the scattering experiments, the value in the external circulator is quoted instead in this chapter. An estimate of the liquid temperature for a range of circulator temperatures, obtained from the calibration, is given in Table 5.4. An error of ± 1.5 K should be considered to account for systematic bias of the thermocouple probe.

| Circulator setting / °C | Estimated liquid T / °C |
|-------------------------|-------------------------|
| 22 | 22 |
| 30 | 29 |
| 35 | 33.2 |
| 40 | 37.6 |
| 45 | 41.9 |
| 50 | 45.8 |
| 55 | 50 |
| 120 | 95 |

Table 5.4. Temperature of the liquid surface for each circulator temperature, estimated from the calibration of the 4-wheel assembly.

5.3. Results

5.3.1. Effect of surface temperature on OH yields

As noted above (Table 5.2), some of the ionic liquids were studied above room temperature. When comparing OH yields, the underlying assumption is that the reactivity of all liquids behaves in a similar fashion with temperature, and that there are not any dramatic changes in the liquid surface structure in the range of 25 – 95 °C. This has been shown to be the case in previous studies with squalane: in analogous $O(^3P)$ reactive scattering experiments, the yield of OH ($v' = 0$) was found to increase only very slightly between surface temperatures of -10 °C and 90 °C [6]. Any dynamical effect of temperature on the yield is expected to be similar for the ILs, since the H abstraction from hydrocarbon sites is analogous to the squalane reaction; however, there could be other temperature-dependent effects on reactivity induced by surface structure. Previous RAS-LIF measurements of $[C_{12}mim][Tf_2N]$ showed no significant variation in the temperature range between 25 °C and 70 °C, which suggests that the surface structure of long-chain ILs is not very temperature-dependent [11]. Of course, the effect could potentially be different depending on the IL. Short-chain ILs, where polar interactions play a more important role in surface ordering (as opposed to the nonpolar interactions present in long-chain liquids), could behave differently. For this reason, further RAS-LIF measurements were carried out at different temperatures with a shorter-chain IL. Due to time constraints, it was not possible to characterise thoroughly the temperature effect for all of the studied liquids. $[C_6mpyrr][Tf_2N]$ was chosen as a representative example and studied at temperatures from 23 to 70 °C. The measured OH appearance profiles, presented in Figure 5.6, were not significantly different from each other.

Since all of the liquids for which the temperature dependence has been investigated present effectively the same interfacial reactivity independently of the temperature, it has been assumed that this holds true for all of the ILs studied in this chapter. Although a temperature effect for some ILs cannot be ruled out categorically, the assumption is believed to hold true for most of the liquids. As will be discussed later, there is no previous evidence in the literature for a dramatic change in IL surface structure in the small range of temperatures employed here.

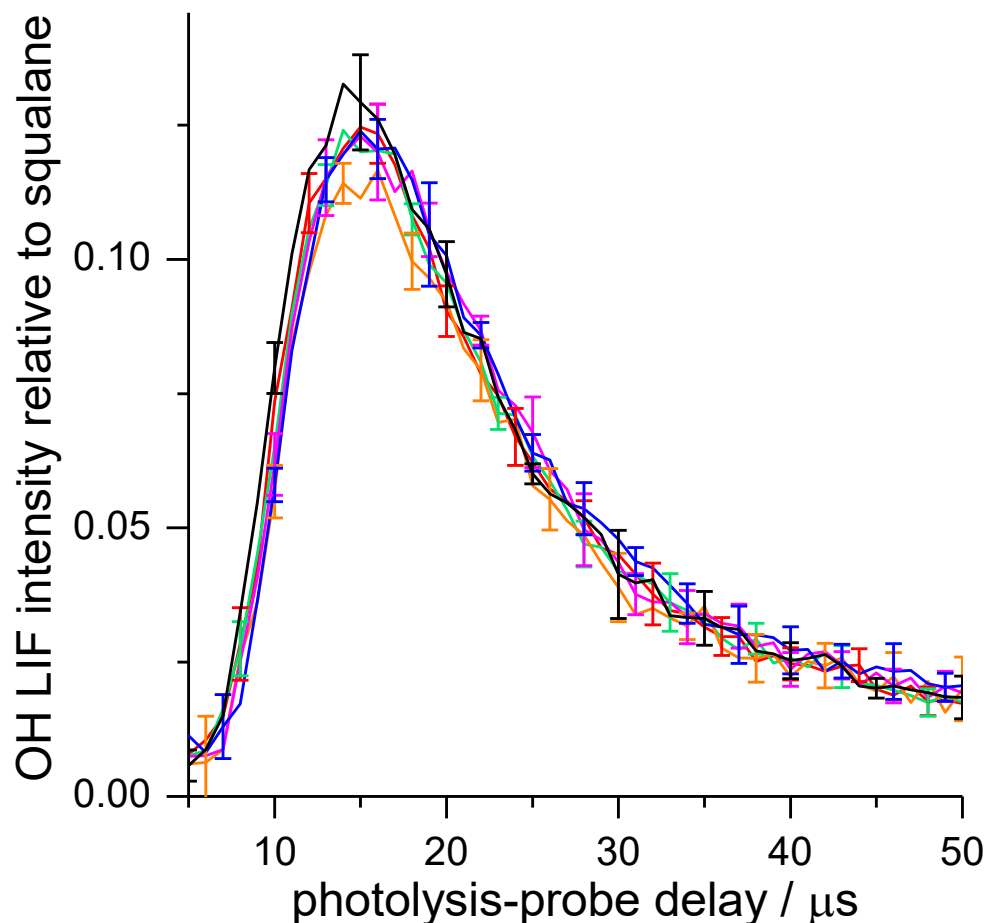


Figure 5.6. $Q_1(1)$ OH appearance profiles from $[C_6\text{mpyrr}][\text{Tf}_2\text{N}]$, acquired at 23 °C (black), 30 °C (red), 40 °C (green), 50 °C (orange), 60 °C (magenta) and 70 °C (blue). The profiles are an average of 5 consecutive measurements and have not been corrected for their HONO background. Some error bars are omitted for clarity.

5.3.2. Excitation spectra

LIF excitation spectra were acquired from each liquid at a photolysis-probe delay of 15 μs , at which the maximum OH LIF intensity is detected. $[C_2\text{mpyrr}][\text{Tf}_2\text{N}]$ and $[C_2\text{mim}][\text{Tf}_2\text{N}]$ did not produce any measurable OH yield so they are excluded from this analysis. For each spectrum, the populations of the $N' = 1 - 5$ levels were obtained by fitting the Q_1 branch to a LIFBASE simulation. The Q_1 populations were fitted to single-temperature Boltzmann distributions (Section 2.6.2). Five independent spectra were recorded from each liquid, and the Boltzmann temperatures were averaged to give a rotational temperature T_{rot} for each of the liquids. The average T_{rot} values are presented in Figure 5.7.

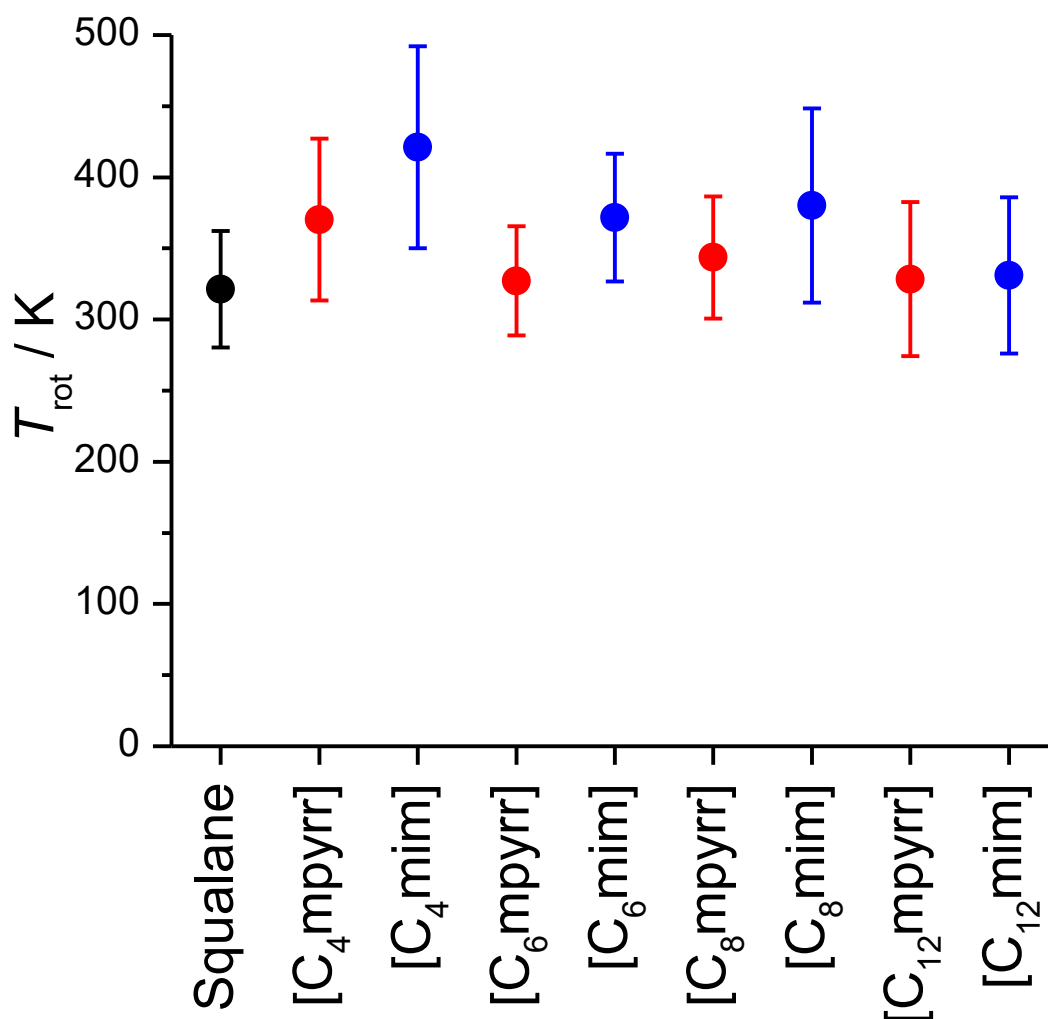


Figure 5.7. OH Q_1 -branch rotational temperatures T_{rot} from squalane, $[C_n\text{mpyrr}][\text{Tf}_2\text{N}]$ and $[C_n\text{mim}][\text{Tf}_2\text{N}]$ (cations along the horizontal axis). Each is an average of 5 independently acquired temperatures. Error bars represent $\pm 1\sigma$ standard error of the mean.

As in the previous chapter, the rotational temperatures are similar for all of the liquids studied. Although some trends can be discerned (longer chains and $[C_n\text{mpyrr}]^+$ cations give systematically slightly lower T_{rot}), the error in the measurements is too large to assert them confidently. Nevertheless, it should be considered that a significant variation in T_{rot} can affect the OH yields measured in Section 5.3.3, since the contribution of $N' = 1$ to the total population would vary between liquids. As an example, the measured OH fluxes from $Q_1(1)$ appearance profiles of $[C_4\text{mim}][\text{Tf}_2\text{N}]$

(highest T_{rot}) and $[\text{C}_{12}\text{mpyrr}][\text{Tf}_2\text{N}]$ (lowest T_{rot}) are in a ratio of 0.084:1. However, if they are corrected to account for their rotational distributions, the ratio is 0.099:1. The OH fluxes in the next section have not been corrected, as the T_{rot} values have large statistical uncertainties which were considered to outweigh the benefit of the smaller systematic correction, but it should be considered when interpreting the results below.

5.3.3. Appearance profiles

The alkyl surface coverage was characterised through the integrated OH flux from the $\text{Q}_1(1)$ appearance profiles, following the same approach as in Chapter 4. OH appearance profiles were recorded on the most intense spectral transition, converted into fluxes and integrated to obtain relative IL:squalane OH yields. The appearance profiles were acquired sequentially in sets of five. At least six of these datasets were recorded from each liquid, measuring the reference liquid immediately after each set by rotating the wheel assembly. The new multi-wheel assembly greatly improved the efficiency of the measurements over the previous single-wheel arrangement. The photolysis and probe laser backgrounds were characterised and subtracted independently for each set of profiles. HONO background measurements were carried out as described in Chapter 4, and subtracted from the data by scaling them to the 1- μs signal of the NO_2 profiles. The average background-subtracted appearance profile from each IL dataset was scaled to the peak signal of the corresponding squalane profile. Finally, all datasets from the same liquid were averaged together.

The approach was slightly different for the ionic liquids with $n = 2$. As noted earlier, the reference liquid for both ILs was $[\text{C}_{12}\text{mim}][\text{Tf}_2\text{N}]$. Each averaged and background-subtracted set of appearance profiles was normalised to the peak signal from $[\text{C}_{12}\text{mim}][\text{Tf}_2\text{N}]$, and multiplied by the $[\text{C}_{12}\text{mim}][\text{Tf}_2\text{N}]:\text{Squalane}$ OH flux ratio obtained previously (0.48, see Table 5.5). Average appearance profiles for all of the ILs studied are presented in Figure 5.8. As shown in the figure, practically no OH radicals were detected for both $[\text{C}_2\text{mpyrr}][\text{Tf}_2\text{N}]$ and $[\text{C}_2\text{mim}][\text{Tf}_2\text{N}]$.

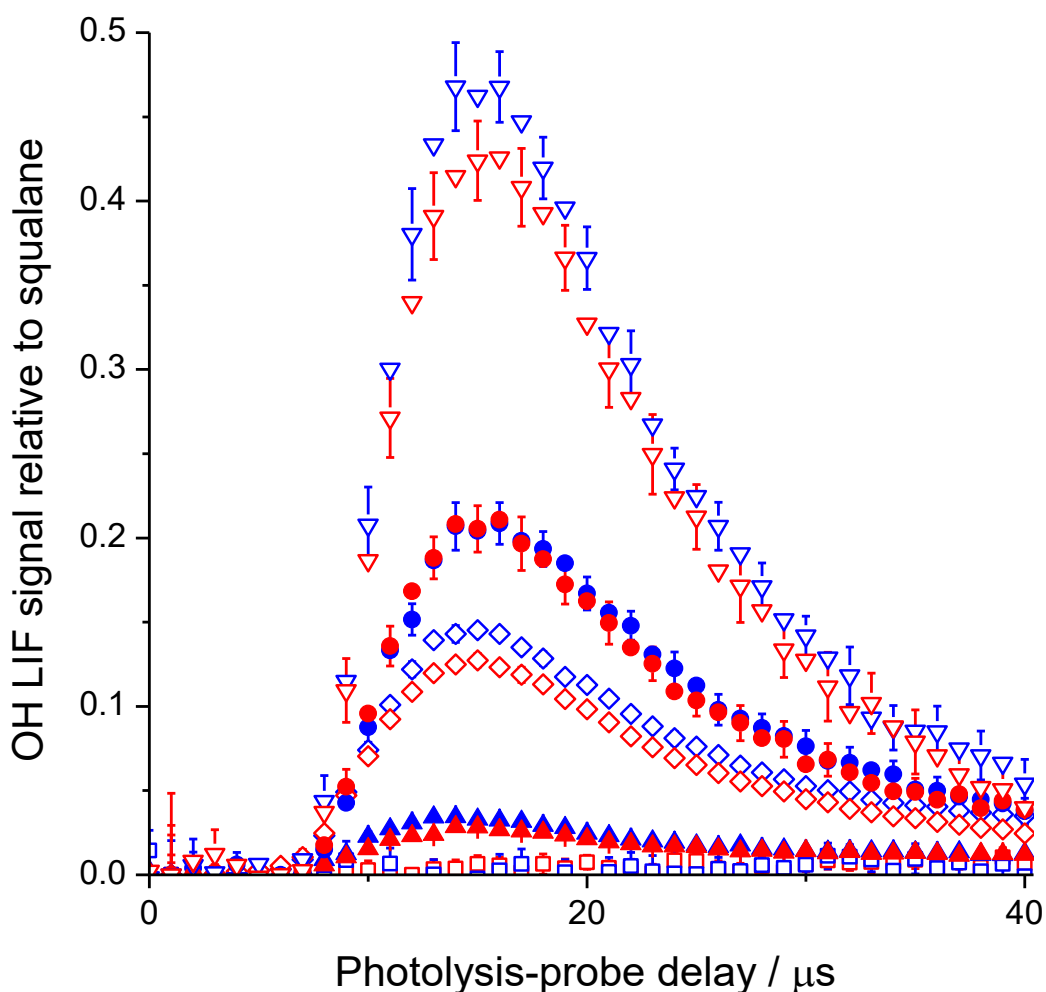


Figure 5.8. Average $Q_1(1)$ OH appearance profiles for $[C_n\text{mpyrr}][\text{Tf}_2\text{N}]$ (red symbols) and $[C_n\text{mim}][\text{Tf}_2\text{N}]$ (blue symbols) ILs: $n = 2$ (blank squares), $n = 4$ (filled triangles), $n = 6$ (blank diamonds), $n = 8$ (filled circles) and $n = 12$ (blank triangles). Error bars (some omitted) are $\pm 1\sigma$ standard error of the mean.

The OH yield was obtained from the appearance profiles by integrating the flux of detected OH between 0 and 30 μs . Similarly to the previous chapter, a density-to-flux conversion was performed to account for the slightly different shapes of the appearance profiles. The experimental profiles were compared to Monte Carlo simulated profiles with Maxwell-Boltzmann product speed distributions described by a temperature T_{trans} . Profiles corresponding to values of T_{trans} between 300 and 2500 K (in intervals of 100 K) were simulated and the best fit to each experimental profile was selected among them. The relative intensities of the corresponding simulated profiles were used to correct the values from the integrated experimental profiles, as described in Chapter 4. The resulting values of OH yield are listed in Table 5.5, and plotted in Figure 5.9.

| | [C_nmpyrr][Tf₂N] relative OH yield | [C_nmim][Tf₂N] relative OH yield |
|---------------|--|--|
| <i>n</i> = 2 | 0.005 ± 0.005 | -0.004 ± 0.004 |
| <i>n</i> = 4 | 0.029 ± 0.001 | 0.037 ± 0.002 |
| <i>n</i> = 6 | 0.136 ± 0.003 | 0.149 ± 0.003 |
| <i>n</i> = 8 | 0.214 ± 0.009 | 0.208 ± 0.008 |
| <i>n</i> = 12 | 0.445 ± 0.013 | 0.482 ± 0.015 |

Table 5.5. Relative OH yield from each of the studied ionic liquids, obtained as the integrated OH flux relative to squalane as described in the text. Errors are $\pm 1\sigma$ standard error of the mean.

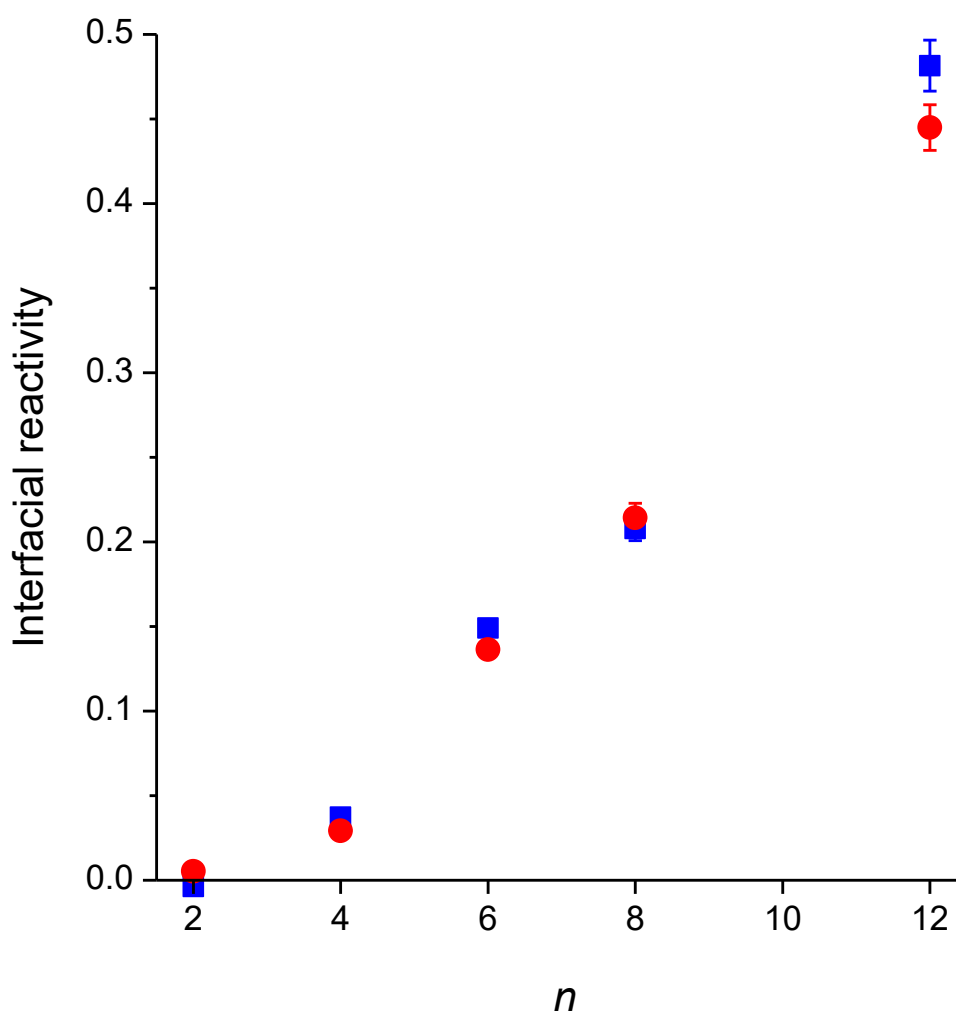


Figure 5.9. Relative OH yield from $[C_n\text{mpyrr}][\text{Tf}_2\text{N}]$ (red circles) and $[C_n\text{mim}][\text{Tf}_2\text{N}]$ (blue squares) as a function of chain length n .

5.4. Discussion

Before launching into a detailed discussion of the OH yields, it is worth considering the potential effect of surface temperature (Section 5.3.1). As previously mentioned, it is thought that a change of 100 K does not have a great effect on the surface structure of ILs. MD simulations have reported a small increase in IL surface disorder as the temperature increases. Lynden-Bell studied $[\text{C}_4\text{mim}]^+$ ILs at 300 and 450 K, and found that the fraction of gauche bonds in the alkyl chains increased from 0.32 to 0.36 [255]. Simulations of $[\text{C}_4\text{mim}][\text{PF}_6]$ in the range of 300 – 500 K [254] and of $[\text{C}_6\text{mim}][\text{Tf}_2\text{N}]$ at 300 – 400 K [258] discovered stronger layering at 300 K, but the general features of

the surface were maintained for all temperatures. The temperature range of the RAS-LIF measurements in this chapter is not as wide, so the effect on surface ordering is expected to be even smaller. Simulations of $[C_4mim][PF_6]$ at 298, 330 and 360 K (more similar to the temperatures used here) revealed that the temperature had only a weak effect on the surface structure [263], in agreement with the lack of temperature-dependence shown for $[C_6mpyrr][Tf_2N]$ in Figure 5.6. Since this appears to be a general feature of most IL surfaces, it is unlikely that the results here are strongly influenced by temperature.

It should also be noted that the increase in RAS-LIF reactivity for $[C_nmim]^+$ is weaker than expected on the basis of previous results for $n = 8$ and 12: the OH yields for $[C_8mim][Tf_2N]$ (0.208 ± 0.008) and $[C_{12}mim][Tf_2N]$ (0.482 ± 0.015) are significantly lower than the previously reported values (0.27 ± 0.01 and 0.62 ± 0.06 respectively, see Chapter 4). These longer-chain liquids were measured several months after the short-chain ILs, and it is possible that intervening changes in experimental conditions resulted in lower IL:squalane reactivity ratios. The $n = 12 / n = 8$ ratio is essentially the same for the previous (0.44) and present measurements (0.43), which suggests a problem with the squalane reference. The most likely cause is a slightly shorter wheel-to-beam distance for the reference squalane bath, which was not detected in the calibration measurements. Nevertheless, the relative imidazolium:pyrrolidinium values for each chain length are expected to be correct as they were obtained under the same conditions. The discussion below centres on the comparison of OH yields from $[C_nmpyrr][Tf_2N]$ and $[C_nmim][Tf_2N]$.

The interfacial reactivities in Figure 5.9 clearly show that the surfaces of $[C_nmpyrr][Tf_2N]$ and $[C_nmim][Tf_2N]$ give remarkably similar OH yields, independently of their chain length. By implication, they have very similar alkyl coverages (if anything, pyrrolidinium produces marginally fewer OH radicals than imidazolium). In both cases, the increase in reactivity with n is stronger than expected from stoichiometry. This confirms that the alkyl enrichment effect previously seen for $[C_nmim][Tf_2N]$ (see Chapter 4 and previous publications [10, 11, 48, 104]) is also present in $[C_nmpyrr][Tf_2N]$ ILs. Other studies of pyrrolidinium-based ILs with different chain lengths reached the same conclusion. The alkyl chains were found to be perpendicular to the surface in an SFG study of the chain lengths $n = 3 - 10$ [283], and ARXPS experiments found alkyl enrichment of the surface for chain lengths of 8 and 10, but not for 4 and 6 [284]. The RAS-LIF results here show a nonstoichiometric

increase in reactivity with n for ILs with $n = 6 - 12$, for both imidazolium and pyrrolidinium ILs. The fact that RAS-LIF can distinguish a nonstoichiometric enrichment for these chain lengths is probably due to the more highly surface-specific character of the RAS-LIF technique compared to ARXPS. More surface-sensitive synchrotron XPS experiments did find an enrichment in alkyl chains for $[C_4\text{mpyrr}][\text{Tf}_2\text{N}]$ [221].

The nonstoichiometric trend in reactivity for $[C_n\text{mpyrr}][\text{Tf}_2\text{N}]$ is perhaps not too unexpected: bulk MD simulations and X-ray scattering experiments on $[C_n\text{mpyrr}][\text{Tf}_2\text{N}]$ have previously found that their alkyl chains aggregate in a similar fashion to imidazolium-based ILs [286], so it is reasonable to expect that their surface behaviour is analogous. The strong similarity between OH yields from $[C_4\text{mim}][\text{Tf}_2\text{N}]$ and $[C_4\text{mpyrr}][\text{Tf}_2\text{N}]$ is, however, very surprising. The bond energies in Table 5.1 imply that the pyrrolidinium headgroups should be reactive and therefore produce higher OH yields than their imidazolium counterparts, if exposed at the surface. It follows from this that the pyrrolidinium rings are not exposed at the surface, even at the shortest chain length ($n = 2$) which might *a priori* be expected to have a high coverage of headgroups at the surface.

In order to understand the issue of ring exposure, the information available regarding imidazolium IL surfaces should be considered. It should be remembered that the MD snapshots of $[C_n\text{mim}][\text{Tf}_2\text{N}]$ surfaces in Chapter 4 (Figure 4.13) present almost no atoms from the headgroup at the surface, regardless of chain length. Cation rings have previously been found at imidazolium surfaces by other MD simulations [130, 255, 258, 263] and experimental techniques such as MIES [224]. However, the rings only make up a small fraction of the surface composition, which is dominated by alkyl chains and anions. Since $[\text{Tf}_2\text{N}]^-$ is very nonpolar and tends to orient its CF_3 groups to the vacuum, the surface becomes enriched in the anion at the expense of the cationic rings. The effect takes place for chains as short as $n = 2$: water adsorption measurements on $[C_2\text{mim}][\text{Tf}_2\text{N}]$ showed that this IL behaves as a hydrophobic surface, therefore the outermost layer must be dominated by CF_3 and ethyl groups [287]. This could explain why $[C_2\text{mim}][\text{Tf}_2\text{N}]$ does not produce any detectable OH in RAS-LIF: the IL surface is dominated by terminal methyl groups (which are rather unreactive) and $[\text{Tf}_2\text{N}]^-$ anions.

The fact that $[C_n\text{mpyrr}][\text{Tf}_2\text{N}]$ ILs have very similar reactivities indicates that the pyrrolidinium cations must also be buried below the surface; otherwise, ILs such as $[C_2\text{mpyrr}][\text{Tf}_2\text{N}]$ would produce higher yields of OH. If the pyrrolidinium rings are

perpendicular to the surface with their alkyl chains protruding from it, they will be shielded by the alkyl chains and therefore not accessible from the gas phase. A parallel orientation of the ring would also agree with the results: the $O(^3P)$ atoms in RAS-LIF must approach the C–H bond collinearly in order to react, so exposed parallel rings might not lead to OH production. Other studies indicate that the preferred orientation of the pyrrolidinium rings is perpendicular: in MD simulations of $[C_4\text{mpyrr}][\text{Tf}_2\text{N}]$, the alkyl chains were preferentially oriented towards the vacuum and the rings were perpendicular to the surface, so that all of the ring was buried inside the liquid [285]. The simulations also found a small excess of anions at the interface [285]. Other experimental studies appear to indicate that the pyrrolidinium headgroup is not very accessible, supporting this interpretation. ARXPS detected an enrichment of N_{anion} over N_{cation} for both $[C_4\text{mpyrr}][\text{Tf}_2\text{N}]$ and $[C_4\text{mim}][\text{Tf}_2\text{N}]$ [221]. In SFG spectroscopy of $[C_n\text{mpyrr}][\text{Tf}_2\text{N}]$ ($n = 2 - 10$), most of the signal came from the alkyl chain and the N–CH₃ vibration was absent for $n > 3$ [283]. Similarly, no N atoms were found at the surface of $[C_4\text{mpyrr}][\text{Tf}_2\text{N}]$ studied by LEIS [240]. The nitrogen atoms in pyrrolidinium were detected by ARXPS [220, 221, 284], although it should be considered that this technique probes a greater depth into the surface.

The striking similarity between imidazolium and pyrrolidinium OH yields implies that alkyl coverage of the surface depends on n but not on the cation headgroup. Considering the differences in molecular structure between $[C_n\text{mpyrr}]^+$ and $[C_n\text{mim}]^+$ cations, this is a surprising result. Even if both headgroups are buried under the surface, the orientation of their alkyl chains should be different, and this could result in different RAS-LIF reactivities. In addition, it would be reasonable to expect the headgroups to induce different packing of the ionic layer leading to different alkyl coverages. Pyrrolidinium rings are non-planar, while imidazolium cations are planar. This is likely to affect the packing efficiency of polar groups at the surface, as pointed out by Steinrück and co-workers [220]. Their ARXPS measurements revealed that the surface of $[C_4\text{mpyrr}][\text{Tf}_2\text{N}]$ was slightly less enriched in alkyl groups than $[C_4\text{mim}][\text{Tf}_2\text{N}]$ (in agreement with the RAS-LIF results here). The authors proposed that it was a packing effect: the planar imidazolium cations occupy a smaller volume and allow more cation-anion pairs to pack at the surface, resulting in more alkyl groups in the outer layer. This effect is however counteracted by the cation-anion electrostatic interactions: $[C_n\text{mim}]^+$ ILs have lower cation-anion interaction strengths than their pyrrolidinium counterparts, due to their more diffuse cationic charge [288, 289]. As discussed in the previous

chapter, a stronger interaction implies that the ionic pairs pack more closely at the surface.

Another important factor is the effect of the cation headgroup on its alkyl chain bond strengths. In hydrocarbons generally, primary and secondary alkyl C–H bonds have typical dissociation energies of 423 and 411 kJ mol⁻¹, respectively [142]. The cationic rings affect the C–H BDEs of the alkyl chains attached to them: in Table 5.1, the predicted pyrrolidinium C₍₆₎–H and C₍₁₀₎–H bonds are stronger than expected, while in imidazolium they are weaker than typical alkyl bonds. Moreover, the C–H bonds in the pyrrolidinium rings are weaker than linear alkyl bonds. In consequence, the similar values of reactivity could, in principle, be the result of two opposing effects: the exposed, more reactive H atoms in pyrrolidinium would lead to higher OH yields, while its alkyl C–H bond strengths would have the opposite effect. This interpretation seems unlikely, however, considering that the contributions from the two effects are likely to be different for different chain lengths. It should also be considered that, although the thermodynamic bond dissociation energy is usually a good indicator of the reactivity of the bond, it is not a measure of the barrier for H abstraction. This is particularly true for C₍₆₎–H and C₍₁₀₎–H: the resulting radicals are stabilised by resonance by the adjacent ring in imidazolium but not in pyrrolidinium, so the calculated BDEs are expected to be very different from the dynamic thresholds.

Besides the details discussed above, the main finding of this study is that the cationic headgroups are not very exposed in [C_nmpyrr][Tf₂N] surfaces, and the preference for alkyl chains to occupy the surface depends on *n* but is almost independent of the cation headgroup. The alkyl groups project out of both [C_nmpyrr][Tf₂N] and [C_nmim][Tf₂N] surfaces, but in the former IL they are bonded to the same atom as the methyl group. Despite their similar alkyl coverages, it can reasonably be expected that the surfaces present different microscopic structures due to the geometry of the cations. The rotational temperatures in Figure 5.7 provide additional information related to the surface structure. The value of T_{rot} decreases slightly with chain length for pyrrolidinium ILs, following a similar trend as the imidazolium ILs studied here and in the previous chapter. Moreover, for any given chain length, the temperatures are always lower for pyrrolidinium ILs. This could indicate that the [C_nmpyrr][Tf₂N] surfaces are rougher than their [C_nmim][Tf₂N] equivalents; however, this is unclear due to the large uncertainty of the results. Further simulations of the IL surfaces are required to clarify these questions.

5.5. Summary points

- (1) The reactivity of $[C_n\text{mpyrr}][\text{Tf}_2\text{N}]$ surfaces increases with chain length n in a nonstoichiometric fashion, evidencing that longer alkyl chains have a stronger preference to occupy the surface. The alkyl enrichment effect takes place in all ILs, including those with relatively short chains.
- (2) The RAS-LIF OH yields for $[C_n\text{mpyrr}][\text{Tf}_2\text{N}]$ are strikingly similar to those for $[C_n\text{mim}][\text{Tf}_2\text{N}]$, demonstrating that the identity of the cation headgroup does not have a great influence on the alkyl coverage of the surface. This result contrasts with the relatively large effect of the anion seen in Chapter 4. From this it follows that $[\text{Tf}_2\text{N}]^-$ anions must be more surface-active than pyrrolidinium or imidazolium headgroups.
- (3) Despite the high reactivity of the pyrrolidinium headgroup, the OH yield from $[C_2\text{mpyrr}][\text{Tf}_2\text{N}]$ is below the RAS-LIF detection limit. One possible explanation is that the pyrrolidinium rings are perpendicular to the surface with their alkyl groups exposed, so that they are not accessible to the incoming $O(^3P)$ atoms. MD simulations reported in the literature support this interpretation.
- (4) OH rotational temperatures from $[C_n\text{mpyrr}][\text{Tf}_2\text{N}]$ follow the same weak trend with n as $[C_n\text{mim}][\text{Tf}_2\text{N}]$. In addition, pyrrolidinium ILs yield marginally lower temperatures than their imidazolium counterparts, which could be the result of rougher surfaces.
- (5) RAS-LIF measurements of $[C_6\text{mpyrr}][\text{Tf}_2\text{N}]$ at 23 – 70 °C indicate that the temperature of this IL surface does not significantly affect its alkyl coverage. Previous measurements of $[C_{12}\text{mim}][\text{Tf}_2\text{N}]$, as well as MD simulations of IL surfaces, suggest that the IL surface structure is in general not greatly affected by temperature.

Chapter 6.

Reactive $O(^3P)$ scattering from ionic liquid mixtures

6.1. Introduction

The previous chapters have demonstrated that RAS-LIF can accurately quantify small differences in alkyl surface coverage of pure ionic liquids. This opens up the possibility of fine-tuning the alkyl character of the IL surface by carefully selecting the ion pair. Building a library of different ILs would give access to a range of alkyl coverages; however, synthesizing many different ion pairs can be demanding and time-consuming. A more efficient approach would be to prepare mixtures of two ILs with distinct alkyl coverages to obtain intermediate surface compositions. Instead of screening a large number of cation-anion pairs, the composition of a binary mixture can be varied in order to meet the desired alkyl coverage. It should, however, not necessarily be assumed that the alkyl coverage of the mixtures is linearly proportional to their bulk mixing ratio. More surface-active components might preferentially occupy the surface, leading to a coverage that is different from the weighted average of the values for the pure components. This is the question that is addressed here by characterising the surface composition of binary IL mixtures using RAS-LIF.

Although there have been some recent reports of IL mixture surface structure, discussed below, most studies to date have focused on their bulk physical properties. Many IL binary mixtures show nonideal mixing behaviour [290-293]. This has led to the suggestion that they are not liquid mixtures as such, and should be named “double salt ionic liquids” instead [294]: their constituting ions interact with each other independently of which IL they are from, so that the resulting physical properties are not necessarily defined by those of the pure components. Their surfaces also show complex mixing behaviour, demonstrated by surface tension measurements of IL binary mixtures [295-302]. In some of these mixtures, especially those containing ethyl ammonium nitrate (EAN) as the solvent (i.e. major component), the component with

lower surface tension shows typical surfactant behaviour: there is a strong decrease in surface tension with concentration until a plateau is reached indicating the formation of aggregates or micelles [295-297, 299, 303]. However, this effect is not as pronounced as that of classical surfactants in water. In general, IL surfactants with longer alkyl chains produce a stronger decrease in surface tension and a lower critical aggregation concentration (defined as the concentration at which the plateau is reached) [297]. ILs with similar properties, in contrast, are miscible over the whole composition range. The surface tension of these mixtures does not indicate the formation of aggregates, but it shows preferential adsorption of one of the components at the surface [298, 301].

Although the surface tension of an IL mixture offers some insight into its mixing behaviour, it is not a direct measurement of its surface composition. Other, more chemically-specific techniques have been used to study the surfaces of IL mixtures; amongst them ARXPS [222], RBS [304, 305], LEIS [306] and ToF-SIMs [305, 307]. They have also been investigated by MD simulations [254, 308]. There are large discrepancies in the degree of surface enrichment reported, ranging from stoichiometric surface compositions (detected by ARXPS [222]) to the complete absence of some constituting ions at the surface (reported in a LEIS study [306]). It should be noted that these studies were concerned with different IL combinations, which might have distinct mixing behaviours. However, the same IL mixture investigated using two techniques (RBS and ToF-SIMs) showed different surface compositions [305]. As will be further discussed later, the nature of the experimental technique employed affects the result. It is evident that further research using other complementary surface probes is required.

In this chapter, RAS-LIF has been employed to characterise the alkyl coverage of IL mixtures in order to investigate the effect of different alkyl chain lengths and counteranions. Two types of binary mixtures, presented in Figure 6.1, were studied. First, IL mixtures containing 1-ethyl-3-methylimidazolium bis(trifluoromethylsulfonyl)imide and 1-dodecyl-3-methylimidazolium bis(trifluoromethylsulfonyl)imide in varying proportions were investigated. These mixtures are abbreviated as $[C_2mim]_{(1-x)}[C_{12}mim]_x[Tf_2N]$, where x is the mole fraction of $[C_{12}mim][Tf_2N]$. Largely different chain lengths, $n = 2$ and 12, were chosen in order to optimise any surface enrichment or depletion effects. In addition, it is known from previous measurements (Chapter 5) that $[C_2mim][Tf_2N]$ does not produce any measurable OH yield in RAS-LIF. This means that practically all of the RAS-LIF signal arises from the $[C_{12}mim]^+$ cation, which is highly advantageous for characterising

its surface coverage. The second type of mixtures studied contained a common cation, 1-hexyl-3-methylimidazolium, with two different anions, $[\text{Tf}_2\text{N}]^-$ and tetrafluoroborate ($[\text{BF}_4]^-$). These mixtures, labelled as $[\text{C}_6\text{mim}][\text{BF}_4]_{(1-x)}[\text{Tf}_2\text{N}]_x$, are composed of two ILs with similar alkyl coverages: their ratio is approximately 1:1.8, as seen in Chapter 4. RAS-LIF does not directly detect the anions, so their relative surface activity must be inferred from the deviations from stoichiometric alkyl coverage. As these deviations are expected to be small, the experiment also serves as a test of the sensitivity of RAS-LIF.

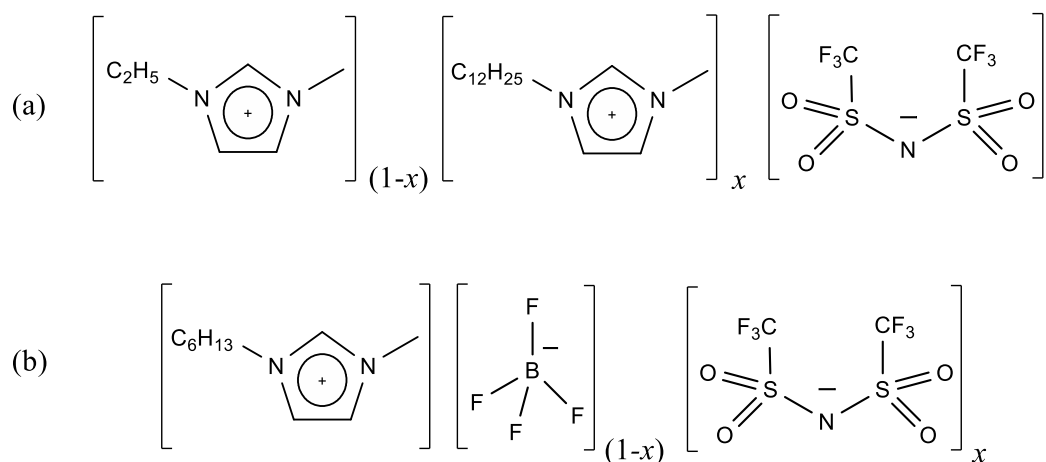


Figure 6.1. Chemical structure of the mixtures (a) $[\text{C}_2\text{mim}]_{(1-x)}[\text{C}_{12}\text{mim}]_x[\text{Tf}_2\text{N}]$ and (b) $[\text{C}_6\text{mim}][\text{BF}_4]_{(1-x)}[\text{Tf}_2\text{N}]_x$.

6.2. Experimental

Pure $[C_2mim][Tf_2N]$, $[C_{12}mim][Tf_2N]$ and their mixtures were provided by John Slattery (University of York). The $[C_{12}mim][Tf_2N]$ mole fractions studied were $x = 0, 0.01, 0.04, 0.08, 0.16, 0.24, 0.32, 0.43, 0.52, 0.63, 0.74, 0.87$ and 1. Pure $[C_6mim][BF_4]$ and $[C_6mim][Tf_2N]$ were purchased from IoLiTec. Their purity and water content are given in Chapter 4 (Table 4.2). $[C_6mim][BF_4]_{(1-x)}[Tf_2N]_x$ mixtures were prepared by stirring at room temperature for 3 hours. The mole fractions of $[C_6mim][Tf_2N]$ studied were $x = 0, 0.125, 0.25, 0.375, 0.5, 0.625, 0.75, 0.875$ and 1. The ILs were found to be miscible across the whole composition range, as previously reported [292].

RAS-LIF experiments were performed in the 4-wheel apparatus described in Chapter 2. A cylindrical probe beam (4 mm diameter) propagating at a distance of 6.5 mm from the surface was used. Due to the large number of samples involved, it was not possible to study all mixtures simultaneously. The experiments were divided into different sets so that in each set three of the baths contained different IL mixtures and the fourth bath contained squalane (Sigma Aldrich). Between datasets, care was exercised to ensure that the wheel-to-beam distances remained unchanged and that there was no cross-contamination between samples.

6.3. Results

6.3.1. Binary mixtures with a common anion, $[C_2mim]_{(1-x)}[C_{12}mim]_x[Tf_2N]$

RAS-LIF excitation spectra were acquired at a photolysis-probe delay of 13 μ s, recording only wavelength sections of interest. At least five spectra were acquired for each of the $[C_2mim]_{(1-x)}[C_{12}mim]_x[Tf_2N]$ mixtures, as well as pure $[C_{12}mim][Tf_2N]$ and squalane. $[C_2mim][Tf_2N]$ was omitted as it did not produce OH radicals above the detection limit. Figure 6.2 presents excitation spectra from squalane, $[C_{12}mim][Tf_2N]$ and selected mixtures. The spectra are extremely similar across liquids, indicating that there are no substantial differences in the OH rotational distributions.

The relative populations of the $N' = 1 - 5$ levels were obtained by fitting the Q_1, R_1 and R_2 branches of the spectra on LIFBASE and interpolating the populations from blended transitions. The distributions within individual branches were well described by single Boltzmann temperatures, but the relative population of the F_2 manifold was smaller than

the theoretical value for a thermal distribution. This result is not unexpected, since it is known that $O(^3P) + \text{hydrocarbon}$ reactions produce OH radicals with a 2:1 preference for the F_1 manifold [182]. In order to use all three branches in the same Boltzmann plot, the sum of populations for R_2 was artificially scaled to achieve a thermal $F_1:F_2$ ratio. This procedure did not alter the relative populations across N' levels within a branch. For each individual spectrum, the Q_1 , R_1 and R_2 populations were plotted together and fitted to a single-temperature Boltzmann distribution. A typical Boltzmann plot is presented in Figure 6.3.

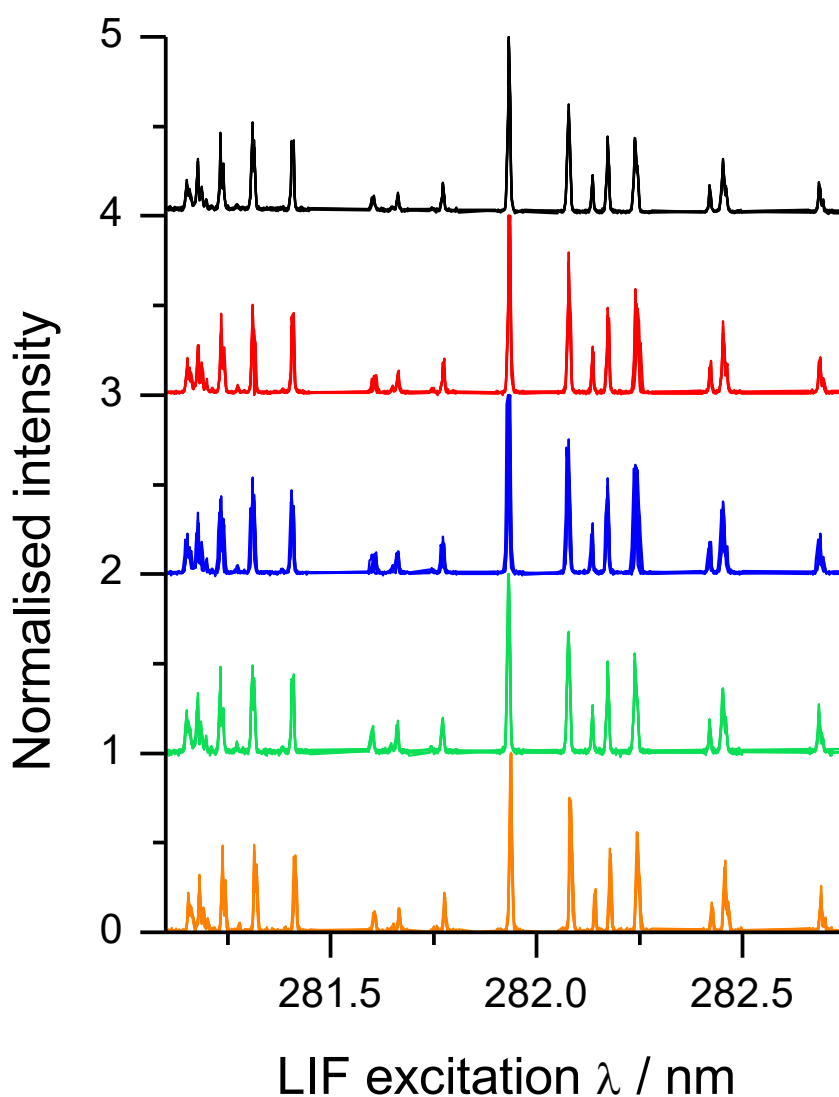


Figure 6.2. OH LIF excitation spectra recorded at a photolysis-probe delay of 13 μs from $[\text{C}_2\text{mim}]_{(1-x)}[\text{C}_{12}\text{mim}]_x[\text{Tf}_2\text{N}]$ mixtures of $x = 0.08$ (orange), 0.52 (green), 0.87 (blue), 1 (red) and from squalane (black). There are five overlapped spectra from each sample, each one normalised to the most intense line. Spectra from different samples are offset for clarity.

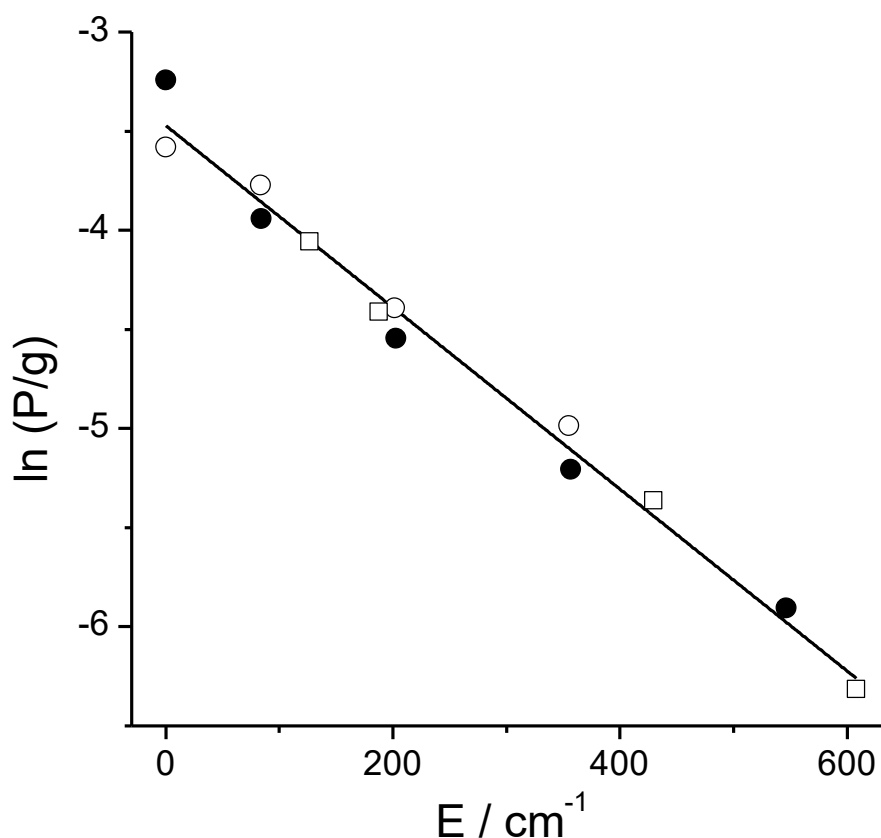


Figure 6.3. Single-temperature Boltzmann fit (black line) obtained from an excitation spectrum recorded from $[\text{C}_2\text{mim}]_{0.37}[\text{C}_{12}\text{mim}]_{0.63}[\text{Tf}_2\text{N}]$. Different symbols correspond to different rotational branches: Q_1 (filled circles), R_1 (open circles) and R_2 (open squares). The summed population of R_2 was scaled to fit a thermal distribution, as described in the text.

The slopes of the individual Boltzmann plots were averaged for each liquid in order to obtain OH rotational temperatures T_{rot} . The resulting values, shown in Figure 6.4, are not statistically different from each other. Squalane also led to a very similar rotational temperature, $T_{\text{rot}} = 305 \pm 17 \text{ K}$.

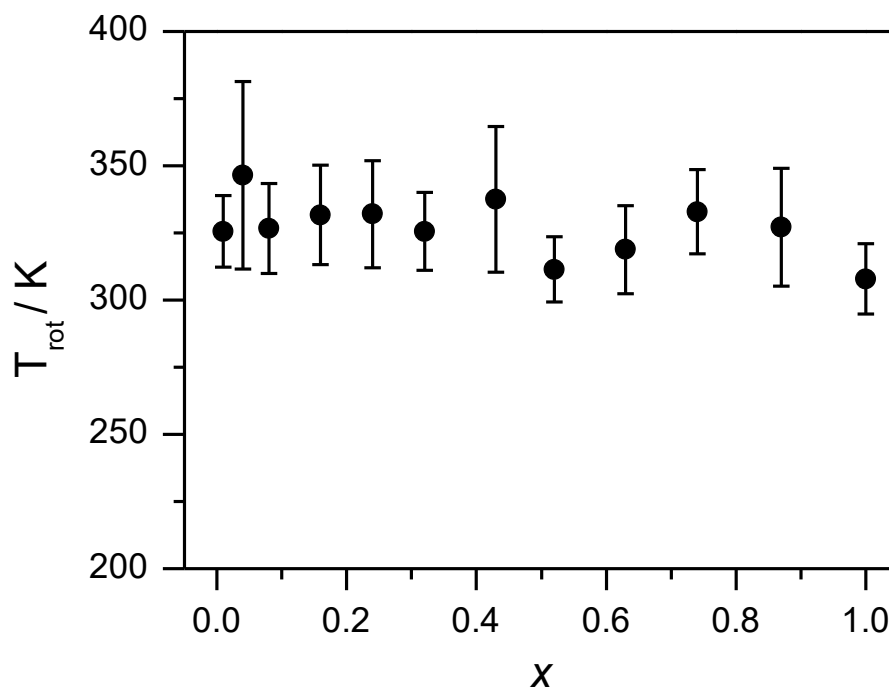


Figure 6.4. Average OH rotational temperatures T_{rot} at the peak of the appearance profile (photolysis-probe delay of 13 μs) derived from all of the $[\text{C}_2\text{mim}]_{(1-x)}[\text{C}_{12}\text{mim}]_x[\text{Tf}_2\text{N}]$ mixtures studied, from $x = 0.01$ to $x = 1$. Error bars represent $\pm 1\sigma$ standard error of the mean.

As previously done, the intensity of the $Q_1(1)$ line, which is partially blended with $R_2(3)$, was taken as representative of the total number density of OH, given the similarity in rotational distributions demonstrated above. Appearance profiles were acquired in sets of 10 using squalane as a reference. Photolysis and probe backgrounds were characterised and subtracted as described in previous chapters. Profiles for scattered photolytic OH were obtained independently for each liquid using HONO as a precursor, scaled to the 1- μs signal and subtracted from the NO_2 -induced appearance profiles. The effect of photolytic OH in the results was negligible for all cases except for pure $[\text{C}_2\text{mim}][\text{Tf}_2\text{N}]$. This procedure was repeated at least three times in order to obtain 30 profiles from each liquid. In addition, one of the mixtures ($x = 0.52$) was measured twice to test the reproducibility between experimental runs. In the second measurement, a different aliquot of the mixture was loaded into the chamber and studied with different mixtures adjacent to it. Average background-subtracted appearance profiles recorded for squalane and some of the $[\text{C}_2\text{mim}]_{(1-x)}[\text{C}_{12}\text{mim}]_x[\text{Tf}_2\text{N}]$ mixtures are shown in Figure 6.5.

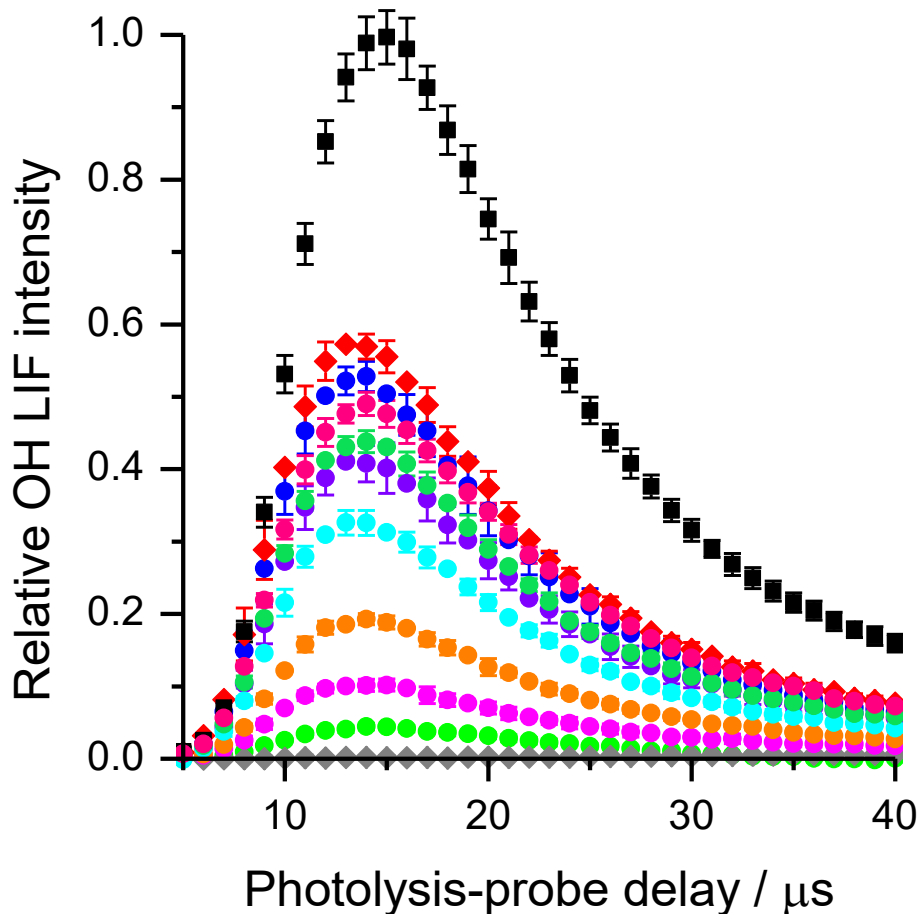


Figure 6.5. Average $Q_1(1)$ appearance profiles from squalane (black squares) and selected $[C_2mim]_{(1-x)}[C_{12}mim]_x[Tf_2N]$ mixtures with $x = 0$ (grey diamonds), 0.01 (light green circles), 0.04 (magenta circles), 0.08 (orange circles), 0.16 (light blue circles), 0.24 (purple circles), 0.52 (green circles), 0.72 (pink circles), 0.87 (blue circles) and 1 (red diamonds). Some error bars are omitted for clarity.

Perhaps not surprisingly, mixtures with greater values of x are more reactive. In agreement with the results presented in Chapter 4 and in previous publications [10, 11, 104], pure $[C_{12}mim][Tf_2N]$ produces approximately half as much OH as squalane, and there is almost no measurable yield from the surface of pure $[C_2mim][Tf_2N]$. The reactivity of the mixtures falls between these two values; however, it can be appreciated in the figure that it is not linearly proportional to the mixture composition: it increases steeply for $x \leq 0.24$, and then grows more slowly towards pure $[C_{12}mim][Tf_2N]$.

In previous chapters, the shapes of the appearance profiles were significantly different and a density-to-flux conversion had to be performed in order to obtain accurate OH yields. In the present results, no significant difference was found between the peak-normalised IL profiles, considering the wheel-to-wheel reproducibility (which was determined to be $\pm 5\%$ in calibration measurements, see Chapter 5). Therefore the integrated appearance profiles can be compared across IL mixtures without any further correction. However, appearance profiles from squalane were significantly later than the IL profiles so, in order to obtain accurate OH yields relative to squalane, a density-to-flux conversion was performed. This analysis followed the same procedure as previously (Chapter 4), using Monte Carlo simulated profiles with Maxwell-Boltzmann temperatures between 600 K and 3000 K. The IL profiles were best described by a temperature of 1100 K, while squalane was fitted to 700 K. The integrated OH fluxes resulting from this conversion are listed in Table 6.1. The table also presents the result of the repeated $x = 0.52$ measurement discussed above. The small but marginally nonzero yield obtained from $[C_2mim][Tf_2N]$ (0.008 ± 0.005) is most likely the result of the contribution from the adjacent wheel at late photolysis-probe delays (see Chapter 5). The data from $[C_2mim][Tf_2N]$ were acquired with two liquid baths adjacent to it, whereas in Chapter 5 it was studied with only the reference wheel at 180° , so that the later contribution did not affect it.

| x | Relative OH yield |
|--------------------------------|-------------------|
| 0 (pure $[C_2mim][Tf_2N]$) | 0.008 ± 0.005 |
| 0.01 | 0.048 ± 0.002 |
| 0.04 | 0.113 ± 0.005 |
| 0.08 | 0.206 ± 0.004 |
| 0.16 | 0.352 ± 0.005 |
| 0.24 | 0.457 ± 0.010 |
| 0.32 | 0.458 ± 0.007 |
| 0.43 | 0.495 ± 0.007 |
| 0.52 | 0.473 ± 0.007 |
| 0.52^b | 0.507 ± 0.007 |
| 0.63 | 0.549 ± 0.007 |
| 0.74 | 0.557 ± 0.010 |
| 0.87 | 0.579 ± 0.012 |
| 1 (pure $[C_{12}mim][Tf_2N]$) | 0.638 ± 0.010 |

Table 6.1. OH flux relative to squalane as a function of mole fraction, x , in $[C_2mim]_{(1-x)}[C_{12}mim]_x[Tf_2N]$ mixtures. Errors are $\pm 1\sigma$ standard error of the mean.

^b Repeated experimental run.

6.3.2. Binary mixtures with a common cation, $[C_6mim][BF_4]_{(1-x)}[Tf_2N]_x$

The common-cation mixtures $[C_6mim][BF_4]_{(1-x)}[Tf_2N]_x$ were studied in the same fashion as those in Section 6.3.1. In this case, only a few survey LIF excitation spectra were acquired, without systematically characterising the OH rotational distributions. The reason for this approach is that, as seen in Chapter 4, $[C_6mim][BF_4]$ and $[C_6mim][Tf_2N]$ lead to similar rotational distributions so they were expected to be the same for the

mixtures. In order to confirm this, excitation spectra from the pure ILs were recorded again. The populations of $N' = 1 - 4$ were fitted to single Boltzmann temperatures using the Q_1 and R_1 branches, following the same approach as in the previous section. The resulting T_{rot} values were 296 ± 26 K for $[\text{C}_6\text{mim}][\text{BF}_4]$ and 330 ± 35 K for $[\text{C}_6\text{mim}][\text{Tf}_2\text{N}]$ (1σ standard error of the mean). Again, the rotational distributions were not significantly different from each other. These values, however, are much lower than those reported in Chapter 4 for the same ILs (403 ± 36 K and 442 ± 37 K for $[\text{C}_6\text{mim}][\text{BF}_4]$ and $[\text{C}_6\text{mim}][\text{Tf}_2\text{N}]$, respectively). This is almost certainly a result of the analysis method employed, as fewer rotational levels were considered. The same is true for the rotational temperatures from the common-anion mixtures shown in Figure 6.4.

$Q_1(1)$ appearance profiles were acquired in sets of 5 consecutive IL profiles followed by 5 squalane profiles. At least six sets were recorded for each liquid, making a total of 30 appearance profiles. The datasets were background-subtracted for laser scattered light and photolytic OH, normalised to the squalane peak signal and averaged together. The final profiles for pure $[\text{C}_6\text{mim}][\text{BF}_4]$, $[\text{C}_6\text{mim}][\text{Tf}_2\text{N}]$ and representative IL mixtures are shown in Figure 6.6 (the average squalane profile is omitted in this case in order to present the results clearly). As it can be seen in the figure, the IL mixtures have quite similar, almost overlapping, reactivity. Nevertheless, it is clear that it decreases with increasing x value. In addition, this decrease is not stoichiometric: the LIF intensity for a mole fraction $x = 0.125$ is substantially lower than that for $x = 0$; whilst $x = 0.85$ and $x = 1$ present very similar appearance profiles.

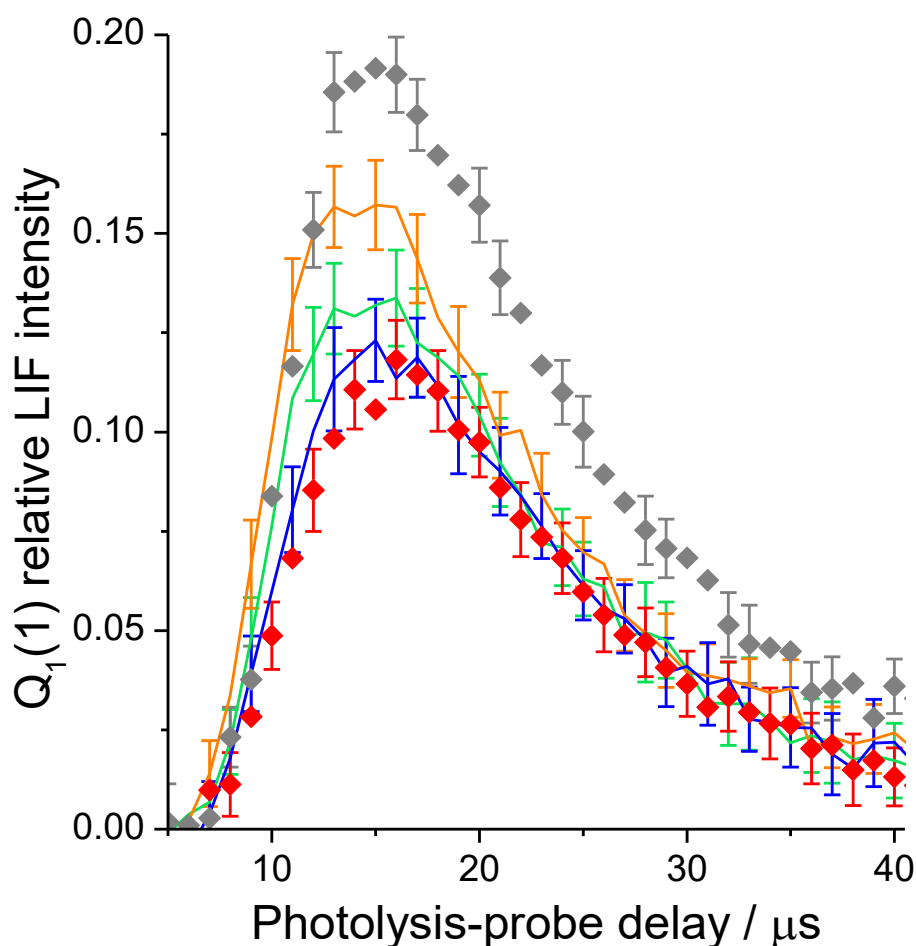


Figure 6.6. Average appearance profiles from selected $[C_6mim][BF_4]_{(1-x)}[Tf_2N]_x$ mixtures: $x = 0$ (grey diamonds), 0.125 (orange line), 0.5 (green line), 0.875 (blue line) and 1 (red diamonds). Error bars correspond to $\pm 1\sigma$ standard error of the mean.

The average appearance profiles for the mixtures and for squalane were found to match Monte Carlo simulations with translational temperatures T_{trans} between 800 and 1200 K, similar to the results in Section 6.3.1. However, the dispersion in the data was too large to confidently use T_{trans} to obtain OH fluxes: the peak of the 800 K and 1200 K profiles only varies by 1 μs , and the error in the experimental appearance profiles is quite large so their shape is not very well defined. It is possible that the differences in T_{trans} are not meaningful; therefore, it was decided not to perform a density-to-flux conversion in this case. Instead, the interfacial reactivities quoted in Table 6.2 are the LIF intensities of the $Q_1(1)$ appearance profiles integrated from 0 to 30 μs .

| x | Relative OH yield |
|--|-------------------|
| 0 (pure [C ₆ mim][BF ₄]) | 0.189 ± 0.004 |
| 0.125 | 0.160 ± 0.005 |
| 0.25 | 0.146 ± 0.005 |
| 0.325 | 0.140 ± 0.006 |
| 0.5 | 0.134 ± 0.003 |
| 0.625 | 0.138 ± 0.006 |
| 0.75 | 0.132 ± 0.005 |
| 0.875 | 0.122 ± 0.005 |
| 1 (pure [C ₆ mim][Tf ₂ N]) | 0.115 ± 0.004 |

Table 6.2. OH number density relative to squalane as a function of mole fraction, x , in [C₆mim][BF₄]_(1-x)[Tf₂N]_x mixtures. Errors are ±1σ standard error of the mean.

6.4. Discussion

6.4.1. Surface structure of [C₂mim]_(1-x)[C₁₂mim]_x[Tf₂N]

As indicated earlier, the interfacial reactivity of [C₂mim]_(1-x)[C₁₂mim]_x[Tf₂N] is not simply a weighted average of the pure IL values, showing that enrichment of one of the components takes place at the surface. To appreciate the trend clearly, OH yield is plotted as a function of [C₁₂mim][Tf₂N] mole fraction, x , in Figure 6.7 (a). The results have been normalised to the interfacial reactivity of pure [C₁₂mim][Tf₂N] so that the yield is 1 for this IL and 0.012 for [C₂mim][Tf₂N]. The error bars reflect the standard error of the mean *within* experimental runs (i.e. several datasets without removing the IL from the reaction chamber), with the exception of $x = 0.52$. For this mixture, the standard error of the mean *between* the two runs has been combined together with the error within runs. Comparing $x = 0.52$ to the other data points, it is clear that the reproducibility between experiments must be accounted for in order not to underestimate the experimental error.

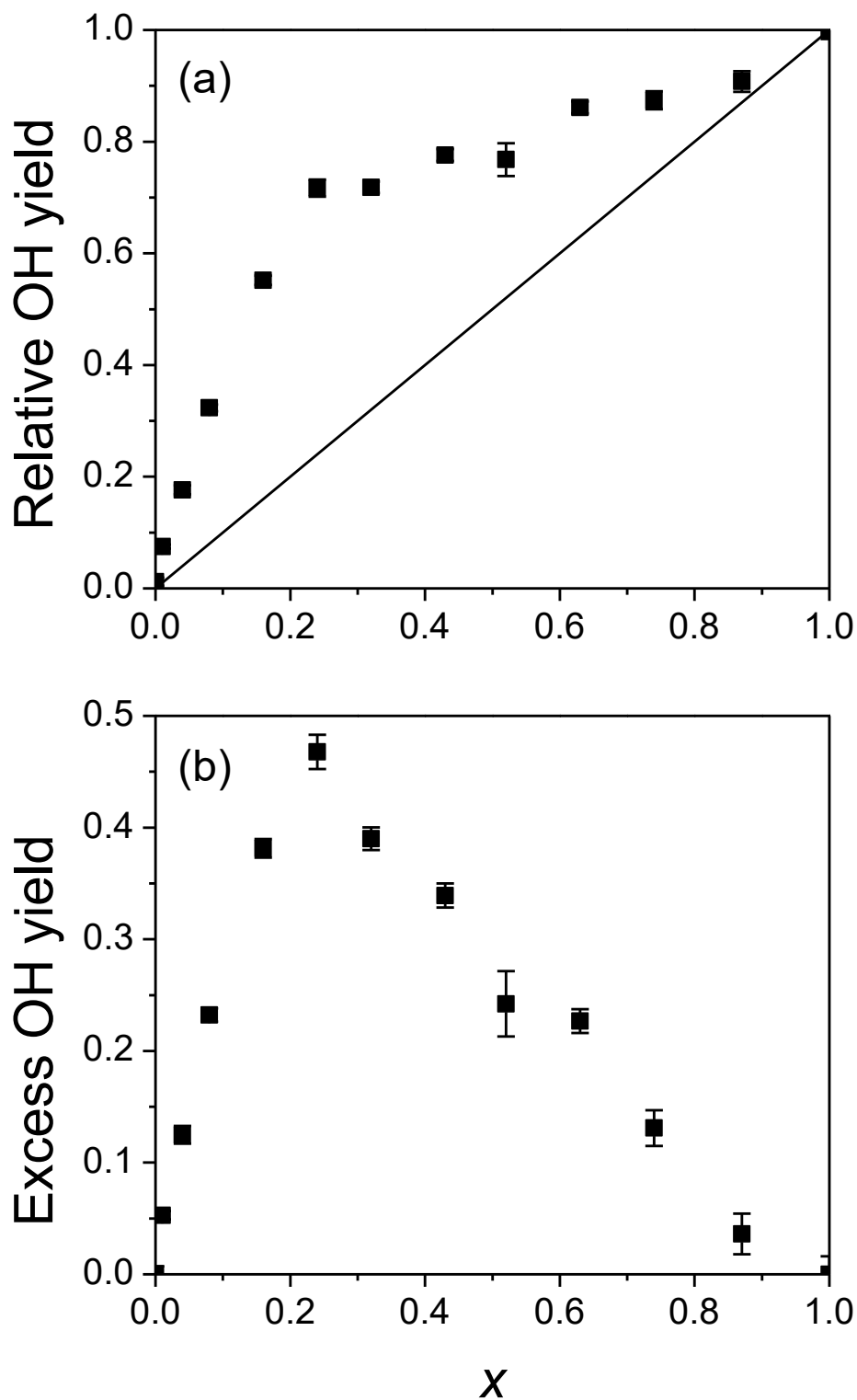


Figure 6.7. (a) OH yield of $[C_2mim]_{(1-x)}[C_{12}mim]_x[Tf_2N]$ mixtures relative to $[C_{12}mim][Tf_2N]$, plotted as a function of x . The diagonal line represents the yield expected for a surface with stoichiometric composition. (b) Excess OH yield, defined as the difference between the observed and stoichiometric yields, as a function of x .

The diagonal line in Figure 6.7 (a) represents the expected OH yield for the surface of a stoichiometric mixture, that is, one with the same composition as the bulk. The observed OH yield is considerably higher than the stoichiometric value for all of the mixture compositions x . This clearly indicates that the surface is preferentially enriched in the component with higher reactivity, $[\text{C}_{12}\text{mim}][\text{Tf}_2\text{N}]$. This finding is in striking contrast to a previous result from Maier [222], who studied a $[\text{C}_2\text{mim}]_{0.9}[\text{C}_{12}\text{mim}]_{0.1}[\text{Tf}_2\text{N}]$ mixture by ARXPS and reported a stoichiometric composition of the surface. The RAS-LIF results in Figure 6.7 indicate that the $x = 0.1$ mixture should contain almost 50% of $[\text{C}_{12}\text{mim}][\text{Tf}_2\text{N}]$ in its surface. The failure of ARXPS to detect any enrichment is likely due to its lower surface sensitivity, as well as the method chosen to analyse the results: the authors proposed that the ARXPS spectrum for a stoichiometric surface composition would be similar to that for $[\text{C}_3\text{mim}][\text{Tf}_2\text{N}]$, as it has the same $C_{\text{alkyl}}/C_{\text{hetero}}$ ratio [222]. However, this approach assumes that the surface coverage for different chain lengths is linearly proportional to the chain length, which has been shown not to be true in Chapter 4 of this thesis. Although the surface of $[\text{C}_2\text{mim}]_{0.9}[\text{C}_{12}\text{mim}]_{0.1}[\text{Tf}_2\text{N}]$ was clearly not as alkyl-rich as $[\text{C}_{12}\text{mim}][\text{Tf}_2\text{N}]$, suggesting the absence of a monolayer at the surface, the evidence was not strong enough to claim stoichiometric behaviour.

Other surface analysis techniques have been applied to common-anion IL mixtures similar to the system studied here. ToF-SIMS measurements of $[\text{C}_2\text{mim}]_{(1-x)}[\text{C}_8\text{mim}]_x[\text{PF}_6]$ and $[\text{C}_2\text{mim}]_{(1-x)}[\text{C}_8\text{mim}]_x[\text{BF}_4]$ revealed a strong surface enrichment of $[\text{C}_8\text{mim}]^+$: in a $[\text{BF}_4]$ -based mixture with $x = 0.01$, there were approximately equal amounts of $[\text{C}_2\text{mim}]^+$ and $[\text{C}_8\text{mim}]^+$ at the interface [307]. The enrichment of $[\text{C}_8\text{mim}]^+$ at the surface has been recently backed up by MD simulations [309]. In contrast, HRBS is far less sensitive to the enrichment of cations: an equimolar mixture of $[\text{C}_2\text{mim}][\text{Tf}_2\text{N}]$ and $[\text{C}_6\text{mim}][\text{Tf}_2\text{N}]$ found no preferential occupation of either of the components at the surface [238]. Again, the surface sensitivity of the technique greatly influences the result. This was later confirmed by a direct comparison of ToF-SIMS and HRBS results for $[\text{C}_2\text{mim}]_{(1-x)}[\text{C}_{10}\text{mim}]_x[\text{Tf}_2\text{N}]$ mixtures: a composition of $x = 0.1$ presented a $[\text{C}_{10}\text{mim}]^+$ surface fraction of 0.18 ± 0.02 by HRBS and 0.42 ± 0.04 by ToF-SIMS, while $x = 0.5$ gave 0.6 ± 0.05 by HRBS and 0.83 ± 0.03 by ToF-SIMS [305]. Assuming that the $[\text{C}_{12}\text{mim}]^+$ cations behave similarly to $[\text{C}_{10}\text{mim}]^+$ when mixed with $[\text{C}_2\text{mim}]^+$, the ToF-SIMS results are in reasonably good agreement with the RAS-LIF experiments. It can be concluded that both techniques are sufficiently surface-sensitive to characterise the enrichment of one of the components.

Figure 6.7 (b) presents the excess OH yield with respect to a stoichiometric surface, that is, the difference between the experimental interfacial reactivity and the weighted average of the pure IL reactivities. The figure shows a sharp increase in $[C_{12}mim][Tf_2N]$ surface occupation at low concentrations, reaching a maximum at $x = 0.24$. At larger x , the interfacial reactivity still increases towards the pure $[C_{12}mim][Tf_2N]$ value (see panel (a)), but it does so at a much lower rate so that the points in Figure 6.7 (b) start to decrease steadily towards zero. The question then arises: is there a physical significance to the maximum deviation being at $x = 0.24$, and is it consistent with previous results for other IL mixtures? In order to answer this, the RAS-LIF results have been compared against thermodynamic models of binary liquid mixtures. The following discussion presents the results of this comparison.

A simple way to predict the surface composition of the mixture is to input the surface tensions of the pure ILs into a thermodynamic Guggenheim model [310]:

$$x_{surf} = \frac{x e^{-\frac{f_{12}}{kT}}}{x e^{-\frac{f_{12}}{kT}} + (1-x) e^{-\frac{f_2}{kT}}} \quad (6.1)$$

In Equation 6.1, x_{surf} is the mole fraction of $[C_{12}mim][Tf_2N]$ at the surface, x is its bulk mole fraction, f_2 is the surface free energy per $[C_2mim][Tf_2N]$ ion pair and f_{12} is the surface free energy per $[C_{12}mim][Tf_2N]$ ion pair. The surface free energy is the product of surface tension σ and surface area, i.e. $f = \sigma \rho^{-\frac{2}{3}}$. This model has been previously employed by Nakajima to predict the surface enrichment of $[C_{10}mim]^+$ in $[C_2mim]_{(1-x)}[C_{10}mim]_x[Tf_2N]$ [305]. Using Nakajima's value for f_2 and approximating the surface area of $[C_{12}mim][Tf_2N]$ to that of $[C_{10}mim][Tf_2N]$ [305], together with its surface tension [311], x_{surf} can be predicted. The result is shown in Figure 6.8 as a blue line (note that mole fractions have been converted into volume fractions in order to make them comparable to another model discussed below). Assuming that the reactivity is a direct measure of the $[C_{12}mim][Tf_2N]$ interfacial concentration, it is clear that the prediction is quite different from the experimental observation. This indicates that the $[C_2mim]_{(1-x)}[C_{12}mim]_x[Tf_2N]$ mixtures do not follow this model, although it should be noted that approximations have been made in the calculation.

Recently, Lemraski [302] has characterised binary IL mixtures using an extended Langmuir model previously developed by Piñeiro *et al.* [312, 313]. This model, described in more detail below, enables the determination of the interfacial

concentration of each component using the bulk compositions and experimental surface tensions of the mixtures. Mixtures of $[C_4mim][Tf_2N]$ and $[C_nmim][Tf_2N]$ ($n = 1 - 10$) showed a small surface excess of the component with the lower surface tension [302]. However, the deviation from stoichiometry was in all cases almost “symmetric” (i.e. the maximum deviation occurred at approximately $x = 0.5$). As seen in Figure 6.7, this is not the case for $[C_2mim]_{(1-x)}[C_{12mim}]_x[Tf_2N]$. There are no available surface tension data for this particular mixture, so it is not possible to determine whether this strongly asymmetric trend is a real effect or a consequence of the RAS-LIF technique. In order to clarify this, a fit to the extended Langmuir model [312, 313] has been attempted. This model accounts for the differences in molecular sizes of the components by using bulk and surface volume fractions instead of mole fractions. The surface volume fraction of $[C_{12mim}][Tf_2N]$, ϕ_{12}^s , according to this model, is:

$$\phi_{12}^s = \frac{\beta \phi_{12}}{1 + (\beta - 1)\phi_{12}} \quad (6.2)$$

where ϕ_{12} is the bulk volume fraction of $[C_{12mim}][Tf_2N]$ and β is an adjustable parameter that measures the surface affinity of the solute (here, $[C_{12mim}][Tf_2N]$ is defined as the solute). The model is based on the Langmuir adsorption isotherm, but it is constrained to account for the surface sites that are already occupied (i.e. the denominator in Equation 6.2 is $1 + (\beta - 1)\phi_{12}$ instead of $1 + \beta\phi_{12}$). In the limit of low ϕ_{12} , β is equivalent to Henry’s constant such that $\phi_{12}^s = \beta\phi_{12}$.

The RAS-LIF reactivity results were used to obtain a value of ϕ_{12}^s for each bulk composition ϕ_{12} , which was then least-squares fitted to Equation 6.2. The fitted curve corresponded to $\beta = 3.44$ and is plotted in Figure 6.8 as a red line, together with the RAS-LIF results. It can be seen that the model is successful in describing the results for $x \leq 0.16$ ($\phi_{12} \leq 0.24$), but it overestimates the reactivity for large x .

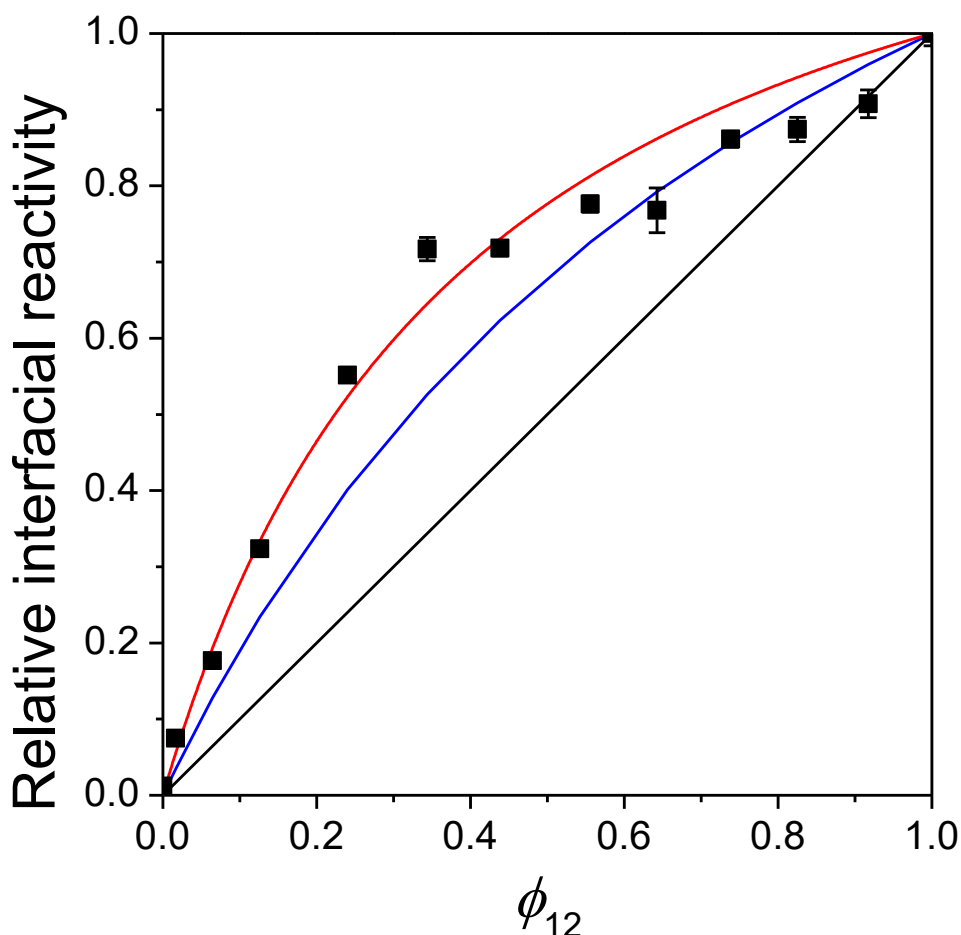


Figure 6.8. OH yield of $[C_2mim]_{(1-x)}[C_{12}mim]_x[Tf_2N]$ mixtures relative to $[C_{12}mim][Tf_2N]$ (black symbols), plotted as a function of its bulk volume fraction ϕ_{12} . The black line represents the yield expected for a stoichiometric surface composition.

The blue line is the surface volume fraction of $[C_{12}mim][Tf_2N]$ predicted by the Guggenheim model, and the red line is a fit of the results to the extended Langmuir isotherm (see text).

The failure of this simple model to describe the mixing behaviour at large x might be due to an interaction effect of the constituent ions. The extended Langmuir model was intended to describe mixtures of two components with similar values of surface tension, where no surface saturation or aggregation takes place [312]. Although other binary IL mixtures are well fitted by this model [298, 302], their components do not differ much in terms of surface affinity: the most dissimilar ILs mixed together were $[C_1mim][Tf_2N]$ and $[C_4mim][Tf_2N]$ [298]. In order to account for interactions that lead to deviations from ideal behaviour, an activity coefficient γ_{12} that modifies ϕ_{12} and varies with composition has been introduced. This activity coefficient would affect the rate of

adsorption when constructing the Langmuir isotherm. The simplest approach is to use a $[C_{12}mim][Tf_2N]$ activity coefficient given by the Porter equation, such that $\ln\gamma_{12} = A\phi_2^2$ [314]. In this equation, A is an empirical parameter and ϕ_2 is the bulk volume fraction of $[C_2mim][Tf_2N]$, which is equal to $1 - \phi_{12}$. Equation 6.2 therefore becomes Equation 6.3:

$$\phi_{12}^S = \frac{\beta\phi_{12}e^{A(1-\phi_{12})^2}}{1 + (\beta - 1)\phi_{12}e^{A(1-\phi_{12})^2}} \quad (6.3)$$

Fitting the RAS-LIF results as above yields $A = 1.19 \pm 0.23$ and $\beta = 1.32 \pm 0.29$. The resulting curve is plotted as a blue line in Figure 6.9. It should be noted that the parameter β has a different physical meaning from that in Equation 6.2: at low ϕ_{12} , $\phi_{12}^S = \beta\phi_{12}e^A$, so that βe^A in this case is equivalent to Henry's constant. At high ϕ_{12} , i.e. when Raoult's law applies, $\phi_{12}^S = \beta\phi_{12}$.

Equation 6.3 provides the correct qualitative trend in ϕ_{12}^S , but it does not provide a very good fit at low ϕ_{12} . The quality of the fit can be improved by introducing a higher-order term in order to account from deviations from the Porter model. This is known as the Margules equation, $\ln\gamma_{12} = [A_1 + 2(A_2 - A_1)\phi_{12}]\phi_2^2$, where $A_1 = A + B$ and $A_2 = A - B$ [314]. The parameters A and B result from a mathematical expansion of the expression for the excess Gibbs free energy, such that A in the Porter equation becomes $A + B(\phi_2 - \phi_{12})$. Introducing the Margules equation into the extended Langmuir model results in Equation 6.4:

$$\phi_{12}^S = \frac{\beta\phi_{12}e^{[A_1+2(A_2-A_1)\phi_{12}][1-\phi_{12}]^2}}{1 + (\beta - 1)\phi_{12}e^{[A_1+2(A_2-A_1)\phi_{12}][1-\phi_{12}]^2}} \quad (6.4)$$

The least-squares fitted curve, shown in red in Figure 6.9, has $A_1 = 1.33 \pm 0.12$, $A_2 = 1.89 \pm 0.14$ and $\beta = 0.80 \pm 0.12$. It provides a better fit than Equation 6.3, which indicates that the mixtures deviate significantly from the Porter equation. This is not an unexpected result, considering that the Porter equation is usually applied to mixtures of nonpolar components with similar sizes [314]. Equation 6.4 can successfully describe the nonideal surface behaviour of the $[C_2mim]_{(1-x)}[C_{12}mim]_x[Tf_2N]$ mixtures.

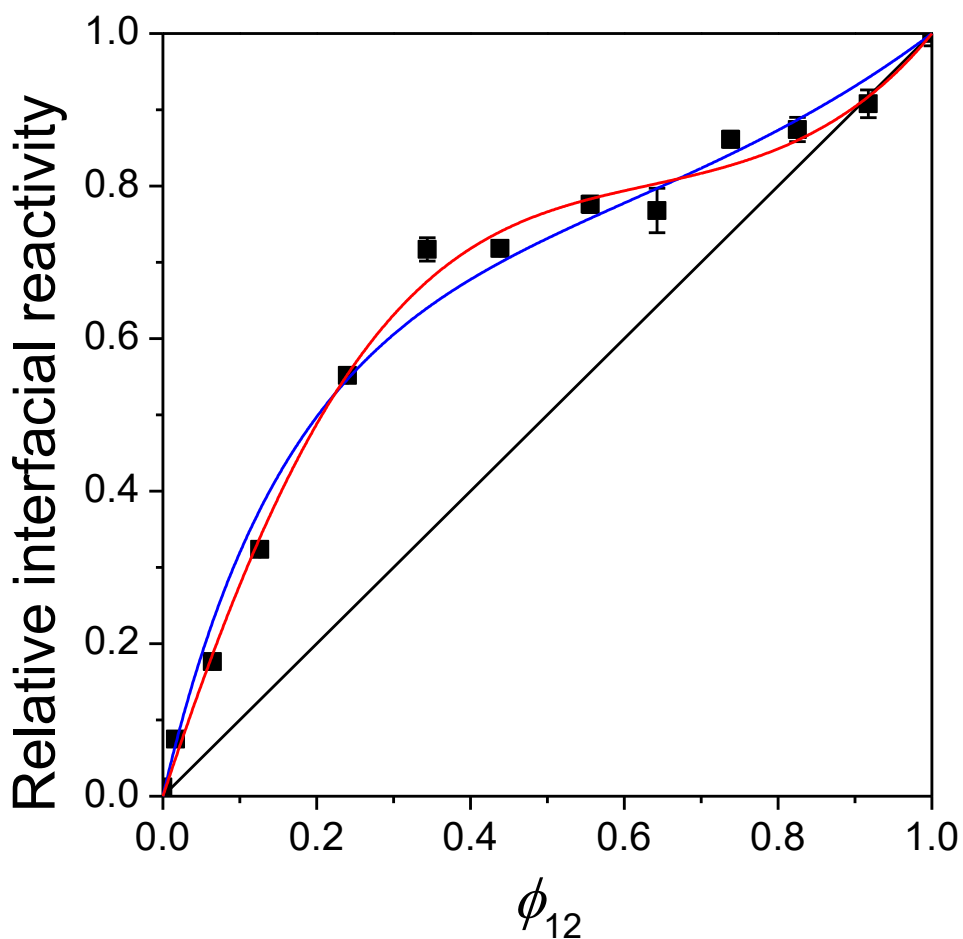


Figure 6.9. OH yield of $[C_2mim]_{(1-x)}[C_{12}mim]_x[Tf_2N]$ mixtures relative to $[C_{12}mim][Tf_2N]$ (black symbols), plotted as a function of its bulk volume fraction ϕ_{12} . The blue line is a fitted extended Langmuir isotherm modified with the Porter model of mixing (Equation 6.3). The red line is a fit to the extended Langmuir isotherm modified with the Margules model (Equation 6.4).

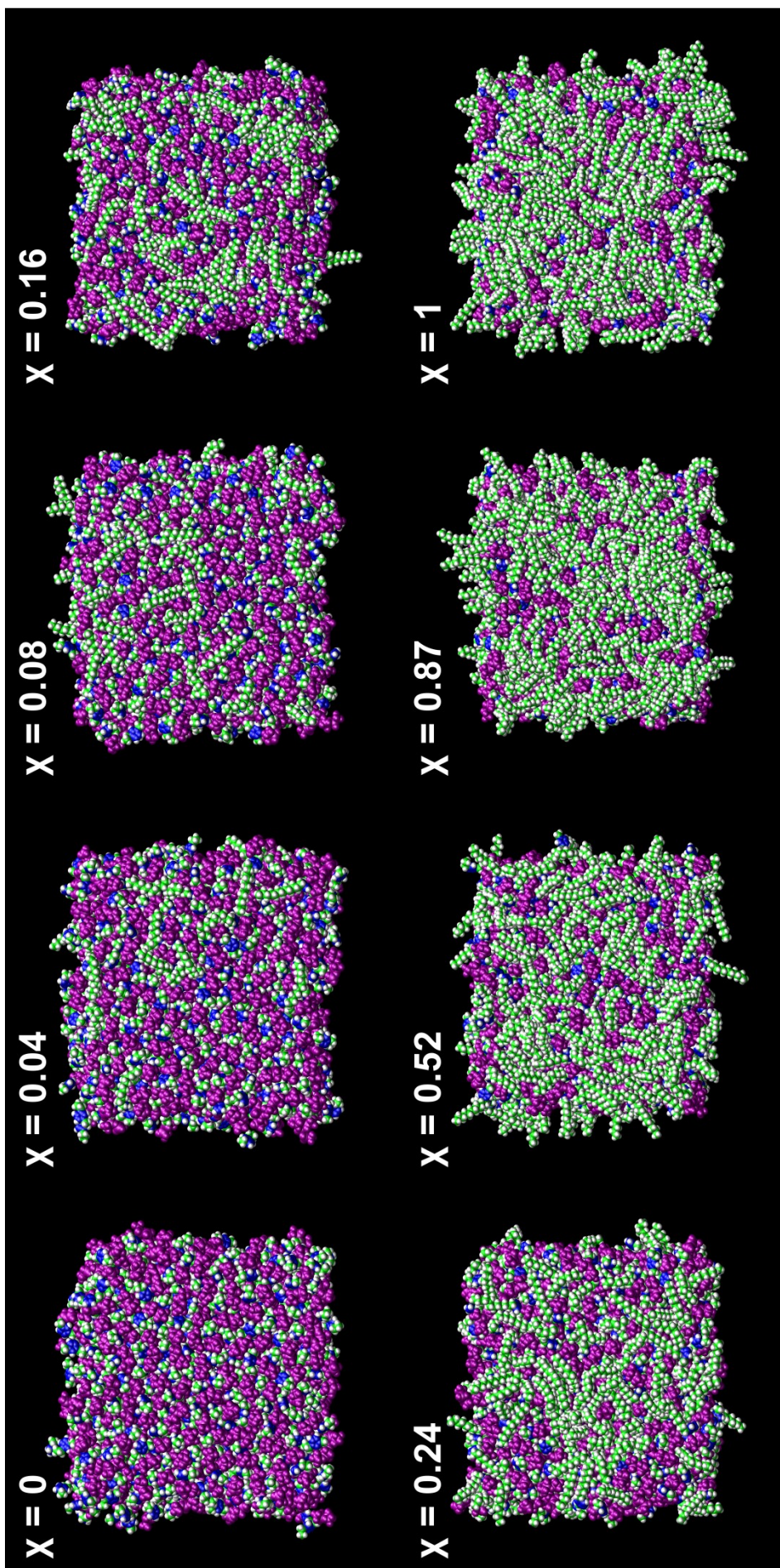


Figure 6.10. Top-down view of the vacuum-liquid surface of $[\text{C}_2\text{mim}]_{1-x}[\text{C}_{12}\text{mim}]_x[\text{Tf}_2\text{N}]$ mixtures for different x , indicated in the figure. Atoms belonging to $[\text{Tf}_2\text{N}]^-$ are purple. The carbon and nitrogen atoms of the imidazolium ring are shown in blue. All C atoms in the cation methyl and alkyl groups are green, and all H atoms are white.

Returning to Figure 6.8, the deviation from the extended Langmuir model for the $[\text{C}_2\text{mim}]_{(1-x)}[\text{C}_{12}\text{mim}]_x[\text{Tf}_2\text{N}]$ mixtures is particularly marked at high x . One possible explanation is the presence of interactions between $[\text{C}_{12}\text{mim}]^+$ cations, such as nonpolar interactions between their alkyl chains. Visual inspection of MD simulated IL mixtures in Figure 6.10 indicates that the $[\text{C}_{12}\text{mim}]^+$ alkyl chains tend to form aggregates at the surface for $x \geq 0.16$. These simulations were performed by collaborators at Montana State University using an OPLS All-Atom force field identical to that employed in Chapter 4. It can also be appreciated in Figure 6.10 that $[\text{C}_{12}\text{mim}]^+$ cations occupy a greater fraction of the surface than expected from stoichiometry. In addition, the surface density of secondary H atoms has been quantified using the double cubic lattice method [268]. This analysis showed that the excess of CH_2 groups at the surface with respect to stoichiometric values follows the excess of RAS-LIF reactivity in Figure 6.7 (b), peaking at $x = 0.24$ [315].

The RAS-LIF and MD simulations results help to build a picture of the surface mixing behaviour of these systems: At low x , the $[\text{C}_{12}\text{mim}]^+$ cations interact mainly with $[\text{C}_2\text{mim}][\text{Tf}_2\text{N}]$ and their surface affinity is well described by a Langmuir-isotherm-type model. At high x , the long-chain cations aggregate together and begin to saturate the surface without reaching full monolayer coverage. Interactions between $[\text{C}_{12}\text{mim}]^+$ cations affect their surface affinity, and the mixture can no longer be thought of as a dilute solution of $[\text{C}_{12}\text{mim}][\text{T}_2\text{N}]$ in $[\text{C}_2\text{mim}][\text{Tf}_2\text{N}]$. Despite the aggregation of $[\text{C}_{12}\text{mim}]^+$ cations, they do not form a monolayer on the surface because it has a high entropic cost compared to traditional surfactants in water.

The $[\text{C}_2\text{mim}]_{(1-x)}[\text{C}_{12}\text{mim}]_x[\text{Tf}_2\text{N}]$ mixtures can be thought of as an intermediate case between the fully miscible systems described by Oliveira [298, 301] and Lemraski [302], and the IL + EAN mixtures discussed in the introduction, which form surface monolayers and aggregates of the least polar component at relatively low concentrations [295, 296, 299]. The closest examples reported in the literature are mixtures of $[\text{C}_n\text{mim}][\text{Br}]$ ($n = 10 - 16$) with $[\text{C}_4\text{mim}][\text{BF}_4]$ studied by Li and co-workers [297]. These mixtures show a decrease in surface tension with $[\text{C}_n\text{mim}][\text{Br}]$ concentration but, instead of having a clearly defined plateau, the surface tension keeps decreasing after the critical aggregation concentration, indicating the absence of a full monolayer of the long-chain IL. The authors argued that electrostatic repulsions between cation headgroups disrupt the formation of aggregates, which is why micellization was not as strong as in IL + EAN and IL + water mixtures [297]. The RAS-LIF results presented

in Figure 6.7 strongly resemble the trend in surface tension with composition for $([C_n\text{mim}][\text{Br}])_x([C_4\text{mim}][\text{BF}_4])_{(1-x)}$ [297]. Li's study defined the critical aggregation concentration as the breakpoint in surface tension as a function of concentration. By analogy, the concentration at which aggregates are formed in $[C_2\text{mim}]_{(1-x)}[C_{12}\text{mim}]_x[\text{Tf}_2\text{N}]$ would be approximately $x = 0.24$. This is in reasonable agreement with the MD snapshots in Figure 6.10, which qualitatively show aggregation of alkyl chains from $x = 0.16$ onwards.

The bulk aggregation behaviour of $[C_2\text{mim}]_{(1-x)}[C_{12}\text{mim}]_x[\text{Tf}_2\text{N}]$ has been investigated by collaborators at the University of York and the Rutherford Appleton Laboratory. The technique employed was small and wide-angle X-ray scattering (SWAXS), previously shown to provide information on IL bulk nanostructure [316]. In the SWAXS measurements, a contribution from nonpolar domains starts to become evident at $x = 0.16 - 0.24$ [317]. This suggests that a percolation network of nonpolar domains is formed through the bulk, as was previously shown for pure $[C_n\text{mim}][\text{Tf}_2\text{N}]$ ILs of sufficiently long chain lengths ($n > 4$) [318]. The fact that the critical concentration for the formation of aggregates in the bulk is close to the breakpoint in RAS-LIF reactivity may indicate that the bulk and surface structures of the mixtures are interrelated.

The discussion above has shown that the RAS-LIF results support the existence of aggregates in $[C_2\text{mim}]_{(1-x)}[C_{12}\text{mim}]_x[\text{Tf}_2\text{N}]$; however, there are some further details that should be considered. Namely, the RAS-LIF reactivity and $[C_{12}\text{mim}][\text{Tf}_2\text{N}]$ surface fraction might not be related in the same way to alkyl coverage. For example, a change in alkyl chain orientation with x would cause this effect. A preliminary analysis of the MD simulations in Figure 6.10 shows that, at higher x , the dodecyl chains in $[C_{12}\text{mim}]^+$ have, on average, a more normal orientation with respect to the surface and are packed closer together [315]. This could partially explain why the reactivity in Figure 6.8 is lower than expected for an ideal mixing behaviour: if the chains are vertically oriented, there will be more CH_3 groups exposed to the $O(^3P)$ atoms and fewer CH_2 groups available to them, and this will reduce the OH yield due to the difference in reactivity between these types of C–H sites. However, the extent of this effect on the RAS-LIF yields is not known. Further simulations and experiments at a higher collision energy, such as RAS-MS, would help to clarify this issue.

6.4.2. Surface structure of $[C_6mim][BF_4]_{(1-x)}[Tf_2N]_x$

The RAS-LIF results for $[C_6mim][BF_4]_{(1-x)}[Tf_2N]_x$ mixtures in Table 6.2 show that the alkyl surface coverage depends on the composition of the mixture, despite the fact that both components contain the same cation. This result is not unexpected: as seen in Chapter 4, the steric bulk of the anion affects the concentration of cations at the surface. In order to discern any deviations from stoichiometric behaviour, the OH yield is plotted as a function of x in Figure 6.11. In this case the alkyl coverage is *below* the stoichiometric value at low x , and very close to it at high x . This may be surprising a priori, considering the high surface activity of the alkyl chains. The deviation from the line must be the result of nonstoichiometric concentrations of anions at the surface, which affect the alkyl coverage indirectly. The reactivity is closer to that of pure $[C_6mim][Tf_2N]$, implying that the surface is enriched in $[Tf_2N]^-$ and depleted in $[BF_4]^-$ anions. It follows that these two anions possess different surface affinities. As discussed in Chapter 4, the anions in pure ILs are located at different average depths from the surface, and the alkyl coverage is not just a consequence of ionic volume, but also of the surface activity of the anion. $[Tf_2N]^-$ anions are very nonpolar and their CF_3 groups tend to be exposed at the surface, whereas $[BF_4]^-$ lies on average deeper into the bulk due to its stronger interaction with the cation headgroup.

In a recent LEIS study, Villar-Garcia and co-workers characterised the anion coverage at the surface of mixtures containing the same cation, $[C_4mim]^+$, and different anion combinations ($[I]^- + [Tf_2N]^-$, $[Cl]^- + [Tf_2N]^-$ and $[HSO_3]^- + [BF_4]^-$) [306]. Their results showed a strong enrichment of the more surface-active anion, in some cases completely depleting the surface of the other component. The deviation from ideality peaked at low concentrations of the more surface-active anion, which agrees qualitatively with the RAS-LIF results for $[C_6mim][BF_4]_{(1-x)}[Tf_2N]_x$ in Figure 6.11. It was proposed that weaker cation-anion interactions are more easily broken, leading to a surface that is more enriched in the less polar anion [306]. The RAS-LIF results presented here are in agreement with this interpretation, since the $[Tf_2N]^- - [C_6mim]^+$ interaction is weaker than the $[BF_4]^- - [C_6mim]^+$ interaction [276]. The enrichment of $[Tf_2N]^-$ at the surface causes a consequent decrease in $[C_6mim]^+$ concentration with respect to stoichiometry, necessary to maintain the electroneutrality of the interface.

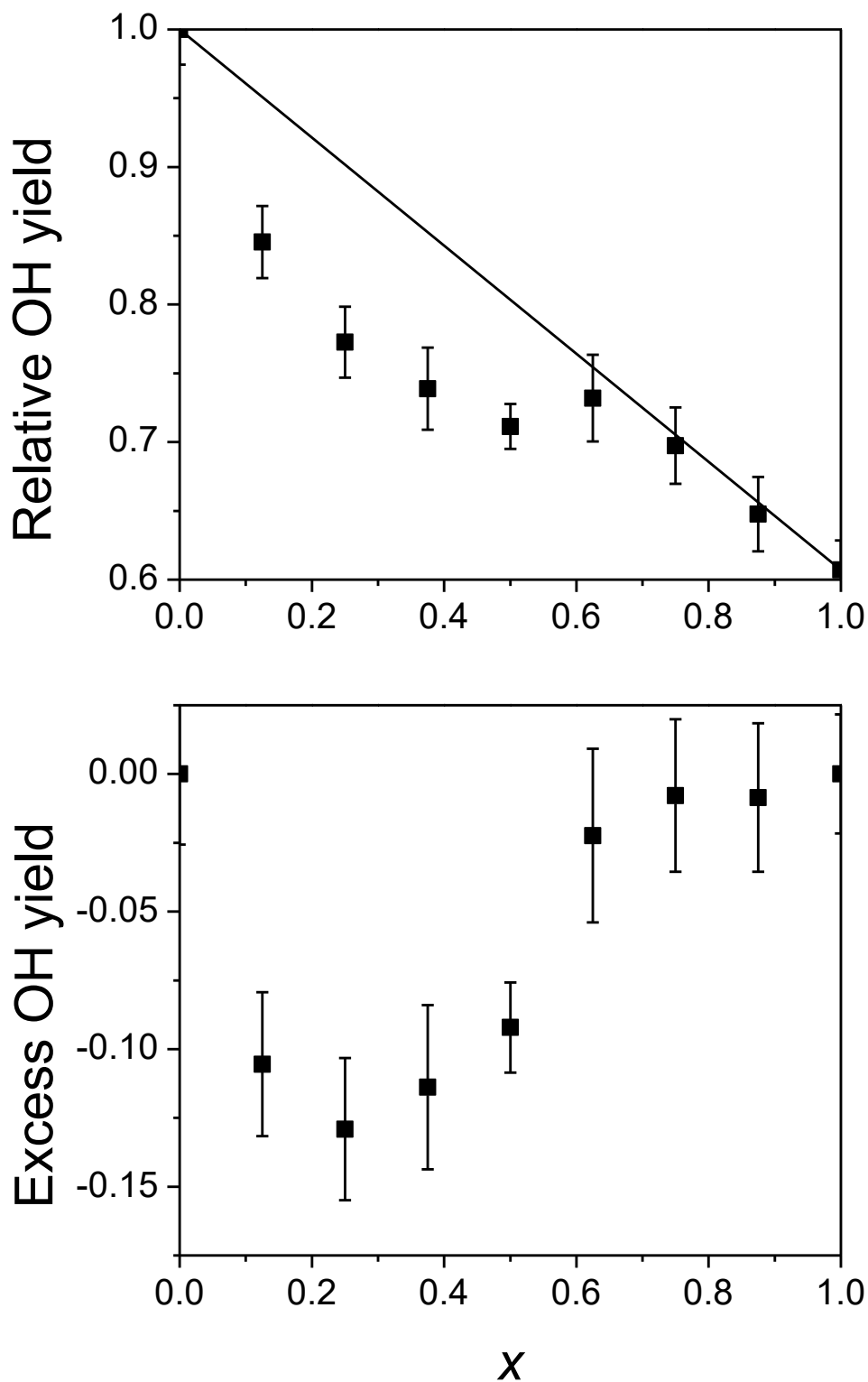


Figure 6.9. Upper panel: OH yield of $[C_6mim][BF_4]_{(1-x)}[Tf_2N]_x$ mixtures relative to $[C_6mim][Tf_2N]$, plotted as a function of x . The diagonal line represents the yield expected for a surface with stoichiometric composition. Lower panel: excess OH yield as a function of x .

No other measurements of $[\text{C}_6\text{mim}][\text{BF}_4]_{(1-x)}[\text{Tf}_2\text{N}]_x$ interfaces have been reported to date, so it is not possible to compare the RAS-LIF results against other techniques. However, there are a few studies of similar systems available in the literature. MD simulations of IL mixtures with a common cation, namely $[\text{C}_4\text{mim}][\text{Cl}]_{0.5}[\text{PF}_6]_{0.5}$, $[\text{C}_4\text{mim}][\text{Cl}]_{0.5}[\text{OTf}]_{0.5}$ [309] and $[\text{C}_4\text{mim}][\text{Cl}]_{(1-x)}[\text{Tf}_2\text{N}]_x$ [308], have been performed. In all cases the more nonpolar anion was found to be close to the surface, consistent with the present results and with the LEIS experiments introduced above. The theoretical study of $[\text{C}_4\text{mim}][\text{Cl}]_{(1-x)}[\text{Tf}_2\text{N}]_x$ [308] found a surface enrichment of $[\text{Cl}]^-$ which agrees qualitatively, but not quantitatively, with Villar-Garcia's LEIS results [306].

Experiments on the same mixture using two different techniques reached conflicting conclusions on its surface composition: TOF-SIMs detected a strong segregation of $[\text{Tf}_2\text{N}]^-$ at the surface of $[\text{C}_4\text{mim}][\text{PF}_6]_{(1-x)}[\text{Tf}_2\text{N}]_x$ [307], whereas HRBS did not find any enrichment for the same mixture [304]. This highlights the importance of surface sensitivity in the analysis of IL mixtures. The results presented in this chapter show that, thanks to its surface-specific character, RAS-LIF enables the detection of small differences in alkyl surface coverage. However, cross-calibration with other experimental techniques and theoretical simulations is necessary in order to fully understand the results and quantify absolute alkyl coverages, as opposed to relative values.

6.5. Summary points

- (1) RAS-LIF of binary IL mixtures efficiently characterises their differences in alkyl coverage, which opens the possibility of fine-tuning the polarity of IL surfaces using mixtures of ions.
- (2) The trends in alkyl coverage deviate from stoichiometry in both $[\text{C}_2\text{mim}]_{(1-x)}[\text{C}_{12}\text{mim}]_x[\text{Tf}_2\text{N}]$ and $[\text{C}_6\text{mim}][\text{BF}_4]_{(1-x)}[\text{Tf}_2\text{N}]_x$. This indicates a preferential surface occupation of the more nonpolar component: $[\text{C}_{12}\text{mim}]^+$ in the $[\text{Tf}_2\text{N}]$ -based mixtures, and $[\text{Tf}_2\text{N}]^-$ in the $[\text{C}_6\text{mim}]$ -based mixtures.
- (3) The surface enrichment is clearly distinguished thanks to the surface-specific character of RAS-LIF. The results are comparable to those from TOF-SIMS and LEIS on similar mixtures, as opposed to ARXPS and HRBS which did not detect any deviations from stoichiometry due to their greater penetration depth (and possibly misinterpretation of the ARXPS data).
- (4) For both mixtures, the deviation from stoichiometry is stronger at low loadings of the more surface-active component, peaking at mole fractions $x \sim 0.25$. At higher loadings the surface starts to become saturated in the solute and the growth is slower; however, full coverage equivalent to the pure liquid is not reached for the highest loading studied, $x \sim 0.87$.
- (5) The saturation behaviour of $[\text{C}_2\text{mim}]_{(1-x)}[\text{C}_{12}\text{mim}]_x[\text{Tf}_2\text{N}]$ at large x could be the result of $[\text{C}_{12}\text{mim}]^+$ aggregates forming at the surface; although other effects on the RAS-LIF yield, such as a difference in chain orientation, should not be dismissed. The turning point between diluted and saturated behaviour in RAS-LIF is approximately the same for nanoscale aggregation in the bulk, determined from SWAXS experiments.

Chapter 7.

Conclusions and future work

The work presented in this thesis has shown that RAS-LIF using $O(^3P)$ atoms is a powerful technique to characterise liquid surfaces containing hydrocarbon groups. The results have provided information on the surface composition of the liquids, as well as the dynamics of their interfacial H-abstraction reactions. The main feature of these reactions is that they proceed mostly through direct IS collisions, but there is some accommodation of translational and rotational energy of the products. The fact that direct scattering dominates the mechanism indicates that the reaction products are formed in the outer surface; therefore, RAS is a surface-sensitive technique.

7.1. Reactive $O(^3P)$ scattering on an unsaturated hydrocarbon surface

The reaction between $O(^3P)$ atoms and squalene has been studied for the first time. The results imply that the addition of $O(^3P)$ to unsaturated sites is a major reaction channel, similar to gas-phase reactions with smaller partially unsaturated hydrocarbons. It follows from this that squalene exposes some of its double bonds at its surface.

The dynamical features of the H-abstraction reaction have been studied in detail by characterising the rotational and vibrational energy of the OH products. The large fraction of high-energy products from squalene indicates that there is a substantial IS component which is similar in its mechanism to a gas-phase reaction. The dynamics are highly specific to the type of C–H bond where abstraction takes place. The rotational and translational energy of the IS component is much higher for squalene than for squalane, which is a consequence of the allylic bonds in squalene having lower dissociation energy, and therefore more energy available to the products. In addition, both liquids produce a fraction of cold products from accommodation at the surface, as demonstrated by the fact that their rotational distributions present a room-temperature component. The fractions of rotational and translational thermalisation are not

equivalent, which supports the idea that a binary IS/TD distribution of products is insufficient to describe the interfacial reactions.

These results tie in with previous OH scattering experiments on squalene and squalane [19, 20], which found that the surface of squalene was more reactive towards OH radicals. Further research on these reactions is currently being undertaken by the McKendrick group in order to better understand their mechanisms. The new experiments employ a molecular beam of OH radicals which provides a defined collision energy, incident angle and internal state of the incident OH. Preliminary results show that the reactivity of squalane is not very dependent on collision energy, whilst squalene is less reactive at higher collision energies. This indicates that addition to unsaturated sites is favoured for cold OH radicals, as shown in previous work using photolytic sources of the OH more similar to the approach in this thesis [19, 20].

In the future, it is intended that a planar LIF imaging system will be implemented in order to improve the spatial resolution of the experiments. The probe beam will be horizontally expanded into a sheet so that it covers the area in front of the wheel. Using an image intensifier and a CCD camera, an image of the OH radicals in the plane of the probe laser will be obtained. This will allow the angular distributions of the products to be studied in detail as the angle of incidence and collision energy are varied.

The LIF imaging experiments are in line with future directions in the field of gas-liquid dynamics. In fact, the velocity distributions of HCl scattering on SAM surfaces have recently been characterised by velocity map imaging [319]. Another long-term goal of fundamental reaction dynamics at surfaces is the study of liquids with high vapour pressure. From the point of view of atmospheric chemistry, it would undoubtedly be interesting to study reactions at other liquid surfaces that resemble aerosol particles. Reaction dynamics at water surfaces are also important in countless environmental and biological processes. These types of reactions cannot be studied with the rotating wheel approach due to the high vapour pressure of the liquids. The solution will likely involve the use of liquid microjets [320, 321] or microfluidic devices under vacuum [322]. A liquid microjet has already been used to study the scattering and evaporation of gases from squalane [43, 44], although scattering from water microjets presents some technical problems. Once these challenges are overcome, it would be possible in principle to apply this approach to the study of $O(^3P)$ reactions on other liquid surfaces.

7.2. Reactive O(³P) scattering for surface analysis of ionic liquids

In this thesis, the use of RAS-LIF as an analytical tool to characterise the alkyl coverage of IL surfaces has been consolidated. Expanding on previous proof-of-concept research on [C_nmim][Tf₂N] [10, 11, 48, 104], the technique has been applied to a wider variety of ILs containing other anions and pyrrolidinium-based cations. Differences in alkyl coverage can be quantitatively characterised by RAS, as opposed to most surface analysis techniques previously employed on ILs. It has been found that alkyl coverage depends strongly on the steric bulk of the anion and the strength of its noncovalent interactions with the cations. The cation headgroup, however, does not have a large effect: in pyrrolidinium- and imidazolium-based ILs, the interfacial reactivity is determined by the length of the alkyl chain, but it is independent of the identity of the headgroup. In all cases nonpolar alkyl chains have a preference to protrude towards the vacuum. Similarly, in binary mixtures of ILs the more nonpolar component preferentially occupies the surface, as shown by their alkyl chain coverage. Trends in alkyl coverage with composition have been accurately characterised for two binary IL mixtures. This makes it possible to fine-tune the nonpolar character of the IL surface by mixing two liquids.

The ultimate goal of this research is the quantitative characterisation of the *absolute* alkyl coverage of the IL surfaces. To achieve this, it is necessary to gain further understanding of the reaction mechanism. One possible approach is to compare the RAS-LIF results with complementary RAS-MS experiments at higher collision energy. The RAS-MS experiments by the Minton group also offer the possibility of detecting other products besides OH, which would provide further information on the reaction mechanism. It would also be possible to selectively deuterate specific groups in the IL and detect the products of D abstraction as opposed to H abstraction. This would allow reaction with different types of H atom at the surface to be distinguished. In addition, in principle other atomic projectiles that react with different types of surface atoms could be employed.

Realistic theoretical simulations of the interfacial reactions can also be used to unravel their mechanisms. QM/MM calculations, which are currently being developed by collaborators, will be of great help in interpreting the RAS-LIF results. However, QM/MM is nowadays still computationally expensive and cannot be performed with the same speed as the experiments.

This thesis has covered only a few examples of the thousands of ILs and mixtures that are currently available. The possibilities for future experiments are almost endless, so it is important to choose systems that can provide the most useful information. At present, mixtures of ILs containing hydrocarbon and fluorocarbon chains are being studied by RAS-LIF in our laboratory. These experiments will investigate the surface affinity of fluorocarbon chains with respect to hydrocarbon chains and give insight into their mixing behaviour.

In the future, it would be interesting to explore systems that are directly relevant to particular applications of ionic liquids. For example, it should be possible to characterise the surface activity of a catalyst with pendant alkyl groups dissolved in an IL, which would be useful for applications such as SILP. The surface enrichment of palladium- and rhodium-containing catalysts in ILs has already been studied by ARXPS [323, 324]. Similar catalysts containing alkyl chains could be probed by RAS-LIF, which would provide superior surface sensitivity and discrimination over ARXPS measurements.

References

1. G.M. Nathanson. Molecular beam studies of gas-liquid interfaces. *Annu. Rev. Phys. Chem.* **55**, 231-255 (2004).
2. R.D. Levine. *Molecular Reaction Dynamics*. (Cambridge University Press, 2005).
3. H. Kelso, S.P.K. Kohler, D.A. Henderson, and K.G. McKendrick. Dynamics of the gas-liquid interfacial reaction of O(³P) atoms with hydrocarbons. *J. Chem. Phys.* **119**(19), 9985-9988 (2003).
4. S.P.K. Kohler, et al. The effects of surface temperature on the gas-liquid interfacial reaction dynamics of O(³P) plus squalane. *J. Chem. Phys.* **122**(2), 024712 (2005).
5. S.P.K. Kohler, M. Allan, M.L. Costen, and K.G. McKendrick. Direct gas-liquid interfacial dynamics: The reaction between O(³P) and a liquid hydrocarbon. *J. Phys. Chem. B* **110**(6), 2771-2776 (2006).
6. M. Allan, P.A.J. Bagot, M.L. Costen, and K.G. McKendrick. Temperature dependence of OH yield, translational energy, and vibrational branching in the reaction of O(³P)(g) with liquid squalane. *J. Phys. Chem. C* **111**(40), 14833-14842 (2007).
7. M. Allan, et al. Dynamics of interfacial reactions between O(³P) atoms and long-chain liquid hydrocarbons. *Phys. Scr.* **76**(3), C42-C47 (2007).
8. M. Allan, et al. Influence of molecular and supramolecular structure on the gas-liquid interfacial reactivity of hydrocarbon liquids with O(³P) atoms. *J. Phys. Chem. C* **112**(5), 1524-1532 (2008).
9. C. Waring, et al. Dynamics of the Reaction of O(³P) Atoms with Alkylthiol Self-assembled Monolayers. *J. Phys. Chem. A* **113**(16), 4320-4329 (2009).
10. C. Waring, et al. O(³P) Atoms as a Probe of Surface Ordering in 1-Alkyl-3-methylimidazolium-Based Ionic Liquids. *J. Phys. Chem. Lett.* **1**(1), 429-433 (2010).
11. C. Waring, et al. O(³P) Atoms as a Chemical Probe of Surface Ordering in Ionic Liquids. *J. Phys. Chem. A* **114**(14), 4896-4904 (2010).
12. C. Waring, et al. How Penetrable Are Thioalkyl Self-Assembled Monolayers? *J. Phys. Chem. Lett.* **1**(13), 1917-1921 (2010).
13. T. Moise and Y. Rudich. Reactive uptake of ozone by proxies for organic aerosols: Surface versus bulk processes. *J. Geophys Res-Atmos* **105**(D11), 14667-14676 (2000).
14. Y. Rudich. Laboratory Perspectives on the Chemical Transformations of Organic Matter in Atmospheric Particles. *Chem. Rev.* **103**(12), 5097-5124 (2003).
15. R.C. Chapleski, Y. Zhang, D. Troya, and J.R. Morris. Heterogeneous chemistry and reaction dynamics of the atmospheric oxidants, O₃, NO₃, and OH, on organic surfaces. *Chem. Soc. Rev.*, Advance Article (2016).
16. T. Moise, J.M. Flores, and Y. Rudich. Optical Properties of Secondary Organic Aerosols and Their Changes by Chemical Processes. *Chem. Rev.* **115**(10), 4400-4439 (2015).
17. T.M. D'Andrea, et al. Oxidation of Organic Films by Beams of Hydroxyl Radicals. *J. Phys. Chem. B* **112**(2), 535-544 (2008).
18. P.A.J. Bagot, C. Waring, M.L. Costen, and K.G. McKendrick. Dynamics of inelastic scattering of OH radicals from reactive and inert liquid surfaces. *J. Phys. Chem. C* **112**(29), 10868-10877 (2008).

19. C. Waring, et al. Collision dynamics and reactive uptake of OH radicals at liquid surfaces of atmospheric interest. *PCCP* **13**(18), 8457-8469 (2011).
20. K.L. King, et al. Inelastic scattering of OH radicals from organic liquids: isolating the thermal desorption channel. *PCCP* **15**(31), 12852-12863 (2013).
21. T. Nishikawa, K. Sonoda, and K. Nakanishi. Effect of atomic oxygen on polymers used as surface materials for spacecrafts. In *Proceedings of the Twenty-First Symposium on Electrical Insulating Materials* (1988).
22. M.R. Reddy. Effect of low earth orbit atomic oxygen on spacecraft materials. *J. Mater. Sci.* **30**(2), 281-307 (1995).
23. T.K. Minton, J. Zhang, D.J. Garton, and J.W. Seale. Collision-Assisted Erosion of Hydrocarbon Polymers in Atomic-Oxygen Environments. *High Perform. Polym.* **12**(1), 27-42 (2000).
24. C. Oehr. Plasma surface modification of polymers for biomedical use. *Nucl. Instr. Meth. Phys. Res., Sect. B* **208**, 40-47 (2003).
25. I. Pashkuleva, A.P. Marques, F. Vaz, and R.L. Reis. Surface modification of starch based biomaterials by oxygen plasma or UV-irradiation. *J. Mater. Sci.-Mater. Med.* **21**(1), 21-32 (2010).
26. B. Halford. Oxygen gives new life to art. *Chemical & Engineering News Archive* **83**(3), 36-37 (2005).
27. K.E. Johnson. What's an ionic liquid? *Interface-Electrochemical Society* **16**(1), 38-41 (2007).
28. M.J. Earle and K.R. Seddon. Ionic liquids. Green solvents for the future. *Pure Appl. Chem.* **72**(7), 1391-1398 (2000).
29. J. Holbrey and K. Seddon. Ionic liquids. *Clean Products and Processes* **1**(4), 223-236 (1999).
30. T. Welton. Room-temperature ionic liquids. Solvents for synthesis and catalysis. *Chem. Rev.* **99**(8), 2071-2083 (1999).
31. N.V. Plechkova and K.R. Seddon. Applications of ionic liquids in the chemical industry. *Chem. Soc. Rev.* **37**(1), 123-150 (2008).
32. T.D. Ho, C. Zhang, L.W. Hantao, and J.L. Anderson. Ionic Liquids in Analytical Chemistry: Fundamentals, Advances, and Perspectives. *Anal. Chem.* **86**(1), 262-285 (2014).
33. J.L. Anthony, J.L. Anderson, E.J. Maginn, and J.F. Brennecke. Anion Effects on Gas Solubility in Ionic Liquids. *J. Phys. Chem. B* **109**(13), 6366-6374 (2005).
34. C. Cadena, et al. Why Is CO₂ So Soluble in Imidazolium-Based Ionic Liquids? *J. Am. Chem. Soc.* **126**(16), 5300-5308 (2004).
35. S. Keskin, D. Kayrak-Talay, U. Akman, and Ö. Hortaçsu. A review of ionic liquids towards supercritical fluid applications. *J. Supercrit. Fluids* **43**(1), 150-180 (2007).
36. J.R. Roscioli and D.J. Nesbitt. Quantum State Resolved Scattering from Room-Temperature Ionic Liquids: The Role of Cation versus Anion Structure at the Interface. *J. Phys. Chem. A* **115**(34), 9764-9773 (2011).
37. O.C. David, et al. On the improved absorption of carbon monoxide in the ionic liquid 1-hexyl-3-methylimidazolium chlorocuprate. *Sep. Purif. Technol.* **97**(0), 65-72 (2012).
38. E. Santos, J. Albo, and A. Irabien. Acetate based Supported Ionic Liquid Membranes (SILMs) for CO₂ separation: Influence of the temperature. *Journal of Membrane Science* **452**(0), 277-283 (2014).
39. A. Riisager, R. Fehrmann, M. Haumann, and P. Wasserscheid. Supported Ionic Liquid Phase (SILP) Catalysis: An Innovative Concept for Homogeneous Catalysis in Continuous Fixed-Bed Reactors. *Eur. J. Inorg. Chem.* **2006**(4), 695-706 (2006).

40. C. Van Doorslaer, et al. Immobilization of molecular catalysts in supported ionic liquid phases. *Dalton Trans.* **39**(36), 8377-8390 (2010).
41. K.R.J. Lovelock. Influence of the ionic liquid/gas surface on ionic liquid chemistry. *PCCP* **14**(15), 5071-5089 (2012).
42. W. Jiang, Y. Wang, T. Yan, and G.A. Voth. A multiscale coarse-graining study of the liquid/vacuum interface of room-temperature ionic liquids with alkyl substituents of different lengths. *J. Phys. Chem. C* **112**(4), 1132-1139 (2008).
43. A.M. Johnson, et al. Ballistic Evaporation and Solvation of Helium Atoms at the Surfaces of Protic and Hydrocarbon Liquids. *J. Phys. Chem. Lett.* **5**(21), 3914-3918 (2014).
44. D.K. Lancaster, et al. Inert Gas Scattering from Liquid Hydrocarbon Microjets. *J. Phys. Chem. Lett.* **4**(18), 3045-3049 (2013).
45. M.E. Saecker, et al. Molecular Beam Scattering from Liquid Surfaces. *Science* **252**(5011), 1421-1424 (1991).
46. C.M. Quintella, A.J. McCaffery, and M.D. Zidan. Direct observation of the kinetics and dynamics of molecular desorption from liquid surfaces. *Chem. Phys. Lett.* **214**(6), 563-568 (1993).
47. K.L. Randall, et al. Scattering of gases from aligned liquid crystals: Collision-induced loss of order at the gas-liquid interface. *J. Chem. Phys.* **105**(21), 9574-9579 (1996).
48. B. Wu, et al. Scattering Dynamics of Hyperthermal Oxygen Atoms on Ionic Liquid Surfaces: [emim][NTf₂] and [C₁₂mim][NTf₂]. *J. Phys. Chem. C* **114**(9), 4015-4027 (2010).
49. K.M. Fiehrer and G.M. Nathanson. Energy and Angle-Resolved Uptake of Organic Molecules in Concentrated Sulfuric Acid. *J. Am. Chem. Soc.* **119**(1), 251-252 (1997).
50. S.R. Cohen, R. Naaman, and J. Sagiv. Translational energy transfer from molecules and atoms to adsorbed organic monolayers of long-chain amphiphiles. *Phys. Rev. Lett.* **58**(12), 1208-1211 (1987).
51. J.W. Lu, et al. Interfacial energy exchange and reaction dynamics in collisions of gases on model organic surfaces. *Prog. Surf. Sci.* **87**(9-12), 221-252 (2012).
52. G. Andersson and C. Ridings. Ion Scattering Studies of Molecular Structure at Liquid Surfaces with Applications in Industrial and Biological Systems. *Chem. Rev.* **114**(17), 8361-8387 (2014).
53. M.E. Saecker and G.M. Nathanson. Collisions of protic and aprotic gases with hydrogen-bonding and hydrocarbon liquids. *J. Chem. Phys.* **99**(9), 7056-7075 (1993).
54. M.E. King, G.M. Nathanson, M.A. Hanninglee, and T.K. Minton. Probing the microscopic corrugation of liquid surfaces with gas-liquid collisions. *Phys. Rev. Lett.* **70**(7), 1026-1029 (1993).
55. M.E. Saecker and G.M. Nathanson. Collisions of protic and aprotic gases with a perfluorinated liquid. *J. Chem. Phys.* **100**(5), 3999-4005 (1994).
56. S.L. Lednovich and J.B. Fenn. Absolute evaporation rates for some polar and nonpolar liquids. *AIChE J.* **23**(4), 454-459 (1977).
57. J.E. Hurst, et al. Observation of Direct Inelastic Scattering in the Presence of Trapping-Desorption Scattering: Xe on Pt(111). *Phys. Rev. Lett.* **43**(16), 1175-1177 (1979).
58. N. Lipkin, R.B. Gerber, N. Moiseyev, and G.M. Nathanson. Atom scattering studies of liquid structure and dynamics: Collisions of Xe with a model of squalane. *J. Chem. Phys.* **100**(11), 8408-8417 (1994).

59. S.R. Cohen, R. Naaman, and J. Sagiv. Rotational and state-resolved translational distributions of NO scattered from organized amphiphilic monolayers. *J. Chem. Phys.* **88**(4), 2757-2763 (1988).
60. J.M. Zhang, D.J. Garton, and T.K. Minton. Reactive and inelastic scattering dynamics of hyperthermal oxygen atoms on a saturated hydrocarbon surface. *J. Chem. Phys.* **117**(13), 6239-6251 (2002).
61. W.A. Alexander, et al. Kinematics and dynamics of atomic-beam scattering on liquid and self-assembled monolayer surfaces. *Faraday Discuss.* **157**(0), 355-374 (2012).
62. M.E. King, M.E. Saecker, and G.M. Nathanson. The thermal roughening of liquid surfaces and its effect on gas-liquid collisions. *J. Chem. Phys.* **101**(3), 2539-2547 (1994).
63. M.E. King, K.M. Fiehrer, G.M. Nathanson, and T.K. Minton. Effects of thermal roughening on the angular distributions of trapping and scattering in gas-liquid collisions. *J. Phys. Chem. A* **101**(36), 6556-6561 (1997).
64. T. Yan, W.L. Hase, and J.C. Tully. A washboard with moment of inertia model of gas-surface scattering. *J. Chem. Phys.* **120**(2), 1031-1043 (2004).
65. S.R. Cohen, R. Naaman, and G.G. Balint-Kurti. Energy distribution between spin-orbit states in NO scattered from organized amphiphilic monolayers. *Chem. Phys. Lett.* **152**(2-3), 269-273 (1988).
66. A.J. Kenyon, A.J. McCaffery, C.M. Quintella, and M.D. Zidan. Liquid surface dynamics: a quantum-resolved scattering study. *Chem. Phys. Lett.* **190**(1-2), 55-58 (1992).
67. A.J. Kenyon, A.J. McCaffery, C.M. Quintella, and M.D. Zidan. Investigation of dynamical processes at liquid surfaces by molecular scattering. *J. Chem. Soc., Faraday Trans.* **89**(21), 3877-3884 (1993).
68. B.G. Perkins, T. Haber, and D.J. Nesbitt. Quantum state-resolved energy transfer dynamics at gas-liquid interfaces: IR laser studies of CO₂ scattering from perfluorinated liquids. *J. Phys. Chem. B* **109**(34), 16396-16405 (2005).
69. B.G. Perkins, Jr. and D.J. Nesbitt. Quantum-state-resolved CO₂ scattering dynamics at the gas-liquid interface: Incident collision energy and liquid dependence. *J. Phys. Chem. B* **110**(34), 17126-17137 (2006).
70. B.G. Perkins, Jr. and D.J. Nesbitt. Quantum-state-resolved CO₂ scattering dynamics at the gas-liquid interface: Dependence on incident angle. *J. Phys. Chem. A* **111**(31), 7420-7430 (2007).
71. B.G. Perkins, Jr. and D.J. Nesbitt. Correlated angular and quantum state-resolved CO₂ scattering dynamics at the gas-liquid interface. *J. Phys. Chem. A* **112**(39), 9324-9335 (2008).
72. B.G. Perkins, Jr. and D.J. Nesbitt. Stereodynamics in state-resolved scattering at the gas-liquid interface. *Proc. Natl. Acad. Sci. U.S.A.* **105**(35), 12684-12689 (2008).
73. B.G. Perkins, Jr. and D.J. Nesbitt. Quantum state-resolved CO₂ collisions at the gas-liquid interface: Surface temperature-dependent scattering dynamics. *J. Phys. Chem. B* **112**(2), 507-519 (2008).
74. J.J. Nogueira, et al. Dynamics of CO₂ Scattering off a Perfluorinated Self-Assembled Monolayer. Influence of the Incident Collision Energy, Mass Effects, and Use of Different Surface Models. *J. Phys. Chem. A* **113**(16), 3850-3865 (2009).
75. B.G. Perkins, Jr. and D.J. Nesbitt. Stereodynamics at the Gas-Liquid Interface: Orientation and Alignment of CO₂ Scattered from Perfluorinated Liquid Surfaces. *J. Phys. Chem. A* **114**(3), 1398-1410 (2010).

76. R. Vasudev, R.N. Zare, and R.N. Dixon. State-selected photodissociation dynamics: Complete characterization of the OH fragment ejected by the HONO \tilde{A} state. *J. Chem. Phys.* **80**(10), 4863-4878 (1984).
77. T.Y. Kang, S.K. Shin, and H.L. Kim. Photodissociation dynamics of allyl alcohol at 193 nm. *J. Phys. Chem. A* **107**(50), 10888-10892 (2003).
78. S.B.M. Bosio and W.L. Hase. Energy transfer in rare gas collisions with self-assembled monolayers. *J. Chem. Phys.* **107**(22), 9677-9686 (1997).
79. G. Li, S.B.M. Bosio, and W.L. Hase. A QM/MM model for O(3P) reaction with an alkyl thiolate self-assembled monolayer. *J. Mol. Struct.* **556**(1-3), 43-57 (2000).
80. T. Yan, W.L. Hase, and J.R. Barker. Identifying trapping desorption in gas-surface scattering. *Chem. Phys. Lett.* **329**(1-2), 84-91 (2000).
81. T. Yan and W.L. Hase. Comparisons of Models for Simulating Energy Transfer in Ne-Atom Collisions with an Alkyl Thiolate Self-Assembled Monolayer. *J. Phys. Chem. B* **106**(33), 8029-8037 (2002).
82. T. Yan, et al. Role of Surface Intramolecular Dynamics in the Efficiency of Energy Transfer in Ne Atom Collisions with a n-Hexylthiolate Self-Assembled Monolayer. *J. Phys. Chem. A* **107**(49), 10600-10607 (2003).
83. N. Isa, et al. Experimental and simulation study of neon collision dynamics with a 1-decanethiol monolayer. *J. Chem. Phys.* **120**(5), 2417-2433 (2004).
84. K.D. Gibson, N. Isa, and S.J. Sibener. Experiments and simulations of Ar scattering from an ordered 1-decanethiol-Au(111) monolayer. *J. Chem. Phys.* **119**(24), 13083-13095 (2003).
85. B.S. Day and J.R. Morris. Packing density and structure effects on energy-transfer dynamics in argon collisions with organic monolayers. *J. Chem. Phys.* **122**(23), 234714 (2005).
86. B. Scott Day, J.R. Morris, and D. Troya. Classical trajectory study of collisions of Ar with alkanethiolate self-assembled monolayers: Potential-energy surface effects on dynamics. *J. Chem. Phys.* **122**(21), 214712 (2005).
87. U.S. Tasić, T. Yan, and W.L. Hase. Dynamics of Energy Transfer in Collisions of O(3P) Atoms with a 1-Decanethiol Self-Assembled Monolayer Surface. *J. Phys. Chem. B* **110**(24), 11863-11877 (2006).
88. W.A. Alexander, et al. Experimental and theoretical studies of the effect of mass on the dynamics of gas/organic-surface energy transfer. *J. Chem. Phys.* **128**(1), (2008).
89. W.A. Alexander, J.R. Morris, and D. Troya. Theoretical Study of the Stereodynamics of CO Collisions with CH₃- and CF₃-Terminated Alkanethiolate Self-Assembled Monolayers. *J. Phys. Chem. A* **113**(16), 4155-4167 (2009).
90. J.W. Lu, W.A. Alexander, and J.R. Morris. Gas-surface energy exchange and thermal accommodation of CO₂ and Ar in collisions with methyl, hydroxyl, and perfluorinated self-assembled monolayers. *PCCP* **12**(39), 12533-12543 (2010).
91. E. Martinez-Nunez, A. Rahaman, and W.L. Hase. Chemical dynamics Simulations of CO₂ scattering off a fluorinated self-assembled monolayer surface. *J. Phys. Chem. C* **111**(1), 354-364 (2007).
92. B.G. Perkins and D.J. Nesbitt. Toward Three-Dimensional Quantum State-Resolved Collision Dynamics at the Gas-Liquid Interface: Theoretical Investigation of Incident Angle. *J. Phys. Chem. A* **113**(16), 4613-4625 (2009).
93. J.J. Nogueira, et al. Chemical Dynamics Simulations of CO₂ in the Ground and First Excited Bend States Colliding with a Perfluorinated Self-Assembled Monolayer. *J. Phys. Chem. C* **114**(43), 18455-18464 (2010).
94. D. Troya. Dynamics of collisions of hydroxyl radicals with fluorinated self-assembled monolayers. *Theor. Chem. Acc.* **131**(1), 1-12 (2012).

95. J.J. Nogueira, Z. Homayoon, S.A. Vázquez, and E. Martínez-Núñez. Chemical Dynamics Study of NO Scattering from a Perfluorinated Self-Assembled Monolayer. *J. Phys. Chem. C* **115**(48), 23817-23830 (2011).
96. M. Monge-Palacios, J.J. Nogueira, and E. Martínez-Núñez. Energy Transfer and Thermal Accommodation in Ozone Scattering from a Perfluorinated Self-Assembled Monolayer. *J. Phys. Chem. C* **116**(48), 25454-25464 (2012).
97. C.D. Wick, J.I. Siepmann, and M.R. Schure. Molecular Simulation of Concurrent Gas-Liquid Interfacial Adsorption and Partitioning in Gas-Liquid Chromatography. *Anal. Chem.* **74**(14), 3518-3524 (2002).
98. S.P.K. Kohler, S.K. Reed, R.E. Westacott, and K.G. McKendrick. Molecular dynamics study to identify the reactive sites of a liquid squalane surface. *J. Phys. Chem. B* **110**(24), 11717-11724 (2006).
99. Y. Peng, et al. Chemical Dynamics Simulation of Ne Atom Scattering off a Squalane Surface. *J. Phys. Chem. C* **112**(51), 20340-20346 (2008).
100. D. Kim and G.C. Schatz. Theoretical investigation of hyperthermal reactions at the gas-liquid interface: O(³P) and squalane. *J. Phys. Chem. A* **111**(23), 5019-5031 (2007).
101. D.J. Garton, et al. Reactive scattering of ground-state and electronically excited oxygen atoms on a liquid hydrocarbon surface. *Faraday Discuss.* **108**, 387-399 (1997).
102. D.J. Garton, et al. Comparative dynamics of Cl(²P) and O(³P) interactions with a hydrocarbon surface. *J. Chem. Phys.* **112**(13), 5975-5984 (2000).
103. J.M. Zhang, H.P. Upadhyaya, A.L. Brunsvold, and T.K. Minton. Hyperthermal reactions of O and O₂ with a hydrocarbon surface: Direct C-C bond breakage by O and H-atom abstraction by O₂. *J. Phys. Chem. B* **110**(25), 12500-12511 (2006).
104. C. Waring, P.A.J. Bagot, M.L. Costen, and K.G. McKendrick. Reactive Scattering as a Chemically Specific Analytical Probe of Liquid Surfaces. *J. Phys. Chem. Lett.* **2**(1), 12-18 (2011).
105. F. Ausfelder and K.G. McKendrick. The dynamics of reactions of O(³P) atoms with saturated hydrocarbons and related compounds. *Prog. React. Kinet. Mec.* **25**(4), 299-370 (2000).
106. P. Andresen and A.C. Luntz. The chemical dynamics of the reactions of O(³P) with saturated hydrocarbons. I. Experiment. *J. Chem. Phys.* **72**(11), 5842-5850 (1980).
107. A.M. Zolot, et al. Quantum-state resolved reaction dynamics at the gas-liquid interface: Direct absorption detection of HF(v,J) product from F(²P) + squalane. *J. Chem. Phys.* **125**(2), 021101 (2006).
108. A.M. Zolot, P.J. Dagdigan, and D.J. Nesbitt. Quantum-state resolved reactive scattering at the gas-liquid interface: F+squalane (C₃₀H₆₂) dynamics via high-resolution infrared absorption of nascent HF(v,J). *J. Chem. Phys.* **129**(19), 194705 (2008).
109. C. Waring, K.L. King, M.L. Costen, and K.G. McKendrick. Dynamics of the Gas-Liquid Interfacial Reaction of O(¹D) with a Liquid Hydrocarbon. *J. Phys. Chem. A* **115**(25), 7210-7219 (2011).
110. A.C. Luntz. Chemical dynamics of the reactions of O(¹D₂) with saturated hydrocarbons. *J. Chem. Phys.* **73**(3), 1143-1152 (1980).
111. C.C. Miller, R.D. van Zee, and J.C. Stephenson. Mechanism of the reaction, CH₄+O(¹D₂) → CH₃+OH, studied by ultrafast and state-resolved photolysis/probe spectroscopy of the CH₄·O₃ van der Waals complex. *J. Chem. Phys.* **114**(3), 1214-1232 (2001).

112. S.T. Govoni and G.M. Nathanson. Exploring the Fate of Water Molecules Striking Concentrated Sulfuric Acid: Scattering versus Solvation. *J. Am. Chem. Soc.* **116**(2), 779-780 (1994).
113. P. Behr, et al. Reaction and desorption of HCl and HBr following collisions with supercooled sulfuric acid. *Geophysical Research Letters* **28**(10), 1961-1964 (2001).
114. B.R. Ringeisen, A.H. Muentner, and G.M. Nathanson. Collisions of DCl with Liquid Glycerol: Evidence for Rapid, Near-Interfacial D \rightarrow H Exchange and Desorption. *J. Phys. Chem. B* **106**(19), 4999-5010 (2002).
115. B.R. Ringeisen, A.H. Muentner, and G.M. Nathanson. Collisions of HCl, DCl, and HBr with Liquid Glycerol: Gas Uptake, D \rightarrow H Exchange, and Solution Thermodynamics. *J. Phys. Chem. B* **106**(19), 4988-4998 (2002).
116. I. Chorny, I. Benjamin, and G.M. Nathanson. Scattering, Trapping, and Ionization of HCl at the Surface of Liquid Glycerol. *J. Phys. Chem. B* **108**(3), 995-1002 (2004).
117. A.H. Muentner, J.L. DeZwaan, and G.M. Nathanson. Collisions of DCl with Pure and Salty Glycerol: Enhancement of Interfacial D \rightarrow H Exchange by Dissolved NaI. *J. Phys. Chem. B* **110**(10), 4881-4891 (2006).
118. J.L. DeZwaan, S.M. Brastad, and G.M. Nathanson. The Roles of Salt Concentration and Cation Charge in Collisions of Ar and DCl with Salty Glycerol Solutions of NaI and CaI₂. *J. Phys. Chem. C* **112**(8), 3008-3017 (2008).
119. J.L. DeZwaan, S.M. Brastad, and G.M. Nathanson. Evidence for Interfacial [FDCl]⁻ in Collisions between DCl and F⁻ in KF-Glycerol Solutions. *J. Phys. Chem. C* **112**(39), 15449-15457 (2008).
120. S.M. Brastad and G.M. Nathanson. Molecular beam studies of HCl dissolution and dissociation in cold salty water. *PCCP* **13**(18), 8284-8295 (2011).
121. L.P. Dempsey, S.M. Brastad, and G.M. Nathanson. Interfacial Acid Dissociation and Proton Exchange Following Collisions of DCl with Salty Glycerol and Salty Water. *J. Phys. Chem. Lett.* **2**(6), 622-627 (2011).
122. A.H. Muentner, J.L. DeZwaan, and G.M. Nathanson. Interfacial interactions of DO with salty glycerol solutions of KI, NaI, LiI, and NaBr. *J. Phys. Chem. C* **111**(41), 15043-15052 (2007).
123. S.M. Brastad, D.R. Albert, M. Huang, and G.M. Nathanson. Collisions of DCl with a Solution Covered with Hydrophobic and Hydrophilic Ions: Tetrahexylammonium Bromide in Glycerol. *J. Phys. Chem. A* **113**(26), 7422-7430 (2009).
124. W.A. Alexander, J.P. Wiens, T.K. Minton, and G.M. Nathanson. Reactions of Solvated Electrons Initiated by Sodium Atom Ionization at the Vacuum-Liquid Interface. *Science* **335**(6072), 1072-1075 (2012).
125. J.P. Wiens, et al. Collisions of Sodium Atoms with Liquid Glycerol: Insights into Solvation and Ionization. *J. Am. Chem. Soc.* **136**(8), 3065-3074 (2014).
126. D. Troya and G.C. Schatz. Theoretical studies of hyperthermal O(³P) collisions with hydrocarbon self-assembled monolayers. *J. Chem. Phys.* **120**(16), 7696-7707 (2004).
127. J.P. Layfield and D. Troya. Theoretical study of the dynamics of F+alkanethiol self-assembled monolayer hydrogen-abstraction reactions. *J. Chem. Phys.* **132**(13), 134307 (2010).
128. B.K. Radak, S. Yockel, D. Kim, and G.C. Schatz. Modeling Reactive Scattering of F(²P) at a Liquid Squalane Interface: A Hybrid QM/MM Molecular Dynamics Study. *J. Phys. Chem. A* **113**(26), 7218-7226 (2009).

129. S. Yockel and G.C. Schatz. Modeling O(³P) and Ar Scattering from the Ionic Liquid [emim][NO₃] at 5 eV with Hybrid QM/MM Molecular Dynamics. *J. Phys. Chem. B* **114**(45), 14241-14248 (2010).
130. X. Li, G.C. Schatz, and D.J. Nesbitt. Anion Effects in the Scattering of CO₂ from the Room-Temperature Ionic Liquids [bmim][BF₄] and [bmim][Tf₂N] : Insights from Quantum Mechanics/Molecular Mechanics Trajectories. *J. Phys. Chem. B* **116**(11), 3587-3602 (2012).
131. E.R. Waclawik, M.C. Goh, and D.J. Donaldson. Inelastic scattering of atoms and molecules from liquid crystal surfaces. *J. Chem. Phys.* **110**(16), 8098-8103 (1999).
132. J.R. Roscioli and D.J. Nesbitt. State-Resolved Scattering at Room-Temperature Ionic Liquid-Vacuum Interfaces: Anion Dependence and the Role of Dynamic versus Equilibrium Effects. *J. Phys. Chem. Lett.* **1**(4), 674-678 (2010).
133. M.P. Ziemkiewich, A. Zutz, and D.J. Nesbitt. Inelastic Scattering of Radicals at the Gas-Ionic Liquid Interface: Probing Surface Dynamics of BMIM-Cl, BMIM-BF₄, and BMIM-Tf₂N by Rovibronic Scattering of NO [²Π_{1/2}(0.5)]. *J. Phys. Chem. C* **116**(27), 14284-14294 (2012).
134. A. Zutz and D.J. Nesbitt. Nonadiabatic Spin-Orbit Excitation Dynamics in Quantum-State-Resolved NO(²Π_{1/2}) Scattering at the Gas-Room Temperature Ionic Liquid Interface. *J. Phys. Chem. C* **119**(16), 8596-8607 (2015).
135. A.W. Gisler and D.J. Nesbitt. On probing ions at the gas-liquid interface by quantum state-resolved molecular beam scattering: the curious incident of the cation in the night time. *Faraday Discuss.* **157**, 297-305 (2012).
136. J.R. Lawrence, S.V. Glass, and G.M. Nathanson. Evaporation of Water through Butanol Films at the Surface of Supercooled Sulfuric Acid. *J. Phys. Chem. A* **109**(33), 7449-7457 (2005).
137. J.R. Lawrence, S.V. Glass, S.-C. Park, and G.M. Nathanson. Surfactant Control of Gas Uptake: Effect of Butanol Films on HCl and HBr Entry into Supercooled Sulfuric Acid. *J. Phys. Chem. A* **109**(33), 7458-7465 (2005).
138. S.V. Glass, S.-C. Park, and G.M. Nathanson. Evaporation of Water and Uptake of HCl and HBr through Hexanol Films at the Surface of Supercooled Sulfuric Acid. *J. Phys. Chem. A* **110**(24), 7593-7601 (2006).
139. D.K. Burden, A.M. Johnson, and G.M. Nathanson. HCl Uptake through Films of Pentanoic Acid and Pentanoic Acid/Hexanol Mixtures at the Surface of Sulfuric Acid. *J. Phys. Chem. A* **113**(51), 14131-14140 (2009).
140. D.K. Burden, A.M. Johnson, J.M. Krier, and G.M. Nathanson. The Entry of HCl through Soluble Surfactants on Sulfuric Acid: Effects of Chain Branching. *J. Phys. Chem. B* **118**(28), 7993-8001 (2014).
141. A.C. Luntz and P. Andresen. The chemical dynamics of the reactions of O(³P) with saturated hydrocarbons. II. Theoretical model. *J. Chem. Phys.* **72**(11), 5851-5856 (1980).
142. D.R. Lide. CRC Handbook of Chemistry and Physics 2004-2005: A Ready-Reference Book of Chemical and Physical Data. (CRC Press, 2004).
143. R.P. Baker, et al. Vector correlations in the 355 nm photolysis of thermal NO₂. *PCCP* **2**(4), 661-664 (2000).
144. B.M. Ocko, et al. Surface freezing in chain molecules: Normal alkanes. *Phys. Rev. E* **55**(3), 3164-3182 (1997).
145. I. Mokbel, A. Blondel-Telouk, D. Vellut, and J. Jose. Vapor-liquid equilibria of two binary mixtures: benzene+n-tetradecane and benzene+squalane. *Fluid Phase Equilib.* **149**(1-2), 287-308 (1998).
146. C.P. Fredlake, et al. Thermophysical Properties of Imidazolium-Based Ionic Liquids. *J. Chem. Eng. Data* **49**(4), 954-964 (2004).

147. M. Kosmulski, J. Gustafsson, and J.B. Rosenholm. Thermal stability of low temperature ionic liquids revisited. *Thermochim. Acta* **412**(1-2), 47-53 (2004).
148. H. Jin, et al. Physical properties of ionic liquids consisting of the 1-butyl-3-methylimidazolium cation with various anions and the bis(trifluoromethylsulfonyl)imide anion with various cations. *J. Phys. Chem. B* **112**(1), 81-92 (2008).
149. M.J. Earle, et al. The distillation and volatility of ionic liquids. *Nature* **439**(7078), 831-834 (2006).
150. M. Bier and S. Dietrich. Vapour pressure of ionic liquids. *Mol. Phys.* **108**(2), 211-214 (2010).
151. S. Baldelli. Influence of Water on the Orientation of Cations at the Surface of a Room-Temperature Ionic Liquid: A Sum Frequency Generation Vibrational Spectroscopic Study. *J. Phys. Chem. B* **107**(25), 6148-6152 (2003).
152. Y. Lauw, et al. X-Ray reflectometry studies on the effect of water on the surface structure of [C₄mpyr][NTf₂] ionic liquid. *PCCP* **11**(48), 11507-11514 (2009).
153. C. Ridings, V. Lockett, and G. Andersson. Significant changes of the charge distribution at the surface of an ionic liquid due to the presence of small amounts of water. *PCCP* **13**(48), 21301-21307 (2011).
154. J.A. Harrison, et al. Photodissociation of NO₂ at 355 and 351 nm Investigated by Photofragment Translational Spectroscopy. *J. Phys. Chem.* **98**(47), 12260-12269 (1994).
155. S.A. Reid and H. Reisler. Experimental studies of resonances in unimolecular decomposition. *Annu. Rev. Phys. Chem.* **47**(1), 495-525 (1996).
156. S.P. Sander, et al. Chemical kinetics and photochemical data for use in atmospheric studies: evaluation number 17. (National Aeronautics and Space Administration, Jet Propulsion Laboratory, California Institute of Technology Pasadena, CA, 2011).
157. C. Chen, B.C. Shepler, B.J. Braams, and J.M. Bowman. Quasiclassical trajectory calculations of the HO₂ + NO reaction on a global potential energy surface. *PCCP* **11**(23), 4722-4727 (2009).
158. K.A. Ramazan, D. Syomin, and B.J. Finlayson-Pitts. The photochemical production of HONO during the heterogeneous hydrolysis of NO₂. *PCCP* **6**(14), 3836-3843 (2004).
159. C. Waring. Collision Dynamics as a Probe of Gas-Liquid and Related Interfaces. PhD thesis, Heriot-Watt University (2011).
160. G. Paterson. Collisional depolarisation of rotational angular momentum in the OH radical. PhD thesis, Heriot Watt University (2011).
161. R.N. Zare and P.J. Dagdigian. Tunable Laser Fluorescence Method for Product State Analysis. *Science* **185**(4153), 739-747 (1974).
162. J.L. Kinsey. Laser-Induced Fluorescence. *Annu. Rev. Phys. Chem.* **28**(1), 349-372 (1977).
163. A. Cessou, U. Meier, and D. Stepowski. Applications of planar laser induced fluorescence in turbulent reacting flows. *Meas. Sci. Technol.* **11**(7), 887 (2000).
164. C.H. Greene and R.N. Zare. Determination of product population and alignment using laser-induced fluorescence. *J. Chem. Phys.* **78**(11), 6741-6753 (1983).
165. J.M. Brown and A. Carrington. Rotational Spectroscopy of Diatomic Molecules. (Cambridge University Press, 2003).
166. H. Lefebvre-Brion and R.W. Field. The Spectra and Dynamics of Diatomic Molecules. (Academic Press, 2004).
167. LabVIEW Professional Development System v. 13.0 (National Instruments, 2013).
168. LIFBASE: Database and spectral simulation v. 1.5 (SRI International, 1999).

169. R. Altkorn and R.N. Zare. Effects of Saturation on Laser-Induced Fluorescence Measurements of Population and Polarization. *Annu. Rev. Phys. Chem.* **35**(1), 265-289 (1984).
170. D.J. Garton, et al. Hyperthermal reactions of O(³P) with alkanes: Observations of novel reaction pathways in crossed-beams and theoretical studies. *J. Phys. Chem. A* **107**(23), 4583-4587 (2003).
171. D. Troya. Barriers of hydrogen abstraction from primary, secondary, and tertiary alkane sites by O(³P). *J. Phys. Chem. A* **111**(42), 10745-10753 (2007).
172. K. Kleinermanns and A.C. Luntz. The chemical dynamics of hydrogen atom abstraction from unsaturated hydrocarbons by O(³P). *J. Chem. Phys.* **77**(7), 3533-3536 (1982).
173. A.M. Schmoltner, P.M. Chu, R.J. Brudzynski, and Y.T. Lee. Crossed Molecular Beam Study of the Reaction O(³P)+C₂H₄. *J. Chem. Phys.* **91**(11), 6926-6936 (1989).
174. R.J. Cvetanović. Addition of Atoms to Olefins in the Gas Phase, in *Advances in Photochemistry*, 115-182 (John Wiley & Sons, 1963).
175. N.J. Dutton, I.W. Fletcher, and J.C. Whitehead. Laser-induced fluorescence determination of the internal state distributions of OH(X²Π) produced in molecular beam reactions of O(³P) with some cyclic hydrocarbons. *Mol. Phys.* **52**(2), 475-483 (1984).
176. Z.Y. Min, T.H. Wong, H.M. Su, and R. Bersohn. Reaction of O(³P) with alkenes: Side chain vs double bond attack. *J. Phys. Chem. A* **104**(44), 9941-9943 (2000).
177. R. Quandt, Z. Min, X. Wang, and R. Bersohn. Reactions of O(³P) with Alkenes: H, CH₂CHO, CO, and OH Channels. *J. Phys. Chem. A* **102**(1), 60-64 (1998).
178. A.N. Hughes, M.D. Scheer, and R. Klein. The Reaction between O(³P) and Condensed Olefins below 100 K. *J. Phys. Chem.* **70**(3), 798-805 (1966).
179. K.D. Gibson and S.J. Sibener. O(³P) reactions with small alkenes adsorbed on Rh, Au, and ice. *Surf. Sci.* **600**(6), L76-L79 (2006).
180. K. Relf. Collision Dynamics as a Tool to Investigate the Interactions of Radicals with Liquid Surfaces. PhD thesis, Heriot-Watt University (2013).
181. K.G. McKendrick, D.J. Rakestraw, and R.N. Zare. Product state distributions from the reaction O(³P) + HBr. *Faraday Discuss.* **84**, 39-52 (1987).
182. G.M. Sweeney, A. Watson, and K.G. McKendrick. Rotational and spin-orbit effects in the dynamics of O(³P_j) + hydrocarbon reactions.1. Experimental results. *J. Chem. Phys.* **106**(22), 9172-9181 (1997).
183. G.M. Sweeney and K.G. McKendrick. Rotational and spin-orbit effects in the dynamics of O(³P_j)+hydrocarbon reactions. 2. Models for spin-orbit propensities. *J. Chem. Phys.* **106**(22), 9182-9189 (1997).
184. G.H. Dieke and H.M. Crosswhite. The ultraviolet bands of OH Fundamental data. *J. Quant. Spectrosc. Radiat. Transfer* **2**(2), 97-199 (1962).
185. J.R. Kanofsky, D. Lucas, and D. Gutman. Direct identification of free-radical products of O-atom reactions with olefins, using high-intensity molecular beams. *Symp. Int. Combust.* **14**(1), 285-294 (1973).
186. J.L. Gardner and S.M. Miller. 2A'-2A' detection of vibrationally excited HCO produced by the O(³P)+C₂H₄ reaction. *J. Chem. Phys.* **121**(12), 5920-5928 (2004).
187. P. Casavecchia, et al. Dynamics of the O(³P)+C₂H₄ reaction: Identification of five primary product channels (vinoxy, acetyl, methyl, methylene, and ketene) and branching ratios by the crossed molecular beam technique with soft electron ionization. *J. Phys. Chem. A* **109**(16), 3527-3530 (2005).

188. S.-H. Lee, W.-K. Chen, and W.-J. Huang. Exploring the dynamics of reactions of oxygen atoms in states $3P$ and $1D$ with ethene at collision energy 3 kcal mol^{-1} . *J. Chem. Phys.* **130**(5), 054301 (2009).
189. B. Fu, et al. Experimental and theoretical studies of the $O(^3P) + C_2H_4$ reaction dynamics: collision energy dependence of branching ratios and extent of intersystem crossing. *J. Chem. Phys.* **137**(22), 22A532 (2012).
190. W. Hu, G. Lendvay, B. Maiti, and G.C. Schatz. Trajectory surface hopping study of the $O(^3P)$ plus ethylene reaction dynamics. *J. Phys. Chem. A* **112**(10), 2093-2103 (2008).
191. W. Zhang, B. Du, and C. Feng. An ab initio dynamics study on the reaction of $O(^3P)$ with $CH_3CH=CH_2$ ($^1A'$). *J. Mol. Struct. THEOCHEM* **806**(1-3), 121-129 (2007).
192. R.J. Cvetanovic, D.F. Ring, and L.C. Doyle. Reaction of oxygen atoms with cyclopentene. *J. Phys. Chem.* **75**(20), 3056-3061 (1971).
193. R. Atkinson and R.J. Cvetanovic. Activation Energies of the Addition of $O(^3P)$ Atoms to Olefins. *J. Chem. Phys.* **56**(1), 432-437 (1972).
194. J.D. Savee, O. Welz, C.A. Taatjes, and D.L. Osborn. New mechanistic insights to the $O(^3P) +$ propene reaction from multiplexed photoionization mass spectrometry. *PCCP* **14**(30), 10410-10423 (2012).
195. J.D. Smith, et al. The heterogeneous reaction of hydroxyl radicals with sub-micron squalane particles: a model system for understanding the oxidative aging of ambient aerosols. *Atmos. Chem. Phys.* **9**(9), 3209-3222 (2009).
196. T. Nah, et al. Isomeric Product Detection in the Heterogeneous Reaction of Hydroxyl Radicals with Aerosol Composed of Branched and Linear Unsaturated Organic Molecules. *J. Phys. Chem. A* **118**(49), 11555-11571 (2014).
197. R.E. Huie, J.T. Herron, and D.D. Davis. Absolute rate constants for addition and abstraction reactions of atomic oxygen with 1-butene over the temperature range 190-491 K. *J. Phys. Chem.* **76**(23), 3311-3313 (1972).
198. G.Y. Adusei and A. Fontijn. Comparison of the Kinetics of $O(^3P)$ Reactions with the Four Butenes over Wide Temperature Ranges. *J. Phys. Chem.* **98**(14), 3732-3739 (1994).
199. J.T. Herron. Evaluated Chemical Kinetic Data for the Reactions of Atomic Oxygen $O(^3P)$ with Saturated Organic Compounds in the Gas Phase. *J. Phys. Chem. Ref. Data* **17**(3), 967-1026 (1988).
200. A.M.G. Ding, et al. Effect of changing reagent energy on reaction probability and product energy-distribution. *Faraday Discuss. Chem. Soc.* **55**(0), 252-276 (1973).
201. J.C. Polanyi. Concepts in reaction dynamics. *Acc. Chem. Res.* **5**(5), 161-168 (1972).
202. T. Suzuki and E. Hirota. Vibrational distribution of CH_3 produced by the reaction of $O(^1D_2)$ atom with CH_4 . *J. Chem. Phys.* **98**(3), 2387-2398 (1993).
203. H. Tsurumaki, Y. Fujimura, and O. Kajimoto. Stereodynamics of the reactions of $O(^3P)$ with saturated hydrocarbons: The dependences on the collision energy and the structural features of hydrocarbons. *J. Chem. Phys.* **112**(19), 8338-8346 (2000).
204. X.H. Liu, et al. Imaging $O(^3P)$ plus alkane reactions in crossed molecular beams: Vertical versus adiabatic H abstraction dynamics. *J. Chem. Phys.* **117**(17), 7947-7959 (2002).
205. X.H. Liu, R.L. Gross, and A.G. Suits. Differential cross sections for $O(^3P)$ +alkane reactions by direct imaging. *J. Chem. Phys.* **116**(13), 5341-5344 (2002).

206. T. Iimori, et al. Orientational ordering of alkyl chain at the air/liquid interface of ionic liquids studied by sum frequency vibrational spectroscopy. *Chem. Phys. Lett.* **389**(4–6), 321-326 (2004).
207. S. Rivera-Rubero and S. Baldelli. Influence of Water on the Surface of Hydrophilic and Hydrophobic Room-Temperature Ionic Liquids. *J. Am. Chem. Soc.* **126**(38), 11788-11789 (2004).
208. J. Sung, et al. Air–liquid interface of ionic liquid+H₂O binary system studied by surface tension measurement and sum-frequency generation spectroscopy. *Chem. Phys. Lett.* **406**(4–6), 495-500 (2005).
209. S. Rivera-Rubero and S. Baldelli. Surface Characterization of 1-Butyl-3-methylimidazolium Br⁻, I⁻, PF₆⁻, BF₄⁻, (CF₃SO₂)₂N⁻, SCN⁻, CH₃SO₃⁻, CH₃SO₄⁻, and (CN)₂N⁻ Ionic Liquids by Sum Frequency Generation. *J. Phys. Chem. B* **110**(10), 4756-4765 (2006).
210. T. Iimori, et al. Local Structure at the Air/Liquid Interface of Room-Temperature Ionic Liquids Probed by Infrared–Visible Sum Frequency Generation Vibrational Spectroscopy: 1-Alkyl-3-methylimidazolium Tetrafluoroborates. *J. Phys. Chem. B* **111**(18), 4860-4866 (2007).
211. C.S. Santos and S. Baldelli. Surface Orientation of 1-Methyl-, 1-Ethyl-, and 1-Butyl-3-methylimidazolium Methyl Sulfate as Probed by Sum-Frequency Generation Vibrational Spectroscopy. *J. Phys. Chem. B* **111**(18), 4715-4723 (2007).
212. C.S. Santos, S. Rivera-Rubero, S. Dibrov, and S. Baldelli. Ions at the Surface of a Room-Temperature Ionic Liquid. *J. Phys. Chem. C* **111**(21), 7682-7691 (2007).
213. T. Iwahashi, et al. Anion configuration at the air/liquid interface of ionic liquid bmim OTf studied by sum-frequency generation spectroscopy. *J. Phys. Chem. B* **112**(38), 11936-11941 (2008).
214. Y. Jeon, et al. Interfacial Restructuring of Ionic Liquids Determined by Sum-Frequency Generation Spectroscopy and X-Ray Reflectivity. *J. Phys. Chem. C* **112**(49), 19649-19654 (2008).
215. C.S. Santos and S. Baldelli. Alkyl Chain Interaction at the Surface of Room Temperature Ionic Liquids: Systematic Variation of Alkyl Chain Length (R = C₁–C₄, C₈) in both Cation and Anion of [RMIM][R–OSO₃] by Sum Frequency Generation and Surface Tension. *J. Phys. Chem. B* **113**(4), 923-933 (2009).
216. I.S. Martinez and S. Baldelli. On the Arrangement of Ions in Imidazolium-Based Room Temperature Ionic Liquids at the Gas-Liquid Interface, Using Sum Frequency Generation, Surface Potential, and Surface Tension Measurements. *J. Phys. Chem. C* **114**(26), 11564-11575 (2010).
217. V. Lockett, R. Sedev, C. Bassell, and J. Ralston. Angle-resolved X-ray photoelectron spectroscopy of the surface of imidazolium ionic liquids. *PCCP* **10**(9), 1330-1335 (2008).
218. C. Kolbeck, et al. Influence of Different Anions on the Surface Composition of Ionic Liquids Studied Using ARXPS. *J. Phys. Chem. B* **113**(25), 8682-8688 (2009).
219. K.R.J. Lovelock, et al. Influence of Different Substituents on the Surface Composition of Ionic Liquids Studied Using ARXPS. *J. Phys. Chem. B* **113**(9), 2854-2864 (2009).
220. C. Kolbeck, et al. Density and Surface Tension of Ionic Liquids. *J. Phys. Chem. B* **114**(51), 17025-17036 (2010).
221. V. Lockett, et al. Orientation and mutual location of ions at the surface of ionic liquids. *PCCP* **12**(41), 13816-13827 (2010).

222. F. Maier, et al. Insights into the surface composition and enrichment effects of ionic liquids and ionic liquid mixtures. *PCCP* **12**(8), 1905-1915 (2010).
223. C. Kolbeck, et al. Influence of Substituents and Functional Groups on the Surface Composition of Ionic Liquids. *Chem. Eur. J.* **20**(14), 3954-3965 (2014).
224. O. Höfft, et al. Electronic Structure of the Surface of the Ionic Liquid [EMIM][Tf₂N] Studied by Metastable Impact Electron Spectroscopy (MIES), UPS, and XPS. *Langmuir* **22**(17), 7120-7123 (2006).
225. S. Krischok, et al. Temperature-Dependent Electronic and Vibrational Structure of the 1-Ethyl-3-methylimidazolium Bis(trifluoromethylsulfonyl)amide Room-Temperature Ionic Liquid Surface: A Study with XPS, UPS, MIES, and HREELS. *J. Phys. Chem. B* **111**(18), 4801-4806 (2007).
226. T. Iwahashi, et al. Surface Structural Study on Ionic Liquids Using Metastable Atom Electron Spectroscopy. *J. Phys. Chem. C* **113**(44), 19237-19243 (2009).
227. A. Ulbrich, M. Reinmöller, W.J.D. Beenken, and S. Krischok. Surface Electronic Structure of [XMIm]Cl Probed by Surface-Sensitive Spectroscopy. *ChemPhysChem* **13**(7), 1718-1724 (2012).
228. J. Bowers, M.C. Vergara-Gutierrez, and J.R.P. Webster. Surface ordering of amphiphilic ionic liquids. *Langmuir* **20**(2), 309-312 (2004).
229. E. Sloutskin, et al. Surface Layering in Ionic Liquids: An X-ray Reflectivity Study. *J. Am. Chem. Soc.* **127**(21), 7796-7804 (2005).
230. E. Sloutskin, R.M. Lynden-Bell, S. Balasubramanian, and M. Deutsch. The surface structure of ionic liquids: Comparing simulations with x-ray measurements. *J. Chem. Phys.* **125**(17), (2006).
231. V. Halka, R. Tsekov, and W. Freyland. Peculiarity of the liquid/vapour interface of an ionic liquid: study of surface tension and viscoelasticity of liquid BMImPF₆ at various temperatures. *PCCP* **7**(9), 2038-2043 (2005).
232. T. Hoshino, Y. Ohmasa, R. Osada, and M. Yao. Dispersion relation of capillary waves on ionic liquids: Observation of the fast overdamped mode. *Phys. Rev. E* **78**(6), 061604 (2008).
233. Y. Ohmasa, T. Hoshino, R. Osada, and M. Yao. Surface waves at the liquid-vapor interface of ionic liquid [bmim][TFSI]. *Chem. Phys. Lett.* **455**(4-6), 184-188 (2008).
234. E. Sloutskin, et al. Dynamics and critical damping of capillary waves in an ionic liquid. *Phys. Rev. E* **77**(6), 060601 (2008).
235. Y. Ohmasa and M. Yao. Surface waves on non-Newtonian viscoelastic liquids. *Phys. Rev. E* **83**(3), 031605 (2011).
236. A. Ohno, et al. Observation of surface structure of 1-butyl-3-methylimidazolium hexafluorophosphate using high-resolution Rutherford backscattering spectroscopy. *J. Chem. Phys.* **130**(20), 204705 (2009).
237. H. Hashimoto, et al. Surface characterization of imidazolium ionic liquids by high-resolution Rutherford backscattering spectroscopy and X-ray photoelectron spectroscopy. *Surf. Sci.* **604**(3-4), 464-469 (2010).
238. K. Nakajima, et al. Observation of surface structure of 1-alkyl-3-methylimidazolium bis(trifluoromethanesulfonyl)imide using high-resolution Rutherford backscattering spectroscopy. *J. Chem. Phys.* **133**(4), 044702 (2010).
239. S. Caporali, U. Bardi, and A. Lavacchi. X-ray photoelectron spectroscopy and low energy ion scattering studies on 1-butyl-3-methyl-imidazolium bis(trifluoromethane) sulfonimide. *J. Electron. Spectrosc. Relat. Phenom.* **151**(1), 4-8 (2006).
240. I.J. Villar-Garcia, et al. The ionic liquid-vacuum outer atomic surface: a low-energy ion scattering study. *Chem. Sci.* **5**(11), 4404-4418 (2014).

241. T. Hammer, M. Reichelt, and H. Morgner. Influence of the aliphatic chain length of imidazolium based ionic liquids on the surface structure. *PCCP* **12**(36), 11070-11080 (2010).
242. M. Reichelt, T. Hammer, and H. Morgner. Influence of water on the surface structure of 1-hexyl-3-methylimidazolium chloride. *Surf. Sci.* **605**(15–16), 1402-1411 (2011).
243. C. Ridings, V. Lockett, and G. Andersson. Effect of the aliphatic chain length on electrical double layer formation at the liquid/vacuum interface in the $[C_n\text{mim}][\text{BF}_4]$ ionic liquid series. *PCCP* **13**(38), 17177-17184 (2011).
244. C. Ridings, V. Lockett, and G. Andersson. Comparing the charge distribution along the surface normal in the $[C_6\text{mim}]^+$ ionic liquid with different anions. *Colloids Surf., A* **413**(0), 149-153 (2012).
245. T.J. Gannon, et al. First Observation of Molecular Composition and Orientation at the Surface of a Room-Temperature Ionic Liquid. *Langmuir* **15**(24), 8429-8434 (1999).
246. G. Law, P.R. Watson, A.J. Carmichael, and K.R. Seddon. Molecular composition and orientation at the surface of room-temperature ionic liquids: Effect of molecular structure. *PCCP* **3**(14), 2879-2885 (2001).
247. G. Law and P.R. Watson. Surface orientation in ionic liquids. *Chem. Phys. Lett.* **345**(1–2), 1-4 (2001).
248. E.F. Smith, et al. Ionic Liquids in Vacuo: Analysis of Liquid Surfaces Using Ultra-High-Vacuum Techniques. *Langmuir* **22**(22), 9386-9392 (2006).
249. J. Günster, O. Höfft, S. Krischok, and R. Souda. A time-of-flight secondary ion mass spectroscopy study of 1-ethyl-3-methylimidazolium bis(trifluoromethylsulfonyl)imide RT-ionic liquid. *Surf. Sci.* **602**(21), 3403-3407 (2008).
250. M.P. Ziemkiewicz, J.R. Roscioli, and D.J. Nesbitt. State-to-state dynamics at the gas-liquid metal interface: Rotationally and electronically inelastic scattering of NO [$^2\Pi_{1/2}(0.5)$] from molten gallium. *J. Chem. Phys.* **134**(23), 234703 (2011).
251. R.M. Lynden-Bell. Gas-liquid interfaces of room temperature ionic liquids. *Mol. Phys.* **101**(16), 2625-2633 (2003).
252. J.N. Canongia Lopes, J. Deschamps, and A.A.H. Pádua. Modeling Ionic Liquids Using a Systematic All-Atom Force Field. *J. Phys. Chem. B* **108**(6), 2038-2047 (2004).
253. J.N. Canongia Lopes and A.A.H. Pádua. Molecular Force Field for Ionic Liquids Composed of Triflate or Bistriflylimide Anions. *J. Phys. Chem. B* **108**(43), 16893-16898 (2004).
254. B.L. Bhargava and S. Balasubramanian. Layering at an Ionic Liquid–Vapor Interface: A Molecular Dynamics Simulation Study of $[\text{bmim}][\text{PF}_6]$. *J. Am. Chem. Soc.* **128**(31), 10073-10078 (2006).
255. R.M. Lynden-Bell and M. Del Popolo. Simulation of the surface structure of butylmethylimidazolium ionic liquids. *PCCP* **8**(8), 949-954 (2006).
256. T.Y. Yan, et al. Structure of the liquid-vacuum interface of room-temperature ionic liquids: A molecular dynamics study. *J. Phys. Chem. B* **110**(4), 1800-1806 (2006).
257. R.M. Lynden-Bell, et al. Simulations of Ionic Liquids, Solutions, and Surfaces. *Acc. Chem. Res.* **40**(11), 1138-1145 (2007).
258. A. Sanmartín Pensado, P. Malfreyt, and A.A.H. Pádua. Molecular Dynamics Simulations of the Liquid Surface of the Ionic Liquid 1-Hexyl-3-methylimidazolium Bis(trifluoromethanesulfonyl)amide: Structure and Surface Tension. *J. Phys. Chem. B* **113**(44), 14708-14718 (2009).

259. G. Hantal, M.N.D.S. Cordeiro, and M. Jorge. What does an ionic liquid surface really look like? Unprecedented details from molecular simulations. *PCCP* **13**(48), 21230-21232 (2011).
260. A.S. Pensado, et al. Effect of alkyl chain length and hydroxyl group functionalization on the surface properties of imidazolium ionic liquids. *PCCP* **13**(30), 13518-13526 (2011).
261. S.S. Sarangi, S.G. Raju, and S. Balasubramanian. Molecular dynamics simulations of ionic liquid-vapour interfaces: effect of cation symmetry on structure at the interface. *PCCP* **13**(7), 2714-2722 (2011).
262. M.H. Ghatee, A.R. Zolghadr, F. Moosavi, and Y. Ansari. Studies of structural, dynamical, and interfacial properties of 1-alkyl-3-methylimidazolium iodide ionic liquids by molecular dynamics simulation. *J. Chem. Phys.* **136**(12), (2012).
263. G. Hantal, I. Voroshylova, M.N.D.S. Cordeiro, and M. Jorge. A systematic molecular simulation study of ionic liquid surfaces using intrinsic analysis methods. *PCCP* **14**(15), 5200-5213 (2012).
264. M. Lisal, Z. Posel, and P. Izak. Air-liquid interfaces of imidazolium-based TF_2N^- ionic liquids: insight from molecular dynamics simulations. *PCCP* **14**(15), 5164-5177 (2012).
265. M. Lisal, Z. Chval, J. Storch, and P. Izák. Towards molecular dynamics simulations of chiral room-temperature ionic liquids. *J. Mol. Liq.* **189**(0), 85-94 (2014).
266. J.K. Konieczny and B. Szeferczyk. Structure of Alkylimidazolium-Based Ionic Liquids at the Interface with Vacuum and Water—A Molecular Dynamics Study. *J. Phys. Chem. B* **119**(9), 3795-3807 (2015).
267. M. Salanne. Simulations of room temperature ionic liquids: from polarizable to coarse-grained force fields. *PCCP* **17**(22), 14270-14279 (2015).
268. F. Eisenhaber, et al. The double cubic lattice method: Efficient approaches to numerical integration of surface area and volume and to dot surface contouring of molecular assemblies. *J. Comput. Chem.* **16**(3), 273-284 (1995).
269. J.D. Holbrey and K.R. Seddon. The phase behaviour of 1-alkyl-3-methylimidazolium tetrafluoroborates; ionic liquids and ionic liquid crystals. *J. Chem. Soc., Dalton Trans.* (13), 2133-2139 (1999).
270. M.A. Tesa-Serrate, et al. Ionic Liquid–Vacuum Interfaces Probed by Reactive Atom Scattering: Influence of Alkyl Chain Length and Anion Volume. *J. Phys. Chem. C* **119**(10), 5491-5505 (2015).
271. E.W. Wilson, et al. Measurement and Estimation of Rate Constants for the Reactions of Hydroxyl Radical with Several Alkanes and Cycloalkanes. *J. Phys. Chem. A* **110**(10), 3593-3604 (2006).
272. W. Beichel, P. Eiden, and I. Krossing. Establishing Consistent van der Waals Volumes of Polyatomic Ions from Crystal Structures. *ChemPhysChem* **14**(14), 3221-3226 (2013).
273. C. Reichardt. Polarity of ionic liquids determined empirically by means of solvatochromic pyridinium N-phenolate betaine dyes. *Green Chem.* **7**(5), 339-351 (2005).
274. A. Oehlke, K. Hofmann, and S. Spange. New aspects on polarity of 1-alkyl-3-methylimidazolium salts as measured by solvatochromic probes. *New J. Chem.* **30**(4), 533-536 (2006).
275. R. Lungwitz, M. Friedrich, W. Linert, and S. Spange. New aspects on the hydrogen bond donor (HBD) strength of 1-butyl-3-methylimidazolium room temperature ionic liquids. *New J. Chem.* **32**(9), 1493-1499 (2008).

276. M.A. Ab Rani, et al. Understanding the polarity of ionic liquids. *PCCP* **13**(37), 16831-16840 (2011).
277. T. Cremer, et al. Towards a Molecular Understanding of Cation-Anion Interactions-Probing the Electronic Structure of Imidazolium Ionic Liquids by NMR Spectroscopy, X-ray Photoelectron Spectroscopy and Theoretical Calculations. *Chem. Eur. J.* **16**(30), 9018-9033 (2010).
278. K. Dong, et al. Understanding Structures and Hydrogen Bonds of Ionic Liquids at the Electronic Level. *J. Phys. Chem. B* **116**(3), 1007-1017 (2011).
279. P.M. Richard, A. Claire, W. Tom, and A.H. Patricia. The impact of anion electronic structure: similarities and differences in imidazolium based ionic liquids. *J. Phys.: Condens. Matter* **26**(28), 284112 (2014).
280. P. Jungwirth and D.J. Tobias. Molecular Structure of Salt Solutions: A New View of the Interface with Implications for Heterogeneous Atmospheric Chemistry. *J. Phys. Chem. B* **105**(43), 10468-10472 (2001).
281. A. Aguado and P.A. Madden. Molecular dynamics simulations of the liquid-vapor interface of a molten salt. III. Size asymmetry effects and binary mixtures. *J. Chem. Phys.* **117**(16), 7659-7668 (2002).
282. P. Wasserscheid and T. Welton. *Ionic Liquids in Synthesis*. (Wiley-VCH Verlag GmbH & Co. KGaA, 2008).
283. C. Aliaga, G.A. Baker, and S. Baldelli. Sum Frequency Generation Studies of Ammonium and Pyrrolidinium Ionic Liquids Based on the Bis-trifluoromethanesulfonimide Anion. *J. Phys. Chem. B* **112**(6), 1676-1684 (2008).
284. S. Men, B.B. Hurisso, K.R.J. Lovelock, and P. Licence. Does the influence of substituents impact upon the surface composition of pyrrolidinium-based ionic liquids? An angle resolved XPS study. *PCCP* **14**(15), 5229-5238 (2012).
285. X. Paredes, et al. Bulk and Liquid-Vapor Interface of Pyrrolidinium-Based Ionic Liquids: A Molecular Simulation Study. *J. Phys. Chem. B* **118**(3), 731-742 (2014).
286. S. Li, et al. Alkyl Chain Length and Temperature Effects on Structural Properties of Pyrrolidinium-Based Ionic Liquids: A Combined Atomistic Simulation and Small-Angle X-ray Scattering Study. *J. Phys. Chem. Lett.* **3**(1), 125-130 (2012).
287. A. Deyko and R.G. Jones. Adsorption, absorption and desorption of gases at liquid surfaces: water on [C₈C₁Im][BF₄] and [C₂C₁Im][Tf₂N]. *Faraday Discuss.* **154**, 265-288 (2012).
288. A.M. Fernandes, et al. Evaluation of Cation-Anion Interaction Strength in Ionic Liquids. *J. Phys. Chem. B* **115**(14), 4033-4041 (2011).
289. S. Men, K.R.J. Lovelock, and P. Licence. X-ray photoelectron spectroscopy of pyrrolidinium-based ionic liquids: cation-anion interactions and a comparison to imidazolium-based analogues. *PCCP* **13**(33), 15244-15255 (2011).
290. J.N. Canongia Lopes, et al. Deviations from Ideality in Mixtures of Two Ionic Liquids Containing a Common Ion. *J. Phys. Chem. B* **109**(8), 3519-3525 (2005).
291. H. Niedermeyer, et al. Mixtures of ionic liquids. *Chem. Soc. Rev.* **41**(23), 7780-7802 (2012).
292. S. Omar, et al. Ionic Liquid Mixtures—An Analysis of Their Mutual Miscibility. *J. Phys. Chem. B* **118**(9), 2442-2450 (2014).
293. M.T. Clough, et al. A physicochemical investigation of ionic liquid mixtures. *Chem. Sci.* **6**(2), 1101-1114 (2015).
294. G. Chatel, et al. Mixing ionic liquids - "simple mixtures" or "double salts"? *Green Chem.* **16**(4), 2051-2083 (2014).

295. S. Bordel Velasco, M. Turmine, D. Di Caprio, and P. Letellier. Micelle formation in ethyl-ammonium nitrate (an ionic liquid). *Colloids Surf., A* **275**(1–3), 50-54 (2006).
296. S. Thomaier and W. Kunz. Aggregates in mixtures of ionic liquids. *J. Mol. Liq.* **130**(1–3), 104-107 (2007).
297. N. Li, et al. Aggregation behavior of long-chain ionic liquids in an ionic liquid. *PCCP* **10**(30), 4375-4377 (2008).
298. M.B. Oliveira, et al. Surface Tension of Binary Mixtures of 1-Alkyl-3-methylimidazolium Bis(trifluoromethylsulfonyl)imide Ionic Liquids: Experimental Measurements and Soft-SAFT Modeling. *J. Phys. Chem. B* **116**(40), 12133-12141 (2012).
299. L. Shi and L. Zheng. Aggregation Behavior of Surface Active Imidazolium Ionic Liquids in Ethylammonium Nitrate: Effect of Alkyl Chain Length, Cations, and Counterions. *J. Phys. Chem. B* **116**(7), 2162-2172 (2012).
300. M. Tariq, et al. Surface tension of ionic liquids and ionic liquid solutions. *Chem. Soc. Rev.* **41**(2), 829-868 (2012).
301. M.B. Oliveira, et al. Surface tensions of binary mixtures of ionic liquids with bis(trifluoromethylsulfonyl)imide as the common anion. *J. Chem. Thermodyn.* **64**(0), 22-27 (2013).
302. E.G. Lemraski and E. Kargar. Standard Gibbs energy of adsorption and surface properties for ionic liquids binary mixtures. *J. Mol. Liq.* **195**(0), 17-21 (2014).
303. A. Klee, S. Prevost, and M. Gradzielski. Self-Assembly of Imidazolium-Based Surfactants in Magnetic Room-Temperature Ionic Liquids: Binary Mixtures. *ChemPhysChem* **15**(18), 4032-4041 (2014).
304. K. Nakajima, S. Oshima, M. Suzuki, and K. Kimura. Surface structures of equimolar mixtures of imidazolium-based ionic liquids using high-resolution Rutherford backscattering spectroscopy. *Surf. Sci.* **606**(21–22), 1693-1699 (2012).
305. K. Nakajima, M. Miyashita, M. Suzuki, and K. Kimura. Surface structures of binary mixtures of imidazolium-based ionic liquids using high-resolution Rutherford backscattering spectroscopy and time of flight secondary ion mass spectroscopy. *J. Chem. Phys.* **139**(22), 224701 (2013).
306. I.J. Villar-Garcia, K.R.J. Lovelock, S. Men, and P. Licence. Tuning the electronic environment of cations and anions using ionic liquid mixtures. *Chem. Sci.* **5**(6), 2573-2579 (2014).
307. R. Souda. Surface segregation in binary mixtures of imidazolium-based ionic liquids. *Surf. Sci.* **604**(19–20), 1694-1697 (2010).
308. G. García, M. Atilhan, and S. Aparicio. Interfacial Properties of Double Salt Ionic Liquids: A Molecular Dynamics Study. *J. Phys. Chem. C* **119**(51), 28405-28416 (2015).
309. S. Palchowdhury and B.L. Bhargava. Segregation of ions at the interface: molecular dynamics studies of the bulk and liquid-vapor interface structure of equimolar binary mixtures of ionic liquids. *PCCP* **17**(30), 19919-19928 (2015).
310. E.A. Guggenheim. Statistical thermodynamics of the surface of a regular solution. *T. Faraday Soc.* **41**(0), 150-156 (1945).
311. H.F.D. Almeida, et al. Cation Alkyl Side Chain Length and Symmetry Effects on the Surface Tension of Ionic Liquids. *Langmuir* **30**(22), 6408-6418 (2014).
312. Á. Piñeiro, et al. Extended Langmuir Isotherm for Binary Liquid Mixtures. *Langmuir* **17**(14), 4261-4266 (2001).
313. P. Brocos, J. Gracia-Fadrique, A. Amigo, and Á. Piñeiro. Application of the Extended Langmuir model to surface tension data of binary liquid mixtures. *Fluid Phase Equilib.* **237**(1–2), 140-151 (2005).

314. J.P. O'Connell and J.M. Haile. Thermodynamics: Fundamentals for Applications. (Cambridge University Press, 2005).
315. J. E. J. Smoll and T.K. Minton. Unpublished results.
316. J. De Roche, et al. Application of complementary experimental techniques to characterization of the phase behavior of [C₁₆mim][PF₆] and [C₁₄mim][PF₆]. *Chem. Mater.* **15**(16), 3089-3097 (2003).
317. S. Rogers, L. D'Andrea, D.W. Bruce, and J.M. Slattery. Unpublished results.
318. K. Shimizu, C.E.S. Bernardes, and J.N. Canongia Lopes. Structure and Aggregation in the 1-Alkyl-3-Methylimidazolium Bis(trifluoromethylsulfonyl)imide Ionic Liquid Homologous Series. *J. Phys. Chem. B* **118**(2), 567-576 (2014).
319. J.R. Roscioli and D.J. Nesbitt. Quantum state resolved velocity-map imaging spectroscopy: A new tool for collision dynamics at gas/self-assembled monolayer interfaces. *Faraday Discuss.* **150**(0), 471-479 (2011).
320. P. Davidovits, et al. Mass Accommodation and Chemical Reactions at Gas-Liquid Interfaces. *Chem. Rev.* **106**(4), 1323-1354 (2006).
321. B. Winter and M. Faubel. Photoemission from Liquid Aqueous Solutions. *Chem. Rev.* **106**(4), 1176-1211 (2006).
322. L. Yang, et al. Making a hybrid microfluidic platform compatible for in situ imaging by vacuum-based techniques. *J. Vac. Sci. Technol., A* **29**(6), 061101 (2011).
323. F. Maier, et al. Surface Enrichment and Depletion Effects of Ions Dissolved in an Ionic Liquid: An X-ray Photoelectron Spectroscopy Study. *Angew. Chem. Int. Ed.* **45**(46), 7778-7780 (2006).
324. C. Kolbeck, et al. Ligand Effects on the Surface Composition of Rh-Containing Ionic Liquid Solutions Used in Hydroformylation Catalysis. *Chem. Eur. J.* **16**(40), 12083-12087 (2010).

Appendix

Publications

I. Published papers

- M. A. Tesa-Serrate, K. L. King, G. Paterson, M.L. Costen, and K. G. McKendrick. Site and bond-specific dynamics of reactions at the gas–liquid interface. *PCCP* **16**(1), 173-183 (2014).
- M. A. Tesa-Serrate, B. C. Marshall, E. J. Smoll, Jr., S. M. Purcell, M. L. Costen, J. M. Slattery, T. K. Minton, and K. G. McKendrick. Ionic Liquid–Vacuum Interfaces Probed by Reactive Atom Scattering: Influence of Alkyl Chain Length and Anion Volume. *J. Phys. Chem. C* **119**(10), 5491-5505 (2015).

II. Papers in press

- M. A. Tesa-Serrate, E. J. Smoll, Jr., T. K. Minton, and K. G. McKendrick. Atomic and Molecular Collisions at Liquid Surfaces. *Annu. Rev. Phys. Chem.*

III. Papers in preparation

- M. A. Tesa-Serrate, E. J. Smoll, Jr., L. D'Andrea, S. M. Purcell, M. L. Costen, D. W. Bruce, J. M. Slattery, T. K. Minton, and K. G. McKendrick. Hiding the headgroup: Remarkable similarity in alkyl coverage of the surfaces of imidazolium- and pyrrolidinium-based ionic liquids.
- D. W. Bruce, C. P. Cabry, J. N. Canongia Lopes, M. L. Costen, L. D'Andrea, B. C. Marshall, K. G. McKendrick, T. K. Minton, S. M. Purcell, S. Rogers, J. M. Slattery, G. C. Schatz, K. Shimizu, E. J. Smoll, Jr., and M. A. Tesa-Serrate. Nano-Segregation and Structuring in the Bulk and at the Surface of ionic Liquid Mixtures.

- S. M. Purcell, B. C. Marshall, M. A. Tesa-Serrate, M. L. Costen, E. J. Smoll, Jr., L. D'Andrea, D. W. Bruce, J. M. Slattery, T. K. Minton, and K. G. McKendrick. Reactive atom scattering from liquid crystals at the vacuum interface: [C₁₂mim][BF₄] and 8CB.
- R. H. Bianchini, M. A. Tesa-Serrate, M. L. Costen, and K. G. McKendrick. Collision-energy dependence of OH reactive uptake by liquid hydrocarbon surfaces.